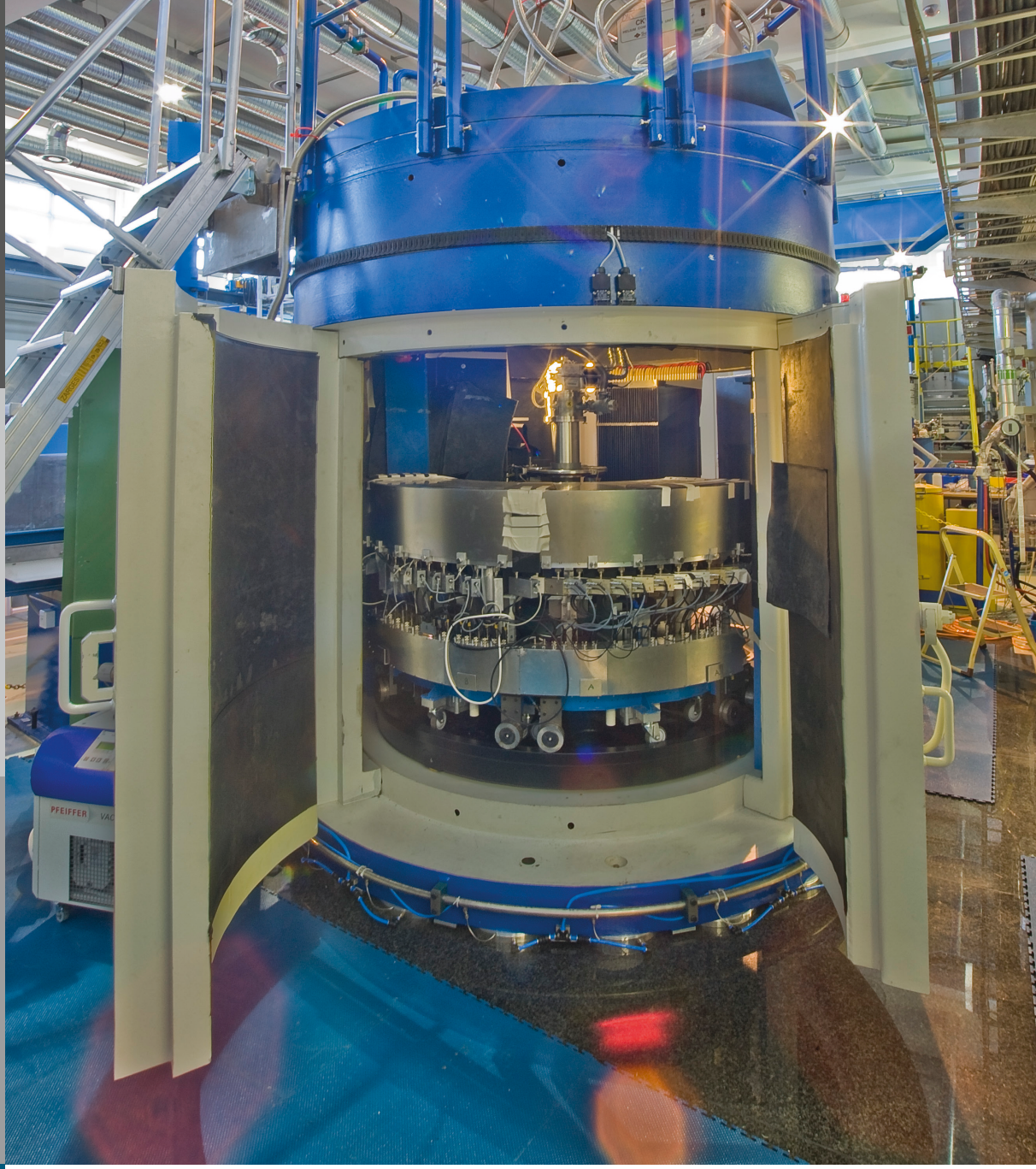

Laboratory Course

Neutron Scattering

Experiment Manuals

Thomas Brückel, Gernot Heger, Dieter Richter,
Georg Roth and Reiner Zorn (Editors)

RWTH Aachen
University Münster

JÜLICH
FORSCHUNGSZENTRUM

Member of the Helmholtz Association

Schriften des Forschungszentrums Jülich
Reihe Schlüsseltechnologien / Key Technologies Band / Volume 64

Forschungszentrum Jülich GmbH
Jülich Centre For Neutron Science (JCNS)

Thomas Brückel, Gernot Heger, Dieter Richter,
Georg Roth and Reiner Zorn (Editors)

Neutron Scattering

Experiment Manuals of the JCNS Laboratory Course held at
Forschungszentrum Jülich and at the
Heinz Maier-Leibnitz Zentrum Garching
In cooperation with
RWTH Aachen and University of Münster

Schriften des Forschungszentrums Jülich
Reihe Schlüsseltechnologien / Key Technologies Band / Volume 64

ISSN 1866-1807 ISBN 978-3-89336-881-5

Bibliographic information published by the Deutsche Nationalbibliothek.
The Deutsche Nationalbibliothek lists this publication in the Deutsche Nationalbibliografie; detailed bibliographic data are available in the Internet at http://dnb.d-nb.de.

Publisher and Distributor:	Forschungszentrum Jülich GmbH Zentralbibliothek 52425 Jülich Phone +49 (0) 24 61 61-53 68 · Fax +49 (0) 24 61 61-61 03 e-mail: zb-publikation@fz-juelich.de Internet: http://www.fz-juelich.de/zb
Cover Design:	Grafische Medien, Forschungszentrum Jülich GmbH
Printer:	Grafische Medien, Forschungszentrum Jülich GmbH
Copyright:	Forschungszentrum Jülich 2013

Schriften des Forschungszentrums Jülich
Reihe Schlüsseltechnologien / Key Technologies Band / Volume 64

ISSN 1866-1807
ISBN 978-3-89336-881-5

The complete volume is freely available on the Internet on the Jülicher Open Access Server (JUWEL) at http://www.fz-juelich.de/zb/juwel

Contents

PUMA

Thermal Triple Axis Spectrometer

O. Sobolev, A. Teichert, N. Jünke

Forschungsneutronenquelle Heinz Maier-Leibnitz (FRM II)
Technische Universität München

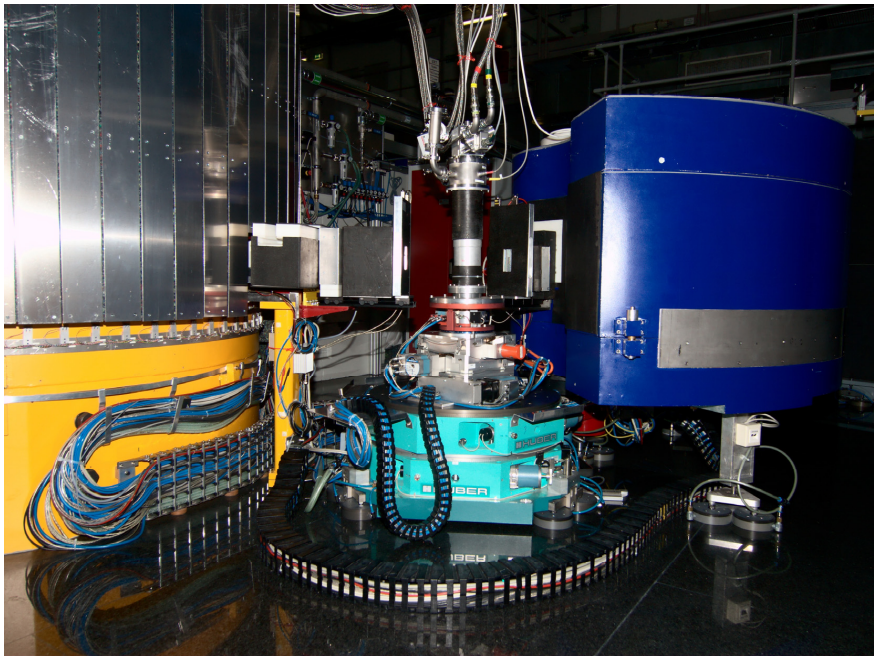

Manual of the JCNS Laboratory Course Neutron Scattering

Contents

1. Introduction

Excitations in crystals can be described using formalism of dispersion relations of the normal modes or quasi-particles (phonons, magnons, etc.). These relations contain the most detailed information on the intermolecular interactions in solids.

The result of a neutron scattering experiment is the distribution of neutrons that have undergone an energy exchange $\hbar\omega = E_i - E_f$, and a wave vector transfer, $\mathbf{Q} = \mathbf{k_i} - \mathbf{k_f}$, after scattering by the sample.:

$$\frac{\mathrm{d}^2\sigma}{\mathrm{d}\Omega \mathrm{d}\omega}(2\theta,\omega) = N\frac{k_f}{k_i}\left\{\frac{\sigma_{coh}}{4\pi}S_{coh}(\mathbf{Q},\omega)+\frac{\sigma_{inc}}{4\pi}S_{inc}(\mathbf{Q},\omega)\right\} \quad (1)$$

σ_{coh} is coherent scattering cross section, σ_{inc} is incoherent scattering cross section. They are constants that can be found in tables (http://www.ncnr.nist.gov/resources/n-lengths/). $S(\mathbf{Q},\omega)$ functions depend only on the structure and dynamics of the sample and do not depend on the interaction between neutrons and the sample. $S_{inc}(\mathbf{Q},\omega)$ reflects individual motions of atoms. $S_{coh}(\mathbf{Q},\omega)$ provides the information on the structure and collective excitations in the sample.

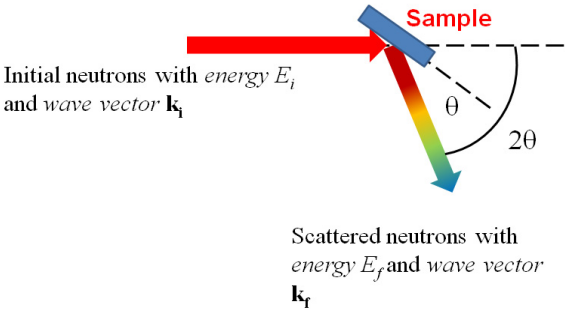

Energy transfer

$\hbar\omega = E_i - E_f$

Momentum transfer

$\mathbf{Q} = \mathbf{k_0} - \mathbf{k_f}$

$$k = \frac{\sqrt{2mE}}{\hbar} = \frac{2\pi}{\lambda}$$

$$Q = \sqrt{k_i^2 + k_f^2 - 2k_i k_f \cos 2\theta}$$

If $k_i = k_f$

$$Q = 2k_i \sin\theta = \frac{4\pi}{\lambda}\sin\theta$$

The triple axis spectrometer is designed for measuring the $S_{coh}(\mathbf{Q},\omega)$ in monocrystals. Therefore this function is of special interest for us.

2. Elastic scattering and Structure of Crystals

In the case of coherent *elastic scattering,* when $\omega = 0$ ($k_i = k_f$) only neutrons, that fulfill the Brags law are scattered by the sample:

$$n\lambda = 2d_{hkl}\sin\theta_{hkl}, \tag{2}$$

where λ is a wavelength of neutron, d_{hkl} is a distance between crystal planes described by corresponding Miller indexes *hkl*. θ_{hkl} denotes the angle between incoming (outgoing) scattering beam and the (hkl) plane.

For the analysis of the scattering processes in crystals it is convenient to use the concept of the *reciprocal space*. For an infinite three dimensional lattice, defined by its primitive vectors $\boldsymbol{a_1}$, $\boldsymbol{a_2}$ and $\boldsymbol{a_3}$, its reciprocal lattice can be determined by generating three reciprocal primitive vectors, through the formulae:

$$\begin{aligned}
\mathbf{g}_1 &= 2\pi \frac{\mathbf{a}_2 \times \mathbf{a}_3}{\mathbf{a}_1 \cdot \mathbf{a}_2 \times \mathbf{a}_3} \\
\mathbf{g}_2 &= 2\pi \frac{\mathbf{a}_1 \times \mathbf{a}_3}{\mathbf{a}_2 \cdot \mathbf{a}_1 \times \mathbf{a}_3} \\
\mathbf{g}_3 &= 2\pi \frac{\mathbf{a}_1 \times \mathbf{a}_2}{\mathbf{a}_3 \cdot \mathbf{a}_1 \times \mathbf{a}_2}
\end{aligned} \tag{3}$$

Note the denominator is the scalar triple product. Geometrically, the scalar triple product $\mathbf{a_1(a_2 \times a_3)}$ is the volume of the parallelepiped defined by the three vectors.

Let us imagine the lattice of points given by the vectors $\mathbf{g_1}$, $\mathbf{g_2}$ and $\mathbf{g_3}$ such that $\boldsymbol{\tau}$ is an arbitrary linear combination of these vectors:

$$\boldsymbol{\tau} = h\mathbf{g}_1 + k\mathbf{g}_2 + l\mathbf{g}_3\,, \tag{4}$$

where *h,k,l* are integers. Every point of the reciprocal lattice, characterized by $\boldsymbol{\tau}$ corresponds in the position space to the equidistant set of planes with Miller indices (*h,k,l*) perpendicular to the vector $\boldsymbol{\tau}$. These planes are separated by the distance

$$d_{hkl} = \frac{2\pi}{|\boldsymbol{\tau}_{hkl}|} \tag{6}$$

The Brag's condition for diffraction can be expressed in the following vector form:

$$\mathbf{Q} = \boldsymbol{\tau}_{hkl} \tag{7}$$

A useful construction for work with wave vectors in reciprocal space is the Brillouin zone (BZ). The BZ is the smallest unit in reciprocal space over which physical quantities such as phonon or electron dispersions repeat themselves. It is constructed by drawing vectors from one reciprocal lattice points to another and then constructing lines perpendicular to these vectors at the midpoints. The smallest enclosed volume is the BZ.

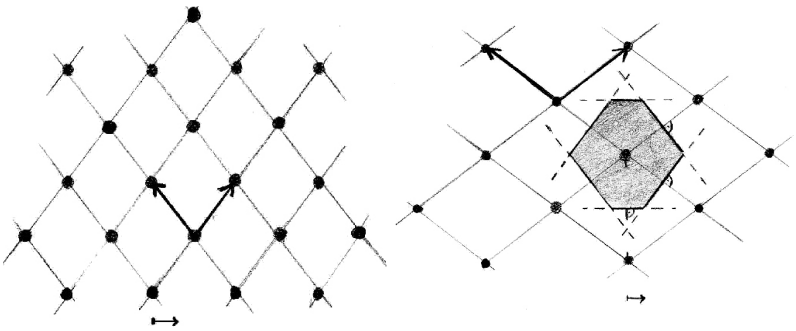

Fig.1 Real (left) and reciprocal (right) two dimensional lattices and BZ (gray area)

3. Inelastic Neutron Scattering and Phonons

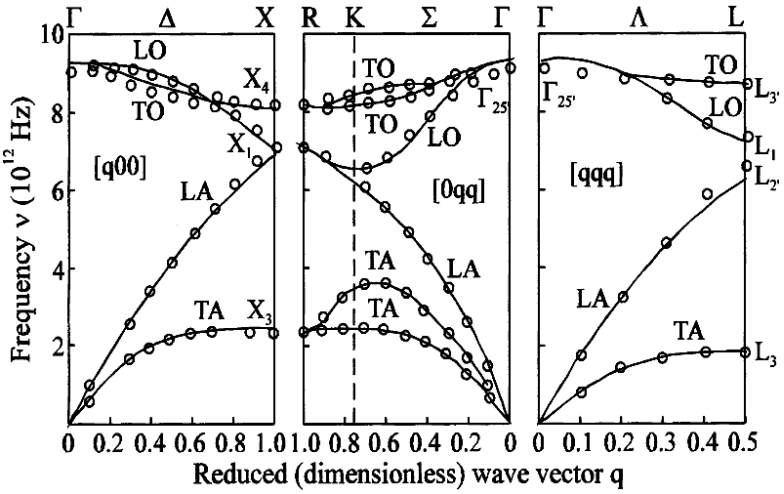

Fig.2 Phonon dispersion curves for Ge.

Atomic vibrations in a crystal can be analyzed in terms of lattice waves which are the normal modes of the crystal. The frequencies of normal modes ω are related to their wave vectors $\mathbf{q}$ ($q = 2\pi/\lambda$) by the dispersion relations

$$\omega = \omega_j(\mathbf{q}), \tag{7}$$

where the index j denotes a particular branch. For a crystal with N atoms per primitive unit cell there are $3N$ branches of the frequency spectrum. Three branches are acoustic ones for which $\omega \to 0$ as $\mathbf{q} \to 0$; the other $3N$-3 are branches are optical branches for which ω tends to a finite value as $\mathbf{q} \to 0$. In certain directions of high symmetry the normal vibrations are strictly transverse or longitudinal. The energy quantum $\hbar\omega$ is called *phonon* in analogy to the phonon for electromagnetic waves.

If we want to measure the frequency of a phonon ω for a certain **q**, the basic scattering conditions must fulfil the energy and momentum conservation laws:

$$E_i - E_f = \frac{\hbar}{2m_n}(k_i^2 - k_f^2) = \pm\hbar\omega(\mathbf{q}) \qquad (9)$$

$$\mathbf{Q} = \mathbf{k_i} - \mathbf{k_f} = \mathbf{G} \pm \mathbf{q}$$

When the above conditions are fulfilled, the function $S_{coh}(\mathbf{Q},\omega)$ shows a peak. We can held **Q** constant and vary $\mathbf{k_i}$ ($\mathbf{k_f}$) to measure intensity of scattered neutrons at different energy transfers. In order to keep **Q**, and thus **q**, constant while varying $\mathbf{k_i}$, the scattering angle must change as well as the relative orientation of the crystal with respect to $\mathbf{k_f}$.

The intensity of neutrons scattered by phonon is proportional to the square of the dynamical structure factor $F(\mathbf{Q})$:

$$S_{coh}(\mathbf{Q},\omega) \sim |F(\mathbf{Q})|^2 = \left| \sum_\kappa b_\kappa \frac{\mathbf{Q}\cdot\mathbf{e}_\kappa(\mathbf{q}_j)}{\sqrt{m_\kappa}} \exp(-W_k)\exp(-i\mathbf{q}\mathbf{r}_\kappa) \right|^2, \qquad (10)$$

Where sum is taken over all atoms in unit cell with coordinates $\mathbf{r}_k$, exp(-W) is a Debye-Waller factor, $\mathbf{e}_k$ denotes the polarization vector of the phonon. The scalar product $\mathbf{Q}\cdot\mathbf{e}_\kappa(\mathbf{q}_j)$ means that only lattice vibrations polarized along the momentum transfer are visible. This makes possible to distinguish transverse (TA) and longitudinal (LA) acoustic modes. For TA modes $\mathbf{e}\perp\mathbf{q}$, and therefore **Q** must be perpendicular to **q**, while for a LA mode, one must take $\mathbf{Q} \,||\, \mathbf{q}$ (Fig. 3)

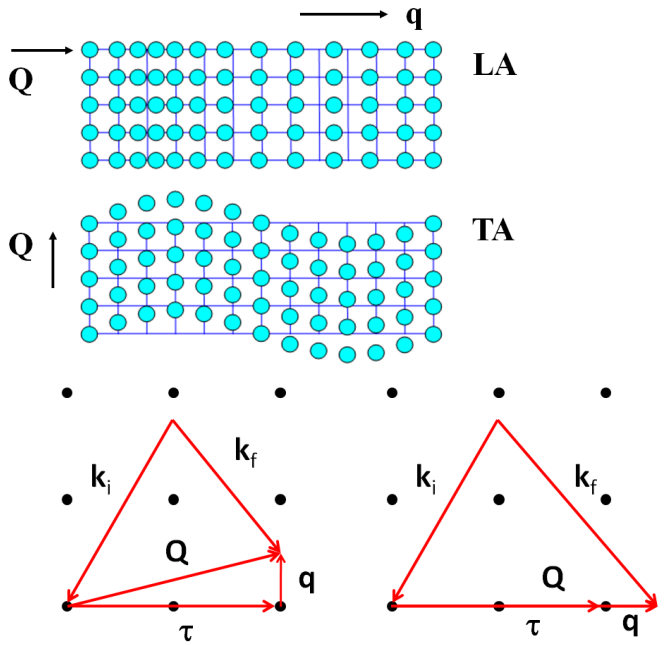

Fig. 3 Top: LA and TA phonons. Bottom: Neutron scattering diagram in the reciprocal space for TA (left) and LA phonons

4. Triple Axis Spectrometer PUMA

The three-axis instrument is the most versatile instrument for use in inelastic scattering because it allows one to probe nearly any coordinates in energy and momentum space in a precisely controlled manner. The three axes correspond to the axes of rotation of the *monochromator* (axis1), *the sample* (axis2), and *the analyzer* (axis3). The monochromator crystal selects neutrons with a certain energy from the white neutron beam emanating from the reactor. The monochromatic beam is then scattered off from the sample (second axis). The neutrons scattered by the sample can have a different energy from those incident on the sample. The energy of these scattered neutrons is then determined by the analyzer crystal (third axis). All three angles (θ_M, θ_S, θ_A) can vary during an experiment, the sample table and analyzer are equipped with air pads, so that they can glide over the "Tanzboden" (dancing floor). Below, we describe in detail each component of a triple-axis spectrometer.

Monochromator

A crystal monochromator is used to select neutrons with a specific wavelength. Neutrons with this wavelength interact with the sample and are scattered off at a similar (elastic) or different wavelength (inelastic). The energy of the neutrons both incident on and scattered from the sample is determined by Bragg reflection from the monochromator and analyzer crystals, respectively. For a specific Bragg plane (hkl) characterized by an interplanar spacing d_{hkl}, the crystal is rotated about a vertical axis. A pyrolytic graphite with d_{002} = 3.35 Å (PG(002)) and a copper with d_{220} = 1.28 Å (Cu(220)) monochromators are available at PUMA. The angular range of the monochromator $2\theta_M$ is of 15^o - 115°. The PG(002) is usually used for energies below 50meV (λ>1.3Å). For higher incident energies the Cu(220) can be used.

Sample table

The sample table from the company Huber provides a possibility to vary independently both $2\theta_S$ and θ_S. It is equipped with a goniometer moving the sample in the three translation axes *x*, *y* and *z* and tilting. The tilt angle is ±15°. Single crystal experiments can be performed with an Euler cradle at PUMA. The sample environment includes magnets, pressure cells, cryostats and high temperature furnace.

Analyzer

Like the monochromator, the PG(002) analyzer consist of 20x5 separate analyzer crystal plates are mounted in an aluminum frame. There is an option to measure with the flat or horisontaly and verticaly focused analyser. The angular range of the analysator $2\theta_M$ is of -130^o - 130°.

Detector and monitor

The detector consists of five counter tubes which are filled with a ^{3}He pressure of 5 bar. To be able to monitor the neutron flux incident on the sample, a low-efficiency neutron counter monitor is usually placed before the sample. Such a monitor is required so that flux variation caused by, for example, the reactor power fluctuations and the change in reflectivity of the monochromator with neutron wavelength can be automatically corrected for.

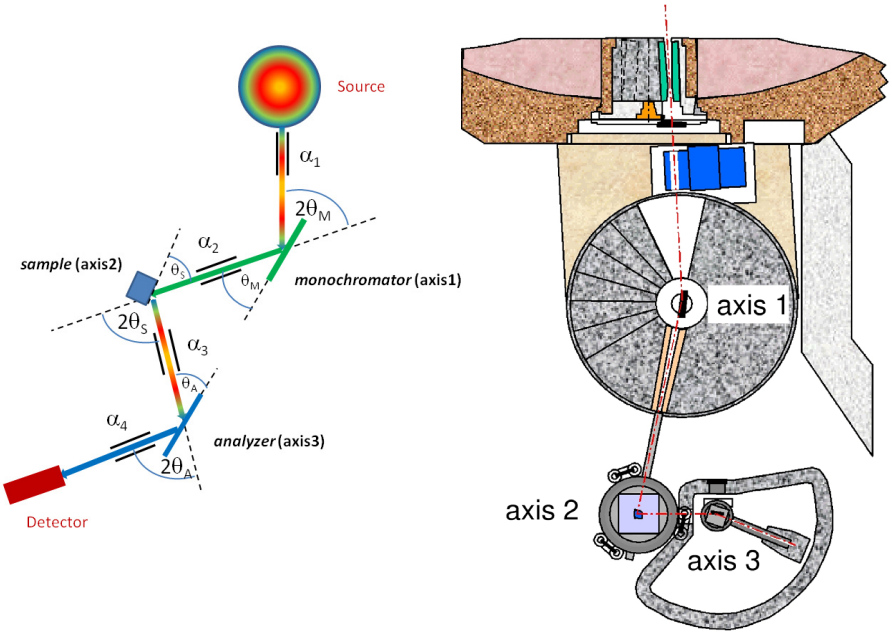

Fig.4 PUMA spectrometer.

Slits, Collimators, Filter

Additional components like slits or collimators are used to define the beam cross section. Collimators (α1- α4) are used for the improvement of the resolution and to specify the beam divergence. They consist of multiple parallel arranged Gd_2O_3 coated foils with a defined angle to the beam. The angular divergence of the collimator in the horizontal plane α is defined by the distance between foils Δd and the length of the collimator l (tan $\alpha = \Delta d / l$). Different collimators with a horizontal divergence between 10' and 60' are available at the instrument.

One of the problems of the TAS method is the possible presence of higher harmonics in the neutron beam. Higher harmonics arise from higher order (hkl) in Bragg's law (2). This means that if the monochromator (analyzer) crystal is set to reflect neutrons with a wavelength of λ from a given (hkl) plane, it will also reflect neutrons with wavelength λ/n. This leads to the appearance of several types of spurious peaks in the observed signal. Different filters are used to eliminate the high-order neutrons and to reduce the background. There are a sapphire filter (Al_2O_3) and an erbium filter (Er) at PUMA. They are installed in front of the monochromator. Sapphire filter is used wavelengths $\lambda > 1$ Å and reduce the background inducing by the epithermal neutrons. Erbium filter is suitable as $\lambda/2$ filter for λ between 0.5 and 1Å as well as $\lambda/3$ filter for λ between 0.7 and 1.6Å.

Components	Axis	PUMAs notation	Description
Monochromator M	θ_M	mth	Monochromator Theta
	$2\theta_M$	mtt	Monochromator 2Theta
		mtx, mty	Monochromator Translation x-, y- direction
		mgx, mgy	Monochromator Goniometer x-, y- direction
		mfh, mfv	Monochromator Focus horizontal, vertical
Sample S	θ_S	psi	Sample Theta
	$2\theta_S$	phi	Sample 2Theta
		stx, sty, stz	Sample Translation x-, y-, z- direction
		sgx, sgy	Sample Goniometer x-, y- direction
Analyzer A	θ_A	ath	Analyzer Theta
	$2\theta_A$	att	Analyzer 2Theta
		atx, aty	Analyzer Translation x-, y- direction
		agx, agy	Analyzer Goniometer x-, y- direction
		afh	Analyzer Focus horizontal
Collimators		alpha1 – alpha4	Collimation

5. Experiment Procedure

The aim of the experiment is to measure acoustic phonons in a germanium sample. The phonons will be measured for [110] (LA) and [001] (TA) directions in [220] BZ.
The experimental procedure shall contain the following steps:

Sample alignment

It is very difficult to align a sample with triple axis spectrometer, if the sample orientation is absolutely unknown. A sample must be pre-aligned, this means that the vertical axis of the sample must be known and roughly perpendicular to the 'Tanzboden'. Than we shall do the following steps:
- Inform the control program of the spectrometer about a scattering plane of the sample. One must set two reciprocal vectors (in our case [110] and [001]) laying in the scattering plane.
- Drive spectrometer (θ_M, $2\theta_M$, θ_S, $2\theta_S$, θ_A, $2\theta_A$,) to the position corresponding to [220] reflection.
- Scan θ_S and find the Brag's peak.
- Scan corresponding goniometer axes to maximize intensity of the peak.
- Do the same for other reflection [004].
- Change the offset of the θ_S so that the nominal θ_S values correspond to intensity maxima for the above reflections.

Phonons measurements

For our measurements we will chose the const-k_f configuration with $k_f = 2.662$ Å^{-1} ($E_f = 14.68$ meV). This means that we will scan the energy transfer $\hbar\omega = E_i - E_f$ by varying incident energy E_i (k_i). We are going to use PG(002) monochromator.

For LA phonon we will do constant-**Q** scans in the energy transfer range $\hbar\omega$ = 0 – 21 meV (0 – 8 THz) for the following points:
Q(r.l.u.) = (2.1, 2.1, 0), (2.2, 2.2, 0), (2.3, 2.3, 0), (2.4, 2.4, 0), (2.5, 2.5, 0), (2.6, 2.6, 0), (2.7, 2.7, 0), (2.75, 2.75, 0).

For TA phonon we will do constant-**Q** scans in the energy transfer range $\hbar\omega$ = 0 – 15 meV (0 – 3.6 THz) for the following points:
Q(r.l.u.) = (2, 2, 0.2), (2, 2, 0.3), (2, 2, 0.4), (2, 2, 0.5), (2, 2, 0.7), (2, 2, 0.8), (2, 2, 0.9), (2, 2, 1).

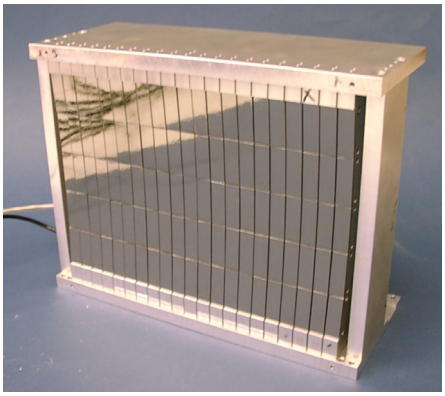

a) PG Analyzer

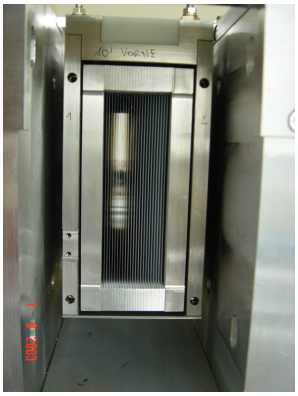

b) Soller collimator

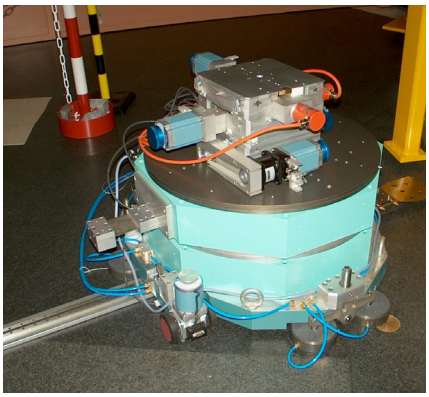

c) Sample table

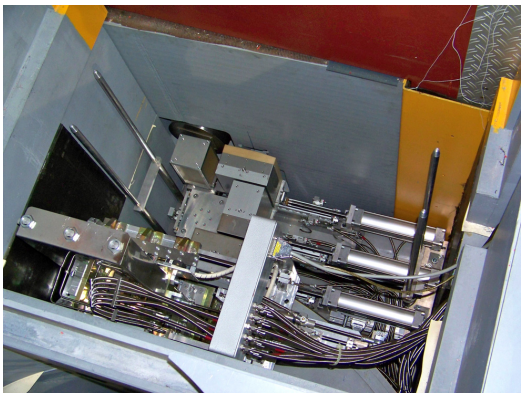

d) Shutter, filters and collimators

e) Analyzer and Detector

f) Detector, consists of 5 ^{3}He tubes

Fig 5 Elements of PUMA

6. Preparatory Exercises

1. Calculate angles θ_M, $2\theta_M$, θ_S, $2\theta_S$ for the reflections [220] and [004] of *germanium* (cubic-diamond, a = 5.66 Å), supposing that $k_f = 2.662$ Å^{-1} = const, monochromator is PG(002), and check, if this reflections are measurable with our experimental setup.

2. Before doing a scan it is important to check that all point in **Q -** $\hbar\omega$ space are available, instrument angles do not exceed high or low limits. Also, an experimental scientist must be sure that the moving instrument will not hit walls or any equipment. Calculate instrument parameters (θ_M, $2\theta_M$, θ_S, $2\theta_S$) for the momentum transfers **Q** (r.l.u.) = (2.1, 2.1, 0), (2.75, 2.75, 0) and energy transfers $\hbar\omega$ = 0 and 21 meV. This can be done using an online triple-axis simulator:
http://www.ill.eu/instruments-support/computing-for-science/cs-software/all-software/vtas/

7. Experiment-Related Exercises

1. Plot obtained spectra for each **Q** as a function of energy (THz). Fit the spectra with Gaussian function and find centers of the phopon peaks. The obtained phonon energies plot as a function of **q.**
2. Why triple-axis spectrometer is the best instrument to study excitations in single crystals?
3. During this practicum we do not consider some problems that are very important for planning experiments with a triple axis instrument such as *resolution* and *intensity zones* [2]. Persons who have a strong interest to the triple-axis spectroscopy should study these topics by oneself. Advanced students should be able to explain our choice of Brillouin zone and parameters of scans for the phonon measurements.

Useful formula and conversions

1 THz = 4.1.4 meV

$n\lambda = 2d_{hkl}\sin\theta_{hkl}$,

$$d_{hkl} = \frac{2\pi}{|\boldsymbol{\tau}_{hkl}|}$$

$$\mathbf{Q} = \mathbf{k_0} - \mathbf{k_f}$$

$$Q = \sqrt{k_i^2 + k_f^2 - 2k_i k_f \cos 2\theta}$$

If $k_i = k_f$ (elastic scattering) $Q = 2k_i \sin\theta = \frac{4\pi}{\lambda}\sin\theta$

E [meV] = 2.072 k^2 [Å^{-1}]

References

[1] Ch. Kittel, Einführung in die Festkörperphysik, Oldenburg, 14th ed., 2006
[2] G. Shirane, S.M. Shapiro, J.M. Tranquada, Neutron Scattering with a Triple-Axis Spektrometer, Cambridge University Press, 2002
[4] G. Eckold, P. Link, J. Neuhaus, Physica B, 276-278 (2000) 122- 123
[5] B.N.Brockhouse and P.K. Iyengar, Physikal Review 111 (1958) 747-754
[6] *http://www.ill.eu/instruments-support/computing-for-science/cs-software/all-software/vtas/*

Contact

PUMA

Phone: + 49 89 289 14914
Web: http://www.frm2.tum.de/wissenschaftliche-nutzung/spektrometrie/puma/index.html

Oleg Sobolev

Georg-August Universität Göttingen
Institut für Physikalische Chemie
Aussenstelle am FRM II
Phone: + 49 89 289 14754
Email: oleg.sobolev@frm2.tum.de

Anke Teichert

Georg-August Universität Göttingen
Institut für Physikalische Chemie
Aussenstelle am FRM II
Phone: + 49 89 289 14756
Email: anke.teichert@frm2.tum.de

Norbert Jünke

Forschungsneutronenquelle Heinz Maier-Leibnitz
ZWE FRM II
Phone: + 49 89 289 14761
Email: norbert.juenke@frm2.tum.de

SPODI

High-resolution powder diffractometer

M. Hoelzel, A. Senyshyn

Forschungsneutronenquelle Heinz Maier-Leibnitz (FRM II)
Technische Universität München

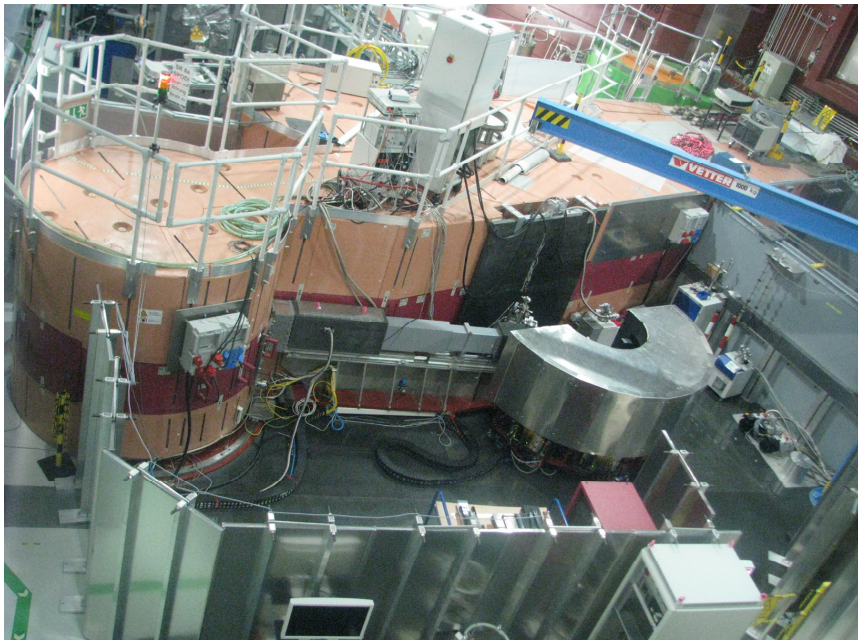

Manual of the JCNS Laboratory Course Neutron Scattering

Contents

1. **Applications of neutron powder diffraction**

Powder diffraction reveals information on the phase composition of a sample and the structural details of the phases. In particular, the positions of the atoms (crystallographic structure) and the ordering of magnetic moments (magnetic structure) can be obtained. In addition to the structural parameters, also some information on the microstructure (crystallite sizes/microstrains) can be obtained. The knowledge of the structure is crucial to understand structure – properties – relationships in any material. Thus, neutron powder diffraction can provide valuable information for the optimisation of modern materials.

Typical applications:

Material	**Task**
Lithium-ion battery materials	Positions of Li atoms, structural changes/phase transitions at the electrodes during operation, diffusion pathways of Li atoms
Hydrogen storage materials	Positions of H atoms, phase transformations during hydrogen absorption/desorption
Ionic conductors for fuel cells	positions of O/N atoms, thermal displacement paramteters of the atoms and disorder at different temperatures, diffusion pathways of O/N atoms
Shape memory alloys	stress-induced phase transforamtions, stress-induced texture development
materials with CMR effect	magnetic moment per atom at different temperatures
catalysers	Structural changes during the uptake of sorbents
Piezoelectric ceramics	Structural changes during poling in electric field, positions of O atoms
Nickel superalloys	Phase transformations at high temperatures, lattice mismatch of phases
magnetic shape memory alloys	Magneto-elastic effects, magnetic moment per atom at different temperatures and magnetic fields

2. Basics of Powder Diffraction

Diffraction can be regarded as detection of interference phenomena resulting from coherent elastic scattering of neutron waves from crystalline matter. Crystals can be imagined by a three-dimenional periodic arrangement of unit cells. The unit cell is characterised by the lattice parameters (dimensions and angles) and the positions of atoms or molecules.
For diffraction experiments the probe should have a wavelength comparable to interatomic distances: this is possible for X-rays, electrons or neutrons.

Structure factor

The structure factor describes the intensity of Bragg reflections with Miller indexes (*hkl*), based on the particular atomic arrangement in the unit cell

$$F_{hkl} = \sum_{j=1}^{n} b_j T_j \exp\left\{2\pi i \vec{H}\vec{R}_j\right\}$$

where
F_{hkl}: structure factor of Bragg reflection with Miller indexes *hkl*.
n: number of atoms in unit cell
$b_{j:}$ scattering lengths (in case of neutron scattering) or atomic form factor (in case of X-ray diffraction) of atom *j*
$T_{j:}$ Debye Waller factor of atom *j*

The scalar product H R_j consists of the reciprocal lattice vector H and the vector R_j, revealing the fractional atomic coordinates of atom j in the unit cell.

$$\vec{H}\vec{R}_j = \begin{pmatrix} h \\ k \\ l \end{pmatrix} \cdot \begin{pmatrix} x_j \\ y_j \\ z_j \end{pmatrix} = hx_j + ky_j + lz_j$$

Thus, the structure factor can also be given as follows:

$$F_{hkl} = \sum_{j=1}^{n} b_j T_j \exp\left\{hx_j + ky_j + lz_j\right\}$$

The intensity of a Bragg reflection is proportional to the square of the absolute value of the structure factor: $I \propto \left|F_{hkl}\right|^2$

Debye-Waller Factor

The Debye-Waller Factor describes the decrease in the intensity of Bragg reflections due to atomic thermal vibrations.

$$T_j(Q) = \exp\left\{-\frac{1}{2}\left\langle\left(\vec{Q}\vec{u}_j\right)\right\rangle\right\}$$

vector $\boldsymbol{u_j}$ reflects the thermal displacements of atom j

Braggs' Law

Braggs' Law provides a relation between distances of lattice planes with Miller indexes *hkl,* i.e. d_{hkl}, and the scattering angle 2θ of the corresponding Bragg peak. Braggs' law can be illustrated in a simplified picture of diffraction as reflection of neutron waves at lattice planes (figure 4). The waves which are reflected from different lattice planes do interfere. We get constructive interference, if the path difference between the reflected waves corresponds to an integer multiple of the wavelength.
The condition for constructive interference (= Braggs' law) is then:

$$2d_{hkl}\sin\theta = n\lambda$$

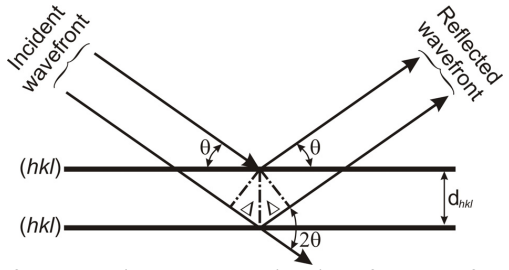

Figure 1: Illustration of Bragg's law: constructive interference of neutron waves, reflected from lattice planes, where θ, 2θ are Bragg angles, $2\Delta=2d_{hkl}\sin\theta$ is the path difference and $2\Delta=n\lambda$ is the constructive interference.

Applying Bragg's law one can derive the lattice spacings ("d-values") from the scattering angle positions of the Bragg peaks in a constant-wavelength diffraction experiment. With the help of d-values a qualitative phase analysis can be carried out.

Ewald's sphere

The Ewald's sphere provides a visualisation of diffraction with help of the reciprocal lattice. At first, we introduce the scattering vector $\boldsymbol{Q}$ and the scattering triangle (Figure 2). The incident neutron wave is described by a propagation vector $\boldsymbol{k_i}$, the scattered wave is given by $\boldsymbol{k_f}$. In the case of elastic scattering (no energy transfer) both vectors $\boldsymbol{k_i}$ and $\boldsymbol{k_f}$ have the same length which is reciprocal to the wavelength.

$$|k_i| = |k_f| = \frac{2\pi}{\lambda}$$

remark:

The length of the wave vectors are sometimes given as $|k_i| = |k_f| = \frac{1}{\lambda}$ *(This definition is found esp. in crystallographic literature, while the other one is more common for physists).*

The angle between vectors $\boldsymbol{k_i}$ and $\boldsymbol{k_f}$ is the scattering angle 2θ. The scattering vector $\boldsymbol{Q}$ is the given by the difference between $\boldsymbol{k_i}$ and $\boldsymbol{k_f}$:

$$\boldsymbol{Q} = \boldsymbol{k_f} - \boldsymbol{k_i} \quad |Q| = 4\pi \frac{\sin\theta}{\lambda}$$

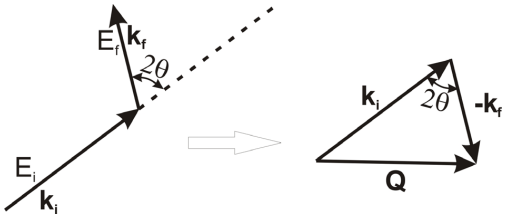

Figure 2: Illustration of scattering vector and scattering angle resulting from incident and scattered waves.

In the visualisation of the diffraction phenomena by Ewald the scattering triangle is implemented into the reciprocal lattice of the sample crystal – at first, we consider diffraction at a single crystal (Figure 3). Note that the end of the incident wave vector coincides with the origin of the reciprocal lattice. Ewald revealed the following condition for diffraction: we have diffraction in the direction of $\boldsymbol{k_f}$, if its end point (equivalently: the end point of scattering vector $\boldsymbol{Q}$) lies at a reciprocal lattice point *hkl*. All possible $\boldsymbol{k_f}$, which fulfil this condition, describe a sphere with radius 2π/λ, the so called Ewald's sphere. Thus we obtain a hkl reflection if the reciprocal lattice point hkl is on the surface of the Ewald's sphere.

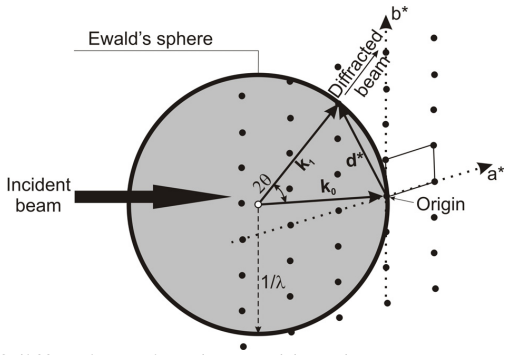

Figure 3: Illustration of diffraction using the Ewald's sphere.

Here, the radius of Ewald's sphere is given by 1/λ (For $|k_i| = \frac{2\pi}{\lambda}$ we obtain a radius of 2π/λ).

We receive the following condition for diffraction: the scattering vector ***Q*** should coincide with a reciprocal lattice vector $\boldsymbol{H_{hkl}}$ (x 2π):

$$\vec{Q} = 2\pi\vec{H}_{hkl};\ \vec{H}_{hkl} = h\vec{a}^{x} + k\vec{b}^{x} + l\vec{c}^{x};\ \left|\vec{H}_{hkl}\right| = d^{x}_{hkl} = \frac{1}{d_{hkl}}$$

From this diffraction condition based on the reciprocal lattice we can derive Bragg's law:

$$\left|\vec{Q}\right| = 2\pi\left|\vec{H}_{hkl}\right| \rightarrow 4\pi\frac{\sin\theta}{\lambda} = \frac{2\pi}{d_{hkl}} \rightarrow 2d_{hkl}\sin\theta = \lambda$$

The Ewald's sphere is a very important tool to visualize the method of single crystal diffraction: At a random orientation of a single crystalline sample a few reciprocal lattice points might match the surface of Ewald's sphere, thus fulfil the condition for diffraction. If we rotate the crystal, we rotate the reciprocal lattice with respect to the Ewald's sphere. Thus by a stepwise rotation of the crystal we receive corresponding reflections.

Powder Diffraction in Debye-Scherrer Geometry

In a polycrystalline sample or a powder sample we assume a random orientation of all crystallites. Correspondingly, we have a random orientation of the reciprocal lattices of the crystallites. The reciprocal lattice vectors for the same *hkl*, i.e. $\boldsymbol{H_{hkl}}$, describe a sphere around the origin of the reciprocal lattice. In the picture of Ewald's sphere we observe diffraction effect, if the surface of the Ewald's sphere intersects with the spheres of $\boldsymbol{H_{hkl}}$ vectors. For a sufficient number of crystallites in the sample and a random distribution of grain orientations, the scattered wave vectors ($\boldsymbol{k_f}$) describe a cone with opening angle 2θ with respect to the inident beam $\boldsymbol{k_i}$.
In the so called Debye-Scherrer Geometry a monochromatic beam is scattered at a cylindrical sample. The scattered neutrons (or X-rays) are collected at a cylindrical detector in the scattering plane. The intersection between cones (scattered neutrons) and a cylinder (detector area) results in segments of rings (= Debye-Scherrer rings) on the detector. By integration of the data along the Debye-Scherrer rings one derives the conventional constant-wavelength powder diffraction pattern, i.e. intensity as a function of the scattering angle 2θ.

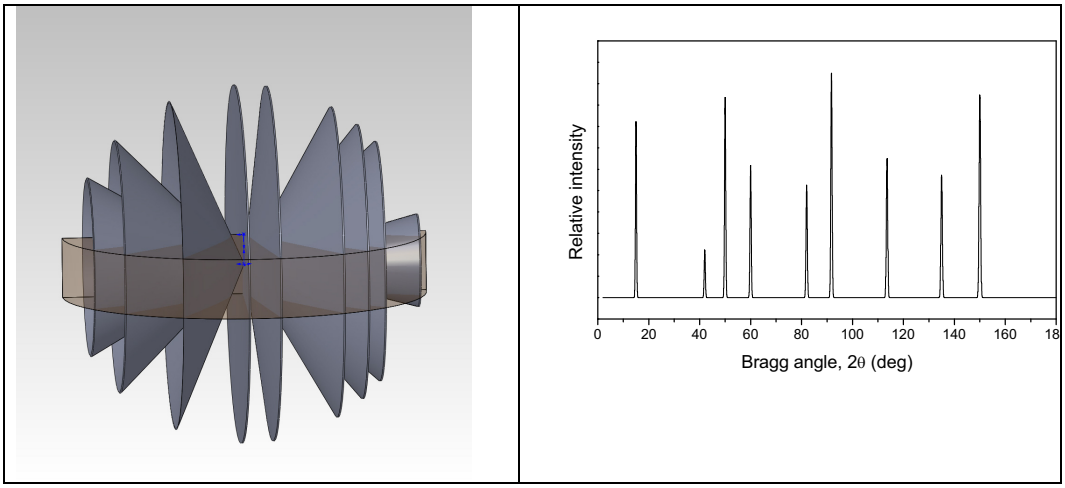

Figure 4: Illustration of powder diffraction in Debye-Scherrer Geometry. On the left: cones of neutrons scattered from a polycrystalline sample are detected in the scattering plane. On the right: resulting powder diffraction pattern.

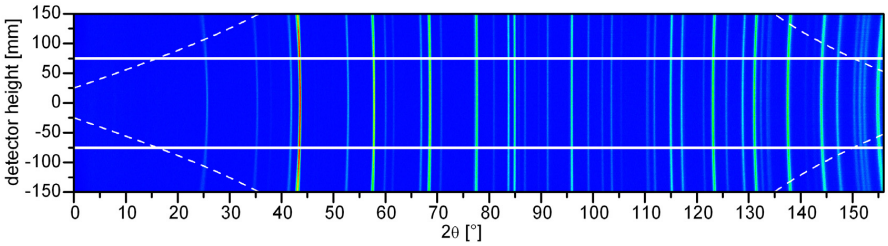

Figure 5: Two dimensional diffraction data (detector height vs. scattering angle 2θ), collected at high-resolution powder diffractometer SPODI, illustrating the Debye-Scherrer rings of a corundum sample.

Relations between Bragg positions and lattice parameters

With the help of Braggs law one can derive the lattice spacings “d-values” directly from the positions of Bragg reflections. The d-values are related with the lattice parameters of the unit cell (the cell dimensions *a,b,c* and the cell angles α,β,γ) and the Miller indexes (hkl) of the corresponding reflections. In the following, the relations are provided for the different crystal systems.

cubic $$\frac{1}{d_{hkl}} = \frac{h^2 + k^2 + l^2}{a^2}$$

hexagonal $$\frac{1}{d_{hkl}} = \frac{4}{3}\frac{h^2 + hk + k^2}{a^2} + \frac{l^2}{c^2}$$

tetragonal $$\frac{1}{d_{hkl}} = \frac{h^2 + k^2}{a^2} + \frac{l^2}{c^2}$$

orthorhombic $$\frac{1}{d_{hkl}} = \frac{h^2}{a^2} + \frac{k^2}{b^2} + \frac{l^2}{c^2}$$

monoclinic $$\frac{1}{d_{hkl}} = \frac{h^2}{a^2 \sin^2\beta} + \frac{k^2}{b^2} + \frac{l^2}{c^2 \sin^2\beta} + \frac{2hl\cos\beta}{ac\sin^2\beta}$$

3. Information from powder diffraction experiments

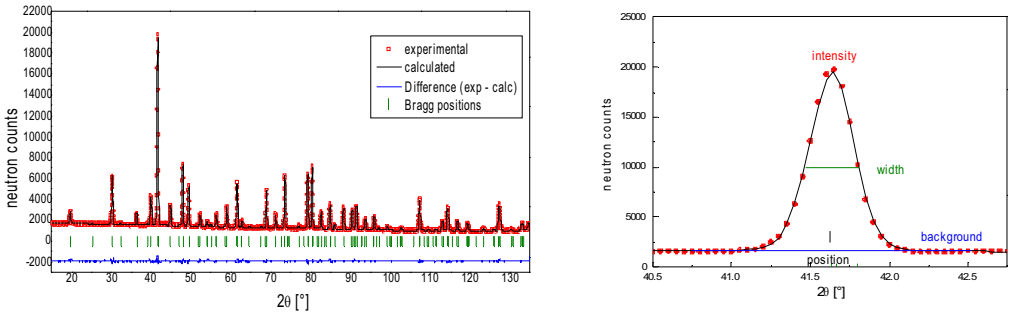

Figure 6: on the left: typical powder diffraction pattern. On the right: zoom on a single Bragg peak.

In the following, we will consider the information which can be derived from different elements of the diffraction patterns.

Positions (scattering angles) of Bragg reflections

- phase identification (from d-values)
- lattice parameters
- symmetry information (space group) by lattice parameters and selection rules (systematic extinction of reflections)

Intensity of Bragg reflections

- crystallographic structure
  - positions of atoms (fractional atomic coordinates)
  - occupancies of atoms on their sites
  - thermal displacement parameters
- magnetic structure
  - magnetic lattice (propagation vector)
  - magnetic symmetry (space group)
  - magnetic moment per atom
- quantitative phase analysis
- preferred orientation effects

Profiles of reflections

The reflection profiles result in a convolution of the instrumental resolution function with broadening effects of the sample

- microstructural information
  - microstrains
  - crystallite sizes

Modulation/Profile of Background

- short range order
- disorder
- amorphous contents

4. Evaluation of Powder Diffraction Data

The methods of data treatment can be classified in analysis of phase composition or phase transformation, structure solution and structure refinement.
Qualitative phase analysis is based on the determination of d-values and relative intensities (in particular intensities of strong reflections have to be considered). The phase identification is supported by crystallographic data bases (ICDD, ISCD), literature data and information from other methods (for instance, analysis of the chemical composition). Such kind of phase analysis is however typically carried out with X-ray diffraction.
The majority of neutron powder diffraction studies is based on experiments at various temperatures to investigate phase transformation behaviour as a function of temperature. There is an increasing demand for parametric studies, i.e. diffraction studies under various environmental conditions (temperature, electric or magnetic field, mechanical stress, gas atmosphere...) with particular attention to reaction pathways/reaction kinetics. This kind of investigations require in general high-intensity powder diffraction.
Powder diffracton data can be used either for phase identification or for the refinement of structural parameters, such as lattice parameters, fractional atomic coordinates, atomic occupancies and atomic displacement parameters by the full profile Rietveld analysis. In the Rietveld method, the full diffraction pattern is calculated by a structure model, taking into account the above mentioned structural parameters, as well as reflection profile parameters, instrumental parameters and background parameters. Using least-squares method, the experimental data can be fitted to the model in a stepwise refinement of the parameters. The complexity of the structures is directly dependent on the instrument specification, in particular, high-resolution powder diffractometers are designed for structure refinements on complex systems.
Besides structure refinement, also structure solution can be done based on powder diffraction patterns by various methods.

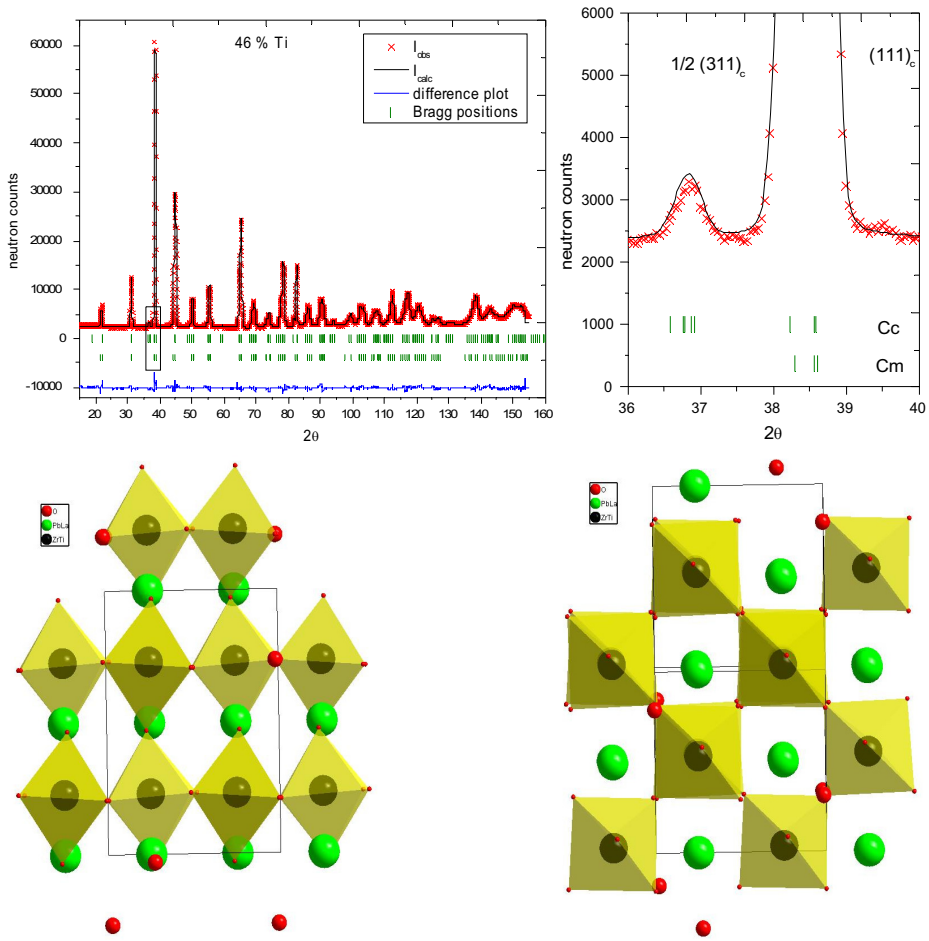

Figure 7: Data treatment of a measurement on the ferroelectric $Pb_{0.99}La_{0.01}Zr_{0.54}Ti_{0.46}O_3$, carried out at 5 K at diffractometer SPODI (FRM II): Diffraction pattern including experimental data, calculated data by Rietveld fit, Bragg reflection positions of the phases (space groups C_C *and* C_m) and difference plot (between experimental and calculated data). - zoom into the diffraction pattern, hightlighting a superlattice reflection of the C_C phase. - structure model of the C_C phase, view in the $[001]_c$ direction - structure model of the C_C phase, view in the $[010]_c$ direction. In particular, the superstructure in the tiltings of oxygen octahedra can be seen.

5. Comparison between Neutron and X-ray diffraction

I) X-rays are scattered at electrons, neutrons are scattered at nuclei

In case of X-ray scattering, the scattering power of an atom (described by the atomic form factor *f*) is proportional to the number of electrons.
Neutrons are scattered at nuclei. Thus the interaction (described by the scattering length b) varies between different isotopes of an element. Scattering length of neighbouring elements in the periodic system can be very different.

implications:

Localisation of light elements next to heavier ones

X-ray diffraction is a powerful tool to determine the positions of heavy atoms, but the localisation of light atoms in the vicinity of much heavier atoms is often difficult or related with high uncertainties. Neutron diffraction is advantageous to localise light atoms such as H, D, Li, C, N, O.

Localisation of neighbouring elements in the periodic table

Neighbouring elements in the periodic table can hardly be distinguished by means of X-ray diffraction. Neutrons are advantageous for such cases: examples: Mn – Fe - Co – Ni or O – N.

Q-dependence of intensities

Since the size of electron clouds is comparable to the wavelength, the atomic form factor depends on $\sin\theta/\lambda$ or Q. Therefore the intensities of X-ray reflections decrease significantly for increasing Q (increasing scattering angles 2θ).
As the range of the neutron–nuclei–interaction is by orders of magnitude smaller than the wavelengths of thermal neutrons, scattering lengths do not depend on Q. As a consequence, neutron diffraction patterns do not show a decrease of Bragg reflection intensities for higher scattering angles, enabling the analysis of larger Q-ranges. In particular, neutron diffraction is advantageous for the analysis of thermal displacement parameters.

II) neutrons interact weakly with matter

implications:

sample volume

The flux from neutron sources much lower compared to X-ray tubes or even synchrotrons. In addition, neutrons interact weakly with matter. Therefore, much larger sample amounts are required compared to X-ray diffraction ("grams instead of milligrams"). On the other hand this weak interaction results in much higher penetration depths of neutrons, compared to laboratory X-ray diffractometers. Thus, polycrystalline bulk samples can be investigated. Furthermore, using large sample volumes avoids possible problems due to preferred orientation effects. In principle, bulk samples can also be investigated with high-energy synchrotron radiation. Anyhow in special cases the very low scattering angles related to low wavelength (in high-energy synchrotron studies) can cause difficulties.

Sample environments

The large penetration depths of neutrons facilitate the usage of sample environments like cryostat, furnaces, magnets... In general neutron scattering experiments are more powerful applying high or low temperatures. On the other hand, the small sample volume required for synchrotron studies gives better possibilities for high-pressure experiments.

III) neutrons exhibit a magnetic moment

Though neutrons do not have an electric charge, the internal charge distribution due to its three quarks along with the spin result in a magnetic moment of the neutron.

implications:

magnetic scattering

The interaction between the magnetic moment of the neutron and a possible magnetic moment of an atom results in a magnetic scattering contribution, incidentally in the same order of magnitude as the nuclear scattering contribution. The magnetic scattering contribution can be easily detected by means of neutron diffraction. In synchrotron diffraction studies, possible magnetic scattering events are by several orders of magnitude weaker than the Thomson scattering.

6. Setup of the high-resolution neutron powder diffractometer SPODI at FRM II

The main components of a constant-wavelength neutron powder diffractometer are: source, monochromator, sample and detector. Between these components collimation systems are installed which have high impact on the instrumental resolution function and the neutron flux.

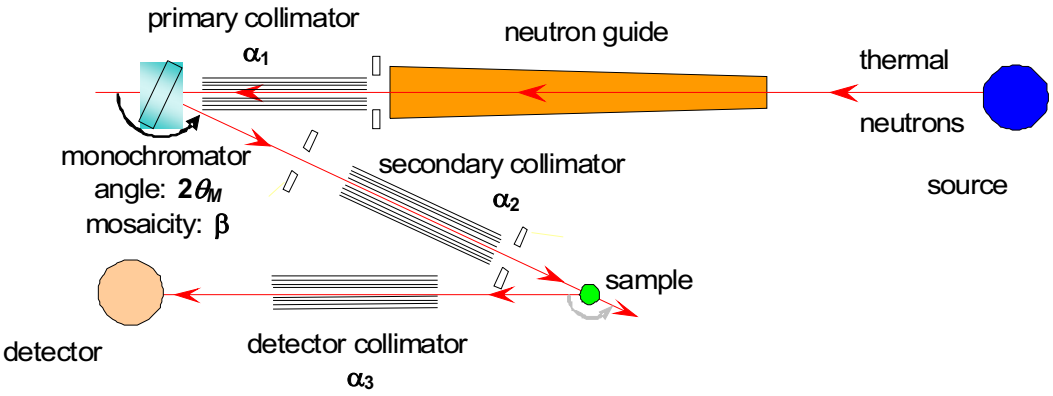

Figure 8: illustration of a typical instrumental layout, introducing the parameters used by Caglioti to describe the instrumental resolution function.

Instrumental resolution function

As shown by Calgioti, the instrumental resolution function of a constant-wavelength powder diffractometer can be approximated by:

$$FWHM = \sqrt{U \tan^2 \theta + V \tan \theta + W}$$

with the Caglioti parameters:

$$U = \frac{4\left(\alpha_1^2\alpha_2^2 + \alpha_1^2\beta^2 + \alpha_2^2\beta^2\right)}{\tan^2\theta_m\left(\alpha_1^2 + \alpha_2^2 + 4\beta^2\right)}$$

$$V = \frac{-4\alpha_2^2\left(\alpha_1^2 + 2\beta^2\right)}{\tan\theta_m\left(\alpha_1^2 + \alpha_2^2 + 4\beta^2\right)}$$

$$W = \frac{\alpha_1^2\alpha_2^2 + \alpha_1^2\alpha_3^2 + \alpha_2^2\alpha_3^2 + 4\beta^2\left(\alpha_2^2 + \alpha_3^2\right)}{\left(\alpha_1^2 + \alpha_2^2 + 4\beta^2\right)}$$

in this approach it is assumed that all components have Gaussian transmission profiles. The resolution function is determined by the horizontal beam divergences $\alpha_1, \alpha_2, \alpha_3$, the monochromator angle $2\theta_m$ and the mosaicity of the monochromator β (Figure 8). As the impact of these parameters on the instrumental resolution function can be estimated, the Caglioti equations help to design an instrument to achieve a designated performance. However, it should be emphasised that in the approximations of Caglioti only the horizontal beam divergences are taken into account, neglecting vertical beam divergences by a vertical focusing monochromator or a vertical divergent neutron guide. Those effects are taken into account by ray-tracing methods, which allow a detailed modelling of the individual components.

The powder diffractometer SPODI has been designed to achieve both high resolution and good profile shape. In its standard configuration (highest resolution mode) SPODI uses a unique very high monochromator take-off angle of 155° along with a large monochromator-to-sample distance of 5 meters. An evacuated beam tube of about 4 m in length is located between the monochromator and the sample which also controls both vertical and horizontal neutron beam divergences at the sample position. Thus the natural neutron beam divergence in horizontal plane is 25' only. It can be reduced down to even 5' by optional Soller collimators in front of the sample.

Monochromator

At constant-wavelength diffractometers, the monochromatisation is perfomed using crystals followings Bragg's equation:

$2d_{hkl}\sin\theta = \lambda$, where the effective transmission band is determined by a derivative

$$\frac{\Delta\lambda}{\lambda} = \Delta\theta_M \cot\theta_M$$

The width of the wavelength band $\Delta\lambda/\lambda$ strongly depends on the monochromator angle $2\theta_m$ and the mosaicity of the monochromator β oρ $\Delta\theta_m$. Thus these parameters have a major impact on the instrumental resolution function and the flux on the sample.

Typically, the monochromator crystals are installed at a vertical focusing unit of 200 – 300 mm, allowing optimization of the intensity distribution at the sample position with respect to the monochromator – sample distance or the sample height. On the other hand, the vertical beam divergence results in a smearing of the Debye-Scherrer rings along the detector height (this effect depends also on the sample height). At the high-resolution powder diffractometer SPODI, 15 Germanium wafer-stack crystals with a (551)-orientation are used. Different wavelengths between 1.0 and 2.6 Å can easily be selected by rotation of the monochromator unit (without changing the monochromator take-off angle $2\theta_m$), i.e. by selecting different (*hkl)* reflection planes. In general, large wavelengths are advantageous to investigate structures exhibiting large d-values. This is the case for large unit cells, but in particular for magnetic ordering. With decreasing wavelengths, larger Q-values can be achieved. Thus, with lower wavelengths, more reflections can be observed in the same scattering angle range. Low wavelengths are in particular advantageous for the analysis of thermal displacement parameters or static disorder phenomena.

Detector array

At constant-wavelength diffractometers the data are collected in an angle-dispersive manner at equidistant 2θ points. Detector systems based on ^{3}He have been most commonly used due to their very high efficiency. Now, the world wide shortage of ^{3}He demands and promotes the development of alternatives, in particular scintillator based systems.
Classical high-resolution powder diffractometers, such as D2B (ILL), SPODI (FRM II), BT1 (NIST), ECHIDNA (ANSTO) use multidetector/multicollimator systems. The data are collected by ^{3}He tubes while the beam divergence is limited by Soller collimators. Such systems enable high Q-resolution over a broad scattering angle regime, while the resolution does not depend on the sample diameter. On the other hand, a multidetector concept requires a data collection by stepwise positioning of the detector array to collect the full diffraction pattern. Therefore, kinetic measurements are not feaible due to the fact that the sample must not change during the collection of a pattern.
The detector array of SPODI consists of 80 ^{3}He tubes, which are position sensitive in the vertical direction. Thus, two-dimensional raw data are obtained, which allow to rapid check for sample crystallinity, alignment and possible preferred orientation effects. The conventional diffraction patterns (intensity vs. scattering angle 2θ) are derived from the two-dimensional raw data by integration along the Debye-Scherrer rings.

7. Experiment: Phase- and structure analysis of lead titanate at various temperatures

samples

Lead zirconate titanates $PbZr_{1-x}Ti_xO_3$ („PZT“) exhibit piezo-, pyro- and ferroelectric properties. Piezoelectricity describes the generation of an electric polarisation as a consequence of a mechanical deformation – or the other way round the development of a macroscopic strain by an electric field. The crystallographic condition of piezoelectricity is the lack of an inversion center: as the balance points of negative and positive charge do not coincide the displacements of the ions in the electric field results in a polarization. Pyroelectrticity refers to a spontaneous polarization of a material as a function of temperature. Ferroelectrics are special pyroelectric materials, in which the polarization can be switched by an electric field, resulting in a ferroelectric hysteresis.

The electromechanical properties of $PbZr_{1-x}Ti_xO_3$ can be understood by their phase transformation behaviour. At high temperatures they exhibit the perovskite structure with simple cubic symmetry (space group Pm-3m). Because of its symmetry (inversion center) this phase is not piezoelectric but paraelectric. During cooling, titanium-rich samples undergo a phase transition to a tetragonal phase (space group P4mm). This phase transformation is accompanied by atomic displacements. In particular, the Ti^{4+}/Zr^{4+} are shifted in the opposite direction than O^{2-} ions, resulting in a dipole moment or a spontaneous polarisation. The material exhibits ferroelectric behaviour, with a polar axis in the direction of the pseudocubic c-axis, i.e. $[001]_c$. Zirconium rich samples undergo a phase transition towards a rhombohedral phase (space group R3m) during cooling. In this case, the atomic displacements result in a polar axis in direction $[111]_c$ with respect to the parent pseudocubic lattice. Materials $PbZr_{1-x}Ti_xO_3$ with compositions (Zr/Ti ratios) close to the so called morphotropic phase boundary between rhombohedral and tetragonal phase, show the highest piezoelectric response, i.e. the largest macroscopic strain as a function of the applied electric field. These compositions are therefore most interesting for technological applications. The piezoelectric properties can be modified further by adding doping elements to substitute Pb^{2+} or Ti^{4+}/Zr^{4+} ions.

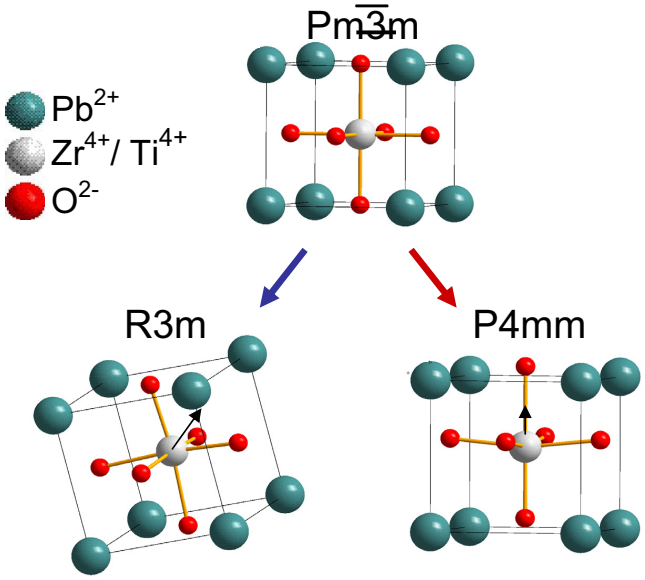

Figure 9: Structure models of the paraelectric cubic phase and the ferroelectric rhombohedral and tetragonal phases.

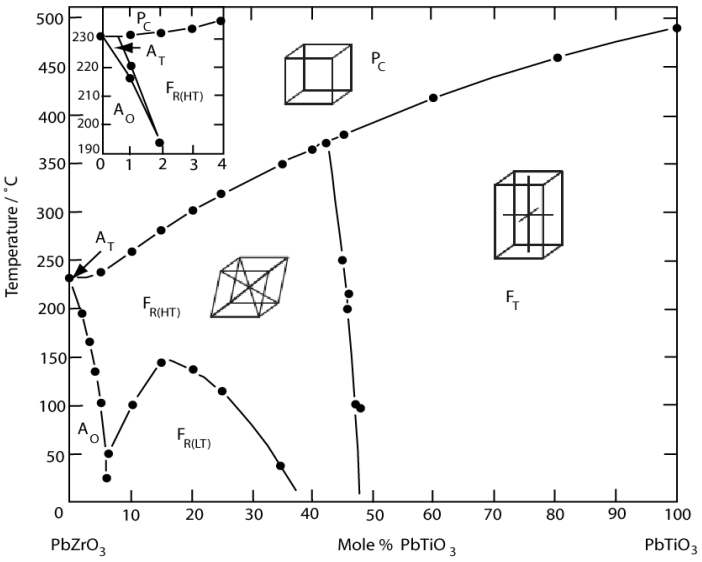

Figure 10: Phase diagram of $PbZr_{1-x}Ti_xO_3$, illustrating regions of phase stability for paraelectric cubic phase P_C, ferroelectric rhomboedral phases $F_{R(HT)}$ (= high temperature) and $F_{R(LT)}$ (= low temperature) and ferroelectric tetragonal phase F_T. From B. Jaffe, W. R. Cook, H. Jaffe, Piezoelectric Ceramics and Related Issues, Academic Press, London, 1971.

$PbZr_{1-x}Ti_xO_3$, find extensive applications

- transformation from mechanical in electric energy: ignition elements, lighters
- transformation from electric in mechanical energy (actuators): loudspeakers, sonar transducers, Active control of vibration
- transformation from mechanical force in an electric signal (sensors): strain gauges, microphones
- data storage, information technology: capacitors, F-RAM

Experiment

In the frame of the practical course, the temperature-dependent phase transformation behavior of a $PbZr_{1-x}Ti_xO_3$ with a composition on the tetragonal side should be investigated. Diffraction patterns at different temperature steps between room temperature and 600 °C will be collected with a vacuum high-temperature furnace. The structural changes at different temperatures will be investigated by an analysis of the lattice parameters. Based on the experimental data, the relations between the structural changes and the corresponding physical properties can be discussed.

Following experimental procedures will be carried out

- sample preparation, filling the sample material into a sample can, adjustment of the sample stick, installation of the sample stick into the furnace
- short test measurement to check the sample adjustment and data quality
- editing a program to run the data collection at various temperatures and starting the scans
- data reduction: Derivation of diffraction patterns from the two-dimensional raw data
- data analysis: analysis of the lattice parameter changes as a function of temperature
- discussing the results with respect to structure – properties relationships

Literature

[1] V. K. Pecharsky, P. Y. Zavalij, Fundamentals of Powder Diffraction and structural Characterisation of Materials (2003).
[2] G. L. Squires, Introduction to the Theory of Thermal Neutron Scattering, Dover Reprints (1978).
[3] C. Kittel, Einführung in die Festkörperphysik, 10. Edition, Oldenbourg (1993).
[4] H. Dachs, Neutron Diffraction, Springer Verlag (1978).
[5] H. Ibach und H. Lüth, Festkörperphysik, Einführung in die Grundlagen, 6. Edition, Springer
Verlag (2002).
[6] J.R.D. Copley, The Fundamentals of Neutron Powder Diffraction (2001), http://www.nist.gov/public_affairs/practiceguides/SP960-2.pdf.
[7] A. D. Krawitz, Introduction to Diffraction in Materials Science and Engineering.
[8] W. Kleber, Einführung in die Kristallographie, Oldenbourg (1998).

Contact

SPODI

Web: http://www.frm2.tum.de/wissenschaftliche-nutzung/diffraktion/spodi/index.html

Dr. Markus Hoelzel

Forschungsneutronenquelle Heinz Maier-Leibnitz (FRM II)
Technische Universität München

Phone: 089/289-14314
e-Mail: markus.hoelzel@frm2.tum.de

Dr. Anatoliy Senyshyn

Forschungsneutronenquelle Heinz Maier-Leibnitz (FRM II)
Technische Universität München

Phone: 089/289-14316
e-Mail: anatoliy.senyshyn@frm2.tum.de

HEiDi

Hot Single Crystal Diffractometer for Structure Analysis with Neutrons

M.Meven

Institut für Kristallographie, RWTH Aachen
and
Jülich Centre for Neutron Science
Forschungszentrum Jülich

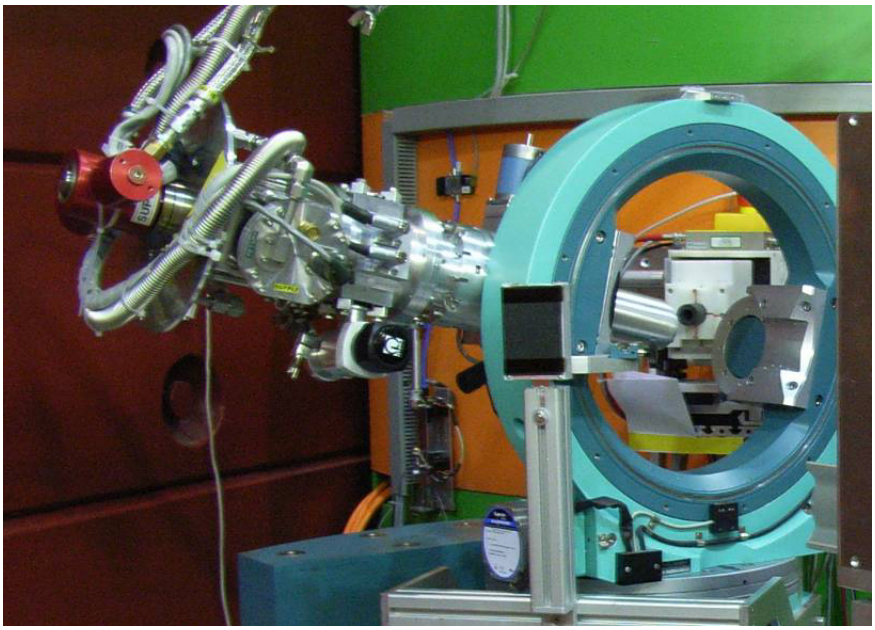

Manual of the JCNS Laboratory Course Neutron Scattering

Contents

1 Introduction

Many properties of solid matter like their mechanical, thermal, optical, electrical and magnetic properties depend strongly on their atomic structure. Therefore, a good understanding of the physical properties needs not only the knowledge about the particles inside (atoms, ions, molecules) but also about their spatial arrangement. For most cases diffraction is *the* tool to answer questions about the atomic and/or magnetic structure of a system. Beyond this, neutron diffraction allows to answer questions where other techniques fail.

2 Crystallographic Basics

In the ideal case a complete solid matter consists of small identical units (same content, same size, same orientation like sugar pieces in a box). These units are called unit cells. A solid matter made of these cells is called a single crystal. The shape of a unit cell is equivalent to a parallelepiped that is defined by its base vectors $\mathbf{a_1}$, $\mathbf{a_2}$ und $\mathbf{a_3}$ and that can be described by its lattice constants a, b, c; α, β and γ (pic. 1). Typical lengths of the edges of such cells are between a few and a few ten Ångström (1Å=10^{-10} m). The combination of various restrictions of the lattice constants between $a \neq b \neq c$; $\alpha \neq \beta \neq \gamma \neq 90°$ (triclinic) and $a = b = c$; $\alpha = \beta = \gamma = 90°$ (cubic) yields seven crystal systems. The request to choose the system with the highest symmetry to describe the crystal structure yields fourteen Bravais lattices, seven primitive and seven centered lattices.

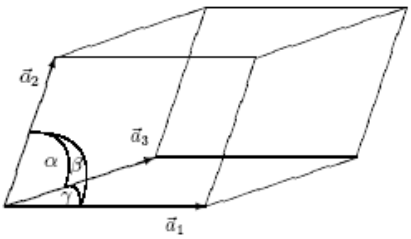

Fig. 1: Unit cell with $|\mathbf{a_1}|=a$, $|\mathbf{a_2}|=b$, $|\mathbf{a_3}|=c$, α, β, γ

Each unit cell contains one or more particles i. The referring atomic positions $\mathbf{x_i}=x_i*\mathbf{a_1} + y_i*\mathbf{a_2} + z_i*\mathbf{a_3}$ are described in relative coordinates $0 \leq x_i; y_i; z_i < 1$. The application of different symmetry operations (mirrors, rotations, glide mirrors, screw axes) on the atoms in one cell yield the 230 different space groups (see [1]).

The description of a crystal using identical unit cells allows the representation as a threedimensional lattice network. Each lattice point can be described as the lattice vector $\mathbf{t} = u*\mathbf{a_1} + v*\mathbf{a_2} + w*\mathbf{a_3}$; $u, v, w \in \mathbf{Z}$. From this picture we get the central word for diffraction in crystals; the *lattice plane* or *diffraction plane*. The orientations of these planes in the crystal are described by the so called *Miller indices* h, k and l with $h, k, l \in \mathbf{Z}$ (see pic. 2). The reciprocal base vectors $\mathbf{a^*_1}$, $\mathbf{a^*_2}$, $\mathbf{a^*_3}$ create the reciprocal space with: $\mathbf{a^*_i} * \mathbf{a_j} = \delta_{ij}$ with $\delta_{ij}=1$ for $i=j$ and $\delta_{ij}=0$ for $i \neq j$. Each point $\mathbf{Q}=h*\mathbf{a^*_1} + k*\mathbf{a^*_2} + l*\mathbf{a^*_3}$ represents the normal vector of

a (*hkl*) Plane. Each plane cuts the crystal lattice along its base vectors $\mathbf{a_1}$, $\mathbf{a_2}$ and $\mathbf{a_3}$ at $1/h^*\mathbf{a_1}$, $1/k^*\mathbf{a_2}$ and $1/l^*\mathbf{a_3}$. A Miller index of zero means that the referring axis will be cut in infinity. Thus, the lattice plane is parallel to this axis.

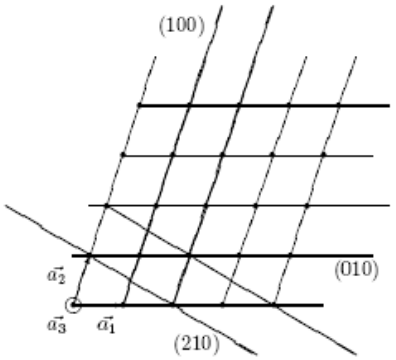

Fig. 2: Different lattice planes in a crystal lattice, $\mathbf{a_3}$ = viewing direction

The atoms in a unit cell are not rigidly fixed at their positions. They oscillate around their positions (e.g. thermal excitation). A simple description for this is the model of coupled springs. In this model atoms are connected via springs whose forces describe the binding forces between the atoms (e.g. van der Waals, Coulomb, valence). The back driving forces of the springs are proportional to the deviation x_i of the atoms from their mean positions and to the force constant D, thus. $F = -D^*\Delta x$ (harmonic approximation).
Therefore, the atoms oscillate with $x_i = A_i^*\sin(\nu^*t)$ around their mean positions with the frequency ν and the amplitude A_i. Both, ν and A_i are influenced by the force constant D_j of the springs and the atomic masses m_i of the neighbouring atoms. The resulting lattice oscillations are called phonons in reference to the photons (light particles) in optics, which as well transport energy in dependence of their frequency. A more complex and detailed description of phonons in dependence on the lattice structure and the atomic reciprocal effects is given in lattice dynamics. In the harmonic approximation the displacements of an atom can be described with an oszillation ellipsoid. This ellipsoid describes the preferred spacial volume in which the atom is placed. Its so called mean square displacements (MSD) U^i_{jk} represent the different sizes of the ellipsoid along the different main directions *j, k* in the crystal. The simplest case is a sphere with the isotrope MSD B_i. In the next paragraph MSD are discussed from the point of view of diffraction analysis.
A full description of a single crystal contains information about lattice class, lattice constants and unit cell, space group and all atomic positions and their MSD. If the occupancy of one or more positions is not exactly 100%, e.g. for a mixed crystal or a crystal with deficiencies there has to be used also an occupancy factor.

3 Structure Determination with Diffraction

3.1 Introduction

Diffraction means coherent elastic scattering of a wave on a crystal. Because of the quantum mechanical wave/particle dualism x-rays as well as neutron beams offer the requested wave properties:

Electrons: $E = h\nu$; $\lambda = c/\nu$
Neutrons: $E_{kin} = 1/2 * m_n * v^2 = h\nu = p^2/2m_n$; $\lambda = h/p$; $p \sim \sqrt{(m_n k_B T)}$

h: Planck's constant; ν: oscillation frequency; λ: wavelength; c: light speed; p: impact; m_n: neutron mass; k_B: Boltzmann constant; T: temperature

Only the cross section partners are different (x-rays: scattering on the electron shell of the atoms, neutrons: core (and magnetic) scattering) as explained in detail below. In scattering experiments informations about structural properties are hidden in the scattering intensities I.
In the following pages we will discuss only elastic scattering ($\lambda_{in}=\lambda_{out}$). The cross section of the radiation with the crystal lattice can be described as following:
Parallel waves of the incoming radiation with constant λ are diffracted by lattice planes which are ordered parallel with a constant distance of d. This is very similar to a light beam reflected by a mirror. The angle of the diffracted beam is equal to the angle of the incoming beam, thus the total angle between incoming and outgoing beam is 2Θ (see fig. 3).

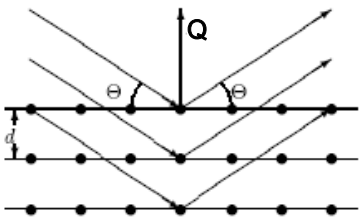

Fig. 3: Scattering on lattice planes

The overlap of all beams diffracted by a single lattice plane results in constructive interference only if the combination of the angle Θ, lattice plane distance d and wavelength λ meet Braggs law:

$$\mathbf{2}d\ \mathbf{sin}\Theta = \lambda$$

The largest distance $d_{hkl} = |\mathbf{Q}|$ of neighboured parallel lattice planes in a crystal is never larger than the largest lattice constant $d_{hkl} \leq \max(a; b; c)$. Therefore, it can only be a few Å or less. For a cubic unit cell ($a = b = c$; $\alpha = \beta = \gamma = 90°$) this means:
$d_{hkl} = a/\sqrt{(h^2+k^2+l^2)}$

With increasing scattering angle also the indices (hkl) increase while the lattice plane distances shrink with a lower limit of $d_{min} = \lambda/2$. Therefore, scattering experiments need

wavelengths λ in the same order of magnitude of the lattice constants or below. This is equal to x-ray energies of about 10 keV or neutron energies about 25 meV (thermal neutrons).

Ewald Construction: In reciprocal space each Bragg reflex is represented by a point $\mathbf{Q} = h^*\mathbf{a}^*_1 + k^*\mathbf{a}^*_2 + l^*\mathbf{a}^*_3$. A scattered beam with the wave vector $\mathbf{k}$ fulfills Braggs law if the relationship $\mathbf{k} = \mathbf{k_0} + \mathbf{Q}$, $|\mathbf{k}|=|\mathbf{k_0}|=1/\lambda$ is true, as shown in fig. 4. During an experiment the available reciprocal space can be described by an Ewald sphere with a diameter of $2/\lambda$ and the (000)-point as cross point of $\mathbf{k_0}$ direction and the centre of the diameter of the sphere. The rotation of the crystal lattice during the diffraction experiment is equal to a synchronous movement of the reciprocal lattice around the (000)-point. If Braggs law is fulfilled, one point (*h k l*) of the reciprocal lattices lies exactly on the Ewald sphere. The angle between the $\mathbf{k}$-vektor and the $\mathbf{k_0}$-vektor is 2Θ. The limited radius of $1/\lambda$ of the Ewald sphere limits also the visibility of (*h k l*) reflections to $|\mathbf{Q}| < 2/\lambda$.

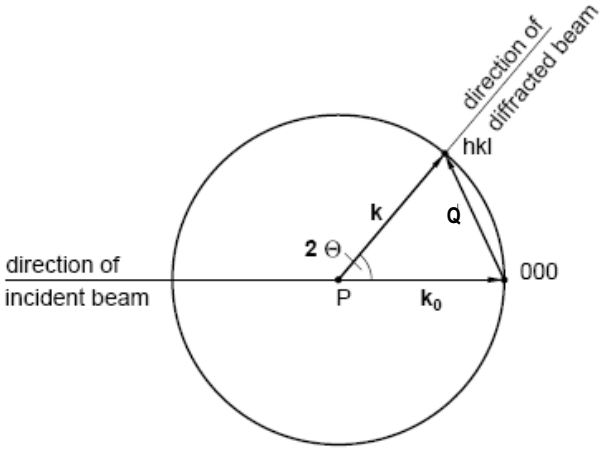

Fig. 4: Ewald construction

Determination of the Unit Cell: Following Braggs law the scattering angle 2Θ varies (for λ=const.) according to the lattice distance d_{hkl}. Thus for a given λ and known scattering angles 2Θ one can calculate the different *d* values of the different layers in the lattice of a crystal. With this knowledge is is possible to determine the lattice system and the lattice constants of the unit cell (although not always unambigously!).

Atomic Positions in the Unit Cell: The outer shape of a unit cell does not tell anything about the atomic positions $\mathbf{x_i}=(x_i\ y_i\ z_i)$ of each atom in this cell. To determine the atomic positions one has to measure also the quantities of the different reflection intensities of a crystal. This works because of the relationship between the intensities of Bragg reflections and the specific cross section of the selected radiation with each element in a unit cell. Generally one can use the following formula for the intensity of a Bragg reflection (*h k l*) with $\mathbf{Q}$ (kinetic scattering theory):

$$I_{hkl} \sim |F_{hkl}|^2 \text{ with } F_{hkl} = \sum^n_{i=1} s_i(\mathbf{Q}) \exp(2\pi\imath(hx_i+ky_i+lz_i))$$

The scattering factor F is a complex function describing the overlap of the scattering waves of each atom i (n per unit cell). $s_i(\mathbf{Q})$ describes the scattering strength of the i-th atom on its position $\mathbf{x}_i$ in dependence of the scattering vector $\mathbf{Q}$, which depends on the character of cross section as described below.
In this context one remark concerning statistics: For measurements of radiation the statistical error σ is the square root of the number of measured events, e.g. x-ray or neutron particles. Thus, 100 events yield an error of 10% while 10,000 events yield an error of only 1%!

Mean Square Displacements (MSD): Thermal movement of atoms around their average positions reduce the Bragg intensities during a diffraction experiment. The cause for this effect is the reduced probability density and therefore reduced cross section probability at the average positions. For higher temperatures (above a few Kelvin) the MSD B_i of the atoms increase linearly to the temperature T, this means $B \sim T$. Near a temperature of 0 K the MSD become constant with values larger than zero (zero point oscillation of the quantum mechanical harmonic oscillator).
Thus, the true scattering capability s_i of the i-th atom in a structure has to be corrected by an angle-dependent factor (the so called Debye-Waller factor):

$$s_i(\mathbf{Q}) \rightarrow s_i(\mathbf{Q}) * \exp(-B_i(\sin \Theta_{\mathbf{Q}}/\lambda)^2)$$

This Debye-Waller factor decreases with increasing temperatures and yields an attenuation of the Bragg reflection intensities. At the same time this factor becomes significantly smaller with larger $\sin\Theta/\lambda \sim |\mathbf{Q}|$. Therefore, especially reflections with large indices loose a lot of intensity. The formula for anisotropic oscillations around their average positions looks like this:

$$s_i(\mathbf{Q}) \rightarrow s_i(\mathbf{Q}) * \exp(-2\pi^2(U^i_{11}\, h^2a^{*2} + U^i_{22}\, k^2b^{*2} + U^i_{33}\, l^2c^{*2} + \\ + 2U^i_{13}\, hl\, a^*c^* + 2U^i_{12}\, hk\, a^*b^* + 2U^i_{23} kl\, b^*c^*))$$

The transformation between B and U_{eq} (from the U_{ij} calculated isotropic MSD for a sphere with identical volume) yields $B = 8\pi^2 U_{eq}$.
For some structures the experimentally determined MSD are significantly larger than from the harmonic calculations of the thermal movement of the atoms expected. Such deviations can have different reasons: Static local deformations like point defects, mixed compounds, anharmonic oscillations or double well potentials where two energetically equal atomic positions are very near to each other and therefore distribute the same atom over the crystal with a 50%/50% chance to one or the other position. In all those cases an additional contribution to the pure Debye-Waller factor can be found which yields an increased MSD. Therefore in the following text only the term MSD will be used to avoid misunderstandings.

3.2 Comparison of X-ray and Neutron Radiation

X-Ray Radiation interacts as electromagnetic radiation only with the electron density in a crystal. This means the shell electrons of the atoms as well as the chemical binding. The scattering capability s (atomic form factor $f(\sin\Theta/\lambda)$) of an atom depends on the number Z of its shell electrons ($f(\sin(\Theta=0)/\lambda) = Z$). To be exact, $f(\sin(\Theta)/\lambda)$ is the Fourier transform of the radial electron density distribution $n_e(r)$: $f(\sin(\Theta)/\lambda) = s \int_0^\infty 4\pi^2 n_e(r)\, \sin(\mu r)/\mu r\, dr$ with $\mu = 4\pi\sin(\Theta)/\lambda$. Heavy atoms with many electrons contribute much stronger to reflection

intensities ($I \sim Z^2$) than light atoms with less electrons. The reason for the $\sin\Theta/\lambda$-dependence of f is the diameter of the electron shell, which has the same order of magnitude as the wavelength λ. Because of this there is no pointlike scattering centre. Thus, for large scattering angles the atomic form factors vanish and also the reflection intensities relying on them. The atomic form factors are derived from theoretical spherical electron density functions (e. g. Hartree-Fock). The resulting $f(\sin\Theta/\lambda)$-curves of all elements (separated for free atoms and ions) are listed in the international tables. Their analytical approximation can be described by seven coefficients (c; a_i; b_i; $1 \leq i \leq 3$) , see [1].

Neutron Radiation radiation interacts with the cores and the magnetic moments of atoms. The analogon to the x-ray form factor (the scattering length b) is therefore not only dependent on the element but the isotope. At the same time b-values of elements neighboured in the periodic table can differ significantly. Nevertheless, the scattering lengths do not differ around several orders of magnitude like in the case of the atomic form factors f . Therefore, in a compound with light and heavy atoms the heavy atoms do not dominate necessarily the Bragg intensities. Furthermore the core potential with a diameter about 10^{-15}Å is a pointlike scattering centre and thus the scattering lengths b_n become independent of the Bragg angle and $\sin\Theta/\lambda$ respectively. This results in large intensities even at large scattering angles. The magnetic scattering lengths b_m can generate magnetic Bragg intensities comparable in their order of magnitude to the intensities of core scattering. On the other hand side the magnetic scattering lengths are strongly dependent on the $\sin\Theta/\lambda$ value due to the large spacial distribution of magnetic fields in a crystal. Therefore, it is easy to measure magnetic structures with neutrons and to separate them from the atomic structure.

Comparison: In summary in the same diffraction experiment the different character of x-ray and neutron radiation yield different pieces of information that can be combined. x-rays yield electron densities in a crystal while neutron scattering reveals the exact atomic positions. This fact is important because for polarised atoms the core position and the centre of gravity of electron densities are not identical any more. In compounds with light an heavy atoms structural changes driven by light elements need additional diffraction experiments with neutrons to reveal their influence and accurate atomic positions respectively. One has to take into account also that for x-rays intensitied depend twice on $\sin\Theta/\lambda$. Once bye the atomic form factor f, and twice by the temperature dependent Debye-Waller factor (see above). The first dependence vanishes if using neutron diffraction with b=const. and decouples the structure factors from the influence of the MSD. In general this yields much more accurate MSD U_{ij} especially for the light atoms and might be helpful to reveal double well potentials.

3.3 Special Effects

From the relation $I \sim |F|^2$ one can derive that the scattering intensities of a homogenous illuminated sample increases with its volume. But there are other effects than MSD that can attenuate intensities. These effects can be absorption, extinction, polarization and the Lorentz factor:

Absorption can be described by the Lambert-Beer law:

$I = I_0 \exp(-\mu x)$, μ/cm^{-1} = linear absorption coefficient, x/cm = mean path through sample

The linear absorption coefficient is an isotropic property of matter and depends on the wavelength and kind of radiation. For x-rays penetration depths are only a few millimetre or below (e.g. for silicon with $\mu_{MoK\alpha}$=1.546 mm^{-1}, $\mu_{CuK\alpha}$=14.84 mm^{-1} with penetration depths of 3 mm and 0.3 mm respectively). This limits transmission experiments to sample diameter of typically below 0.3 mm. To correct bias of intensities due to different scattering paths through the sample one has to measure accurately the sample size in all directions. Even for sphere liek samples the mean path lenghts depend on 2Θ! In addition the sample environment must have an extraordinary small absorption
Thermal neutrons have for most elements a penetration depth of several centimeters. Thus, sample diameters of several millimeters and large and complex sample environments (furnaces, magnets, etc.) can be used. On the other hand side one needs sufficiently large samples for neutron diffraction which is often a delicate problem.

Extinction reduces also radiation intensities. But the character is completely different form that of absorption. In principle extinction can be explained quite easily by taking into account that each diffracted beam can be seen as a new primary beam for the neighbouring lattice planes. Therefore, the diffracted beam becomes partially backscattered towards the direction of the very first primary beam (Switch from kinetic to dynamic scattering theory!). Especially for very strong reflections this effect can reduce intensities dramatically (up to 50% and more). Condition for this effect is a merely perfect crystal.
Theoretical models which include a quantitative description of the extinction effect were developed from Zachariasen (1962) and Becker and Coppens [2, 3, 4, 5, 6]. These models base on an ideal spherical mosaic crystal with a very perfect single crystal (primary Extinction) or different mosaic blocks with almost perfect alignment (secundary Extinction) to describe the strength of the extinction effect. In addition, it is possible to take into account anisotropic extinction effect if the crystal quality is also anisotropic. Nowadays extinction correction is included in most refinement programs [7]. In general extinction is a problem of sample quality and size and therefore more commonly a problem for neutron diffraction and not so often for x-ray diffraction with much smaller samples and larger absorption.

Polarisation*:* X-ray radiation is electromagnetic radiation. Therefore, the primary beam of an x-ray tube is not polarized. The radiation hits the sample under an diffraction angle of Θ where it can be separated into two waves of same intensity, firstly with an electrical field vector parallel $E_{||}$ and secondly perpendicular $E_{\perp}$ towards the Θ-axis. Whilst the radiation with $E_{||}$ will not be attenuated the radiation with $E_{\perp}$ will be attenuated with $E_{\perp} \rightarrow \cos(2\Theta)\, E_{\perp}$. The polarization factor P for the attenuation has then the following formula ($I \sim E^2$):

$$P = (1+\cos(2\Theta)^2)/2$$

Additional optical components like monochromator crystals also have an impact on the polarization and have to be taken into account accordingly.

Lorentz factor: The Lorentz factor L is a purely geometrical factor. It describes that during an ω- and Θ-scan respectively of Bragg reflections towards higher 2Θ values for the same angular speed $\Delta\omega/\Delta t$ an effectively elongated stay of the sample in the reflection position results.:

$$L = 1/\sin(2\Theta)$$

This has to be taken into account for any kind of radiation in an diffraction experiment.

3.4 Summary of Theory of Method

The different interactions of x-ray and neutron radiation with the atoms in a crystal make neutrons in general the better choice for a diffraction experiment. But on the other hand one has to take into account the available flux of x-rays and neutrons respectively. The flux of modern neutron sources like the Heinz Maier-Leibnitz neutron source (FRM II) is spread around a broad spectrum of neutron energies. In a sharp band of energies/wavelengths, e.g. $\Delta\lambda/\lambda<10^{-3}$, there is the flux of neutrons several order of magnitude smaller than the flux of x-rays of a corresponding synchtrotron source or x-ray tube in the laboratory. The reason for this is the fact that in an x-ray tube most x-rays are generated in a small energy band, the characteristic lines of the tube target (K_α, K_β, etc.). Additional metal foil used as filter allow to cut off unwanted characteristic lines which yields quasi monochromatic radiation of a single wavelength.
To use neutrons around a small energy band one has to use monochromator crystals. This reduces significantly the number of available neutrons for the diffraction experiment. Thus, the weak flux of neutrons and the weak cross section of neutrons with matter has to be compensated with large sample sizes of several millimeters. For the same reason the monochromatization of the neutrons is normally chosen to be not too sharp (resolution about $\Delta\lambda/\lambda\approx10^{-2}$ for neutrons, $\Delta\lambda/\lambda\approx10^{-5} - 10^{-6}$ for synchrotron).

3.5 From Measurement to Model

To get a structural model from the experimentally collected integral Bragg intensities one needs several steps in advance. Firstly on has to make sure that all reflections are measured properly (no shading, no $\lambda/2$-contamination, no Umweganregung (Renninger-effect)). Damaged reflections have to be excluded from further treatment.
During data refinement not only the quantities of the relative intensities but also their errors are taken into account. The total statistical error σ of an integral intensity I_{obs} of a single reflection is calculated as following:

$$\sigma^2 = I_{obs} + I_{background} + (k\, I_{total})^2$$

The part $\sigma_0^2 = I_{total}$, $I_{total} = I_{obs} + I_{background}$ refers to the error caused by counting statistics. It contains as well the effective intensity Iobs as well as the contribution of the background. But there are other effects that influence the reproducibility of a measurement (and thus the total error), e.g. specific errors of the instrumental adjustment. Those errors are collected in the so called *McCandlish-Factor k* and contribute to the total error. Therefore, the total error cannot drop below the physically correct limit of the experiment and thus the impact of strong reflections does not become exaggerated in the refinement. The determination of *k* is done by measurent the same set of reflections several times during an experiment (the so called standard reflections). The mean variation of the averaged value represents *k*. In addition, the repeated measurement of standard reflections offers the opportunity to notice unwanted changes during experiment like structural changes or release from the sample holder.

To make sure the comparisability of all reflections with each other, all intensities and errors are normalized to the same time of measurement (or monitor count rate) and undergo the Lorentz and (in the x-ray case) polarization correction.
Finally in advance of the data refinement there can be done an numerical (e.g. with DataP, [8]) or an empirical absoprtion if necessary. The quality of a measurement is checked in advance of the data refinement by comparing symmetry equivalent reflections and systematic extinctions to confirm the Laue group and space group symmetry. The result is written as internal *R*-value:

$$R_{\mathrm{int}} = (\sum_{k=1}^{m}(\sum_{j=1}^{n_k} (<I_k>- I_j)^2))/ (\sum_{k=1}\sum_{j=1}^{n_k}(I_j^2)_k)$$

R_{int} represents the mean error of a single reflection j of a group k of n_k symmetry equivalent reflections, corresponding to its group and the total number m of all symmetrically independent groups. Therefore R_{int} is also a good mark to check the absorption correction. After these preliminary steps one can start the final data refinement.
At the beginning one has to develop a structural model. The problem with that is that we measure only the absolut values $|F_{\mathrm{hkl}}|$ and not the complete structure factor $F_{\mathrm{hkl}} = |F_{hkl}|\exp(\imath\phi)$ including its phase ϕ. Therefore, generally the direct fouriertransform of the reflection information F_{hkl} from reciprocal space into the density information ρ in the direct space (electron density for x-rays, probability density of atomic cores for neutrons) with

$$\rho(\mathbf{x}) \sim \sum_h\sum_k\sum_l F_{hkl} \exp(-2\pi(hx+ky+lz))$$

not possible. This can be done only by direct methods like patterson, heavy atom method or anomal dispersion for x-rays.
In the so called refinement program a given structural model (space group, lattice constants, atomic form factors, MSD, etc.) are compared with the experimental data and fitted. In a leas squares routine those programs try to optimize (typically over several cycles) the free parameters to reduce the difference between the calculated structure factors F_{calc} and intensities $|F_{calc}|^2$ respectively and the experimentally found F_{obs} and $|F_{\mathrm{obs}}|^2$ respectively. To quantisize the quality of measurement there are several values in use:

1. *unweighted R*-value: $R_{\mathrm{u}} = \sum_{hkl} |F_{\mathrm{obs}}^2-F_{\mathrm{calc}}^2|/\sum_{hkl} F_{\mathrm{obs}}^2$
This value gives the alignment of the whole number of reflections without their specific errors.

2. weighted *R*-value: $R_{\mathrm{w}} = (\sum_{hkl} w (F_{\mathrm{obs}}^2-F_{\mathrm{calc}}^2)^2)/\sum_{hkl} w F_{\mathrm{obs}}^4$
This value represents the alignment of the whole number of reflections including their specific errors or weights ($w\sim1/\sigma^2$). Sometimes weights are adopted in a way to suppress unwanted influence of the refinement algorithm by weak or badly defined reflections. Be aware that such corrections have to be done extremely carefully because otherwise the refinement adopts the data to the selected structural model and not the model to the experimental data!

3. *Goodness of Fit S*: $S^2 =(\sum_{hkl} w (F_{\mathrm{obs}}^2-F_{\mathrm{calc}}^2)/(n_{\mathrm{hkl\text{-}reflections}} - n_{\mathrm{free\ parameter}})$

S should have a value near one if the weighting scheme and the structure model fit to the experimental data set.

4 Sample Section

4.1 Introduction

$La_{2-x}Sr_xCuO_4$ is one of the cuprate superconductors with K_2NiF_4- structure for whose discovery the noble prize was granted in 1988 (Bednorz and Müller [9]) . Pure La_2CuO_4 is an isolator. Doping with earth alcali metals (Ca^{2+}, Sr^{2+}, Ba^{2+}) on the La^{3+} lattice positions generates in dependence of the degree of doping superconductivity. Sr doping of x=0.15 yields a maximum T_c of 38 K.

Pure La_2CuO_4 undergoes at $T_{t\text{-}o}$=530 K a structural phase transition from the tetragonal high temperature phase (HTT)

F4/mmm: a=b=5.384 Å, c=13.204 Å, α=β=γ=90° at T=540 K

to the orthorhombic low temperature phase (LTO)

Abma: a=5.409 Å, b=5.357 Å, c=13.144 Å, α=β=γ=90° at room temperature.

The phase transition temperature $T_{t\text{-}o}$ drops for $La_{2-x}Sr_xCuO_4$ with increased doping and disappears above x=0.2.

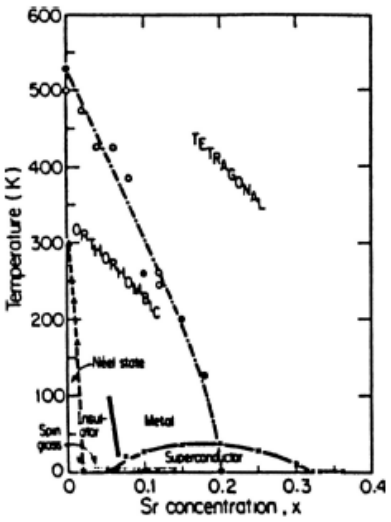

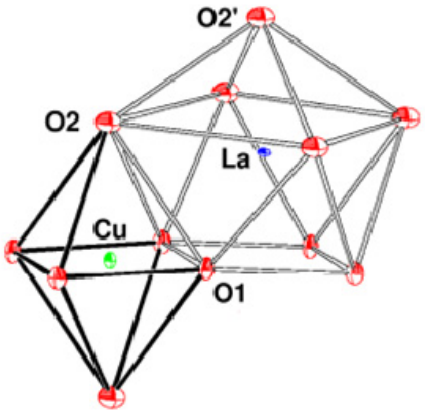

Fig.. 6 left: J. Birgenau, G. Shirane, HTC Superconductors I, World Scientific (1989)
Fig.. 6 right: Stuctural parts of La_2CuO_4 in the LTO phase

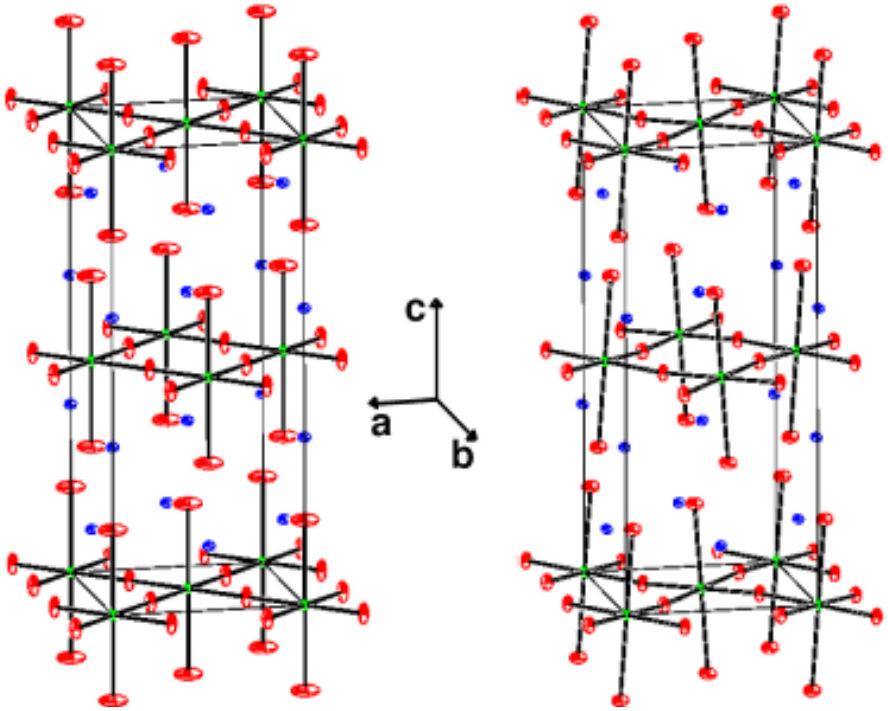

Fig. 7 left: tetragonal HTT phase Fig. 7 right: orthorhombic´LTO phase

4.2 Twinning

During the transition into the low temperature phase the CuO_6 octahedrons are tilted around their [010] axis. Thus, the two axes of identical length in the HTT phase, a_1 and a_2, are not equal in the LTO phase anymore. Instead, the longer one becomes the new *a* axis, the shorter one becomes the *b* axis. Whether a_1 or a_2 becomes the new a axis depends only on the real structure of the crystal, for instance grain boundaries or point defects. Therefore, one can find two equivalent crystallographic space groups in the LTO phase:

Abma ($a_1 \rightarrow a$, $a_2 \rightarrow b$) and B*mab* ($a_1 \rightarrow b$, $a_2 \rightarrow a$)

For the structure factors in the LTO is valid:

$F_{\mathrm{Abma}}(hkl)=F_{\mathrm{Bmab}}(khl)$

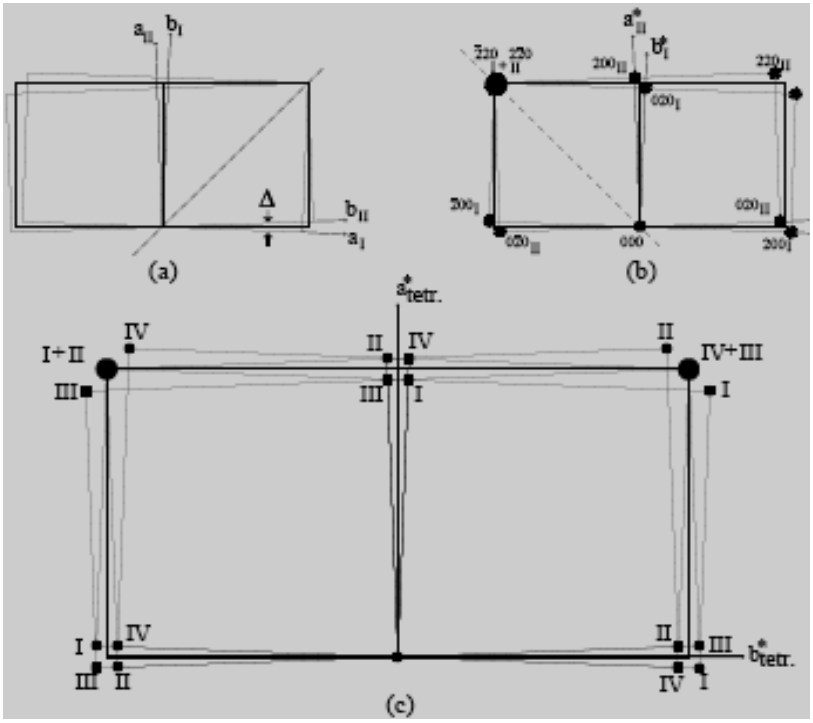

Fig. 8
(a) orthorhombic distortion with twinning correspondint to a (1-10) mirroring
(b) corresponding reciprocal lattice
(c) Overlay of (110)- and (1-10)-mirroring in reciprocal space

In the HTT phase only reflections with *h, k, l* of equal parity (*g* for even, *u* for uneven) are allowed - (*uuu*) and (*ggg*). They are called in the following main structrure reflections.
In the LTO phase additional reflections occur, called super structure reflections: In the *Abma*-Structure (*ugg*), l≠0 and (*guu*), in the *Bmab* structure (*gug*), l≠0 and(*ugu*).
Forbidden in both the HTT and the LTO phase are (*uug*), (*ggu*), (*ug*0) and (*gu*0).
These extinction rules will become important later.
In the real structure of the crystal there exist four domain types in total. They are separated into two pairs with the couple $Abma_1/Bmab_1$ (I/II) with the (1-10) mirror plane as grain boundary and the couple $Abma_2/Bmab_2$ (III/IV) with the (110) mirror plane as grain boundary (fig. 8).

The following overlaps of reflections result from this twinning:

- No splitting of the (00l) reflections,
- triple splitting of the (hh0) reflections
- fourfold splitting of the (h00) reflections.

An equal distribution of the volumetric portion of each single domain yields a ratio of intensities of 1:2:1 for the triple splitting. The distance $\Delta\omega$ between the centre and the side

peaks of a (*hkl*) reflex gives because of $(a+b)/2 = a_{1/2}$ an information about the orthorhombic *a/b* splitting. For the triple splitting of a (*hh*0) reflex is valid:

$\Delta\omega = 90°\text{-}2\arctan(b/a)$

Thus, although the real crystal is twinned, one can quantify the orthorhombic distortion.

The intensity contribution of the single domains corresponding to the whole intensity of a reflection can be described (taking into account the incoherent overlap of single intensities and the volumetric portions V_{A1} to V_{B2} of the domains) as follows:

$$I_{obs}(hkl) = I_{Abma1}(hkl) + I_{Bmab1}(hkl) + I_{Abma2}(hkl) + I_{Bmab2}(khl) \text{ or}$$

$$V_{total}|F_{obs}(hkl)|^2 = V_{A1}|F_{Abma1}(hkl)|^2 + V_{B1}|F_{Bmab1}(hkl)|^2 + V_{A2}|F_{Abma2}(hkl)|^2 + V_{B2}|F_{Bmab2}(hkl)|^2$$

$$= (V_{A1} + V_{A2})|F_{Abma1}(hkl)|^2 + (V_{B1}| + V_{B2})|F_{Bmab1}(hkl)|^2$$

$$= V_{total}\ \{\alpha|F_{Abma}(hkl)|^2 + (1\text{-}\alpha)\ |F_{Abma}(khl)|^2\ \}$$

with α being the relative portion of the volume of *Abma* domains to the crystal..

Because of the extinction rules in the LTO phase for the super structure reflections is valid: $I_{obs}(hkl) \sim \alpha|F_{Abma}(hkl)|^2$ for *Abma* and $I_{obs}(hkl) \sim (1\text{-}\alpha)|F_{Abma}(khl)|^2$ for *Bmab*. Thus, one can classify directly intensities to the volumetric portions of the domain types *Abma* and *Bmab* respectively. Therefore, by using one single additional parameter α to describe the relation between the twins in the structure one can determine the orthorhombic single crystal structure! This holds true although the Bragg reflections contain contributions of up to four different domains.

4.3 Oxygen Position

The oxygen atoms undergo the largest shift of their positions during the transition to the LTO phase. For the structure factor of a any Bragg reflection forbidden in *F4/mmm* is valid:

$$F(hkl) \sim \sum_i s_i \exp(-2\pi\imath(hx_i+ky_i+lz_i) = F(hkl)_{\text{apex oxygen}}+F(hkl)_{\text{in plane oxygen}}+F(hkl)_{\text{structure w/o O}}$$
$$\rightarrow F(hkl)_{\text{apex oxygen}}+F(hkl)_{\text{in plane oxygen}}$$

In the LTO phase the atomic position of the apex oxygens is (x 0 z), the atomic position for the in-plane oxygens is (1/4 1/4 -z). This yields the following intensities for the superstructure reflections:

$F(hkl)_{\text{apex oxygen}} = \cos(2\pi hx)\cos(2\pi lz)$ for h even or
$F(hkl)_{\text{apex oxygen}} = \sin(2\pi hx)\cos(2\pi lz)$ for h uneven

In the case of x-rays the form factor $f_i \sim Z_i$, Z_i=order number is much smaller for oxygen (Z=16) than for Cu (Z=29) and La (Z=57). Because of $I_{\text{obs}}(hkl) \sim |F(hkl)|^2$ the oxygen shift is hardly measurable. In the case of neutrons the scattering lengths b_i of all atoms are in the same order of magnitude (b_{O}=5.803 barn, b_{Cu}= barn, b_{La}= barn, 1 barn = 10^{-24} cm^{-2}). Therefore, the intensity contribution of the oxygen atoms increeases in relation to the other elements in the structure and allows a much more precise determination of the structural change of the oxygen positions

5 Preparatory Exercises

1. What is the fundamental difference between powder/single crystal diffraction and what are the advantages and disadvantages of both techniques (Compare d-values and orientations of different reflections in a cubic structure)?
2. What is wrong with fig. 2?
3. Which reflections are not allowed in a face centered structure (structure factor)?
4. There is no space group F4/mmm in the international tables. Why (Which other space group in the international tables yields the same pattern in direct space)?

6 Experiment Procedure

During this practical course not all physical and technical aspects of structure analysis with neutrons can be discussed in detail. Nevertheless this course is supposed point out the basic similarities and dissimilarities of x-rays and neutron radiation as well as their specific advantages and disadvantages in general and referring to single crystal diffraction. The sample selected for this practical course is most suitable for this purpose because of its special crystallographic peculiarities.

6.1 The Instrument

Fig. 5 shows the typical setup of a single crystal diffractometer with a single detector. Outgoing from the radiation source a primary beam defined by primary optics (in our case the beam tube) reaches the single crystal sample. If one lattice plane (*hkl*) fulfills Braggs laws, the scattered beam, called secondary beam, leaves the sample under an angle 2Θ to the primary beam. The exact direction of this beam depends only on the relative orientation of the sample to the primary beam.
For the diffractometer shown in fig. 5 the movement of the neutron detector is limited to a horizontal rotation around the 2Θ axis. Thus, only those reflections can be measured, whose scattering vector **Q** lies exactly in the plane defined by the source, the sample and detector circle. This plane is also called scattering plane.

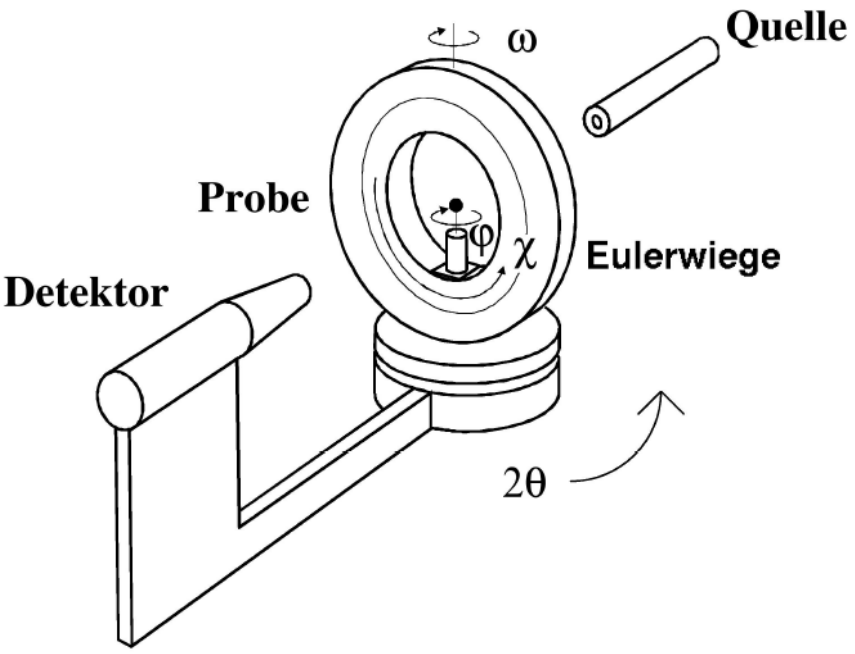

Fig. 5: Scheme of a single crystal diffractometer

To direct the secondary beam towards the detector position one has to orient the sample around the three axes ω, χ and ϕ. These three axes allow a virtually random orientation of the crystal in the primary beam. During the experiment the sample has to stay exactly in the cross point of all four axes (2Θ, ω, χ and ϕ) and the primary beam. Additionally, for $2\Theta = \omega = \chi = \phi = 0°$ the primary beam direction and the χ axis on one hand side and the 2Θ-, ω- and ϕ-axes on the other hand side are identical while the angle between the primary beam and the 2Θ-is exactly 90°. Because of the four rotational axes (2Θ, ω, χ, ϕ) this kind of single crystal diffractometer is often called four circle diffractometer. Another often used geometry - the so called κ-Geometrie - will not be discussed in detail here.

Further details of the experimental setup:

1. Beam source and primary optics: The primary beam is generated by a suitable source (x-rays: x-ray tube, synchrotron; neutrons: nuclear fission, spallation source). The primary optics defines the path of the beam to the sample in the Eulerian cradle. Furthermore, the primary optics defines the beam diameter using slits to make it fit to the sample size for homogeneous illumination. This homogeneity is very important because the quality of the data refinement relies on the comparison of the intensity ratios between the different reflections measured during an experiment. Wrong ratios caused by inhomogeneous illumination can yield wrong structural details! Other components of the primary optics are collimators defining beam divergence and filters or monochromators which define the wavelength λ of the radiation.

2. Sample and sample environment: The sample position is fixed by the centre of the Eulerian cradle which is defined by the cross point of the axes ω, χ and ϕ. As described above, the cradle itself has in combination with the ω-circle the task to orient the sample according to the observed reflection in a way that it hits the detector. The sample itself is mounted on a goniometer head. This head allows the adjustment of the sample in all three directions **x***;* **y***;* **z**, via microscope or camera. To avoid scattering from the sample environment and goniometer head the sample is usually connected to the head via a thin glass fibre (x-rays) or aluminum pin (neutrons). This reduces significantly background scattering. For experiments at high or low temperatures adjustable cooling or heating devices can be mounted into the Eulerian cradle.

3. Secondary optics and detector: The 2Θ arm of the instrument hold the detector which – in the ideal case – catches only radiation scattered from the sample and transforms it to an electrical signal. There exists a variety of detectors, single detectors and position sensitive 1D and 2D detectors. Area detectors have a large sensitive area that allows the accurate observation of spatial distribution of radiation. Other components of the secondary optics are slits and collimators or analyser (as optional units). They fulfil the task to shield the detector from unwanted radiation like scattering from sample environment, scattering in air, wrong wavelengths or flourescence

6.2 Sequence of measurement in Theory

1. Centering: In advance of the planned scientific program (profile analysis, Bragg data collection) the orientation of the sample in relation to the coordinate system of the diffractometer has to be determined. First of all the sample has to be centered optically to assure a homogeneous illumination of the sample. Afterwards, a reflection search routine has to be started to optimize the intensity of a found reflection by moving several angles after each other.
In many cases there are some structural informations like the unit cell and hkl values of strong reflections available from previous studies, e.g. from powder diffraction, thus, one can limit the reflection search to 2Θ values around these strong reflections to spare some time and to classify manually the found reflections with the correct indices.

2. Determination of orienting matrix and lattice constants: The comparison of the **Q** vectors of the found and centered reflections yields generally one or more suggestions for a suitable unit cell. This is done by a least squares routine minimizing the error bars between the calculated and measured **Q** vectors. This method allows to determine accurately the orientation matrix $\mathbf{M_o} = (\mathbf{a^*}\ \mathbf{b^*}\ \mathbf{c^*})^T$ of the sample relative to the coordinate system of the diffractometer and the lattice constants of the unit cell.

On HEiDi the axes are defined as following: **x**=primary beam, **z** || 2Θ axis, **y**=**z** x **x**.
A proposed unit cell is only acceptable if all experimentally found reflections can be indexed with integer *hkl* , this means $\mathbf{Q} = (h\ k\ l)^*\mathbf{M_o}$. In addition the found reflection intensities *I* offer a course check, e.g. whether extinction rules are followed or intensities of symmetrically identical reflections are identical.

3. Profile analyses and scan types: During profile analysis reflex profiles are analysed via so called ω scans. During this scan the sample is turned for *n* steps around a center position ω_0. This scan makes different crystallites in one large sample visible. In addition one has to take into account that even in perfectly grown crystals there are grain boundaries and slight mismatches of the crystallites. These mosaic blocks are perfect crystals whose orientations are misaligned only a few tenths of a degree or less. By the way, the axis position $2\Theta/2=\Theta=\omega$ is called the bisecting orientation of the Eulerian cradle.
As long as the vertical aperture is large enough, a rotation of the crystal around a ω_0, that is equivalent to the ideal Θ_0 Bragg angle of a reflex allows to catch the intensity portion of each crystallite in the sample in the neutron detector on the fixed 2Θ position, even those that can only be found for slightly differing ω. Therefore, a crystal with large mosaicity gives measurable intensities over a broader ω area than a perfect crystal. Thus it gives a broader reflex profile. Also the tearing and cracking of a crystal creates broad but unregular profiles.
Beside the crystal quality also the instrumental resolution limits the measurable profile widths in the following sense: The divergence of a primary beam in real experiment is limited, for instance to 0.2°.
If a reflection fulfills Bragg's Law at Θ, the total divergence is a convolution of the divergence of the primary beam *and* the mosaicity/divergence of the sample. Thus, the reflection profile will never be sharper than the divergence of the primary beam itself.
In addition one has to take into account that for larger diffraction angles a fixed detector window will not be sufficient to catch the whole reflection intensities during a rocking scan.

For a given spectrum $\Delta\lambda/\lambda$ of the primary beam, with increasing scattering angle Θ angular range $\Delta\Theta$ increases with $\sin(\Delta\Theta/2)=\tan(\Theta)*\Delta\lambda/\lambda$ for which all wavelengths in the interval $\lambda\pm\Delta\lambda/2$ fulfilling Bragg's law are distributed. Because of the limited width of the detector window this yields a cut off of intensities for larger scattering angles for ω-scans.
To compensate this cut off effect it is necessary to begin at a certain 2Θ-angle to move the detector window with the ω-angle.. This can be done by so called $\omega/2\Theta$-scans. The start position of this 2Θ range depends on the primary beam divergence and sample quality and has to be checked individually for each sample.

4. Collection of Bragg reflections: If a sample was found good after the described preliminary studies one can start with the Bragg data collection. In this data collection all (or selected) reflections in a given 2Θ intervall are collected automatically. The usual strategy follows the rule „Only as many as necessary". This means the following: On one hand side the quality of the measured reflections has to fulfil certain standards (like small standard deviations σ and a good shape of the profiles) to reach an acceptable accuracy. On the other side there is only a limited amount of time available for each reflection due to the huge number of them (up to several thousands). and the limited beam time. A rule of thumb is therefore to measure about 10 non symmetry equivalent reflections for each free parameter used in the data refinement to get the correct structure. To achieve this goal a typical algorithm is to do a prescan with t_{min} per point of measurement in combination with a given larger (e.g. I/σ=4 and 25%, respectively) and a smaller (e.g. I/σ=20 and 5%, respectively) relative error limit. t_{min} is chosen in a way that the statistics of strong reflections is fine already after the prescan. Weak reflections are also noticed in the prescan and stored as weak reflections without additional treatment. Reflections in between get an additional chance to improve their statistics by performing a second scan with a limited amount of time up to t_{max}-t_{min}. This method avoids to spend unreasonable beam time to weak reflections which will not help to improve the quality of the structure model.

6.3 and in Practice

1. **Adjust optically the sample in the neutron beam :** Alignment of the sample in the rotational centre of the instrument. This is necessary for a homogeneous illumination of the sample for all possible orientations.

2. **Search for Bragg reflections and center them, , "Reflex centering**": Sample and detector position are controlled by a special diffractometer software. The main goal is to find suitable angular positions for the detector first and afterwards for the sample to get a measurable signal. Afterwards the orientation of the sample in the Eulerian cradle have to be optimized for maximum intensity.

3. **Analyse profiles of selected reflections:** Study different reflex profiles and reveal the impact of twinning

4. **Determine the orthorhombic lattice parameters a, b and c**: Estimate the misalignment of a and b in reference to $a_{1/2}$ in the real tetragonal cell.

5. **Determine the average tetragonal unit cell**: The centering of different reflections allows the calculation of all lattice constants including the averaged tetragonal parameters.

6. **Observe super structure reflections:** Measuring pairs of (*hkl*)/(*khl*) allows the estimation of the volumetric contribution of each single domain to the whole crystal.

7. **Select measurement parameters for Bragg data collection:** In order to optimize the number and statistical quality of collected Bragg reflections suitable scan parameters (time/step, no. of steps, stepwidths, etc.) have to be determined.

8. **Collect a Bragg data set**

6.4 Data analysis

After having measured a Bragg data set one has to do the final step, the alignment of model and measurement:

1. **Data Reduction:** In this process the measured reflection profiles are analysed and reduced to a simple list of all measured reflections and their integrated intensities including error bars and some other useful information. This so-called *hkl*-list is the base for the next step:

2. **Structure refinement:** Here the measured *hkl*-list and our structure model are combined to determine structural details like atomic positions and mean square displacements.

7 Experiment-Related Exercises

1. Why is the optical adjustment of the sample so important?
2. How large is the *a/b*-splitting at room temperature (=|*a*-*b*|/(*a*+*b*))?
3. What is the benefit/enhancement of studying the room temperature structure with neutrons instead of X-rays?

References

[1] Th. Hahn (ed.), Space-group symmetry, International Tables for Crystallography Vol. A, Kluver Academic Publishers (2006).
[2] W.H. Zachariasen, Acta Cryst. 18 703 (1965).

[3] W.H. Zachariasen, Acta Cryst. 18 705 (1965).

[4] P. Coppens and W.C. Hamilton, Acta Cryst. A 26 71-83 (1970).

[5] P.J. Becker and P. Coppens, Acta Cryst. A 30 129-147 (1974).

[6] P.J. Becker and P. Coppens, Acta Cryst. A 30 148-153 (1974).

[7] U.H. Zucker, E. Perrenthaler, W.F. Kuhs, R. Bachmann and H. Schulz J. of Appl. Crystallogr., 16 358 (1983).
[8] P. Coppens, W.C. Hamilton, S. Wilkins, M.S. Lehmann and Savariault, Datap, http://www.ill.fr/data treat/diftreat.html#single (1999).
[9] J. Bednorz and K. Müller, Z. Phys. B 64 189 (1986).

Literature

N.W. Ashcroft and N.D. Mermin, Festkörperphysik, Oldenbourg 2001.

H. Ibach and H. Lüth, Festkörperphysik, Einführung in die Grundlagen, 6. Edition Springer 2002.

C. Kittel, Einführung in die Festkörperphysik, 10. Edition, Oldenbourg 1993.

W. Borchardt-Ott, Kristallographie. Eine Einführung für Naturwissenschaftler, 6. Auflage Springer 2002.

W. Kleber, Einführung in die Kristallographie, Oldenbourg 1998

H. Dachs, Neutron Diffraction, Springer (1978)

D.J. Dyson, X-Ray and Electron Diffraction Studies in Material Science, Maney Pub 2004.

C. Giacovazzo, Fundamentals of Crystallography, 2nd Ed., Oxford University Press 2002.

L.A. Aslanov, Crystallographic Instrumentation, Oxford University Press 1998.

M.T. Dove, Structure and Dynamics. An Atomic View of Materials, Oxford University Press 2003. W. Clegg, Crystal Structure Analysis. Principles and Practice, Oxford University Press 2001.

Appendix (Tables and space groups from [1])

3.1. SPACE-GROUP DETERMINATION AND DIFFRACTION SYMBOLS

Table 3.1.4.1. *Reflection conditions, diffraction symbols and possible space groups* (*cont.*)

ORTHORHOMBIC, Laue class *mmm* ($2/m\ 2/m\ 2/m$) (*cont.*)

Reflection conditions								Laue class *mmm* ($2/m\ 2/m\ 2/m$)		
								Point group		
hkl	0*kl*	*h*0*l*	*hk*0	*h*00	0*k*0	00*l*	Extinction symbol	222	*mm*2 *m*2*m* 2*mm*	*mmm*
	$k+l$	l	k		k	l	*Pncb*			*Pncb* (50)
	$k+l$	l	$h+k$	h	k	l	*Pncn*			*Pncn* (52)
	$k+l$	$h+l$		h	k	l	*Pnn* –		***Pnn2*** (34)	***Pnnm*** (58)
	$k+l$	$h+l$	h	h	k	l	*Pnna*			***Pnna*** (52)
	$k+l$	$h+l$	k	h	k	l	*Pnnb*			*Pnnb* (52)
	$k+l$	$h+l$	$h+k$	h	k	l	*Pnnn*			***Pnnn*** (48)
$h+k$	k	h	$h+k$	h	k		*C* – – –	***C222*** (21)	***Cmm2*** (35) *Cm2m* (38) *C2mm* (38)	***Cmmm*** (65)
$h+k$	k	h	$h+k$	h	k	l	*C*– –2_1	***C222*$_1$** (20)		
$h+k$	k	h	h, k	h	k		*C*– –(*ab*)		*Cm2e* (39) *C2me* (39)	***Cmme*** (67)
$h+k$	k	h, l	$h+k$	h	k	l	*C*–*c* –		***Cmc2*$_1$** (36) *C2cm* (40)	***Cmcm*** (63)
$h+k$	k	h, l	h, k	h	k	l	*C*–*c*(*ab*)		*C2ce* (41)	***Cmce*** (64)
$h+k$	k, l	h	$h+k$	h	k	l	*Cc* – –		*Ccm*2_1 (36) *Cc2m* (40)	*Ccmm* (63)
$h+k$	k, l	h	h, k	h	k	l	*Cc* –(*ab*)		*Cc2e* (41)	*Ccme* (64)
$h+k$	k, l	h, l	$h+k$	h	k	l	*Ccc* –		***Ccc2*** (37)	***Cccm*** (66)
$h+k$	k, l	h, l	h, k	h	k	l	*Ccc*(*ab*)			***Ccce*** (68)
$h+l$	l	$h+l$	h	h		l	*B* – – –	*B*222 (21)	*Bmm*2 (38) *Bm2m* (35) *B2mm* (38)	*Bmmm* (65)
$h+l$	l	$h+l$	h	h	k	l	*B*–2_1–	*B*22_12 (20)		
$h+l$	l	$h+l$	h, k	h	k	l	*B*– –*b*		*Bm*2_1*b* (36) *B2mb* (40)	*Bmmb* (63)
$h+l$	l	h, l	h	h		l	*B* –(*ac*)–		*Bme*2 (39) *B2em* (39)	*Bmem* (67)
$h+l$	l	h, l	h, k	h	k	l	*B* –(*ac*)*b*		*B2eb* (41)	*Bmeb* (64)
$h+l$	k, l	$h+l$	h	h	k	l	*Bb* – –		*Bbm*2 (40) *Bb*2_1*m* (36)	*Bbmm* (63)
$h+l$	k, l	$h+l$	h, k	h	k	l	*Bb*–*b*		*Bb2b* (37)	*Bbmb* (66)
$h+l$	k, l	h, l	h	h	k	l	*Bb*(*ac*)–		*Bbe*2 (41)	*Bbem* (64)
$h+l$	k, l	h, l	h, k	h	k	l	*Bb*(*ac*)*b*			*Bbeb* (68)
$k+l$	$k+l$	l	k		k	l	*A* – – –	*A*222 (21)	***Amm2*** (38) *Am2m* (38) *A2mm* (35)	*Ammm* (65)
$k+l$	$k+l$	l	k	h	k	l	*A*2_1– –	*A*2_122 (20)		
$k+l$	$k+l$	l	h, k	h	k	l	*A*– –*a*		***Am2a*** (40) *A*2_1*ma* (36)	*Amma* (63)
$k+l$	$k+l$	h, l	k	h	k	l	*A*–*a* –		***Ama2*** (40) *A*2_1*am* (36)	*Amam* (63)
$k+l$	$k+l$	h, l	h, k	h	k	l	*A*–*aa*		*A2aa* (37)	*Amaa* (66)
$k+l$	k, l	l	k		k	l	*A*(*bc*)– –		***Aem2*** (39) *Ae2m* (39)	*Aemm* (67)
$k+l$	k, l	l	h, k	h	k	l	*A*(*bc*)– *a*		*Ae2a* (41)	*Aema* (64)
$k+l$	k, l	h, l	k	h	k	l	*A*(*bc*)*a* –		***Aea2*** (41)	*Aeam* (64)
$k+l$	k, l	h, l	h, k	h	k	l	*A*(*bc*)*aa*			*Aeaa* (68)
$h+k+l$	$k+l$	$h+l$	$h+k$	h	k	l	*I* – – –	[***I222*** (23) ***I2*$_1$*2*$_1$*2*$_1$ (24)]*	***Imm2*** (44) *Im2m* (44)	***Immm*** (71)

3. DETERMINATION OF SPACE GROUPS

Table 3.1.4.1. *Reflection conditions, diffraction symbols and possible space groups* (*cont.*)

ORTHORHOMBIC, Laue class *mmm* ($2/m\ 2/m\ 2/m$) (*cont.*)

Reflection conditions								Laue class *mmm* ($2/m\ 2/m\ 2/m$)		
								Point group		
hkl	0*kl*	*h*0*l*	*hk*0	*h*00	0*k*0	00*l*	Extinction symbol	222	*mm*2 *m*2*m* 2*mm*	*mmm*
									*I*2*mm* (44)	
$h+k+l$	$k+l$	$h+l$	h,k	h	k	l	$I--(ab)$		*Im*2*a* (46)	***Imma*** (74)
									*I*2*mb* (46)	*Immb* (74)
$h+k+l$	$k+l$	h,l	$h+k$	h	k	l	$I-(ac)-$		***Ima*2** (46)	*Imam* (74)
									*I*2*cm* (46)	*Imcm* (74)
$h+k+l$	$k+l$	h,l	h,k	h	k	l	$I-cb$		*I*2*cb* (45)	*Imcb* (72)
$h+k+l$	k,l	$h+l$	$h+k$	h	k	l	$I(bc)--$		*Iem*2 (46)	*Iemm* (74)
									*Ie*2*m* (46)	
$h+k+l$	k,l	$h+l$	h,k	h	k	l	$Ic-a$		*Ic*2*a* (45)	*Icma* (72)
$h+k+l$	k,l	h,l	$h+k$	h	k	l	$Iba-$		***Iba*2** (45)	***Ibam*** (72)
$h+k+l$	k,l	h,l	h,k	h	k	l	$Ibca$			***Ibca*** (73)
										Icab (73)
$h+k,h+l,k+l$	k,l	h,l	h,k	h	k	l	$F---$	***F*222** (22)	***Fmm*2** (42)	***Fmmm*** (69)
									*Fm*2*m* (42)	
									*F*2*mm* (42)	
$h+k,h+l,k+l$	k,l	$h+l=4n;\ h,l$	$h+k=4n;\ h,k$	$h=4n$	$k=4n$	$l=4n$	$F-dd$		*F*2*dd* (43)	
$h+k,h+l,k+l$	$k+l=4n;\ k,l$	h,l	$h+k=4n;\ h,k$	$h=4n$	$k=4n$	$l=4n$	$Fd-d$		*Fd*2*d* (43)	
$h+k,h+l,k+l$	$k+l=4n;\ k,l$	$h+l=4n;\ h,l$	h,k	$h=4n$	$k=4n$	$l=4n$	$Fdd-$		***Fdd*2** (43)	
$h+k,h+l,k+l$	$k+l=4n;\ k,l$	$h+l=4n;\ h,l$	$h+k=4n;\ h,k$	$h=4n$	$k=4n$	$l=4n$	$Fddd$			***Fddd*** (70)

* Pair of space groups with common point group and symmetry elements but differing in the relative location of these elements.

3.1. SPACE-GROUP DETERMINATION AND DIFFRACTION SYMBOLS

Table 3.1.4.1. *Reflection conditions, diffraction symbols and possible space groups* (*cont.*)

TETRAGONAL, Laue classes $4/m$ and $4/mmm$ (*cont.*)

Reflection conditions							Extinction symbol	Laue class						
								$4/m$			$4/mmm$ ($4/m\ 2/m\ 2/m$)			
								Point group						
hkl	*hk*0	0*kl*	*hhl*	00*l*	0*k*0	*hh*0		4	$\bar{4}$	$4/m$	422	4*mm*	$\bar{4}2m$ $\bar{4}m2$	$4/mmm$
	$h+k$	k			k		*Pnb* –							*P*4/*nbm* (125)
	$h+k$	k	l	l	k		*Pnbc*							*P*4$_2$/*nbc* (133)
	$h+k$	l		l	k		*Pnc* –							*P*4$_2$/*ncm* (138)
	$h+k$	l	l	l	k		*Pncc*							*P*4/*ncc* (130)
	$h+k$	$k+l$		l	k		*Pnn* –							*P*4$_2$/*nnm* (134)
	$h+k$	$k+l$	l	l	k		*Pnnc*							*P*4/*nnc* (126)
$h+k+l$	$h+k$	$k+l$	l	l	k		$I---$	*I*4 (79)	*I*$\bar{4}$ (82)	*I*4/*m* (87)	*I*422 (97)	*I*4*mm* (107)	*I*$\bar{4}$2*m* (121)	*I*4/*mmm* (139)
													I$\bar{4}m$2 (119)	
$h+k+l$	$h+k$	$k+l$	l	$l=4n$	k		$I4_1--$	*I*4$_1$ (80)			*I*4$_1$22 (98)			
$h+k+l$	$h+k$	$k+l$	‡	$l=4n$	k	h	$I--d$					*I*4$_1md$ (109)	*I*$\bar{4}$2*d* (122)	
$h+k+l$	$h+k$	k,l	l	l	k		$I-c-$					*I*4*cm* (108)	*I*$\bar{4}$*c*2 (120)	*I*4/*mcm* (140)
$h+k+l$	$h+k$	k,l	‡	$l=4n$	k	h	$I-cd$					*I*4$_1cd$ (110)		
$h+k+l$	h,k	$k+l$	l	$l=4n$	k		$I4_1/a--$			*I*4$_1$/*a* (88)				
$h+k+l$	h,k	$k+l$	‡	$l=4n$	k	h	$Ia-d$							*I*4$_1$/*amd* (141)
$h+k+l$	h,k	k,l	‡	$l=4n$	k	h	$Iacd$							*I*4$_1$/*acd* (142)

† Pair of enantiomorphic space groups, *cf.* Section 3.1.5.
‡ Condition: $2h+l=4n;\ l$.

International Tables for Crystallography (2006). Vol. A, Space group 139, pp. 478–479.

$I4/mmm$ D_{4h}^{17} $4/mmm$ Tetragonal

No. 139 $I\ 4/m\ 2/m\ 2/m$ Patterson symmetry $I4/mmm$

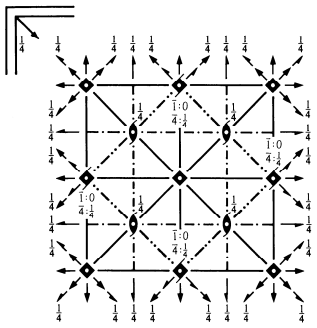

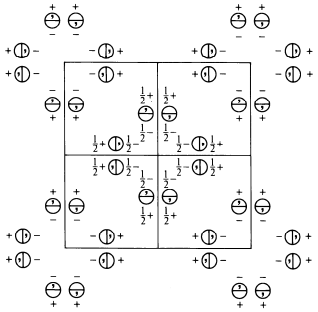

Origin at centre $(4/mmm)$

Asymmetric unit $0 \le x \le \frac{1}{2};\quad 0 \le y \le \frac{1}{2};\quad 0 \le z \le \frac{1}{4};\quad x \le y$

Symmetry operations

For $(0,0,0)+$ set

(1) 1	(2) 2 $0,0,z$	(3) 4^+ $0,0,z$	(4) 4^- $0,0,z$
(5) 2 $0,y,0$	(6) 2 $x,0,0$	(7) 2 $x,x,0$	(8) 2 $x,\bar{x},0$
(9) $\bar{1}$ $0,0,0$	(10) m $x,y,0$	(11) $\bar{4}^+$ $0,0,z$; $0,0,0$	(12) $\bar{4}^-$ $0,0,z$; $0,0,0$
(13) m $x,0,z$	(14) m $0,y,z$	(15) m $x,\bar{x},z$	(16) m x,x,z

For $(\frac{1}{2},\frac{1}{2},\frac{1}{2})+$ set

(1) $t(\frac{1}{2},\frac{1}{2},\frac{1}{2})$	(2) $2(0,0,\frac{1}{2})$ $\frac{1}{4},\frac{1}{4},z$	(3) $4^+(0,0,\frac{1}{2})$ $0,\frac{1}{2},z$	(4) $4^-(0,0,\frac{1}{2})$ $\frac{1}{2},0,z$
(5) $2(0,\frac{1}{2},0)$ $\frac{1}{4},y,\frac{1}{4}$	(6) $2(\frac{1}{2},0,0)$ $x,\frac{1}{4},\frac{1}{4}$	(7) $2(\frac{1}{2},\frac{1}{2},0)$ $x,x,\frac{1}{4}$	(8) 2 $x,\bar{x}+\frac{1}{2},\frac{1}{4}$
(9) $\bar{1}$ $\frac{1}{4},\frac{1}{4},\frac{1}{4}$	(10) $n(\frac{1}{2},\frac{1}{2},0)$ $x,y,\frac{1}{4}$	(11) $\bar{4}^+$ $\frac{1}{2},0,z$; $\frac{1}{2},0,\frac{1}{4}$	(12) $\bar{4}^-$ $0,\frac{1}{2},z$; $0,\frac{1}{2},\frac{1}{4}$
(13) $n(\frac{1}{2},0,\frac{1}{2})$ $x,\frac{1}{4},z$	(14) $n(0,\frac{1}{2},\frac{1}{2})$ $\frac{1}{4},y,z$	(15) c $x+\frac{1}{2},\bar{x},z$	(16) $n(\frac{1}{2},\frac{1}{2},\frac{1}{2})$ x,x,z

---

Maximal non-isomorphic subgroups *(continued)*

IIa
[2] $P4_2/nmc$ (137) 1; 2; 7; 8; 11; 12; 13; 14; (3; 4; 5; 6; 9; 10; 15; 16) + $(\frac{1}{2},\frac{1}{2},\frac{1}{2})$
[2] $P4_2/mnm$ (136) 1; 2; 7; 8; 9; 10; 15; 16; (3; 4; 5; 6; 11; 12; 13; 14) + $(\frac{1}{2},\frac{1}{2},\frac{1}{2})$
[2] $P4_2/nnm$ (134) 1; 2; 5; 6; 11; 12; 15; 16; (3; 4; 7; 8; 9; 10; 13; 14) + $(\frac{1}{2},\frac{1}{2},\frac{1}{2})$
[2] $P4_2/mmc$ (131) 1; 2; 5; 6; 9; 10; 13; 14; (3; 4; 7; 8; 11; 12; 15; 16) + $(\frac{1}{2},\frac{1}{2},\frac{1}{2})$
[2] $P4/nmm$ (129) 1; 2; 3; 4; 13; 14; 15; 16; (5; 6; 7; 8; 9; 10; 11; 12) + $(\frac{1}{2},\frac{1}{2},\frac{1}{2})$
[2] $P4/mnc$ (128) 1; 2; 3; 4; 9; 10; 11; 12; (5; 6; 7; 8; 13; 14; 15; 16) + $(\frac{1}{2},\frac{1}{2},\frac{1}{2})$
[2] $P4/nnc$ (126) 1; 2; 3; 4; 5; 6; 7; 8; (9; 10; 11; 12; 13; 14; 15; 16) + $(\frac{1}{2},\frac{1}{2},\frac{1}{2})$
[2] $P4/mmm$ (123) 1; 2; 3; 4; 5; 6; 7; 8; 9; 10; 11; 12; 13; 14; 15; 16

IIb none

Maximal isomorphic subgroups of lowest index

IIc [3] $I4/mmm$ ($\mathbf{c}' = 3\mathbf{c}$) (139); [9] $I4/mmm$ ($\mathbf{a}' = 3\mathbf{a}, \mathbf{b}' = 3\mathbf{b}$) (139)

Minimal non-isomorphic supergroups

I [3] $Fm\bar{3}m$ (225); [3] $Im\bar{3}m$ (229)

II [2] $C4/mmm$ ($\mathbf{c}' = \frac{1}{2}\mathbf{c}$) ($P4/mmm$, 123)

CONTINUED No. 139 $I4/mmm$

Generators selected (1); $t(1,0,0)$; $t(0,1,0)$; $t(0,0,1)$; $t(\frac{1}{2},\frac{1}{2},\frac{1}{2})$; (2); (3); (5); (9)

Positions

Multiplicity, Wyckoff letter, Site symmetry			Coordinates $(0,0,0)+$	$(\frac{1}{2},\frac{1}{2},\frac{1}{2})+$			Reflection conditions
							General:
32	o	1	(1) x,y,z (5) $\bar{x},y,\bar{z}$ (9) $\bar{x},\bar{y},\bar{z}$ (13) $x,\bar{y},z$	(2) $\bar{x},\bar{y},z$ (6) $x,\bar{y},\bar{z}$ (10) $x,y,\bar{z}$ (14) $\bar{x},y,z$	(3) $\bar{y},x,z$ (7) $y,x,\bar{z}$ (11) $y,\bar{x},\bar{z}$ (15) $\bar{y},\bar{x},z$	(4) $y,\bar{x},z$ (8) $\bar{y},\bar{x},\bar{z}$ (12) $\bar{y},x,\bar{z}$ (16) y,x,z	hkl : $h+k+l=2n$ $hk0$: $h+k=2n$ $0kl$: $k+l=2n$ hhl : $l=2n$ $00l$: $l=2n$ $h00$: $h=2n$
							Special: as above, plus
16	n	. m .	$0,y,z$ $0,y,\bar{z}$	$0,\bar{y},z$ $0,\bar{y},\bar{z}$	$\bar{y},0,z$ $y,0,\bar{z}$	$y,0,z$ $\bar{y},0,\bar{z}$	no extra conditions
16	m	. . m	x,x,z $\bar{x},x,\bar{z}$	$\bar{x},\bar{x},z$ $x,\bar{x},\bar{z}$	$\bar{x},x,z$ $x,x,\bar{z}$	$x,\bar{x},z$ $\bar{x},\bar{x},\bar{z}$	no extra conditions
16	l	m . .	$x,y,0$ $\bar{x},y,0$	$\bar{x},\bar{y},0$ $x,\bar{y},0$	$\bar{y},x,0$ $y,x,0$	$y,\bar{x},0$ $\bar{y},\bar{x},0$	no extra conditions
16	k	. . 2	$x,x+\frac{1}{2},\frac{1}{4}$ $\bar{x},\bar{x}+\frac{1}{2},\frac{3}{4}$	$\bar{x},\bar{x}+\frac{1}{2},\frac{1}{4}$ $x,x+\frac{1}{2},\frac{3}{4}$	$\bar{x}+\frac{1}{2},x,\frac{1}{4}$ $x+\frac{1}{2},\bar{x},\frac{3}{4}$	$x+\frac{1}{2},\bar{x},\frac{1}{4}$ $\bar{x}+\frac{1}{2},x,\frac{3}{4}$	hkl : $l=2n$
8	j	m 2 m .	$x,\frac{1}{2},0$	$\bar{x},\frac{1}{2},0$	$\frac{1}{2},x,0$	$\frac{1}{2},\bar{x},0$	no extra conditions
8	i	m 2 m .	$x,0,0$	$\bar{x},0,0$	$0,x,0$	$0,\bar{x},0$	no extra conditions
8	h	m . 2 m	$x,x,0$	$\bar{x},\bar{x},0$	$\bar{x},x,0$	$x,\bar{x},0$	no extra conditions
8	g	2 m m .	$0,\frac{1}{2},z$	$\frac{1}{2},0,z$	$0,\frac{1}{2},\bar{z}$	$\frac{1}{2},0,\bar{z}$	hkl : $l=2n$
8	f	. . 2/m	$\frac{1}{4},\frac{1}{4},\frac{1}{4}$	$\frac{3}{4},\frac{3}{4},\frac{1}{4}$	$\frac{3}{4},\frac{1}{4},\frac{1}{4}$	$\frac{1}{4},\frac{3}{4},\frac{1}{4}$	hkl : $k,l=2n$
4	e	4 m m	$0,0,z$	$0,0,\bar{z}$			no extra conditions
4	d	$\bar{4}$ m 2	$0,\frac{1}{2},\frac{1}{4}$	$\frac{1}{2},0,\frac{1}{4}$			hkl : $l=2n$
4	c	m m m .	$0,\frac{1}{2},0$	$\frac{1}{2},0,0$			hkl : $l=2n$
2	b	4/m m m	$0,0,\frac{1}{2}$				no extra conditions
2	a	4/m m m	$0,0,0$				no extra conditions

Symmetry of special projections

Along [001] $p4mm$
$\mathbf{a}' = \frac{1}{2}(\mathbf{a}-\mathbf{b})$ $\mathbf{b}' = \frac{1}{2}(\mathbf{a}+\mathbf{b})$
Origin at $0,0,z$

Along [100] $c2mm$
$\mathbf{a}' = \mathbf{b}$ $\mathbf{b}' = \mathbf{c}$
Origin at $x,0,0$

Along [110] $p2mm$
$\mathbf{a}' = \frac{1}{2}(-\mathbf{a}+\mathbf{b})$ $\mathbf{b}' = \frac{1}{2}\mathbf{c}$
Origin at $x,x,0$

Maximal non-isomorphic subgroups

I [2] $I\bar{4}2m$ (121) (1; 2; 5; 6; 11; 12; 15; 16)+
[2] $I\bar{4}m2$ (119) (1; 2; 7; 8; 11; 12; 13; 14)+
[2] $I4mm$ (107) (1; 2; 3; 4; 13; 14; 15; 16)+
[2] $I422$ (97) (1; 2; 3; 4; 5; 6; 7; 8)+
[2] $I4/m11$ ($I4/m$, 87) (1; 2; 3; 4; 9; 10; 11; 12)+
[2] $I2/m2/m1$ ($Immm$, 71) (1; 2; 5; 6; 9; 10; 13; 14)+
[2] $I2/m12/m$ ($Fmmm$, 69) (1; 2; 7; 8; 9; 10; 15; 16)+

(*Continued on preceding page*)

International Tables for Crystallography (2006). Vol. A, Space group 69, pp. 316–318.

$F\,m\,m\,m$ D_{2h}^{23} $m\,m\,m$ Orthorhombic

No. 69 $F\ 2/m\ 2/m\ 2/m$ Patterson symmetry $F\,m\,m\,m$

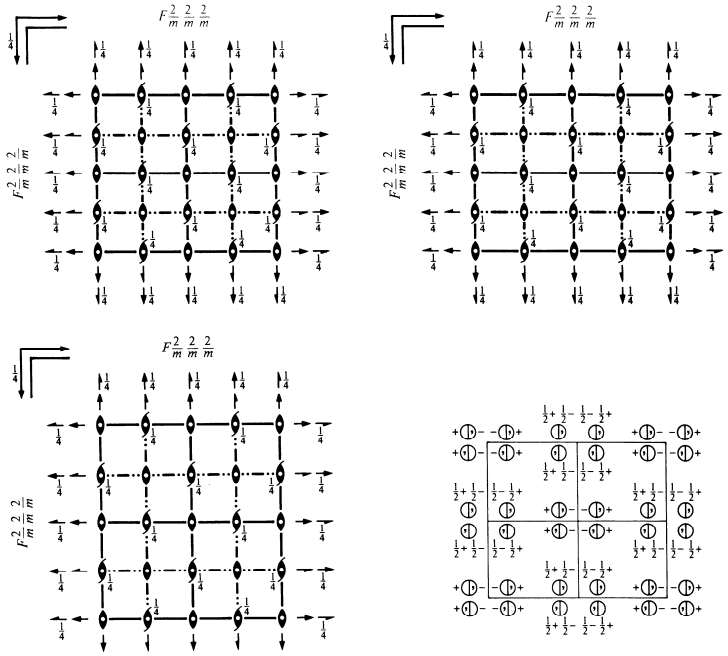

Origin at centre $(m\,m\,m)$

Asymmetric unit $0 \le x \le \frac{1}{4};\quad 0 \le y \le \frac{1}{4};\quad 0 \le z \le \frac{1}{2}$

Symmetry operations

For $(0,0,0)+$ set

(1) 1	(2) 2 $0,0,z$	(3) 2 $0,y,0$	(4) 2 $x,0,0$
(5) $\bar{1}$ $0,0,0$	(6) m $x,y,0$	(7) m $x,0,z$	(8) m $0,y,z$

For $(0,\frac{1}{2},\frac{1}{2})+$ set

(1) $t(0,\frac{1}{2},\frac{1}{2})$	(2) $2(0,0,\frac{1}{2})$ $0,\frac{1}{4},z$	(3) $2(0,\frac{1}{2},0)$ $0,y,\frac{1}{4}$	(4) 2 $x,\frac{1}{4},\frac{1}{4}$
(5) $\bar{1}$ $0,\frac{1}{4},\frac{1}{4}$	(6) b $x,y,\frac{1}{4}$	(7) c $x,\frac{1}{4},z$	(8) $n(0,\frac{1}{2},\frac{1}{2})$ $0,y,z$

For $(\frac{1}{2},0,\frac{1}{2})+$ set

(1) $t(\frac{1}{2},0,\frac{1}{2})$	(2) $2(0,0,\frac{1}{2})$ $\frac{1}{4},0,z$	(3) 2 $\frac{1}{4},y,\frac{1}{4}$	(4) $2(\frac{1}{2},0,0)$ $x,0,\frac{1}{4}$
(5) $\bar{1}$ $\frac{1}{4},0,\frac{1}{4}$	(6) a $x,y,\frac{1}{4}$	(7) $n(\frac{1}{2},0,\frac{1}{2})$ $x,0,z$	(8) c $\frac{1}{4},y,z$

For $(\frac{1}{2},\frac{1}{2},0)+$ set

(1) $t(\frac{1}{2},\frac{1}{2},0)$	(2) 2 $\frac{1}{4},\frac{1}{4},z$	(3) $2(0,\frac{1}{2},0)$ $\frac{1}{4},y,0$	(4) $2(\frac{1}{2},0,0)$ $x,\frac{1}{4},0$
(5) $\bar{1}$ $\frac{1}{4},\frac{1}{4},0$	(6) $n(\frac{1}{2},\frac{1}{2},0)$ $x,y,0$	(7) a $x,\frac{1}{4},z$	(8) b $\frac{1}{4},y,z$

CONTINUED **No. 69** ***F m m m***

Generators selected (1); $t(1,0,0)$; $t(0,1,0)$; $t(0,0,1)$; $t(0,\frac{1}{2},\frac{1}{2})$; $t(\frac{1}{2},0,\frac{1}{2})$; (2); (3); (5)

Positions

Multiplicity, Wyckoff letter, Site symmetry			Coordinates $(0,0,0)+$	$(0,\frac{1}{2},\frac{1}{2})+$	$(\frac{1}{2},0,\frac{1}{2})+$	$(\frac{1}{2},\frac{1}{2},0)+$	Reflection conditions
							General:
32	*p*	1	(1) x,y,z (5) $\bar{x},\bar{y},\bar{z}$	(2) $\bar{x},\bar{y},z$ (6) $x,y,\bar{z}$	(3) $\bar{x},y,\bar{z}$ (7) $x,\bar{y},z$	(4) $x,\bar{y},\bar{z}$ (8) $\bar{x},y,z$	hkl : $h+k,h+l,k+l=2n$ $0kl$: $k,l=2n$ $h0l$: $h,l=2n$ $hk0$: $h,k=2n$ $h00$: $h=2n$ $0k0$: $k=2n$ $00l$: $l=2n$
							Special: as above, plus
16	*o*	. . *m*	$x,y,0$	$\bar{x},y,0$	$x,\bar{y},0$	$\bar{x},\bar{y},0$	no extra conditions
16	*n*	. *m* .	$x,0,z$	$\bar{x},0,z$	$x,0,\bar{z}$	$\bar{x},0,\bar{z}$	no extra conditions
16	*m*	*m* . .	$0,y,z$	$0,\bar{y},z$	$0,y,\bar{z}$	$0,\bar{y},\bar{z}$	no extra conditions
16	*l*	2 . .	$x,\frac{1}{4},\frac{1}{4}$	$\bar{x},\frac{3}{4},\frac{1}{4}$	$\bar{x},\frac{3}{4},\frac{3}{4}$	$x,\frac{1}{4},\frac{3}{4}$	hkl : $h=2n$
16	*k*	. 2 .	$\frac{1}{4},y,\frac{1}{4}$	$\frac{3}{4},\bar{y},\frac{1}{4}$	$\frac{3}{4},\bar{y},\frac{3}{4}$	$\frac{1}{4},y,\frac{3}{4}$	hkl : $h=2n$
16	*j*	. . 2	$\frac{1}{4},\frac{1}{4},z$	$\frac{3}{4},\frac{1}{4},z$	$\frac{3}{4},\frac{3}{4},z$	$\frac{1}{4},\frac{3}{4},z$	hkl : $h=2n$
8	*i*	*m m* 2	$0,0,z$	$0,0,\bar{z}$			no extra conditions
8	*h*	*m* 2 *m*	$0,y,0$	$0,\bar{y},0$			no extra conditions
8	*g*	2 *m m*	$x,0,0$	$\bar{x},0,0$			no extra conditions
8	*f*	2 2 2	$\frac{1}{4},\frac{1}{4},\frac{1}{4}$	$\frac{3}{4},\frac{3}{4},\frac{3}{4}$			hkl : $h=2n$
8	*e*	. . 2/*m*	$\frac{1}{4},\frac{1}{4},0$	$\frac{3}{4},\frac{1}{4},0$			hkl : $h=2n$
8	*d*	. 2/*m* .	$\frac{1}{4},0,\frac{1}{4}$	$\frac{3}{4},0,\frac{1}{4}$			hkl : $h=2n$
8	*c*	2/*m* . .	$0,\frac{1}{4},\frac{1}{4}$	$0,\frac{3}{4},\frac{1}{4}$			hkl : $h=2n$
4	*b*	*m m m*	$0,0,\frac{1}{2}$				no extra conditions
4	*a*	*m m m*	$0,0,0$				no extra conditions

Symmetry of special projections

Along [001] $p2mm$
$\mathbf{a}' = \frac{1}{2}\mathbf{a}$ $\mathbf{b}' = \frac{1}{2}\mathbf{b}$
Origin at $0,0,z$

Along [100] $p2mm$
$\mathbf{a}' = \frac{1}{2}\mathbf{b}$ $\mathbf{b}' = \frac{1}{2}\mathbf{c}$
Origin at $x,0,0$

Along [010] $p2mm$
$\mathbf{a}' = \frac{1}{2}\mathbf{c}$ $\mathbf{b}' = \frac{1}{2}\mathbf{a}$
Origin at $0,y,0$

International Tables for Crystallography (2006). Vol. A, Space group 64, pp. 302–303.

$Cmce$ D_{2h}^{18} mmm Orthorhombic

No. 64 $C\ 2/m\ 2/c\ 2_1/e$ Patterson symmetry $Cmmm$

Former space-group symbol $Cmca$; *cf.* Chapter 1.3

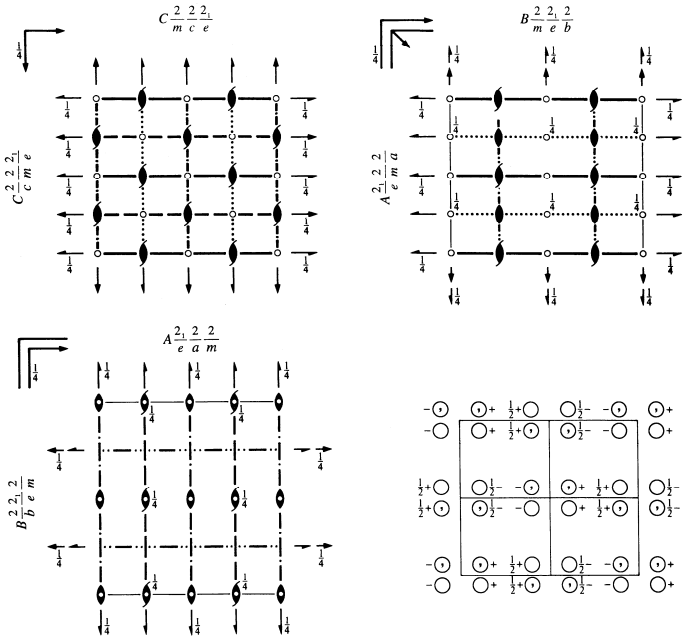

Origin at centre $(2/m)$ at $2/mn1$

Asymmetric unit $0 \le x \le \frac{1}{4}$; $0 \le y \le \frac{1}{2}$; $0 \le z \le \frac{1}{2}$

Symmetry operations

For $(0,0,0)+$ set

(1) 1	(2) $2(0,0,\frac{1}{2})$ $0,\frac{1}{4},z$	(3) $2(0,\frac{1}{2},0)$ $0,y,\frac{1}{4}$	(4) 2 $x,0,0$
(5) $\bar{1}$ $0,0,0$	(6) b $x,y,\frac{1}{4}$	(7) c $x,\frac{1}{4},z$	(8) m $0,y,z$

For $(\frac{1}{2},\frac{1}{2},0)+$ set

(1) $t(\frac{1}{2},\frac{1}{2},0)$	(2) $2(0,0,\frac{1}{2})$ $\frac{1}{4},0,z$	(3) 2 $\frac{1}{4},y,\frac{1}{4}$	(4) $2(\frac{1}{2},0,0)$ $x,\frac{1}{4},0$
(5) $\bar{1}$ $\frac{1}{4},\frac{1}{4},0$	(6) a $x,y,\frac{1}{4}$	(7) $n(\frac{1}{2},0,\frac{1}{2})$ $x,0,z$	(8) b $\frac{1}{4},y,z$

CONTINUED **No. 64** *Cmce*

Generators selected (1); $t(1,0,0)$; $t(0,1,0)$; $t(0,0,1)$; $t(\frac{1}{2},\frac{1}{2},0)$; (2); (3); (5)

Positions

Multiplicity, Wyckoff letter, Site symmetry			Coordinates $(0,0,0)+$ $(\frac{1}{2},\frac{1}{2},0)+$				Reflection conditions
							General:
16	*g*	1	(1) x,y,z (5) $\bar{x},\bar{y},\bar{z}$	(2) $\bar{x},\bar{y}+\frac{1}{2},z+\frac{1}{2}$ (6) $x,y+\frac{1}{2},\bar{z}+\frac{1}{2}$	(3) $\bar{x},y+\frac{1}{2},\bar{z}+\frac{1}{2}$ (7) $x,\bar{y}+\frac{1}{2},z+\frac{1}{2}$	(4) $x,\bar{y},\bar{z}$ (8) $\bar{x},y,z$	hkl : $h+k=2n$ $0kl$: $k=2n$ $h0l$: $h,l=2n$ $hk0$: $h,k=2n$ $h00$: $h=2n$ $0k0$: $k=2n$ $00l$: $l=2n$
							Special: as above, plus
8	*f*	*m* . .	$0,y,z$	$0,\bar{y}+\frac{1}{2},z+\frac{1}{2}$	$0,y+\frac{1}{2},\bar{z}+\frac{1}{2}$	$0,\bar{y},\bar{z}$	no extra conditions
8	*e*	. 2 .	$\frac{1}{4},y,\frac{1}{4}$	$\frac{3}{4},\bar{y}+\frac{1}{2},\frac{3}{4}$	$\frac{3}{4},\bar{y},\frac{3}{4}$	$\frac{1}{4},y+\frac{1}{2},\frac{1}{4}$	hkl : $h=2n$
8	*d*	2 . .	$x,0,0$	$\bar{x},\frac{1}{2},\frac{1}{2}$	$\bar{x},0,0$	$x,\frac{1}{2},\frac{1}{2}$	hkl : $k+l=2n$
8	*c*	$\bar{1}$	$\frac{1}{4},\frac{1}{4},0$	$\frac{3}{4},\frac{1}{4},\frac{1}{2}$	$\frac{3}{4},\frac{3}{4},\frac{1}{2}$	$\frac{1}{4},\frac{3}{4},0$	hkl : $k,l=2n$
4	*b*	2/*m* . .	$\frac{1}{2},0,0$	$\frac{1}{2},\frac{1}{2},\frac{1}{2}$			hkl : $k+l=2n$
4	*a*	2/*m* . .	$0,0,0$	$0,\frac{1}{2},\frac{1}{2}$			hkl : $k+l=2n$

Symmetry of special projections

Along [001] $p2mm$
$\mathbf{a}' = \frac{1}{2}\mathbf{a}$ $\mathbf{b}' = \frac{1}{2}\mathbf{b}$
Origin at $0,0,z$

Along [100] $p2gm$
$\mathbf{a}' = \frac{1}{2}\mathbf{b}$ $\mathbf{b}' = \mathbf{c}$
Origin at $x,0,0$

Along [010] $p2mm$
$\mathbf{a}' = \frac{1}{2}\mathbf{c}$ $\mathbf{b}' = \frac{1}{2}\mathbf{a}$
Origin at $0,y,0$

Maximal non-isomorphic subgroups

I	[2] $C2ce$ ($Aea2$, 41)	(1; 4; 6; 7)+
	[2] $Cm2e$ ($Aem2$, 39)	(1; 3; 6; 8)+
	[2] $Cmc2_1$ (36)	(1; 2; 7; 8)+
	[2] $C222_1$ (20)	(1; 2; 3; 4)+
	[2] $C12/c1$ ($C2/c$, 15)	(1; 3; 5; 7)+
	[2] $C112_1/e$ ($P2_1/c$, 14)	(1; 2; 5; 6)+
	[2] $C2/m11$ ($C2/m$, 12)	(1; 4; 5; 8)+
IIa	[2] $Pmnb$ ($Pnma$, 62)	1; 3; 6; 8; (2; 4; 5; 7) + $(\frac{1}{2},\frac{1}{2},0)$
	[2] $Pbca$ (61)	1; 3; 5; 7; (2; 4; 6; 8) + $(\frac{1}{2},\frac{1}{2},0)$
	[2] $Pbna$ ($Pbcn$, 60)	1; 2; 3; 4; (5; 6; 7; 8) + $(\frac{1}{2},\frac{1}{2},0)$
	[2] $Pmca$ ($Pbcm$, 57)	1; 2; 7; 8; (3; 4; 5; 6) + $(\frac{1}{2},\frac{1}{2},0)$
	[2] $Pbnb$ ($Pccn$, 56)	1; 2; 5; 6; (3; 4; 7; 8) + $(\frac{1}{2},\frac{1}{2},0)$
	[2] $Pmcb$ ($Pbam$, 55)	1; 2; 3; 4; 5; 6; 7; 8
	[2] $Pbcb$ ($Pcca$, 54)	1; 4; 6; 7; (2; 3; 5; 8) + $(\frac{1}{2},\frac{1}{2},0)$
	[2] $Pmna$ (53)	1; 4; 5; 8; (2; 3; 6; 7) + $(\frac{1}{2},\frac{1}{2},0)$
IIb	none	

Maximal isomorphic subgroups of lowest index

IIc [3] $Cmce$ ($\mathbf{a}' = 3\mathbf{a}$) (64); [3] $Cmce$ ($\mathbf{b}' = 3\mathbf{b}$) (64); [3] $Cmce$ ($\mathbf{c}' = 3\mathbf{c}$) (64)

Minimal non-isomorphic supergroups

I none

II [2] $Fmmm$ (69); [2] $Pmcm$ ($\mathbf{a}' = \frac{1}{2}\mathbf{a}, \mathbf{b}' = \frac{1}{2}\mathbf{b}$) ($Pmma$, 51); [2] $Cmme$ ($\mathbf{c}' = \frac{1}{2}\mathbf{c}$) (67)

Contact

HEiDi

Phone: 089/289-14828
Web: http://www.frm2.tum.de/wissenschaftliche-nutzung/diffraktion/heidi/index.html

Martin Meven
Institut für Kristallographie Aachen, RWTH Aachen
JCNS Outstation at Forschungsneutronenquelle Heinz Maier-Leibnitz (FRM II)
Phone: 089/289-14727
e-Mail: Martin.Meven@frm2.tum.de

PANDA

Three-axis spectrometer

P. Link (TUM), A. Schneidewind

Jülich Centre for Neutron Science
Forschungszentrum Jülich

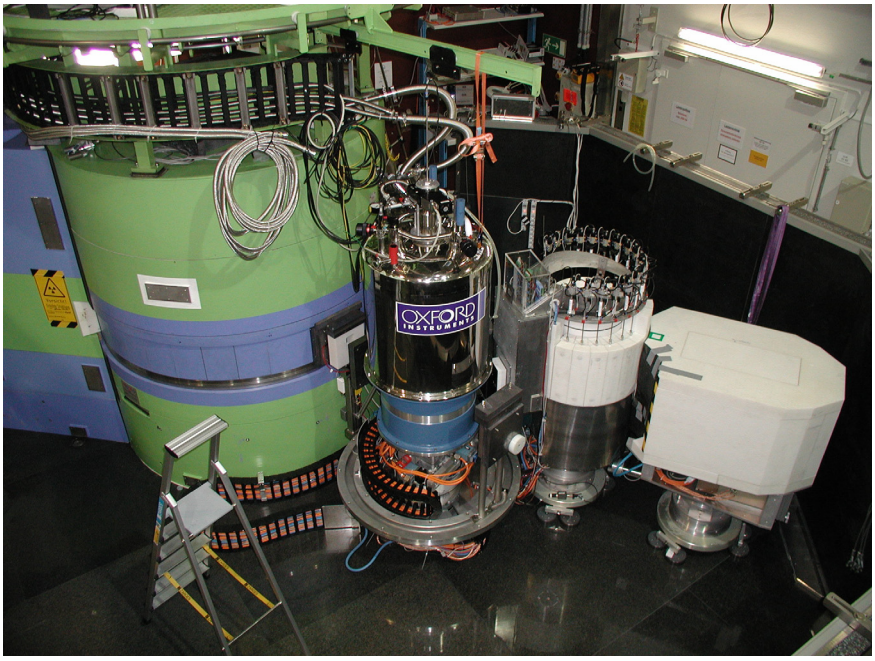

Manual of the JCNS Laboratory Course Neutron Scattering

Contents

1 Introduction and theoretical basics

This summary is thought as a repetition of the basic knowledge needed for this experiment. It is expected to be familiar with the different types of the crystal lattices, the terms of *unit cell* and *basis* as well as the use of *Miller's indices*.

1.1 Inelastic scattering cross section

In the experiment a sample is illuminated by a *monoenergetic* (energy E_i) neutron beam with a *direction* (wave vector $\boldsymbol{k}_i$). The ratio of the intensity scattered in a decent solid angle $d\Omega$ (wave vector $\boldsymbol{k}_f$) with the energy $Ef + dE$ to the intensity of the incoming beam is the differential scattering cross section

$$\frac{I_{\Omega,E_f}}{I_0} = \frac{d\sigma^2}{d\Omega\, dE_f}. \tag{1}$$

The scattering of the neutrons at the nuclei is handled within the quantum mechanics as a weak perturbation of the system. The calculation can be found as "Fermi's golden rule" in the textbooks.Reference: [6]

Generally, the scattering cross section is:

$$\frac{d^3\sigma}{d\Omega\, dE_f} = \frac{|\boldsymbol{k}_f|}{|\boldsymbol{k}_i|} S(\boldsymbol{Q}, \omega). \tag{2}$$

The scattering function S depends on the momentum transfer[1] $\boldsymbol{Q} = \boldsymbol{k}_i - \boldsymbol{k}_f$ and the energy transfer, to be written in a change of the wave length $\omega = \frac{E}{\hbar}$. The relation between ω or E and $|\boldsymbol{k}_f|$ is of squared, therefore the scattering cross section used in 1.9 is for the following calculations (Reference: [11], chap.4):

$$\frac{d^3\sigma}{d\boldsymbol{k}_{fx}\, d\boldsymbol{k}_{fy}\, d\boldsymbol{k}_{fz}} \propto \frac{1}{|\boldsymbol{k}_i|} S(\boldsymbol{Q}, \omega). \tag{3}$$

We start with elastic scattering ($|\boldsymbol{k}_i| = |\boldsymbol{k}_f|$). We will find that this is given by the assumption of a time-independent distribution of the scattering centers.

1.2 Elastic scattering function

We describe the incoming neutron beam as a plane wave. Its amplitude at every time t depends on the site $\boldsymbol{P} = \boldsymbol{R} + \boldsymbol{r}$ (see Fig. 1):

$$\mathcal{A}_P = \mathcal{A}_0\, e^{i[\boldsymbol{k}_i \cdot (\boldsymbol{R}+\boldsymbol{r})] - i\omega_0 t}. \tag{4}$$

It excited the scattering centers to emit spherical waves with an amplitude $\mathcal{A}'$, having a fix phase relation to the original (incident) wave.

$$\mathcal{A}'_P = \rho(\boldsymbol{P})\, \mathcal{A}_P, \tag{5}$$

[1] Really: the change of the wave vector. In units of $\hbar$ this is exactly the momentum transfer.

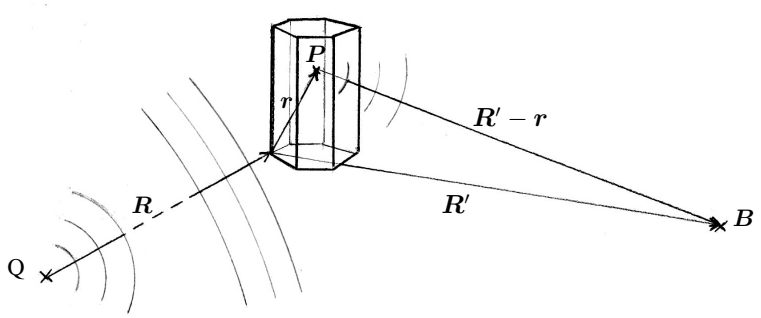

Figure 1: *General scattering geometry and notation*

$\rho(\boldsymbol{r})$ is the local scattering density with the unit m^{-2}. No multiple scattering occurs [2]. At a site $\boldsymbol{B}$ we get for a wave starting from a site $\boldsymbol{P}$:

$$\mathcal{A}_B(\boldsymbol{r},t) = \mathcal{A}_P(\boldsymbol{r},t)\,\rho(\boldsymbol{r})\frac{e^{i[\boldsymbol{k}_f\cdot(\boldsymbol{R'}-\boldsymbol{r})]}}{|\boldsymbol{R'}-\boldsymbol{r}|} \tag{6}$$

where $\boldsymbol{k}_f$ is pointing into the direction of $(\boldsymbol{R'}-\boldsymbol{r})$t.

We assume the distance between R and R' to be large compared to r.

$$\mathcal{A}_B(\boldsymbol{r},t) = \mathcal{A}_P(\boldsymbol{r},t)\,\rho(\boldsymbol{r})\frac{1}{R'}e^{i[\boldsymbol{k}_f\cdot(\boldsymbol{R'}-\boldsymbol{r})]} \tag{7}$$

with the same direction of $\boldsymbol{k}_f$ for all $\boldsymbol{P}$. After replacing $\mathcal{A}_P$ and ordering:

$$\mathcal{A}_B(\boldsymbol{r},t) = \frac{\mathcal{A}_0}{R'}e^{i(\boldsymbol{k}_i\cdot\boldsymbol{R}+\boldsymbol{k}_f\cdot\boldsymbol{R'})}\rho(\boldsymbol{r})e^{-i[(\boldsymbol{k}_f-\boldsymbol{k}_i)\cdot\boldsymbol{r}]-i\omega_i t}. \tag{8}$$

The first term is a constant phase factor, which is now space-independent within the sample. The whole scattering amplitude is given by integration of the scattering region.

$$\mathcal{A}_B(t) \propto e^{-i\omega_i t}\int_V \rho(\boldsymbol{r})e^{-i[(\boldsymbol{k}_f-\boldsymbol{k}_i)\cdot\boldsymbol{r}]}d\boldsymbol{r}. \tag{9}$$

As long as ρ is time-independent, the time dependence of $\mathcal{A}_B$ includes only the frequency ω_i (elastic scattering).

In the experiment, we do not have access to the amplitude of the wave but only to the square of it. For the scattering function one gets:

$$S(\boldsymbol{Q}) \propto \left|\int_V \rho(\boldsymbol{r})e^{-i\,\boldsymbol{Q}\cdot\boldsymbol{r}}d\boldsymbol{r}\right|^2 \tag{10}$$

$$\text{with:}\quad \boldsymbol{Q} = \boldsymbol{k}_f - \boldsymbol{k}_i. \tag{11}$$

Therefore, we identify the scattering function except a factor as the square of the Fourier transform of the scattering density.References: [7], [12]

[2] according to the Born approximation in the quantum-mechanical scattering theory

1.3 Coherent vs. incoherent scattering

Restricting on the interactions with the nuclei and using thermal neutron wavelengths ($\approx$ Å) which are large compared to the radii of the nuclei (10^{-4} Å) the sample can be assumed to be an array of point-shaped scattering centers. The scattering density follows as:

$$\rho(\boldsymbol{r}) = \sum_i b_i \delta(\boldsymbol{r}_i - \boldsymbol{r}) \tag{12}$$

with the positions of the scattering centers $\boldsymbol{r}_i$ and their scattering lengths b_i, respectively. b represents the amplitude of the spherical wave emitted by an atom and $\bar{b}$ its average.

The scattering function of a material with identical atoms in regular order is again a regular point lattice (see next chapter). But, a normal crystal is a mixture of several isotopes having different neutron scattering lengths. In this case, the interference condition is valid only for an averaged scattering length. Taking (12) for (10), the scattering function is s

$$S = \left(\bar{b}\right)^2 S_{\text{coh.}} + \left(\bar{b}^2 - \left(\bar{b}\right)^2\right) S_{\text{inc.}}. \tag{13}$$

assuming a statistical distribution of the different scattering centers. $S_{\text{inc.}}$ is now independent of the relative positions of the atoms to each other and therefore independent of the concrete structure of the sample. It is a term of background signal, independent of the scattering angle and the sample orientation. This so-called incoherent scattering is always observed when the scattering density varies locally and non-correlated, also for point defects in the lattice and randomly distributed spin orientations in nuclei and atomic shells. A distinguished incoherent scatterer - almost without a coherent distribution - is vanadium which is often used for spectrometer alignments. Reference: [12]

1.4 Reciprocal space and Brillouin-zones

The samples to be investigated are normally good coherent scatterers, it is necessary to know $S_{\text{coh.}}$. Let's start on a Bravais-lattice with a one-atom basis. The scattering density is:

$$\rho(\boldsymbol{r}) = \sum_{h,k,l} b\, \delta^3[(h\,\boldsymbol{a}_1 + k\,\boldsymbol{a}_2 + l\,\boldsymbol{a}_3) - \boldsymbol{r}], \tag{14}$$

with generating lattice vectors $\boldsymbol{a}_i$. The Fourier transform of such a function is:

$$\tilde{\rho}(\boldsymbol{q}) = \frac{1}{\sqrt{2\pi}} \int \sum_{h,k,l} b\, \delta^3[(h\,\boldsymbol{a}_1 + k\,\boldsymbol{a}_2 + l\,\boldsymbol{a}_3) - \boldsymbol{r}] e^{-i\boldsymbol{q}\cdot\boldsymbol{r}} d\boldsymbol{r} \tag{15}$$

$$= \sum_{h,k,l} b e^{-i\boldsymbol{q}\cdot[(h\,\boldsymbol{a}_1 + k\,\boldsymbol{a}_2 + l\,\boldsymbol{a}_3)]}. \tag{16}$$

Summarizing for a sufficient number of indices, one gets a point lattice again, the *reciprocal lattice* [3]. The wave vector space is named the *reciprocal space*.

[3] It can be shown that the reciprocal lattice of a Bravais lattice is a Bravais lattice again having all symmetry elements of the original lattice.

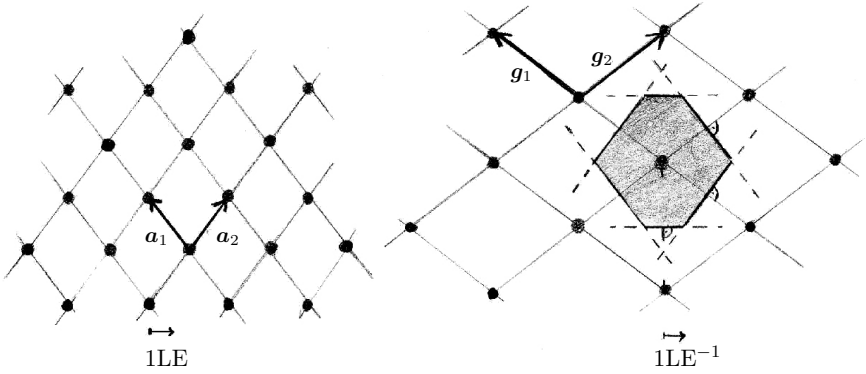

Figure 2: *2-dimensional point lattice in the real and reciprocal spaces. The first Brillouin zone is plotted around a reciprocal lattice point. Note the generating vectors of both lattices satisfying equation (17).*

By

$$\boldsymbol{g}_i \cdot \boldsymbol{a}_j = 2\pi\delta_{i,j} \tag{17}$$

we get the generating vectors $\boldsymbol{g_i}$ of the reciprocal space from the original vectors [4]: The reciprocal lattice vector $\boldsymbol{g_1}$ is perpendicular to the vectors $\boldsymbol{a_2}$ and $\boldsymbol{a_3}$ with an absolute value of:

$$\frac{2\pi}{(a_1 \cos \sphericalangle(\boldsymbol{a}_1, (\boldsymbol{a}_2 \times \boldsymbol{a}_3)))}. \tag{18}$$

In the simple case of the sc lattice all real lattice vectors are pairwise perpendicular. Thus, the directions of the reciprocal space are identical to that of the real space. But, the dimensions of the reciprocal lattice as well as of the wave vectors are'm^{-1}' (see eq. (17)).

In (10) we identified the scattering function as the square of the Fourier transformed of the scattering density. It is different from zero if

$$\boldsymbol{Q} = \boldsymbol{G} = h\boldsymbol{g}_1 + k\boldsymbol{g}_2 + l\boldsymbol{g}_3 \qquad \text{(Laue condition)}. \tag{19}$$

Wave vectors satisfying this condition built the Bragg reflections in the sample spectrum and are enumerated by the indices h, k, l.

fcc and bcc lattices are normally not presented by their primitive unit cells but as sc lattices with a polyatomic basis. Therefore, not all reflections of the sc lattice occur. This is described by the *structure factor*. Here eq. (17) does not give the generating wave vectors of the reciprocal space.

A useful construction to work with the wave vectors of the reciprocal space is the construction of the Brillouin zones. For this, in the reciprocal lattice the perpendicular bisector planes of the vectors connecting one lattice point with all the others are created. [5] (see also Fig. 2).

[4] The definition (17) is used in physics. The 2π factor depends on the definition of the wave vector and is sometimes omitted, especially in crystallography.

[5] All incoming plane waves with wave vectors ending at the Brillouin zone boundary satisfy the elastic scattering condition (19) since incident and final wave vector are of the same length.

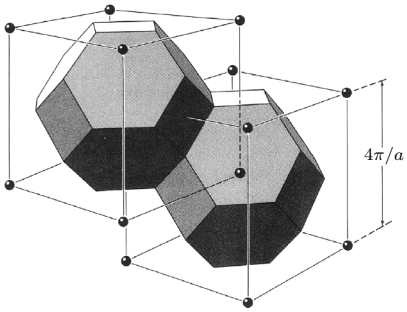

(a) The reciprocal lattice of a fcc crystals is a bcc lattice. The first two Brillouin zones are drawn. If the crystal consists of two interlocking fcc lattices (i.e. Silicon), not all reflections occur.

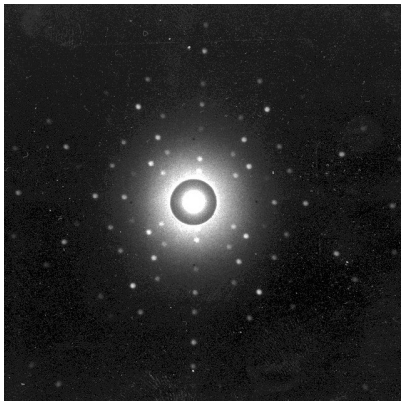

(b) Laue picture of a Silicon crystal ([110]-direction) irradiated by polychromatic x-rays. We get a two-dimensional projection of the reciprocal lattice up to decent indices, depending on the minimum wavelength of the x-rays.

Figure 3: *3-dimensional view of the elastic scattering.*

Remark: The construction of the Brillouin zones is of the basis Bravais lattice. I.e., Germanium and Silicon have a fcc lattice with a 2-atomic basis. The scattering function in influenced in a way that several refections vanish, others are amplified. The reciprocal lattice stays to be of fcc symmetry.

The first Brillouin zones around the points of the reciprocal lattice fill the reciprocal space. By this, points of high symmetry are easy to identify. They are used to be named by letters (see Fig. 6).

References: [7] Chapter about scattering on periodic structures.

1.5 Inelastic scattering processes

We allow a change of the scattering density ρ with time now.

$$\rho(\boldsymbol{r}(t)) \propto \sum_n \delta(\boldsymbol{r}_n(t) - \boldsymbol{r}). \tag{20}$$

The atoms are oscillating with weak amplitudes around their average position.

$$\boldsymbol{r}_n(t) = \boldsymbol{r}_n + \boldsymbol{u}_n(t). \tag{21}$$

Assuming the forces between neighboring atoms to be proportional to their displacement (harmonic approximation) every oscillation state of the crystal can be described as a superposition

of plane waves with wave vectors $\boldsymbol{q}$. [6]:

$$\boldsymbol{u}_n(t) = \sum_{\boldsymbol{q}} \boldsymbol{u}\, e^{\pm i(\boldsymbol{q}\cdot\boldsymbol{r}_n - \omega(\boldsymbol{q})\, t)}. \tag{22}$$

The scattering amplitude is from (10) and (20):

$$\mathcal{A} \propto e^{-i\omega_i t} \sum_n e^{-i\,\boldsymbol{Q}\cdot\boldsymbol{r}_n(t)}. \tag{23}$$

Take eq. (21) to develop the exponential function for small u's:

$$\mathcal{A} \propto e^{-i\omega_i t} \sum_n e^{-i\,\boldsymbol{Q}\cdot\boldsymbol{r}_n} e^{-i\,\boldsymbol{Q}\cdot\boldsymbol{u}_n(t)} \tag{24}$$

$$\approx e^{-i\omega_i t} \sum_n e^{-i\,\boldsymbol{Q}\cdot\boldsymbol{r}_n} [1 - i\,\boldsymbol{Q}\cdot\boldsymbol{u}(t)] \tag{25}$$

$$= e^{-i\omega_i t} \sum_n e^{-i\,\boldsymbol{Q}\cdot\boldsymbol{r}_n} - i\,\boldsymbol{Q}\cdot\boldsymbol{u}\, e^{-i\,\boldsymbol{Q}\cdot\boldsymbol{r}_n} e^{\pm i(\boldsymbol{q}\cdot\boldsymbol{r}_n - \omega(\boldsymbol{q})\, t)}. \tag{26}$$

In (26) we find in addition to the terms from elastic scattering for every $\boldsymbol{q}$ a term:

$$\sum_n i\,\boldsymbol{Q}\cdot\boldsymbol{u}\, e^{-i[(\boldsymbol{Q}\mp\boldsymbol{q})\cdot\boldsymbol{r}_n] - i[\omega_i \pm \omega(\boldsymbol{q})]t}. \tag{27}$$

Thus, there are scattering waves with frequencies shifted from the frequency of the primary wave just by the frequency of the crystal oscillations. In addition, in analogy to the elastic case, the sum in (27) is non-zero only if eq.

$$\boldsymbol{Q} = \boldsymbol{k}_i - \boldsymbol{k}_f = \boldsymbol{G} \mp \boldsymbol{q} \tag{28}$$

is satisfied by a reciprocal wave vector $\boldsymbol{G}$. The condition for the frequency is:

$$\omega_f = \omega_i \pm \omega(\boldsymbol{q}). \tag{29}$$

Multiplying both equations with $\hbar$ and choosing $\boldsymbol{G} = 0$ gives:

$$\hbar\Delta\omega \mp \hbar\omega(\boldsymbol{q}) = 0, \tag{30}$$

$$\hbar\boldsymbol{k}_f - \hbar\boldsymbol{k}_i \mp \hbar\boldsymbol{q} = 0. \tag{31}$$

This is just the quantum-mechanical description of the momentum and energy conservation for neutron scattering on a particle generally called a *phonon*. The analogy is confirmed also quantum-mechanically.

See i.e. [1] appendix N.

As to be seen from the equation, the momentum of a phonon is determined only modulo to one reciprocal lattice vector. Really two lattice oscillations of wave vectors differing by one

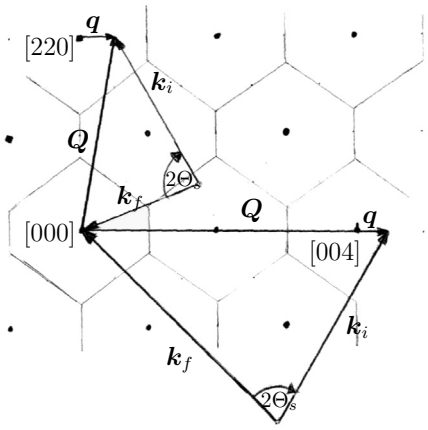

Figure 4: *Scattering diagrams for inelastic scattering of neutrons on a fcc crystal. The reciprocal* $[1\bar{1}0]$ *plane is drawn. Notation similar to the text. The energy transfer is represented by the different lengths of* $\mathsf{k_i}$ *and* $\mathsf{k_f}$

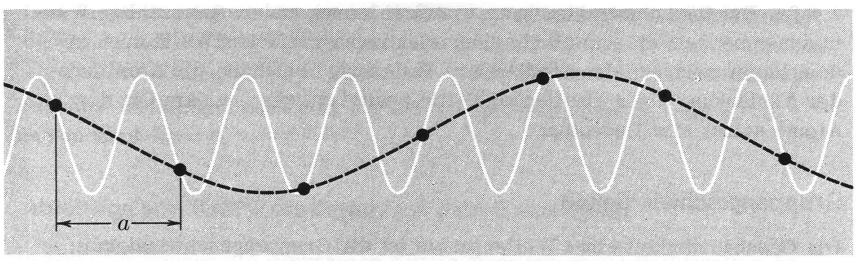

Figure 5: *Equivalence of lattice vibrations taken from [9]: Both of the shown waveslead to the same displacement of the atoms from their avarage position. They are physically identical. All waves with a wavelength* λ_1 *smaller than* $2\mathsf{a}$ *(white line) can be reduced to these with* $\lambda_2 \geq 2\mathsf{a}$ *(black line).* $\frac{2\pi}{\lambda_1} = \frac{2\pi}{\lambda_2} - \mathsf{n}\frac{2\pi}{\mathsf{a}}$*, with* $\mathsf{n}\frac{2\pi}{\mathsf{a}}$ *the length of a reciprocal lattice vector. The waves with* $\lambda \geq 2\mathsf{a}$ *are just these with wavevectors in the first Brilloin zone.*

reciprocal lattice vectors are similar by physics (see fig. 5). Thus, the wave vector of every phonon can be related to the nearest reciprocal lattice point and the theoretical considerations are restricted to the 1. Brillouin zone. The probability of the excitation of a phonon scales with the intensity of the nearest elastic reflection. See for example fig. 9. Phonons are therefore particles with a quasi-momentum [7].

Reference: see [7] chapter 4

For the visualization of the inelastic scattering process one can assume that the neutron initiates an oscillation in the crystal. By this, the neutron looses energy or gains energy when scattered on an oscillating atom which results in the annihilation of this oscillation. For the energy loss, a decent mode has to be already excited in the crystal. Such a consideration of the energies leads to the "'detailed balance"' principle:

$$S(\boldsymbol{Q}, -\omega) = e^{-\frac{\hbar\omega}{k_B T}}\ S(\boldsymbol{Q}, \omega) \tag{32}$$

with the Boltzmann factor $k_B T$. At room temperature, both sides are almost equivalent.

What is now the advantage of neutrons for the study of lattice vibrations, compared to x-rays - which are easier to handle and available with much higher flux, especially at synchrotron sources where in addition higher brilliance is achieved? The energy of thermal neutrons is in average circa $30\,\mathrm{meV}$ which is related to a wavevector of $3.8\,\mathrm{\AA}^{-1}$. The dimensions of the reciprocal space are given by eq. (17), i.e. circa $2\,\mathrm{\AA}^{-1}$ for Germanium. X-rays with similar wave vectors have energies of $\approx 10\,\mathrm{keV}$. The excitation of a lattice vibration with an energy of $10\,\mathrm{meV}$ would be according to a relative energy change of 10^{-6} for photons. For neutrons the change is in the order of kinetic energies.

1.6 Dispersion relation

One purpose of the experiment is to determine the correlation $\omega(\boldsymbol{q})$ experimentally. $\omega(\boldsymbol{q})$ is the (phonon) dispersion relation. It contains all information about the dynamic properties of the studied material. Physical quantities as velocity of sound and the phonon contribution of the heat capacity can be deduced from it. But, also the dominating interaction potentials between the atoms can be derived. For the visualization the 3-dimensional relation is drawn for several directions of symmetry abreast.

The principle of $\omega(\boldsymbol{q})$ can be shown at an one-dimensional atomic chain. See the textbook derivation (i.e. [1]). The generalization is done by the transition to parallel crystal planes oscillating contrary.

[6] This is the first-order Taylor series approximation of anharmonic potentials.

[7] The real momentum transfer of the neutrons is - as for elastic scattering - absorbed by the whole sample and is not relevant due to the mass ratio.

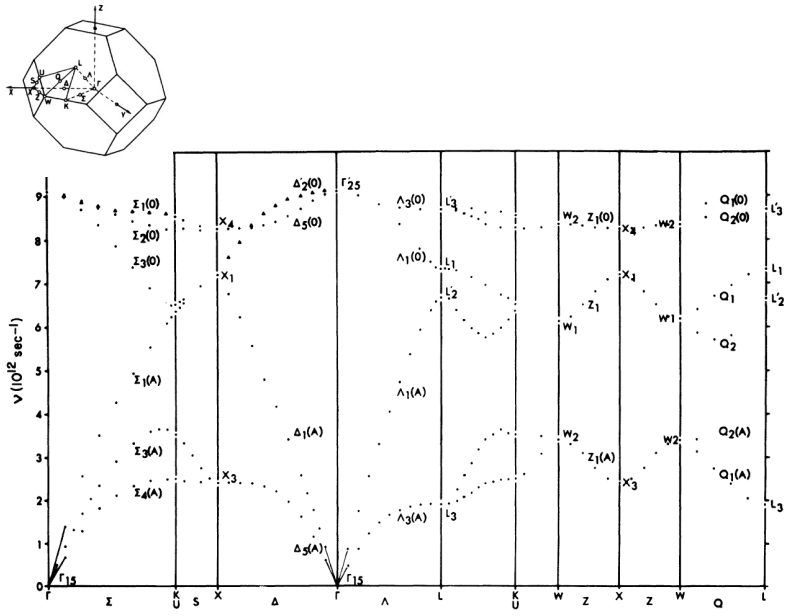

Figure 6: *Dispersion relation of Germanium at 80 K taken from [10]. Points of exceptionally high symmetry are indicated by letters. (small picture).*

1.7 Transverse and longitudinal phonons

As known from mechanics, for propagating waves the displacement of the single atoms can be chosen parallel (longitudinal) or perpendicular (transversal) to the propagation direction. In general, both excitation have different energies. For every $\boldsymbol{q}$ there are two transverse phonons with polarizations perpendicular to each other, but only one of them is in the scattering plane. In crystals of high symmetry these excitations are degenerated in energy. A crystal with a one-atomic basis has three dispersion modes. For a basis of n atoms,this number increases to $3n$ (3 acoustic ($E = 0$ in the center of the B-zone) and $3(n-1)$ optical modes ($E \neq 0$ at $q = 0$)). Fig. 6 shows this for the simple case of Germanium.

Reference: [9]

How can transverse and longitudinal oscillations to be distinguished in the experiment? The equation of the inelastic scattering function (27) contains the scalar product $\boldsymbol{Q} \cdot \boldsymbol{u}$ with the polarization of the wave $\boldsymbol{u}$ (fig. 7). Thus, an oscillation is only excited for $\boldsymbol{Q}$ with a component in the polarization direction, in analogy to the classical assumption. Fig. 4 shows the measurement of a longitudinal and of a transverse phonon. The wave vector $\boldsymbol{q}$ points in the same direction for both measurements.

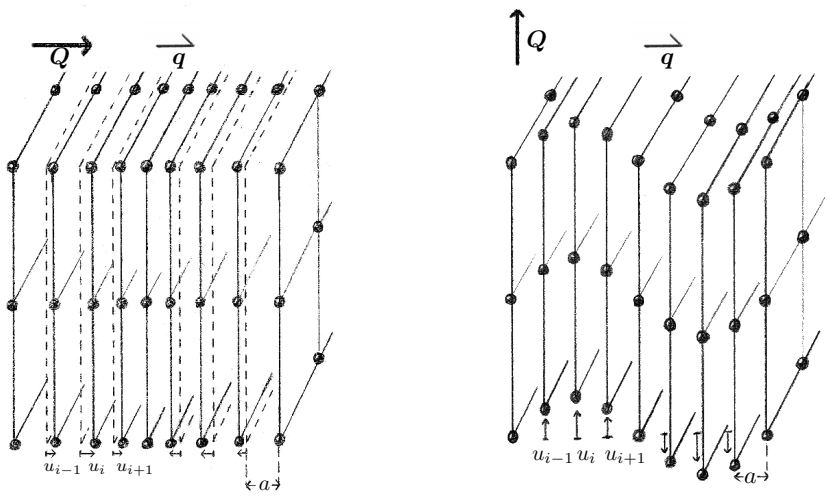

(a) longitudinal... (b) and transversal oscillations

Figure 7: *Note: The momentum transfer of the neutrons* Q *points always into the direction of the real displacements* u_i.

1.8 What is measured - what can we conclude for the sample

We look now at the correlation between the configuration of the spectrometer and the variables $\boldsymbol{Q}$ and ΔE. The absolute values of $\boldsymbol{k}_i$ and $\boldsymbol{k}_f$ (incident and outgoing wave vectors) are determined by the scattering angles at the monochromator and the analyzer crystals $2\Theta_m$ and $2\Theta_a$, respectively [8]. Having neutron waves we need

$$E_{\text{kin}} = \frac{(\hbar\, k_{\text{n}})^2}{2m}\,, \tag{33}$$

with $\boldsymbol{p}$ the momentum and m the mass of the neutron.
Thus, we know also

$$\omega = \frac{\Delta E}{\hbar} = \hbar\,\frac{|\boldsymbol{k}_i|^2 - |\boldsymbol{k}_f|^2}{2\,m_{\text{n}}}. \tag{34}$$

The orientation of the sample determines the direction of $\boldsymbol{k}_i$ relatively to the crystal lattice (characterized by the sample rotation angle ω_s) and the scattering plane. Within the scattering plane $2\Theta_s$ determines the direction of $\boldsymbol{k}_f$. $\boldsymbol{Q}$ results from eq. (11).

Conversely, we do not get the configuration of the instrument from ω and $\boldsymbol{Q}$.

In standard experiments, the scans are done at constant $\boldsymbol{Q}$ or constant energy transfer ΔE. While for very stiff dispersion modes, in the vicinity of the Brillouin zone center, constant-E is chosen (Fig. 8(b)), most of the Brillouin zone is normally measured with const.-$\boldsymbol{Q}$ (Fig. 8(a)).

[8] $2\Theta_m$ and $2\Theta_a$ are the relevant numbers. The rotation of the crystals Θ_m and Θ_a are fixed in relation to $2\Theta_m/2$ and $2\Theta_a/2$.

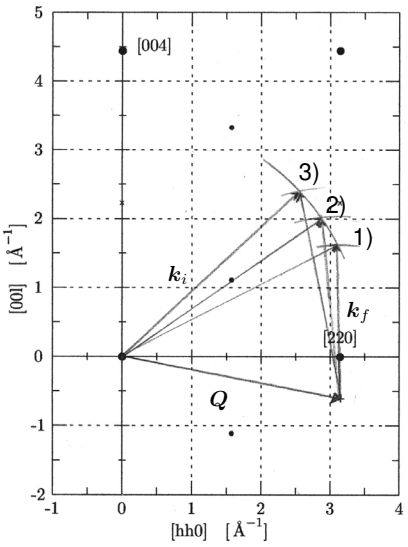

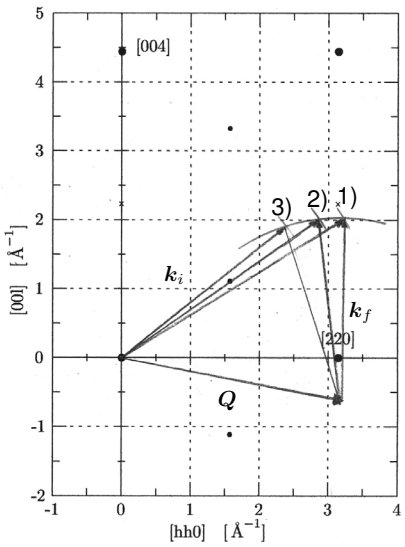

(a) Example for constant-Q scans

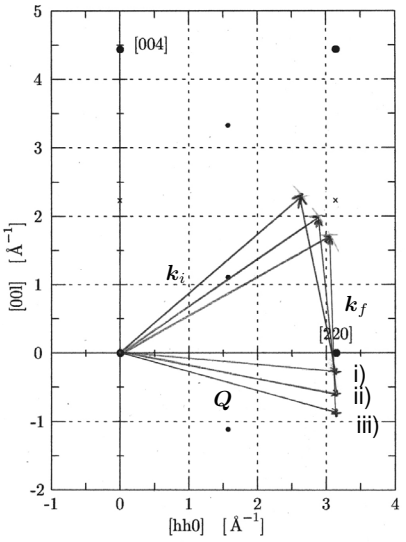

(b) A constant-E scan

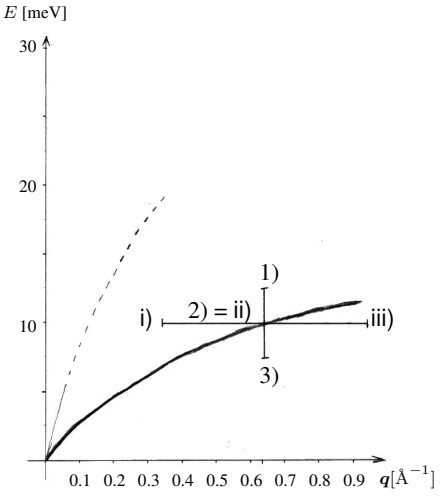

(c) corresponding points of the dispersion relation

Figure 8: *Examples for different scans (scattering triangles and dispersion relation.)*

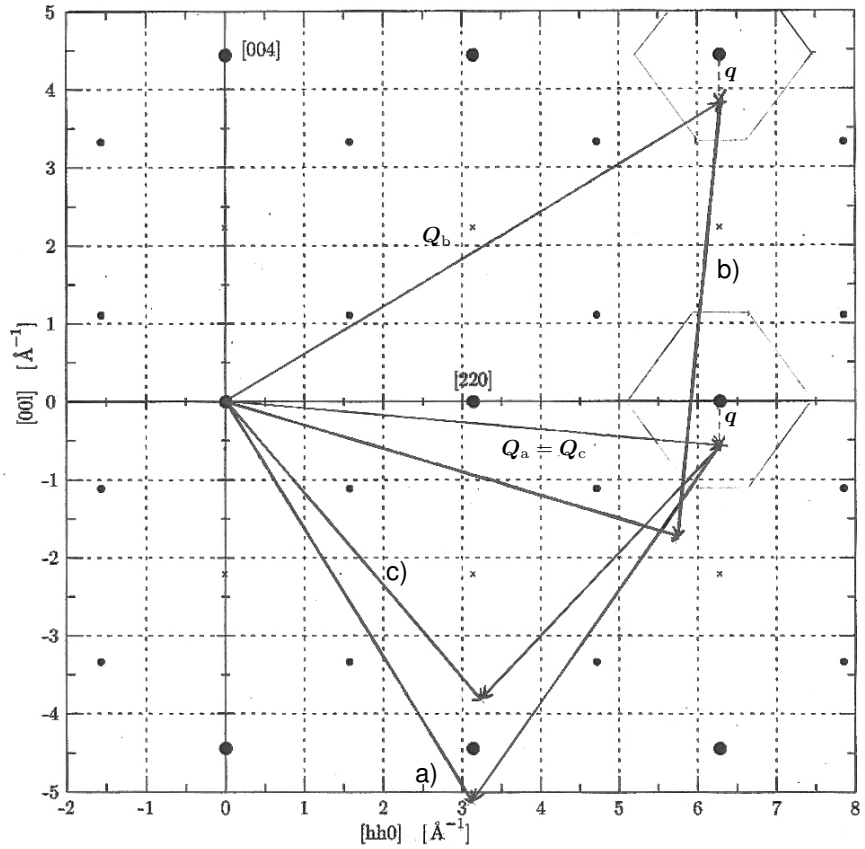

Figure 9: *The same phonon excitation measured in different ways:*
(a)↔(b): Measurements at different elastic peaks but with identical $|\boldsymbol{k}_i|$ *and* $|\boldsymbol{k}_f|$.
(a)↔(c): Identical position of the reciprocal space measured with different $\boldsymbol{k}_i$.

Please take time and think about the reason and how the different angles change during the two measurements shown in the figures.

As demonstrated in fig. 9, the lengths of $\boldsymbol{k}_i$ or $\boldsymbol{k}_f$ can be fixed. This is a way to change the resolution of the instrument optimizing the measurement for different problems.

1.9 Normalization of the counting rates

Planning an experiment, it seems to be native to count the scattered neutrons in the detector at every point for a useful time. But, the counting rate Z_{Det} depends not only on the scattering cross section. It also depends on instrument parameters which possibly change during the measurement or within a scan.

$$Z_{\mathrm{Det}} \propto I_{\mathrm{prim}}(\boldsymbol{k}_i) \cdot R_{\mathrm{Mono}}(|\boldsymbol{k}_i|) \, \frac{d^3\sigma}{d\boldsymbol{k}_{fx}\, d\boldsymbol{k}_{fy}\, d\boldsymbol{k}_{fz}} \, R_{\mathrm{Anal}}(|\boldsymbol{k}_f|) \cdot P_{\mathrm{Det.}}(|\boldsymbol{k}_f|) \tag{35}$$

$$= I_{\mathrm{prim}}(\boldsymbol{k}_i) \cdot R_{\mathrm{Mono}}(|\boldsymbol{k}_i|) \, \frac{1}{|\boldsymbol{k}_i|} \, S(\boldsymbol{Q},\omega) \, R_{\mathrm{Anal}}(|\boldsymbol{k}_f|) \cdot P_{\mathrm{Det.}}(|\boldsymbol{k}_f|). \tag{36}$$

with $R(|\boldsymbol{k}|)$ the reflectivities of the Bragg crystals, $P_{\mathrm{Det.}}(|\boldsymbol{k}_f|)$ the efficiency of the detector and $I_{\mathrm{prim.}}(|\boldsymbol{k}_i|)$ the incident intensity at the used energy.

In our experiment here we are especially interested at the *positions* of the phonon excitations in the $\boldsymbol{Q}$-ωspace and not too much in their intensities. We therefore do not ask for the comparability of *different* scans. We only need sufficient count rates *within* the scans and possibly the normalization of different points in a scan to determine the peak position in a right way.

We use a monitor detector usually mounted after the monochromator and before the sample. The probability to be detected is for neutrons with a velocity v proportional to the time t the neutrons stay in a detector (monitor) of the width d:

$$t = \frac{d}{v} = \frac{d\, m_{\mathrm{n}}}{\hbar\, |\boldsymbol{k}|} \tag{37}$$

One expects as monitor count-rate:

$$Z_{\mathrm{Mono}} \propto I_{\mathrm{prim}}(\boldsymbol{k}_i) \cdot R_{\mathrm{Mono}}(|\boldsymbol{k}_i|) \frac{1}{|\boldsymbol{k}_i|} \tag{38}$$

To perform a measurement, events are counted in the detector until a particular number of monitor counts is reached. The real count rate in the detector with monitor Z'_{Det} is:

$$Z'_{\mathrm{Det}} = \frac{Z_{\mathrm{Det}}}{Z_{\mathrm{Moni}}} \propto S(\boldsymbol{Q},\omega) \, R_{\mathrm{Anal}}(|\boldsymbol{k}_f|) \cdot P_{\mathrm{Det.}}(\boldsymbol{k}_f). \tag{39}$$

For constant $|\boldsymbol{k}_f|$, as illustrated in fig. 8(a)(right), this dependence vanishes. This is therefore the common mode. If $|\boldsymbol{k}_f|$ is varied by any reasons during the scan, the corresponding corrections have to be done for the data analysis.

1.10 Resolution function

Up to now we did not consider the fact that at every point of the $\boldsymbol{Q}$-ω-space the spectrometer is pointing to the measured intensity is scattered in a finite volume around this point. A sharp (δ-) peak in the scattering function at $(\boldsymbol{Q}_0, \omega_0)$ gives a measured signal of the form:

$$Z_{\mathrm{Det}}(\boldsymbol{Q}, \omega) \propto R(\boldsymbol{Q} - \boldsymbol{Q}_0, \omega - \omega_0). \tag{40}$$

R is the *resolution function* and depends on the configuration of the spectrometer only. Ordinary R is assumed to be Gaussian in its components.

The measured signal results from the convolution:

$$Z_{\mathrm{Det}}(\boldsymbol{Q}, \omega) \propto \int S(\boldsymbol{Q}', \omega')\, R(\boldsymbol{Q}' - \boldsymbol{Q}, \omega' - \omega)\, d\boldsymbol{Q}' d\omega'. \tag{41}$$

For illustration take a contour line of the resolution function (exactly: the 2-dimensional projection of the resolution function). It is normally elliptically and shows the region of the scattering function 'seen' by the instrument. In fig. 10 the projections of the resolution function are plotted into the dispersion relation, at the right the intensities to be expected, respectively. A measurement is characterized to be *focused* if the short axes of the resolution ellipsoid is perpendicular to the dispersion surface (to be measured).

It is important to understand in which cases a sharp resolution function is helpful or not. E. g., see a const.-Q-scan through a sharp 'horizontal' dispersion surface:

$$S(\boldsymbol{Q}, \omega) = S_0\, \delta(\omega - \omega_0). \tag{42}$$

The measurement is focused, i.e.

$$R(\boldsymbol{Q}, \omega) = e^{-\frac{\omega^2}{\sigma_\omega}} \cdot R(\boldsymbol{Q}). \tag{43}$$

Eq.(41) gives:

$$Z(\omega) \propto e^{-\frac{\omega^2}{\sigma_\omega}} \int R(\boldsymbol{Q}) d\boldsymbol{Q}. \tag{44}$$

Expanding the resolution ellipsoid in the momentum coordinates, the measured intensity increases. The line width depends only on $e^{-\frac{\omega^2}{\sigma_\omega}}$.

Reference: [11] Chap.4

The real form of the resolution function is influenced now by several effects: The Bragg-crystals are not of perfect lattices but have a finite mosaicity (which means it consists of several small single crystals, and their lattice parameters have weak deviations from the average). This 'mosaicity spread' - given by the angle η_m - broadens the Bragg peaks e.g. at the monochromator. Further influences are the finite angle resolution of the detectors, a finite size of the sample and diverging beams.

The beam reflected at the monochromator is a bunch of wave-vectors with a distribution $p_m(\boldsymbol{k}_i)$, the transmission function of the monochromator. The analyzer has to be described in analogy.

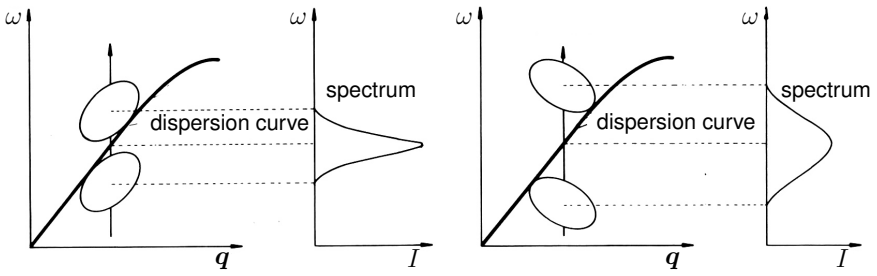

Figure 10: *Focused vs. unfocused measurement.*

To calculate the resolution function of the spectrometer, the two transmission functions have to be convoluted with respect to $2\Theta_s$. This simulation can be done by software tools. You will get some qualitative ideas about this within the experiment.

Reference: [4]

1.11 Peak forms

We learned: For sharp peaks in the scattering function we get a Gaussian signal in the measurement. This will be found in most of the experiments. However, some compounds exhibit broadened phonon resonances, so-called *soft modes*. They are originated by phonon-phonon- and phonon-electron-interactions [9] and result in a finite lifetime τ of the single oscillation states. Calculating the damped harmonic oscillator the line shape is identified to be Lorentzian:

$$S(\omega) \propto \frac{\omega^2}{\left(\omega_0^2 - \omega^2\right)^2 + \left(\frac{\omega}{\tau}\right)^2} \tag{45}$$

with the line width (FWHM):

$$\delta\omega = \frac{1}{2\tau}. \tag{46}$$

The resulting signal of such a 'soft' peak is the convolution of a Lorentzian with a Gaussian curve called Voigt profile. This profile is not easy to be calculated mathematically. In the case of comparable widths of the single profiles it can be sufficient to take the width of the Voigt curve as the sum of the widths of the Gaussian and the Lorentzian contributions.

If it is necessary for the data analysis to determine the peak *widths*, the resolution function has to be deconvoluted from the measured signal. This can be done by software.

Reference: [3], [5]

[9] These effects are neglected by the assumption of harmonic oscillations.

2 Performance of the experiment

PANDA is a three axis spectrometer (TAS) at the cold source of FRM II. The first thermal TAS was built 1954 and generally improved 1959 by Bertram N. Brockhouse at NRU Reactor in Chalk River. For his merit in the field of inelastic neutron scattering he got the Nobel price 1994. Even if the intensities at the detector were increased by magnitudes, the instrument is remote controlled and the safety is improved today, the general principle of the method is still the same:

The beam of cold neutrons (energy $E \approx 5(30)\,\mathrm{meV}$, momentum $p \approx 1.5(4) \cdot 10^{-24}\,\mathrm{kg\,m/s}$), which has de Broglie wavelength

$$\lambda = \frac{h}{p}, \tag{47}$$

or a wavevector of the length $k = \frac{2\pi}{\lambda}$, exits the moderator tank of the reactor through a beam port. The neutrons enter a monochromator being of single crystals with a d-spacing d.

By the Bragg equation

$$n\lambda = 2d \sin \Theta_m \tag{48}$$

the angle $2\Theta_m$ defines the energy of a monochromatic neutron beam (wave vector $\boldsymbol{k}_i$, energy E_i), which points to the sample to be investigated.

Direction and energy of the neutrons are changed at the sample following the inelastic scattering laws. At the secondary spectrometer (analyzer) neutrons with the wave vector $\boldsymbol{k}_f$ and the energy E_f are selected by Bragg reflection at a second crystal and are counted in the detector. By this, the momentum transfer ($\boldsymbol{Q}$) of the neutrons to the sample as well as the energy transfer (ΔE) from the sample to the neutrons can be determined.

$$\boldsymbol{Q} = \boldsymbol{k}_i - \boldsymbol{k}_f, \qquad \Delta E = E_i - E_f. \tag{49}$$

For useful statistics normally a fixed configuration of the instrument - related to a decent energy and momentum transfer - is taken for counting at the detector. The scattering function of the sample is therefore taken pointwise. These scans are measured at constant $\boldsymbol{Q}$ or at constant energy E, depending on the experimental strategy (see below).

PANDA is located at the beamport SR2 in the experimental hall of FRM II and has a comparably large neutron flux at low background. For more detail see:
`http://www.mlz-garching.de/panda`.

We now discuss the components of the three axis spectrometer. Photos of the main components are collected at the gallery 22 for better understanding.

Shielding Since neutrons damage biological matter the region of the primary beam has to be shielded. This is done by a so-called drum (in the case of PANDA blue / green colored) with the monochromator in its centre. The drum is made of heavy concrete with a large amount of chemically combined water, boron added. Also used are boron-treated (PE) sheets. Chemically combined water and PE contain a large amount of hydrogen which is able to decelerate fast

Notation:

$\mathcal{Q}$	Neutron source
$\mathcal{M}$	Monochromator
$\mathcal{S}$	Sample table
$\mathcal{A}$	Analyzer
$\mathcal{D}$	Detector
$\alpha 1$ $\alpha 2$ $\alpha 3$ $\alpha 4$	collimators
$2\Theta_m$ $2\Theta_s$ $2\Theta_a$	angles of the Spectrometer-axis
Abs	Shielding
Sel	Selector
Mob	Mobile blocks
Sh	Primary shutter

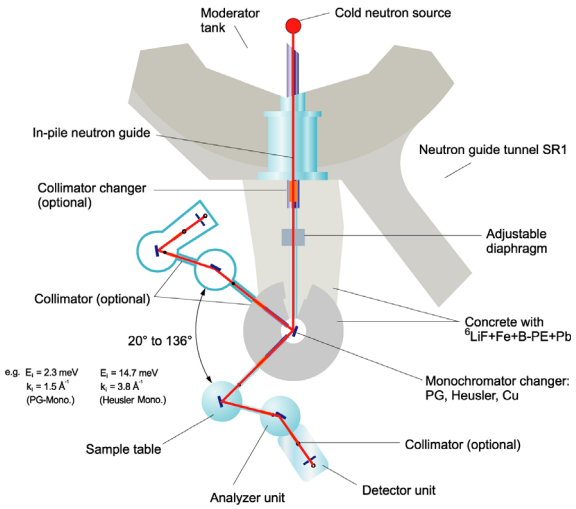

Figure 11: *Schematic design of a three axis spectrometer.*
Remark: all angles are counted in the region $[-180°, 180°]$. ($0°$ is directed in beam, positive angles are counter-clockwise.) $2\Theta_s$ is therefore positive.

neutrons. Boron as a large absorption coefficient for cold and thermal neutrons [10], and the isotope emerging at the neutron capture is not radioactive. But, normally materials are activated by the nuclear reactions and therefore activated (and the reactor emits hard Gamma radiation also if the primary shutter is closed), so the shielding has to be opened only after measurements of the remaining radiation even if the reactor is down. A part of the installation is shown here at the photos. The drum is made to shield γ-radiation as well as neutrons.

During the movement of the monochromator axes a ring of the shielding which contains the beam channel for the beam scatered at the monochromator is entrained. To avoid a closing of the primary beam during the ongoing rotation, the ring partially consists of 11 so-called mobile blocks (made of the same concrete as the ring) which are moved by an automatic control from one side of the opening to the the other. The geometry and the control ensure a proper shielding where necessary (see fig.11).

Monochromator In the rotation centre of the shielding the monochromator is positioned. It consists of 121 single crystals of pyrolytic graphite (PG) mounted on a crystal holder. The crystal holder and therfore the grapite lattice planes are rotated by the angle Θ_m to the primary beam. The intensity of the monochromatic beam scattered at the angle $2\Theta_m$ [11] depends on the lattice parameter of the monochromator material (here PG) and on the incoming angle..

To avoid contamination of higher-order Bragg reflection in the incoming beam, $n = 2, 3 \ldots$ (Gl. (48)), filter materials are positioned between monochromator and sample. In the case of

[10] Typical reaction: $^{10}_{5}\mathrm{B} + ^{1}_{0}\mathrm{n} \rightarrow ^{7}_{3}\mathrm{Li} + ^{4}_{2}\mathrm{He} + 2.8\,\mathrm{Mev}$

[11] Remark: Sometimes the angles Θ_m, Θ_s and Θ_a are named α_1 to α_3.

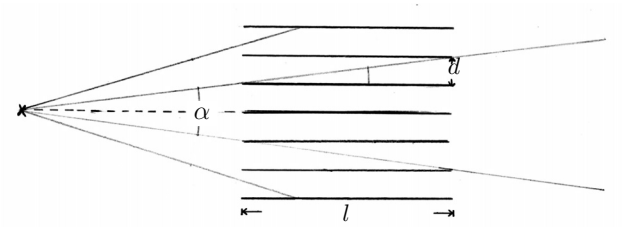

Figure 12: *Drawing of a Soller collimator. The divergence of the outgoing beam is* $\tan(\alpha/2) = \mathsf{d}/\mathsf{l}$*, which is in the example ca.* 18°*. On PANDA the collimation can be chosen between 15 and 80 minutes.*

PANDA this is polycrystalline boron or, sometimes, pyrolytic graphite.

Maximum intensity at sample and detector can be achieved by focusing the monochromator and the analyzer in horizontal and vertical direction. Here the 121 monochromator (55 analyzer) crystals are curved in both directions by complex mechanics to get the crystal surfaces into a paraboloid-like shape. The radius of the curvature depends on the neutron wavelength. By taking into account the distances also a focus of the momentums is possible.

Sample table The sample is mounted on a table which can be moved on air-pressure. In addition to motors rotating the sample and the analyzer/detector around the sample - giving Θ_s and the scattering angle $2\Theta_s$, the sample orientation can be adjusted by goniometers and translation stages. For studies of magnetism, the sample is normally positioned in a cryostat or a cryomagnet - cooling down to temperatures of 0.03 K and appying fields up to 13.2 T.

Analyzer The analyzer is also located in a shielding, but here the reason is to decrease the background in the detector. The crystal holder located again on a goniometer and translation stages allows a horizontal focus of the analyzer, the crystals are mounted to have a fixed vertical focus. The crystals are at the angle Θ_a to the beam, the detector is rotated by $2\Theta_a$.

Detector The neutrons are counted by a beamtube, filled with $^3\mathrm{He}$ under high pressure (ca 10 bar). A neutron can be trapped by a $^3\mathrm{He}$ nucleus and converted to $^4\mathrm{He}$. The emitted γ quant ionizate the gas and is detected like in a Geiger-Müller counter. This allows to count ca. 90% of the incoming neutrons.

Diaphragms, collimators and attenuators In addition to the already described parts several components are needed in the beam path dor beam conditioning. For example variable diaphragms (slits) are installed before and after the sample which are adjusted to the sample size to decrease the background. A secondary shutter is mounted after the monochromator. More diaphragms are with the primary shutter in the reactor wall and between the primary shutter and the monochromator.

Beyond that in every part of the beam path so-called Soller collimators can be applied. It con-

tains of ca. 20 cm long, coated with white GdO_2 foils, which are exactly parallel and therefore limit the divergence of the beam . The value of the divergence is described by the angle α (see fig. 12). Collimators with $\alpha = 15'$ to $\alpha = 60'$ are available. Small divergence corresponds with high resolution but small intensity. The primary collimators are placed in the primary shielding and are changed automatically, the others have to be changed by hand (motorization planned). The beam size is limited only horizontally, i.e. within the scattering plane. For increase of intensity we normally allow a large divergence of the beam in the direction perpendicular to the scattering plane.

Sometimes, e.g. for alignment, the detector is in the straight beam or Bragg reflections have a very large intensity. To avoid a saturation of the detectors, the incoming beam ist attenuated by PE-plates of different thicknesses which can moved into the beam (and combined) automatically.

Monitor To compare or to combine data from different scans or measurements the intensities are normalized to an intensity counted by the monitor in the primary beam. Its signal is proportional to the incoming intensity. This is also important for energy scans, where the incoming intensity changes with $2\Theta_m$ due to the energy-dependent spectrum. Also different reactor power can be corrected in this way (see paragraph 1.9).

Goniometer Monochromator, analyzer and sample are placed on 2-axis goniometers. This allows tilts around two perpendicular to each other which meet in the centre of the beam. So the sample does not move out of the beam centre during the tilt. The available angles are limited ($\pm 15^\circ$), the sample can be adjusted but has to be pre-oriented before measuring on the three-axis instrument. It is also possible to translate the sample a few millimeters horizontally and vertically.

Cover page: Overview over PANDA
From left: Monochromator shielding, sample table with 15T cryomagnet, analyzer box and detector shielding.

Figure 13: *(Following page) Components of PANDA taken in different phases of the construction.*

(a) Side view into the (opened) Monochromator shielding onto the PG-monochromator.

(b) PG-analyzer in the (opened) analyzer box. The horizontal curvature is changed by rotating the individual segments.

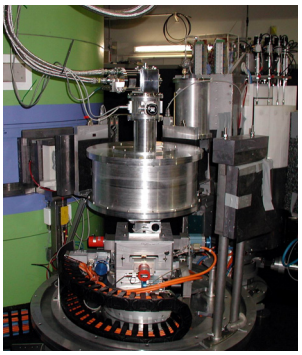

(c) Detailed view onto the sample table with vacuum chamber. From bottom: Rotation table, xy-stage, goniometer, z-stage

(d) Soller collimators in the automatic changer for $\alpha 1$ (in the primary beam.)

(e) Typical sample mounting for use of cryostat.

(f) Detector tubes to be built into the detector shielding

3 Experiment

PANDA is a complex research instrument, where normally measurements on samples at very low temperature, high magnetic fields and / or high pressure are performed. Phonons for example are measured to learn about the interaction potentials in solids. Measurements of spin wave dispersions contribute to determine magnetic interactions.

The goal of this practice is to give inside to the potential of neutron scattering on a three-axis spectrometer. To get results, you have to understand the functionality of the instrument. This can include the alignment of the instrument and the sample. Some data can be taken on a well-known sample, e.g. lead, which can be measured at room temperature (necessary due to the limited time of the practice. A normal experiment needs several days.)

1. Preparation
   - Gather theoretical basics.
   - Generate a strategy for the measurements and a plan of the experiment.
   - Safety instruction at the instrument PANDA.
2. Alignment
   - Proof of the instrument alignment by scans of the monochromator or analyzer axis
   - Determination of the (energy) resolution of the spectrometer for (min.) three different wave vectors by measuring of the incoherent elastic intensity on vanadium. Choose an appropriate configuration for the following measurements.
   - Alignment of the sample, define the scattering plane, optimize background.
   - Perform control scans and learn the use of the user interface on PANDA.
3. Measurements
   - Perform the planned scans to determine the resolution ellipsoid.
   - Measure (min.) one mode of the dispersion relation of lead by different scans.

4 Report

After the experiment you have to report your work. Please explain the experiment and your work in a short way to show how you understand the aim of the different steps. You can prepare this by doing notes during the experiment.

Please analyze the data and interpret it. It is not necessary to repeat the theoretic aspects already discussed in front of the experiment. But your report should be conclusive.

Please:

- Show the measured energy resolution depending on the wave vector. Explain your choice.

- Determine the direction of the resolution ellipsoid, add it to a scheme of the dispersion and show the single scans.
- For the measurements of lead, plot the measured points with the error bars into a dispersion relation(s) and compare to references. Explain how different scan types influence the result.

Finally: please give us a short feedback about the preparation, experiment and support. This can also be done after the experiment. We like to give you an impression about neutron scattering experiments even if practices are complicated. A feedback will help us to improve it for future students.

P.S. Do not forget ruler and calculator.

References

[1] N. W. Ashcroft and N. D. Mermin. *Festkörperpysik*. Oldenbourg, 2001.

[2] B. N. Brockhouse and P. K. Iyengar. Normal modes of germanium by neutron spektrometry. *Phys. Rev.*, 111(3):747, Aug 1958.

[3] W. Demtröder. *Laserspektroskopie*, Kapitel 3 (Linienbreiten und Profile von Spektrallinien). Springer, 4. edition, 2000.

[4] B. Dorner. *Coherent Inelastic Neutron Scattering in Lattice dynamics*. Springer-Verlag, 1982.

[5] K. Dransfeld, P. Kienle, and G. M. Kalvius. *Physik I*, Kapitel 8. Oldenbourg, 8. edition, 1998.

[6] H. Friedrich. *Theoretische Atomphysik*. Springer, 1990.

[7] H. Ibach and H. Lüth. *Festkörperpysik, Einführung in die Grundlagen*. Springer-Verlag, 6. edition, 2002.

[8] J. Kauppinen and J. Partanen. *Fourier Transforms in Spectroscopy*. Wiley-VCH, Berlin, 2001.

[9] C. Kittel. *Einführung in die Festkörperpysik*. Oldenbourg, 10. edition, 1993.

[10] G. Nillson and G. Nellin. Normal vibrations of germanium by neutron spektrometry. *Phys. Rev. B*, 3(2):364, Jan 1971.

[11] G. Shirane, S. m. Shapiro, and J. M. Tranquada. *Neutron scattering with a triple-axis Spektrometer*. Oxford University Press, 2002.

[12] B. T. Willis, editor. *Chemical Applications of Thermal Neutron Scattering*. Oxford University Press, 1973.

[13] R. Zorn. Fourier transforms. In *Neutron Scattering*. T. Brückel, G. Heger, D. Richter and R. Zorn, 2006.

Internet resources

`http://http://www.mlz-garching.de/panda`
"PANDA" homepage.

`http://www.env-it.de/umweltdaten/`
Environmental data from the federal Ministry for the Environment, Nature Conservation and Nuclear Safety.

`http://www.umweltdaten.de/utk/kapitel22/E-22-1-2.pdf`
Estimations of natural and civil exposure in Germany from 1999.

Contact

PANDA

Phone: 089/289-14749
Web: http://www.mlz-garching.de/panda

Astrid Schneidewind

JCNS at Maier-Leibnitz Zentrum Garching, Forschungszentrum Jülich GmbH

Phone: 089/289-14749
e-Mail: Astrid.Schneidewind@frm2.tum.de

Petr Cermak

Phone: 089/289-11773
e-Mail: p.cermak@fz-juelich.de

SPHERES

Backscattering spectrometer

J. Wuttke

Jülich Centre for Neutron Science
Forschungszentrum Jülich

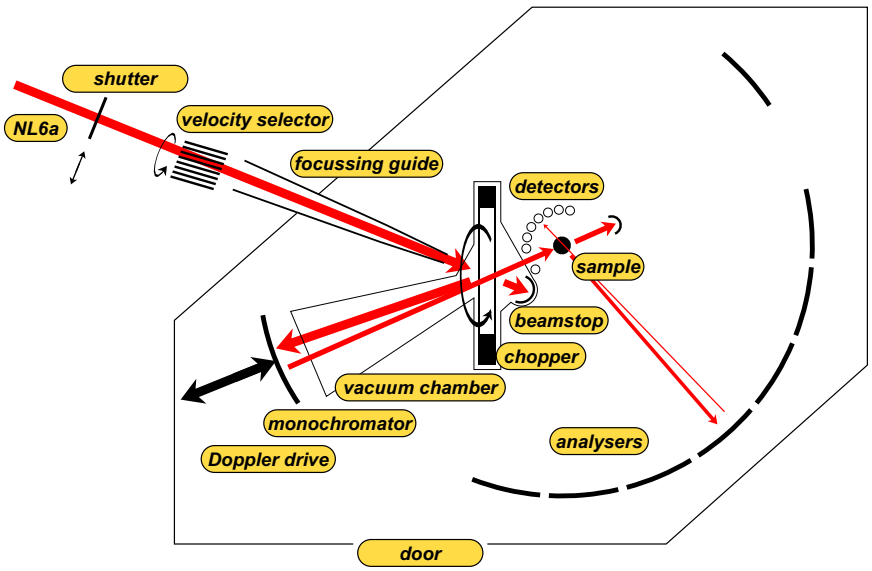

Contents

1 Introduction

Neutron *backscattering spectrometers* are used to measure *inelastic scattering* with very high *energy resolution*. What does this mean?

In inelastic scattering, scattering intensity is measured as function of the energy exchanged between the scattered neutron and the sample. As in other areas of physics, a data set of the form intensity-versus-energy is called a *spectrum*. An instrument that resolves inelastic scattering is therefore called a *spectrometer*.

While elastic scattering experiments yield information about *structure* or *texture* of a sample, inelastic scattering is used to investigate its *dynamics*. Specifically, inelastic neutron scattering yields information about the thermal motion of atomic nuclei.

The most common instrument for inelastic neutron scattering is the triple-axis spectrometer. It is routinely used to measure phonon and magnon dispersions, with energy exchanges of the order of meV. In contrast, the *high resolution* of a backscattering spectrometer allows to resolve very *small energy shifts* of the order of μeV. By the time-energy uncertainty relation, small energy means long times. Hence, backscattering addresses relatively *slow* nuclear motion — much slower than the lattice vibrations typically seen in triple-axis spectrometry.

What processes take place on the energy or time scale made accessible by neutron backscattering? For instance the following:

- hyperfine splitting of nuclear spin orientations in a magnetic field,
- rotations or hindered reorientations of molecules or molecular side groups,
- quantum tunneling,
- hydrogen diffusion in solids,
- relaxation (molecular rearrangements) in viscous liquids,
- innermolecular rearrangements in polymers.

During your lab course day, you will use the backscattering spectrometer SPHERES (SPectrometer for High Energy RESolution) to study one example of these applications.

2 Spectrometer Physics

2.1 Energy Selection by Backscattering

In crystal spectrometers, neutron energies are selected by Bragg reflection from crystals, according to the *Bragg condition*

$$n\lambda_n = 2d_{hkl}\sin\Theta \tag{1}$$

where d_{hkl} is the distance of lattice planes $[hkl]$, and Θ is the glancing angle of reflection from these planes. The index n indicates that along with a fundamental wavelength λ_1, integer fractions $\lambda_n = \lambda_1/n$ are transmitted as well. To suppress these unwanted higher orders, experimental setups include either a mechanical neutron velocity selector (Fig. 1), or a beryllium filter.

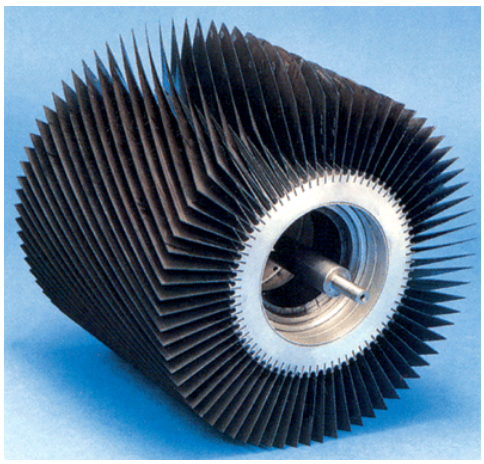

Fig. 1: *Rotor of a mechanical neutron velocity selector. The blades are coated with neutron absorbing material. In SPHERES, such a selector is used as a pre-monochromator that reduces the incoming white spectrum to about* $\pm 6\%$. *© Astrium GmbH.*

In practice, the parameters d and Θ on the right-hand side of Eq. (1) are not sharp: Imperfections of the crystal lead to a distribution of lattice constants, characterized by a width δd. And similarly, imperfections of the neutron optics (inevitable because the incoming beam, the sample, and the detector all have finite size) lead to a distribution of reflection angles, characterized by a width $\delta\Theta$. By differentiating the Bragg equation (1), one obtains the relative width of the wavelength distribution reflected by a crystal monochromator:

$$\frac{\delta\lambda}{\lambda} = \frac{\delta d}{d} + \cot\Theta\,\delta\Theta. \tag{2}$$

In usual crystal spectrometers, the second term is the dominant one. However, by choosing $\Theta = 90°$, the prefactor $\cot\Theta$ can be sent to zero. This is the fundamental idea of the backscattering spectrometer. If a monochromator crystal is used in backscattering geometry, with $\Theta \simeq 90°$, then the reflected wavelength distribution is in first order insensitive to the geometric imperfection $\delta\Theta$; it depends only on the crystal imperfection δd and on a second-order $(\delta\Theta)^2$ term.

The monochromator of SPHERES is made of silicon crystals in (111) orientation (Fig. 2). The backscattered wavelength is $\lambda = 2d_{111} = 6.27$ Å, corresponding to a neutron energy of 2.08 meV. The crystals are cut from wafers produced by the semiconductor industry. They are perfectly monocrystalline, so that their intrinsic resolution[1] of $\delta d/d \simeq 10^{-6}$ is actually too good because it does not match the spectrometer's second-order geometric imperfection $(\delta\Theta)^2 \lesssim 10^{-4}$. As a remedy, the crystals are glued to a spherical support so that the resulting strain induces a lattice constant gradient of the order $\delta d/d \simeq 10^{-4}$.

[1] In perfect crystals, the intrinsic resolution $\delta d/d$ is limited by *primary extinction*: Say, each crystalline layer has a reflectivity of about 10^{-6}. Then only about 10^6 layers contribute to the Bragg reflection. This limits $\delta\lambda/\lambda$ to about 10^{-6}.

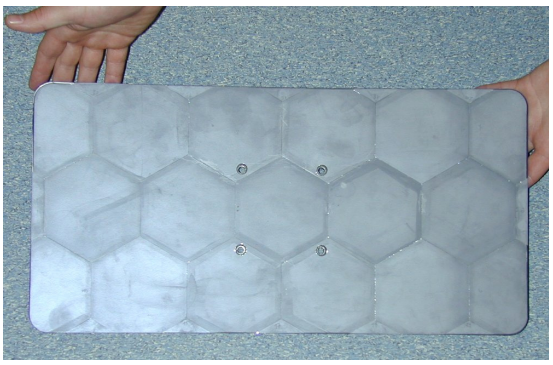

Fig. 2: *The monochromator of SPHERES consists of hexagonal Si(111) wafers of 750 µm thickness, glued onto a spherical support made of carbon fiber.*

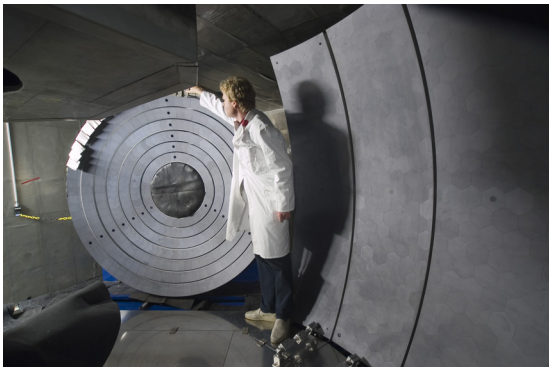

Fig. 3: *The analyzers of SPHERES are made of the same Si(111) as the monochromator. For small scattering angles, they are shaped as rings; for large scattering angles, they are approximately rectangular sections of a sphere.*

2.2 Spectrometer Layout

In a crystal spectrometer, a *monochromator* is used to send a neutron beam with a narrow energy distribution $E_\mathrm{i} \pm \delta E$ onto the sample. After the sample, a second monochromator, called *analyzer*, is used to select a narrow energy distribution $E_\mathrm{f} \pm \delta E$ out of the scattered spectrum. In SPHERES, we actually have a huge array of analyzers (Fig. 3), covering a solid angle of about 2.5, which is 20% of 4π. These analyzers send energy-selected neutrons towards 16 different detectors, depending on the scattering angle ϑ.

Fig. 4 shows the complete layout of SPHERES. The incoming beam is pre-monochromatized by a mechanical velocity selector. Then, it is transported by a focussing neutron guide into the instrument housing where it hits a rotating chopper. The chopper rotor (Fig. 5) carries mosaic crystals made of pyrolitic graphite on half of its circumference. When the incoming neutrons hit

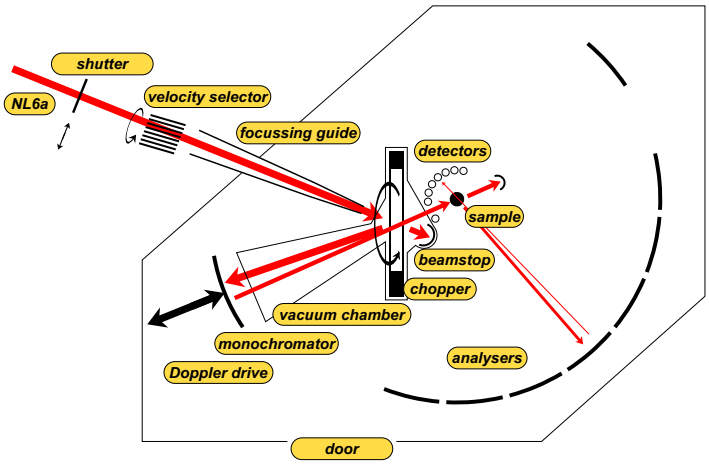

Fig. 4: *Layout of the Jülich backscattering spectrometer SPHERES at FRM II.*

Fig. 5: *Schematic front view of the chopper rotor of SPHERES. The red bands indicate the mosaic crystals that deflect the incident beam towards the monochromator.*

these crystals, they undergo a Bragg reflection towards the monochromator.[2] Otherwise, they are transmitted towards a beamstop.

The backscattering monochromator selects a neutron band $E_\mathrm{i} \pm \delta E$ as described above. Neutrons within this band are sent back towards the chopper. When they reach the chopper, the rotor has turned by $60°$: the mosic crystals have moved out of the way; the neutrons coming from the monochromator are transmitted towards the sample.

The sample scatters neutrons into 4π. About 20% of this is covered by analyzers. If a scattered neutron hits an analyzer and fullfills the backscattering Bragg condition, it is sent back towards the sample. It traverses the sample[3] and reaches a detector. To discriminate energy-selected neutrons from neutrons that are directly scattered from the sample into a detector, the time of arrival is put in relation to the chopper phase.

[2] As a side effect, the Bragg deflection by rotating mosaic crystals achieves a favorable *phase-space transform* (PST): the incoming wavevector distribution is spread in angle, but compressed in modulus. This results in a higher spectral flux in the acceptance range of the monochromator.

[3] Of course not all neutrons are transmitted: some are lost, some are scattered into a wrong detector. This inaccuracy is inevitable in neutron backscattering. We strive to keep it small by using rather thin samples with typical transmissions of 90% to 95%.

While the primary spectrometer (everything before the sample) is mainly in vacuum, the secondary spectrometer is not. To minimize neutron losses in the secondary spectrometer, the entire instrument housing can be flooded with argon. For the labcourse, we preferentially remove the argon so that participants can accede the housing. However, since refilling takes at least one full day, time constraints may prevent us from doing so. In this case, a video will be shown to present the interior of the spectrometer.

2.3 Measuring Spectra

So far we have introduced a static arrangement with fixed energies $E_\mathrm{i} = E_\mathrm{f}$. Such an arrangement is actually used to measure the fraction of elastic versus total scattering, called the *Debye-Waller factor* for coherent scattering and the *Lamb-Mössbauer factor* for incoherent scattering. More often, however, one wants to measure full spectra $S(Q, \omega)$. Therefore, one must find a way to modify the energy transfer

$$\hbar\omega = E_\mathrm{i} - E_\mathrm{f}. \tag{3}$$

This can be done using the *Doppler effect*: The monochromator is mounted on a linear drive that performs a cyclic motion. In the monochromator's rest frame, the backscattered energy is always the value $E_0 = 2.08$ meV given by the lattice constant of Si(111). Depending on the monochromator's velocity v, the value in the laboratory frame is

$$E_\mathrm{i}(v) = \frac{m_\mathrm{n}}{2}\,(v_0 + v)^2 \tag{4}$$

where $v_0 = 631$ m/s is the neutron velocity at $E_0 = m_\mathrm{n}/2\,v_0^2$. The Doppler drive of SPHERES has a linear amplitude of ± 75 mm and achieves a velocity amplitude of ± 4.7 m/s, resulting in an energy range

$$-30.7\ \mu\mathrm{eV} < \hbar\omega < 30.9\ \mu\mathrm{eV}. \tag{5}$$

This is called the *dynamic range* of the spectrometer.

When a scattered neutron is detected, its time of flight is traced back to the moment when it has been backscattered by the monochromator. From the recorded trace of the linear drive, the monochromator velocity at that moment is infered, ω is computed from (4) and (3), and the corresponding histogram channel is incremented. To determine $S(Q, \omega)$, one needs to normalize to the time spent in channel ω. This normalization is routinely done by the instrument's raw-data reduction program SLAW.

2.4 Instrument Characteristics

The performance of a spectrometer can be characterized by its *resolution function*. To obtain the resolution function, one measures the spectrum of a purely elastic scatterer. Fig. 6 shows the result of a resolution measurement from a user experiment on SPHERES. Note the logarithmic intensity scale.

Conventionally, the resolution of an instrument is characterized by the *full width at half maximum* (FWHM). For SPHERES, a typical value is 0.65 μeV. Note however that the FWHM is

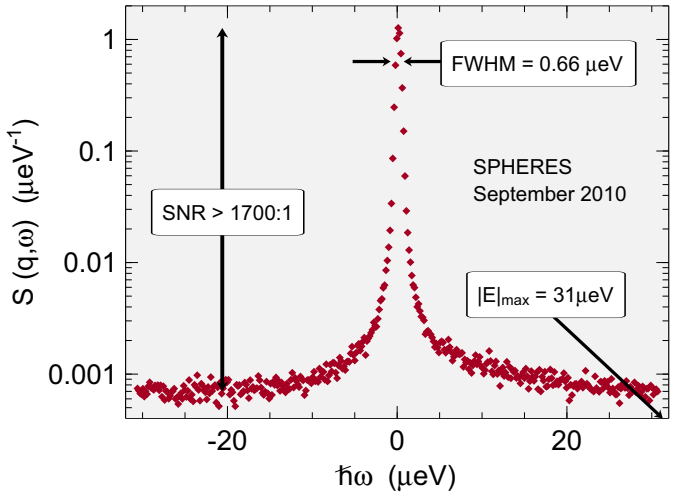

Fig. 6: *Resolution function of SPHERES, measured on a user provided sample at a low temperature where the scattering is purely elastic.*

not the full story: the quality of an instrument also depends on the *shape* of the resolution functions, especially of the deep wings. The resolution of SPHERES is slightly asymmetric. This is related to the $(\delta\Theta)^2$ term in the wavelength spread of a backscattering analyzer: all deviations from the perfect $\Theta = 90°$ geometry lead to the transmission of longer wavelengths, never of shorter ones.

Another important figure of merit is the *signal-to-noise ratio* (SNR). It depends strongly on the ratio of scattering to absorption cross sections and on the thickness and geometry of the sample. With argon filling, the best value obtained in user experiments has been 1700:1; without argon, 1200:1. On the other hand, for strongly absorbing samples it is sometimes less than 100:1.

3 Applications

In the following, two different applications of neutron backscattering are explained: hyperfine splitting in a magnetic material, and methyl group tunneling.

3.1 Hyperfine Splitting

The measurement of hyperfine splitting has been historically the first application of neutron backscattering,[4] and to this day, it is the conceptually simplest one.

Since the neutron has spin $S = 1/2$, its magnetic quantum number can take the values $S_z = \pm 1/2$. In a scattering event, this quantum number can change. In more pictorial words: when a

[4] A. Heidemann, Z. Phys. 238, 208 (1970).

neutron is scattered, it may or may not undergo a *spin flip*.

As angular momentum is conserved, a change of S_z must be accompanied by an opposite change of the magnetic quantum number I_z of the nucleus by which the neutron is scattered, $\Delta I_z = -\Delta S_z$. Therefore, spin-flip scattering is only possible if the sample contains nuclei with nonzero spin I.

Nuclei with nonzero spin quantum number I possess a magnetic moment

$$\mu = Ig\mu_{\mathrm{N}} \tag{6}$$

with the nuclear magneton

$$\mu_{\mathrm{N}} = \frac{e\hbar}{2m_{\mathrm{p}}} = 3.153 \cdot 10^{-8}\ \mathrm{eV/T}. \tag{7}$$

The g factor is different for each nucleus.[5]

A local magnetic field B leads to a splitting of energy levels,

$$E = I_z g\mu_{\mathrm{N}} B, \tag{8}$$

called *hyperfine splitting*. Consequently spin-flip scattering is accompanied by an energy exchange $\Delta E = \pm g\mu_{\mathrm{N}} B$. By measuring the neutron energy gain or loss $\pm\Delta E$, one can accurately determine the local field B in ferromagnetic or antiferromagnetic materials.

3.2 Molecular Rotation and Quantum Tunneling

Rotational motion of molecules or molecular side groups is one of the most important applications of neutron backscattering. Here, we specialize on the rotation of methyl (CH_3) groups. We consider these groups as stiff, with fixed[6] CH bond length 1.097 Å and HCH angle 106.5.°

The only degree of freedom is then a rotation around the RC bond that connects the methyl group to the remainder R of the molecule. This RC bond coincides with the symmetry axis of the CH_3 group. The rotational motion can therefore be described by a wave function ψ that depends on one single coordinate, the rotation angle ϕ.

The Schrdinger equation is

$$\left\{ B\frac{\partial^2}{\partial\phi^2} - V(\phi) + E \right\} \psi(\phi) = 0. \tag{9}$$

For free rotation ($V = 0$), solutions that possess the requested periodicity are sine and cosine functions of argument $J\phi$, with integer J. Accordingly, the energy levels are $E = BJ^2$.

Given the value $B = 670$ μeV, it is obvious that free rotor excitations occur only far outside the dynamic range of neutron backscattering. Conversely, if we observe an inelastic signal from methyl groups on a backscattering spectrometer, then we must conclude that $V \neq 0$: the

[5] Tabulation: http://ie.lbl.gov/toipdf/mometbl.pdf.

[6] Ignoring the variations of empirical values, which are of the order of ± 0.004 Å and $\pm 1.5°$.

methyl group rotation is *hindered* by a rotational potential. This potential can be caused by the remainder R of the molecule as well as by neighbouring molecules.

Due to the symmetry of the CH_3 group, the Fourier expansion of $V(\phi)$ contains only sine and cosine functions with argument $3m\phi$, with integer m. In most applications, it is sufficient to retain only one term,

$$V(\phi) \doteq V_3 \cos(3\phi). \tag{10}$$

The strength of the potential can then be expressed by the dimensionless number V_3/B. In the following we specialize to the case of a *strong potential*, $V_3/B \gg 10$, which is by far the most frequent one.

In a strong potential of form (10), the CH_3 group has three preferential orientations, separated by potential walls. The motion of the CH_3 group consists mainly of small excursions from the preferred orientations, called *librations*. Essentially, they are harmonic vibrations.

At low temperatures, almost exclusively the vibrational ground state is occupied. Yet reorientational motion beyond librations is possible by means of quantum mechanical tunneling: the wave functions of the three localised *pocket states* ψ_m ($m = 1, 2, 3$) have nonzero overlap. Therefore, the ground state is a linear combination of pocket states.[7] Periodicity and threefold symmetry allow three such combinations: a plain additive one

$$\psi_1 + \psi_2 + \psi_3, \tag{11}$$

and two superpositions with phase rotations

$$\psi_1 + \mathrm{e}^{\pm i2\pi/3}\psi_2 + \mathrm{e}^{\pm i4\pi/3}\psi_3. \tag{12}$$

In the language of group theory, state (11) has symmetry A, the degenerate states (12) are labelled E^a, E^b. It is found that A is the ground state. The *tunneling splitting* $\hbar\omega_\mathrm{t}$ between the states A and E is determined by the overlap integral $\langle\psi_m|V|\psi_n\rangle$ ($m \neq n$). It depends exponentially on the height of the potential wall. Provided it falls into the dynamic range of neutron scattering, it leads to a pair of inelastic lines at at $\pm\hbar\omega_\mathrm{t}$.

With rising temperatures, the occupancy of excited vibrational levels increase. This facilitates transitions between A and E sublevels and results in a decrease of $\hbar\omega_\mathrm{t}$ and a broadening of the inelastic lines.

Upon further temperature increase, thermal motion of neighbouring molecules causes so strong potential fluctuations that the picture of quantum tunneling is no longer applicable. Instead, the motion between different pocket states can be described as *stochastic jump diffusion*.

Let $p_m(t)$ be the probability of being in pocket state m ($m = 1, 2, 3$). Assume that jumps between the three main orientations occur with a constant rate τ^{-1}. Then, the p_m obye rate equations

$$\frac{\mathrm{d}}{\mathrm{d}t}p_m(t) = \frac{1}{\tau}\left\{-p_m + \sum_{n\neq m}\frac{1}{2}p_n\right\}. \tag{13}$$

[7] This is an extremely simplified outline of the theory. In a serious treatment, to get all symmetry requirements right, one must also take into account the nuclear spins of the H atoms. See W. Press, Single-Particle Rotations in Molecular Crystals, Springer: Berlin 1981.

The stationary equilibrium solution is just $p_m = 1/3$ for all m. When perturbed, the system relaxes into equilibrium with a time dependence of $\exp(-t/\tilde{\tau})$. Explicit solution of the linear differential equation system (13) yields $\tilde{\tau} = 2\tau/3$.

According to a fundamental theorem of statistical mechanics (the *fluctation dissipation theorem*), the relaxation by which a slightly perturbed system returns *into* equilibrium has the same time dependence as the pair correlation function *in* equilibrium. Therefore, we can employ the solution of (13) to write down the self-correlation function of the protons that constitute our methyl group. Fourier transform yields then the incoherent scattering function

$$S(q,\omega) = a(q)\delta(\omega) + b(q)\frac{\Gamma}{\omega^2 + \Gamma^2}. \tag{14}$$

The first term describes elastic scattering. The second term, the Fourier transform of the exponential $\exp(-t/\tilde{\tau})$, is a Lorentzian with linewidth $\Gamma = \tilde{\tau}^{-1}$; such *broadening* of the elastic line is often called *quasielastic*.

4 Preparatory Exercises

1. Relate the relative wavelength spread $\delta\lambda/\lambda$ to the relative energy spread $\delta E/E$.
2. In SPHERES, useable detectors are located at scattering angles 2θ ranging from 12.5° to 134°. Calculate the corresponding wavenumbers in Å^{-1}. Recommendation: use the following constants in *atomic units*: $\hbar c = 1973$ eVÅ and $m_n c^2 = 940$ MeV.
3. Convert dynamic range and resolution of SPHERES into GHz. To make contact with optical spectroscopy, you might also wish to convert into cm^{-1}.
4. Empirically, it is found that the centre of the resolution function can be fitted by a Gaussian $a\exp(-E^2/2/\sigma^2)$. Derive an expression that relates the Gaussian standard deviation σ to the FWHM.
5. Note that the above mentioned fit applies only to the very centre of the resolution function. How does a Gaussian look like on the lin-log representation of Fig. 6? And a Lorentzian?
6. In SPHERES, the distance sample-analyzer is 2 m. Calculate the time neutrons need for a round trip sample-analyzer-sample, and deduce the rotation frequency of the chopper.
7. Assume that the monochromator motion is perfectly sinusoidal. Sketch how the measuring time per energy channel varies with $\hbar\omega$.
8. Draw a sketch of the expected backscattering spectrum $S(q,\omega)$ of a ferromagnetic material with $I \neq 0$.
9. Assume a hyperfine splitting of $\Delta E = 2$ μeV. To which temperature do you have to cool the sample to observe a 10% difference between the probabilities of energy gain and energy loss scattering?
10. How do you expect ΔE to evolve when the sample is heated towards the Curie or Néel temperature?

11. Calculate the moment of inertia, $I = \sum mr_\perp^2$, of a methyl group. Verify that the *rotational constant* $B = \hbar^2/(2I)$ has a value of about 670 µeV.

12. Expand $V(\phi)$ around a potential minimum, and compare the resulting Schrödinger equation with that of a harmonic oscillator. Show that the splitting of oscillator levels is of the order of meV.

13. Draw a coordinate system energy-versus-angle. Sketch $V(\phi)$, the harmonic approximation, the ground state's $\psi(\phi)$, and the lowest oscillator energy levels. What does that imply for the validity of the oscillator approximation?

14. Sketch the expected spectra for different temperatures.

5 Experiment Procedure

5.1 The experiment itself

After an initial discussion, the group chooses which experiment to perform: hyperfine splitting, methyl group tunneling, or participation in an ongoing research project. For a given chemical composition, the group computes the sample thickness that yields 90% transmission. Depending on the group's interest, a sample is prepared, or a standard sample is used. The tutor shows how to insert the sample in the instrument's cryostat. Using the instrument's graphical user interface, starting a measurement is rather trivial. Log entries are written to the instrument log wiki.

5.2 Raw data reduction

The program SLAW is used to convert raw neutron counts into $S(Q, \omega)$. It is parametrized by a script, called `Slawfile`. The tutor provides a sample script, which is then modified to convert the results of the current experiment.

SLAW can save $S(Q, \omega)$ in a variety of output formats. Most relevant are plain tabular formats `recttab` and `spectab`, and a self-documenting format `y08` required by our standard data-analysis software FRIDA.

5.3 Data evaluation

In a first approach, labcourse participants should analyse plain tabular data using whatever all-purpose data-analysis software they are used to.

1. Plot a representative selection (choose a few Q) of measured spectra.

2. Determine the FWHM of the elastic line, and of the inelastic lines if there are any.

3. Try to fit these lines with a Gaussian, with a Lorentzian, with a squared Lorentzian.

4. Summarize the temperature dependence of the spectra.

For a more quantitative analysis, it is necessary to convolute a theoretical model with a measured resolution function. This can be done with the data-analysis package FRIDA. For a tutorial, refer to the SPHERES wiki.[8]

[8] Follow the link at `http://www.jcns.info/jcns_spheres`.

Contact

SPHERES

Phone: 089/289-14875
Web: http://www.jcns.info/jcns_spheres/

Michaela Zamponi

JCNS at FRM II, Forschungszentrum Jülich GmbH

Phone: 089/289-10793
e-Mail: m.zamponi@fz-juelich.de

Gerald J. Schneider

Phone: 089/289-10718
e-Mail: g.j.schneider@fz-juelich.de

DNS

Neutron Polarization Analysis

Y. Su

Jülich Centre for Neutron Science
Forschungszentrum Jülich

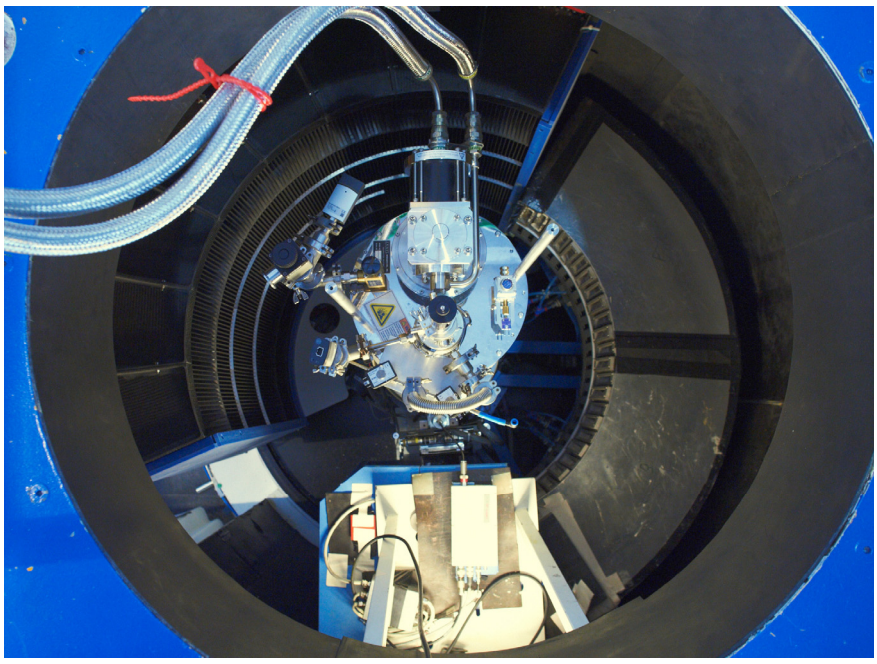

Manual of the JCNS Laboratory Course Neutron Scattering

Contents

1 Introduction

Polarized neutron scattering and polarization analysis represents a powerful technique for the studies of complex ordering phenomena and dynamics of condensed matters. The elements of this technique and its advanced applications in particular in magnetism have been comprehensively covered in a number of recent lecture notes [1-4] and several seminal papers [5-7]. The aim of this exercise on *Neutron Polarization Analysis* is to provide you with some hands-on experience on the practical aspects of polarized neutron scattering based on the multi-detector time-of-flight spectrometer DNS at FRM II. The details on the handling of polarized neutrons and the fundamentals of polarization analysis will be demonstrated from a range of carefully designed experiments and exercises.

In Section 2 of this manual, an overview of the instrument DNS as well as its unique capabilities will be given. Section 3 consists of necessary preparatory exercises and questions which can be studied before the experiment. Section 4 describes the details of the experiment procedure and provides the experiment-related exercises.

2 Overview of the DNS instrument

DNS is a versatile diffuse scattering cold neutron time-of-flight spectrometer with polarization analysis at the neutron guide NL6a, FRM II. DNS has the capability to allow unambiguous separations of nuclear coherent, spin incoherent and magnetic scattering contributions simultaneously over a large range of scattering vector **Q** and energy transfer E. A schematic layout of DNS is shown in Fig. 1.

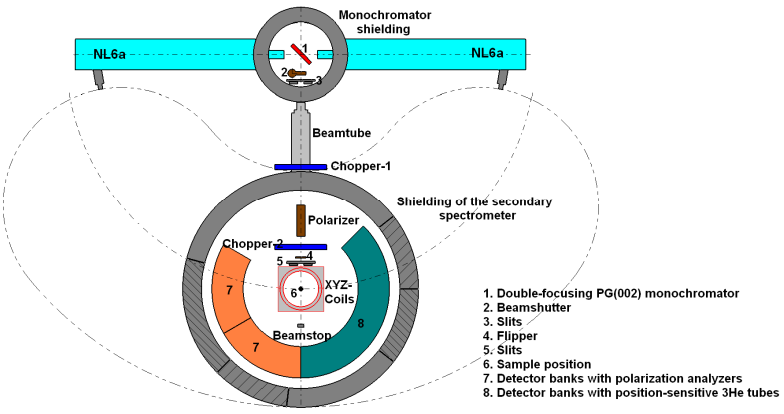

Fig. 1 The schematic layout of DNS

DNS has a number of unique features such as wide-angle polarization analysis, a large position-sensitive detector array and a high frequency double disc chopper system. With its compact design and the powerful double-focusing PG(002) monochromator, DNS is optimized as a high intensity instrument with medium resolution. The monochromatic neutron beams with the wavelength ranging from 2.4 to 6 Å are available at DNS. Newly constructed polarizer and polarization analyzers, both using m = 3 Schärpf bender-type focusing supermirrors, perform very well. A polarized neutron flux as high as 5×10^6 n/(s·cm^2) has been achieved at 4.74 Å. The polarization rate of the incident neutron beams is nearly 96%. The wide-angle polarization analysis in the horizontal scattering plane is achieved via using 24 units of polarization analyzers simultaneously. The neutron spins are manipulated using a Mezei-type π-flipper, followed by a set of orthogonal XYZ-coils situated around the sample position for providing guide fields. In addition to high polarized flux, the unique strength of DNS lies on its extreme versatility. DNS can be operated in a number of modes for a wide range of samples. There are three polarization analysis (PA) modes at DNS: uniaxial-PA for separation of coherent and spin-incoherent scattering in non-magnetic samples; longitudinal-PA for separation of magnetic scattering in paramagnetic and antiferromagnetic samples; vector-PA for the determination of complex magnetic structures.

Time-of-flight spectroscopy is another important application at DNS. The installation of 128 position-sensitive ^{3}He tubes of 1m height and half inch diameter has just been completed at DNS, and the commissioning is expected soon. This will increase the covered solid angle up to 1.9 sr. DNS will be running with a double disc chopper system with the frequency up to 300 Hz. The setup with two phase-controlled choppers would allow to eliminate high-order (e.g. λ/2) background or to select only high orders. DNS is targeted as a high count-rate cold neutron time-of-flight spectrometer with medium resolution. DNS is thus ideal for the studies of spin dynamics in many novel magnetic materials. The technical details of DNS are shown in Table 1.

Monochromator	horizontal- and vertically adjustable double-focusing	PG(002), d = 3.355 Å (at NL6a)
	crystal dimensions	2.5 × 2.5 cm^2 (5 × 7 crystals)
	wavelengths	2.4 Å ≤ λ ≤ 6 Å
Double-chopper system	chopper frequency	≤ 300 Hz
	repetition rate	≤ 900 Hz
	chopper disks	Titanium, 3 slits, ϕ = 420 mm
Expected flux at sample (n/cm^{2}s)	Non-polarized	~ 10^8
	Polarized (polarizer: m = 3 supermirror benders)	~ 5×10^6–10^7
Detector banks for non-polarized neutrons	position sensitive ^{3}He detector tubes	128 units, ϕ = 1.27 cm, height ~100 cm
	total solid angle covered	1.9 sr
	covered scattering angles in the horizontal plane	0° < 2θ ≤ 135°
Detector banks for polarized neutrons	polarization analyzers	24 units, m = 3 supermirror
	^{3}He detector tubes	24 units, ϕ = 2.54 cm, height 15 cm
	covered scattering angles in the horizontal plane	0° < 2θ ≤ 150°
Q_{max}	λ_i = 2.4 Å (E_i = 14.2 meV)	4.84 Å^{-1}
	λ_i = 6 Å (E_i = 2.28 meV)	1.93 Å^{-1}
Expected energy resolution	λ_i = 2.4 Å (E_i = 14.2 meV)	~ 1 meV
	λ_i = 6 Å (E_i = 2.28 meV)	~ 0.1 meV
Suitable samples	single crystals, powders, soft matters (e.g. polymer, liquid etc.)	
Sample environments	top-loading CCR, closed-cycle cold head, orange cryostat, cryo-furnace, ^{3}He/^{4}He dilution cryostat (~20mK), cryomagnet (self-shielding, vertical field up to 5T)	

Table 1 The technical details of the DNS instrument

Typical scientific applications at DNS are the studies of complex magnetic correlations, such as in highly frustrated magnets and strongly correlated electrons, as well as the structures of soft condensed matter systems, such as the nanoscale confined polymers and proteins, via polarization analysis. The exploration of unusual magnetic properties can also be efficiently undertaken on single-crystal samples by reciprocal space mapping. Fig. 2(a) shows an example of the measured magnetic diffuse scattering patterns in frustrated spin-ice pyrochlore compound $(Ho_{1-x}Y_x)_2Ti_2O_7$, due to in-plane magnetic correlations as determined by the spin-flip scattering of the initial P_z polarization [8]. In addition to the separation of magnetic cross section from nuclear and spin-incoherent ones, polarization analysis can also be used to explore possible anisotropy of spin correlations in complex materials. Polarized powder diffraction carried out at DNS is complementary to standard neutron powder diffraction and may be extremely useful for magnetic structure refinements, particularly in case of small magnetic moments by improving the signal to background ratio. Fig. 2(b) shows the magnetic and nuclear scattering of iron-based superconductor Sr_2CrO_3FeAs measured at DNS via polarization analysis and the corresponding Rietveld refinements [9]. Fig. 2(c) shows the magnetic diffuse scattering derived with the same approach on the $\{Mo_{72}Fe_{30}\}$ molecule magnet [10]. DNS also represents a powerful instrument for the soft condensed matter

community for the separation of nuclear coherent scattering from often dominating spin incoherent scattering background in hydrogenous materials.

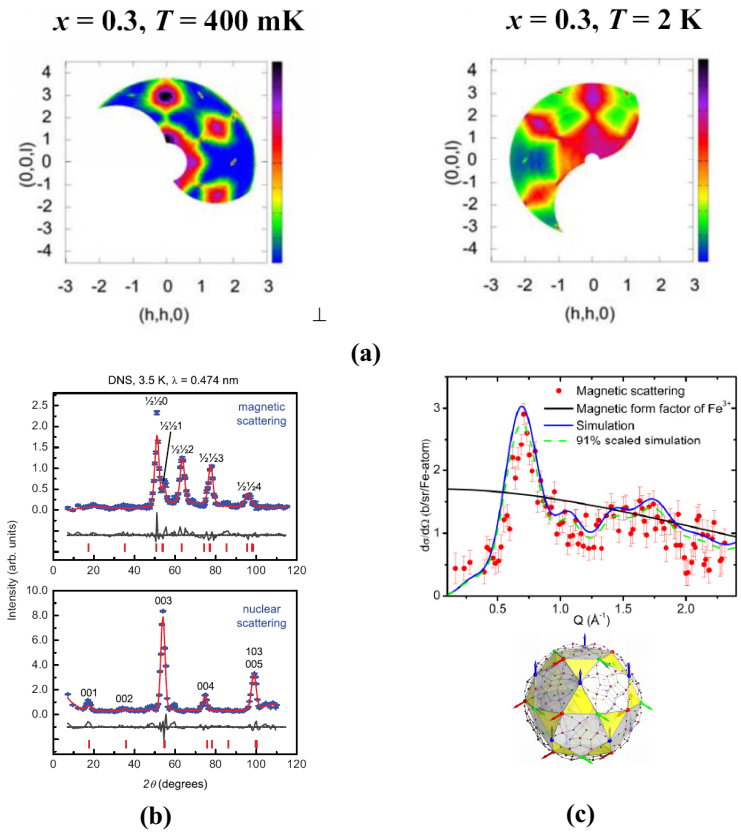

Fig. 2 Examples of the scientific applications at DNS: (a) peculiar magnetic diffuse scattering patterns observed on the frustrated spin-ice pyrochlore compound $(Ho_{1-x}Y_x)_2Ti_2O_7$ via polarization analysis [8]; (b) magnetic and nuclear scattering of iron-based superconductor Sr_2CrO_3FeAs at 3.5 K as measured (blue) at DNS via polarization analysis and the Rietveld refinements (red) [9]; (c) differential magnetic scattering cross section measured at 1.5 K and the theoretical simulation with the three-sublattice spin model of the $\{Mo_{72}Fe_{30}\}$ molecule magnet [10].

3 Preparatory Exercises

The practical aspects and the experimental setup of DNS with respect to polarization analysis have been addressed and discussed in great details in the lecture [1]. Therefore, it is strongly recommended to go through the relevant sections of the lecture notes thoroughly before the exercises. Try to answer the following general questions would greatly improve your understandings:

1. What is the Larmor precession? How to calculate the Larmor frequency (ω_L)?
2. How neutron spins would respond to changing magnetic fields? What are adiabatic and non-adiabatic behaviour?
3. How to produce polarized neutrons and how to analyze the spin state of the neutrons after the scattering process?
4. What is the spin flipper? How does it work?
5. What is the flipping ratio? What is the polarization rate of the neutron beams?
6. What are nuclear coherent, spin incoherent, isotopic incoherent and magnetic scattering processes? Whether and how the spin states of the scattered neutrons would be changed in those scattering processes?

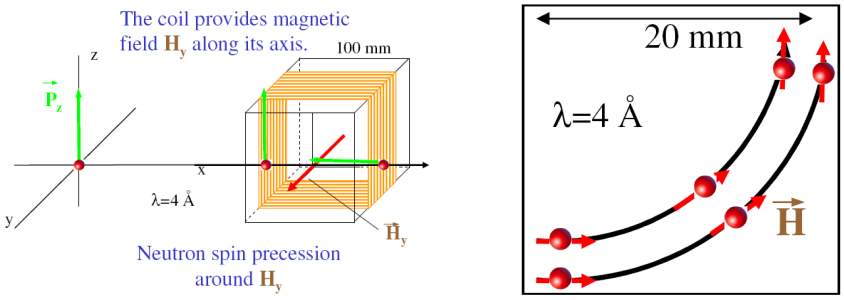

Fig. 3 Preparatory exercises

In addition to these general questions, the following exercises are provided:

1. How strong the magnetic fields $\mathbf{H}_y$ should be provided in the coil of length L = 100 mm to perform 90° turn for neutrons with λ=4 Å? (see Fig. 3(a))
2. A magnetic field **H** changes its space direction by 90° over a distance of L = 20 mm (as shown in Fig. 3(b)). How strong **H** should be to provide adiabatic evolution of the neutron spins guided by such fields? The neutrons wavelength is λ=4 Å.

4 Experiment Procedure and Experiment-related Exercises

4.1 Manipulating neutron spins

After the DNS instrument and its major instrument components are briefly introduced by the tutor, the first task for students is to learn how to manipulate neutrons spins via the Larmor precession and properly set guide fields. The following experiments are planned:

- Alignment of the π-flipper and z-compensation field coils for the incident neutrons with λ=4.74 Å
- Alignment of the magnetic guide fields at the sample position along three orthogonal directions via XYZ-coils
- Measurement of the flipping ratio and the polarization rate of the incident neutron beams at DNS

In addition, the following exercises are provided:

1. For neutrons with a wavelength λ=4.74 Å and a flight path of 10 mm through the flipper coil, how strong the flipping field would be required to achieve a π-flip?
2. The measured flipping ratio (R) is 25, what is the polarization rate (P) of the incident neutron beams?

4.2 Demonstration of the principle of neutron polarization analysis

The principle of neutron polarization analysis will be demonstrated here by the measurement of various standard samples. The following samples are planned,

- (002) Bragg reflection of pyrolytic graphite: nuclear coherent scattering
- Vanadium hollow-cylinder: nuclear spin-incoherent scattering
- Non-magnetic alloy $Ni_{0.89}Cr_{0.11}$: isotopic incoherent scattering
- A prototypical antiferromagnet: magnetic scattering

The students are expected to perform the experiment to measure the spin-flip and non-spin-flip scattering intensities of each sample via wide-angle polarization analyzers at DNS. The basic rules for the separation of different scattering cross-sections can thus be derived. The students will be encouraged to compare the results obtained at DNS to those reported in the seminal work by R.M. Moon [5].

The polarization efficiency can never achieve 100% due to polarization losses by depolarizations in the polarizer, the analyzer and the guide fields and the imperfections of the polarizer, the analyzer and the flipper. This would always lead to a finite flipping ratio even for an ideal non-spin-flip scatter. The correction for finite flipping ratio thus becomes an

important and always necessary practical issue in order to obtain a precise separation. Therefore, the following exercise related to the flipping ratio correction is provided,

1. The measured flipping ratio from an ideal isotopic incoherent scatter $Ni_{0.89}Cr_{0.11}$ is 20, the spin-flip scattering intensity is $I_{\uparrow\uparrow}$ and the non-spin-flip scattering intensity is $I_{\uparrow\downarrow}$, how to calculated the corrected intensities for $I_{\uparrow\uparrow}$ and $I_{\uparrow\downarrow}$ by taking into account the finite flipping ratio?

4.3 Case studies

In the final part, two case studies will be provided for students to maser neutron polarization analysis via the measurements on two real samples. The first one is the separation of nuclear coherent scattering from incoherent scattering in heavy water D_2O [11]. The second case study is the measurement of magnetic ordering in the novel superconducting compound via the XYZ-method [9]. The following exercises are provided,

1. How to separate nuclear coherent scattering from spin-incoherent scattering in soft condensed matter?
2. How to obtain the magnetic scattering cross section via the XYZ-method? Which necessary corrections need to be done for a precise separation?

References

[1] W. Schweika, *Polarized Neutron Scattering and Polarization Analysis,* in *Lecture Notes on Laboratory Course Neutron Scattering,* Eds. Th. Brückel, G. Heger, D. Richter, G. Roth and R. Zorn (Forschungszentrum Jülich, 2010)

[2] J. Schweiza, *Polarized Neutron and Polarization Analysis*, in *Neutron Scattering from Magnetic Materials*, Ed. T. Chatterji (Elsevier, Amsterdam, 2006)

[3] P.J. Brown, *Spherical Neutron Polarimetry*, in *Neutron Scattering from Magnetic Materials*, Ed. T. Chatterji (Elsevier, Amsterdam, 2006)

[4] L.P. Regnault, *Inelastic Neutron Polarization Analysis*, in *Neutron Scattering from Magnetic Materials*, Ed. T. Chatterji (Elsevier, Amsterdam, 2006)

[5] R.M. Moon, T. Riste, W.C. Koehler, Phys. Rev. **181**, 920 (1969)

[6] O. Schärpf, H. Capellmann, Phys. Stat. Sol. (a) **135**, 359 (1993)

[7] J.R. Stewart *et al.*, J. Appl. Cryst. **42**, 69 (2009)

[8] L.J. Chang *et al.*, Phys. Rev. B **82**, 172403 (2010)

[9] M. Tegel *et al.*, EPL **89**, 37006 (2010)

[10] Z.D. Fu *et al.*, New Journal of Physics **12**, 083044 (2010)

[11] L. Temleitner *et al.*, J. Phys.: Condens. Matter **19**, 335207 (2007)

Contact

DNS

Phone: 089/289-14339
Web: http://www.frm2.tum.de/wissenschaftliche-nutzung/spektrometrie/dns/index.html

Yixi Su

Juelich Centre for Neutron Science JCNS-FRM II
Forschungszentrum Juelich GmbH
Outstation at FRM II

Phone: 089/289-10714
e-Mail: Y.Su@fz-juelich.de
Web: http://www.fz-juelich.de/SharedDocs/Personen/JCNS/EN/Su_Y

J-NSE

Neutron spin echo spectrometer

O. Holderer, M. Zamponi and M. Monkenbusch

Jülich Centre for Neutron Science
Forschungszentrum Jülich

Manual of the JCNS Laboratory Course Neutron Scattering

Contents

1 Introduction

Aim of the experiment is to study the dynamics of a polymer chain in solution with Neutron Spin Echo spectroscopy (NSE), the technique which offers the highest energy resolution in neutron scattering. The technique is well suited for soft matter systems where the molecules or nanoscopic structures like membranes or micelles exhibit fluctuating Brownian motions, driven by the thermal energy. NSE is able to analyze these fluctuations on the nanosecond and nanometer time- and lengthscale.

In this neutron course experiment PEP (poly(ethylene propylene)) with a molecular weight of 70 kg/mol is dissolved in deuterated decane with a concentration of 3 %. The dynamics of the polymer in solution will be studied here at room temperature. The results will be interpreted in terms of the Zimm model which allows to draw conclusions about the internal motions of the polymer chains.

2 Neutron Spin Echo Spectroscopy

The neutron spin echo technique uses the neutron spin as an indicator of the individual velocity change the neutron suffered when scattered by the sample. Due to this trick the instrument accepts a broad wavelength band and at the same time is sensitive to velocity changes down to 10^{-5}. However the information carried by the spins can only be retrieved modulo an integer number of spin precessions as intensity modulation proportional to the cosine of a precession angle difference. The measured signal is the cosine transform $I(Q,t)$ of the scattering function $S(Q,\omega)$. All spin manipulations only serve to establish this special type of velocity analysis. For details see Reference [1].

Due to the intrinsic Fourier transform property of the NSE instrument it is especially suited for the investigation of relaxation-type motions that contribute at least several percent to the entire scattering intensity at the momentum transfer of interest. In those cases the Fourier transform property yields the desired relaxation function directly without numerical transformation and tedious resolution deconvolution. The resolution of the NSE may be corrected by a simple division.

For a given wavelength the Fourier time range is limited to short times (about 3 ps for the FRM II-setup) by the lower limit of the field integral and to long times by the maximum achievable field integral $J = \int Bdl$. The lower limit results from the lowest field values that are needed as "guide" field in order to prevent neutrons from depolarization effects. The upper limit results either from the maximum field that can be produced by the main solenoid, powersupply and cooling combination or by the maximum field integral inhomogeniety ($\rightarrow$ variation of precession angle between different paths within the neutron beam) that can be tolerated respectively corrected for, depending which condition applies first. The Fourier time is proportional to $J \cdot \lambda^3$. The J-NSE may achieve a $J = 0.5$ Tm corresponding to t = 48 ns at λ = 8 Å.

The instrument itself (see Figure 1) consists mainly of two large water-cooled copper solenoids that generate the precession field. The precession tracks are limited by the π/2-flippers in front of the entrance respectively exit of the first and second main solenoids and the π-flipper near the sample position. The embedding fields for the flippers are generated by Helmholtz-type coil

pairs around the flipper locations. After leaving the last flipper the neutrons enter an analyzer containing 60 (30 x 30 cm^2) magnetized CoTi supermirrors located in a solenoid set. These mirrors reflect only neutrons of one spin direction into the multidetector. By the addition of compensating loops the main coils and the analyzer coil are designed such that the mutual influence of the different spectrometer components is minimized.

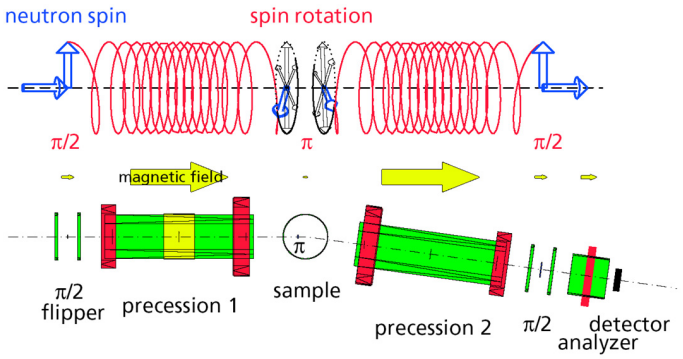

Fig. 1: *Working principle of the NSE spectrometer [2].*

Depending on its velocity, each neutron undergoes a number of precessions in the first solenoid before hitting the sample. The second solenoid after the scattering process rewinds exactly these precessions for elastically scattered neutrons, whereas inelastically scattered neutrons collect a different phase angle of rotation, $\Delta\Psi \simeq \Delta v/v^2\,\gamma\,J$, with $\gamma = 2\pi \times 2913.06598 \times 10^{-4}\,\mathrm{s}^{-1}\,\mathrm{T}^{-1}$.

The distribution of velocity changes Δv of the neutrons suffer during scattering at the sample –in terms of it's cos-Fourier transform– is measured as polarization of the neutron beam at the end of the second solenoid after the last $\pi/2$-flipper. The small velocity changes are proportional to the small energy changes $\hbar\omega$, ω being the frequency of the Fourier transform. The time parameter (Fourier time) is proportional to $\lambda^3 J$ and here in first instance is controlled by the current setting of the main coils (i.e. J). The polarization then is determined by scanning the magnetic field in one of the main coils slightly with the so called phase coil. If first and second arm are symmetric, a maximum of the polarization is measured, if the phase of the spins is shifted by 180 degree by variation of the field of one coil, one gets to a minimum of intensity. With a 360 degree variation one gets to the next maximum and so on. These oscillations are shown in Figure 2. The amplitude of this echo is normalized to the difference between maximum intensity (up-value), where all flippers are switched off, and the minimum intensity where only the π-flipper is switched on (down-value). Assuming that this normalization accounts for all imperfections of the polarization analysis in the instrument, the result yields the desired degree of polarization reduction due to inelastic/quasielastic scattering of the sample. Since the thus determined polarization reduction also contains the effects due to field integral inhomogeniety a further renormalization step is needed, which is equivalent to a resolution deconvolution in a spectroscopic instrument as e.g. the backscattering spectrometer. In order to be able to perform this resolution correction the same experimental and data treatment procedure has to be carried out with an elastic scatterer.

The scattering vector Q is determined by the angle 2θ of the second arm of the spectrometer with respect to the first one by $Q = 4\pi/\lambda \sin(\theta)$. The Fourier time t is proportional to the magnetic field of the main solenoids. At a given scattering vector Q, the magnetic field is successively increased and an echo group is recorded for each setting to obtain $I(Q, t)$ as a function of t.

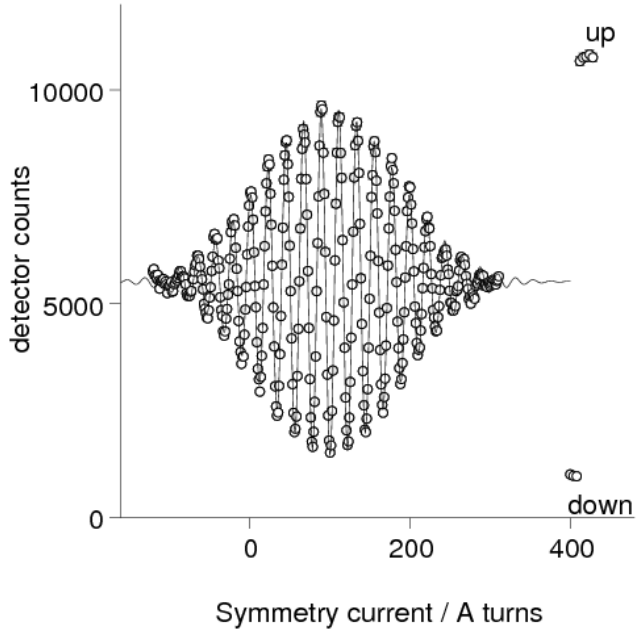

Fig. 2: *Echo group measured with the NSE instrument.*

2.1 Separation of coherent and incoherent scattering

By the use of polarized neutrons it is possible to separate the coherent and spin incoherent part of the scattering, since the incoherent scattering changes the polarisation to $-1/3$. For different scattering vectors Q the scattering intensity is measured, once in the spin-up configuration and once in the spin-down setup. In the spin-up configuration all spin flippers are switched off and the longitudinal, in forward direction (i.e. parallel to the magnetic field) polarized beam can pass through the spectrometer. The analyzer in front of the detector transmits those polarized neutrons. The measured intensity at the detector in this configuration is the maximum possible intensity. In the spin-down configuration only the π flipper at the sample position is switched on, which rotates the neutron spin orientation by $180°$. The spin direction is now against the magnetic field direction and in the ideal case the analyzer completly absorbs the neutrons, so that the minimal possible detector intensity is measured. Omitting background effects and assuming perfect flipping ratio (ratio spin-up/spin-down = ∞ in the direct beam) coherent and incoherent

scattering contributions can be separated as follow (with Up: detector intensity in the diffraction run with all flippers off, $Down$: detector intensity in the diffraction run with only π flipper at sample position on, I_{coh}: coherent scattered intensity, I_{inc}: incoherent scattered intensity)

$$Up + Down = I_{coh} + I_{inc} \tag{1}$$

$$Up - Down = I_{coh} - 1/3 * I_{inc} \tag{2}$$

which gives

$$Up = I_{coh} + 1/3 I_{inc} \tag{3}$$

$$Down = 2/3 I_{inc} \tag{4}$$

respectively

$$I_{inc} = 3/2 Down \tag{5}$$

$$I_{coh} = Up - 1/2 Down \tag{6}$$

To include nonideal flipping ratio and background count rate the calculation is more difficult.

3 Polymer dynamics

There are different models to describe the dynamics of large molecules. A nice overview is given in the book "Neutron Spin Echo in Polymer Systems", which is also available online [3].

The conformation of a linear polymer chain follows a random walk, this means a chain segment of length l can move freely around the neighboring segment (within the limitation of chemical bonds). With a set of segment vectors $\mathbf{r}_n = \mathbf{R}_n - \mathbf{R}_{n-1}$, where $\mathbf{R}_n$ is the position vector of segment n, the distance between segments which are n steps apart follows a Gaussian distribution [3]:

$$\Phi(R, n) = \left(\frac{3}{2\pi n l^2}\right)^{3/2} \exp\left(-\frac{3R^2}{2nl^2}\right) \tag{7}$$

with l the segment length.

By summing up the scattering amplitudes of the centres of the segments of a polymer chain with the correct phases, one obtains the scattering function of the polymer chain (see Lecture on Dynamics of Macromolecules for more details):

$$I(Q, t) = \langle \sum_{n,m=1}^{N} \exp[i\mathbf{Q} \cdot (\mathbf{R}_n(t) - \mathbf{R}_m(t))] \rangle \tag{8}$$

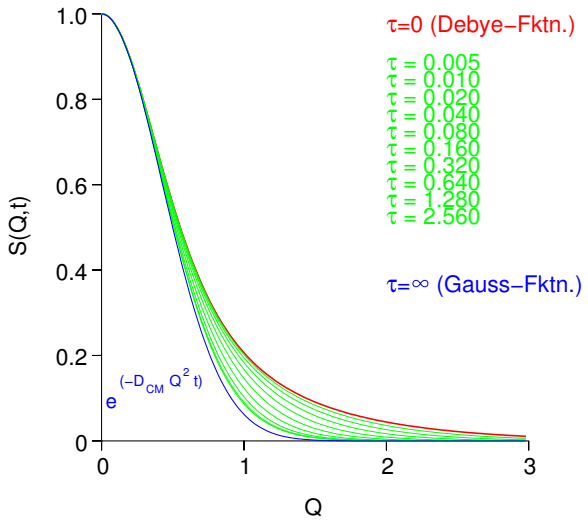

Fig. 3: *Time development of $I(Q,t)/I(Q,0)$ (here denoted $S(Q,t)$ for a Gaussian chain in the Rouse model.*

A snapshot of the chain, i.e. the static structure factor, is obtained for $t = 0$. One gets the well known Debye funktion:

$$I(Q) = N f_{Debye}(Q^2 R_g^2) \tag{9}$$

$$f_{Debye}(x) = \frac{2}{x^2}(e^{-x} - 1 + x) \tag{10}$$

with R_g the radius of gyration of the chain. In Figure 3 the Debye function and its time evolution is displayed.

3.1 Rouse dynamics

In the Rouse model the Gausssian polymer chain is described as beads connected by springs. The springs correspond to the entropic forces between the beads and the distance between the beads corresponds to the segment length of the polymer. The polymer chain is in a heat bath. The Rouse model describes the movement of the single chain segments of such a polymer chain as Brownian movement. Thermally activated fluctuations (by the stochastic force $\mathbf{f}_n(t)$ with $< \mathbf{f}_n(t) >= 0$), friction force (with friction coefficient ζ) and the entropic force determine the relaxation of polymer chains.

The movement of the chain segments is described by a Langevin equation:

$$\zeta \frac{d\mathbf{R}_n}{dt} + \frac{\partial U}{\partial \mathbf{R}_n} = \mathbf{f}_n(t) \tag{11}$$

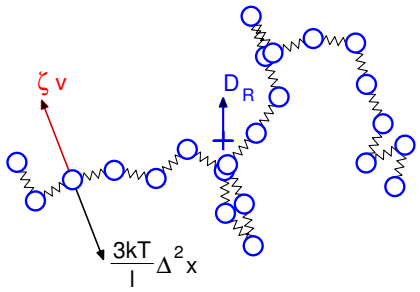

Fig. 4: *Polymer chain in the Rouse model [3] as Gaussian chain with beads connected by springs.*

The Langevin equation can be solved and one can calculate with equation 8 the intermediate scattering function, which is measured by NSE (for details, see the lecture on "Dynamics of Macromolecules"):

$$I(Q,t) = \exp(-Q^2 Dt) I_{intern}(Q,t) \tag{12}$$

with a diffusive part with a relaxation rate proportional to Q^2 and the part describing the internal relaxation, which can be written for $QR_G >> 1$:

$$I_{intern}(Q,t) = \frac{12}{Q^2 l^2} \int_0^\infty du \exp(-u - \sqrt{(\Gamma_Q t)} h(u/\sqrt{(\Gamma_Q t)})) \tag{13}$$

with the relaxation rate

$$\Gamma_Q = \frac{k_B T}{12\zeta} Q^4 l^2 \tag{14}$$

and

$$h(u) = \frac{2}{\pi} \int dx \cos(xu)(1 - e^{-x^2})/x^2 \tag{15}$$

Note that the local relaxation rate depends on Q^4. When $I(Q,t)/I(Q,0)$ is plotted against the Rouse variable $\sqrt{\Gamma_Q t}$, all curves collapse onto a master curve if the Rouse model holds.

With this model e.g. the dynamic of short polymers in the melt can be described. With increasing molecular weight other effects like the constraints imposed by mutual entanglements of the polymer chains become important, which are described in the reptation model by DeGennes (Nobel prize 1991). In this experiment polymers in solution, not in the melt, are considered. The Rouse model then needs to be extended by hydrodynamic interactions as will be described in the following section.

3.2 Zimm dynamics

Polymers in solution can be described by the Zimm model, where hydrodynamic interaction between the chain segments mediated by the solvent are dominant. Moving chain segments exert forces on other segments due to the flow of the surrounding solvent. Within some approximations the system can be described by a Langevin equation analogous to that of the Rouse model which includes the friction coefficient $\xi = 6\pi\eta a_{seg}$ with η the viscosity of the solvent. The diffusion of a chain segment depends on its hydrodynamic radius a_{seg}. More details can be found in literature [3].

In general the intermediate scattering function for polymers in solution is

$$\frac{I(Q,t)}{I(Q,0)} = F\left(\frac{k_B\,T\,Q^3\,t}{6\,\pi\,\eta}\right) \tag{16}$$

with a function $F(x)$ which depends on the polymer conformation and the quality of the solvent. The relaxation rate $\Gamma_Q = k_B\,T\,Q^3/(6\,\pi\,\eta)$ is mainly determined by the viscosity of the solvent. Internal dynamics is dominant at higher scattering vectors Q, where also the typical Q^3 dependence of the relaxation rate can be observed. At smaller scattering vectors the contribution from the center of mass diffusion is more prominent so that rather a Q^2 dependence of the relaxation rate is expected (see below). For not too small Q values and long polymer chains, where the end-to-end distance of the chain segments follow Gaussian statistics (Gaussian chain), the function $F(x)$ can be written as:

$$\begin{aligned} F(x) &= \int_0^\infty \exp\Big(-u - x^{2/3}\frac{2}{\pi}\int_0^\infty \frac{\cos(y\,u\,x^{-2/3})}{y^2} \\ &\quad \times\Big[1-\exp\Big(-\frac{y^{2/3}}{\sqrt{2}}\Big)\Big]\mathrm{d}y\Big)\mathrm{d}u \end{aligned} \tag{17}$$

This more complex function can be approximated by a stretched exponential function over a wide Q range:

$$F(x) \simeq \exp\Big(-\Big(\frac{x}{b}\Big)^\beta\Big) \tag{18}$$

with the parameters $b \simeq 1.354$ and $\beta \simeq 0.85$. For the evaluation of this experiment this approximation of $F(x)$ can be used.

3.3 Center of mass diffusion

With NSE spectroscopy the movements on length scales in the order of nanometer and time scales in the order of nanoseconds can be observed. This matches e.g. the center of mass diffusion of macromolecules in solution or micelles. The mean square displacement of a particle is $< r^2(t) >= 6D_0t$ with the diffusion constant $D_0 = k_BT/(6\pi\eta R_G)$, where R_G is the hydrodynamic particle radius and η the viscosity (Stokes-Einstein-relation). The dynamic structure factor which is measured by NSE is then

$$I(Q,t)/I(Q,0) = \exp\left(-1/6 < r^2(t) > Q^2\right) = \exp\left(-D_0tQ^2\right) \tag{19}$$

A simple diffusion therefore has a quadratic dependence on the scattering vector Q.

4 Preparatory Exercises

1. How fast do neutrons with a wavelength of 8 Å fly?

2. What is the value of the earth's magnetic field?

3. What is the magnetic field at the surface of a common permanent magnet?

4. How many mm fall neutrons on their way from the entrance of the spectrometer to the detector (about 7 m) due to gravity?

5. How many precessions does a neutron of $\lambda = 8$ Å perform in the main coils if the Fourier time is set to 20 ns? (Angle $\Psi = \gamma/v \int Bdl$ with $\gamma = 2\pi \cdot 2913.06598 \times 10^4 (s \cdot T)^{-1}$.

5 Experiment Procedure

5.1 The experiment itself

First, the function of the key components of the neutron spin-echo spectrometer will be explained and demonstrated.

The generation of the "Spin Echo" will be demonstrated with an auxiliary phase coil, wound around one of the main precession coils with a simple wire. With a laboratory DC-powersupply connected to this coil, the magnetic field inside this main coil is slightly varied. A fully symmetrical setup with identical magnetic path integrals in both main coils results in a maximum count rate at the detector. Increasing the current in the auxiliary coil from this point results in an additional phase shift of the neutron spin and thus the intensity varies from the maximum to a minimum and further to the next maximum and so on. In this way, the echo group is scanned.

The experimental sample under investigation is a polymer chain (PEP, polyethylenepropylene) with a molecular weight of 70 kg/mol in solution (deuterated decane). The PEP concentration is 3 wt %. The first experiment with the sample is to measure the elastic scattering by recording the spin-up and spin-down intensity at the detector.

- The coherent and incoherent scattering of the sample shall be extracted from this reading and plotted versus the scattering vector Q.

The dynamics of the sample is measured. For some selected scattering vectors Q, a series of Fourier times is measured for the sample, for a background sample containing everything but the objects under investigation, in this case the pure deuterated solvent (d-decane), and for an elastic scatterer as reference.

5.2 Data reduction

Each Fourier time is determined by measuring 2-3 oscillations of the echo bunch and fitting the theoretical curve (a cosine oscillation with a gaussian envelope) to the points. In short, the normalized amplitude of the fitted curve is the degree of polarization wanted in this measurement. This procedure is done with a program called `echodet`, which creates the files containing the intermediate scattering function $I(Q,t)$.

5.3 Data evaluation

The $I(Q,t)$ vs. t is contained in the files b_XXXXX as ascii-data.

- Read in the data with some data treatment program (e.g. `qtiKWS9`).
- Fit the data with a model function. First use a simple exponential function $I(Q,t) = A\exp(-\Gamma t)$ and determine the relaxation rate Γ. For diffusion like behaviour with the Stokes-Einstein diffusion coefficient, $\Gamma = DQ^2$ should be valid. Plot Γ/Q^2 to check the validity of the model. It also allows for the determiation of the hydrodynamic radius of the particle assuming a viscosity of d-decane of $\eta = 0.954 \times 10^{-3}$ kg/(m s).
- Use a stretched exponential function as model function: $I(Q,t) = A\exp(-[\Gamma t]^{\beta})$ and determine the relaxation rate Γ and the stretching exponent β. The Zimm model would predict that the rate depends on the viscosity η as $\Gamma = k_B T/(6\pi\eta)Q^3$. Which is the viscosity of d-decane? Does the Q-dependence of the model describes that of the data correctly (i.e. is $\Gamma/Q^3 = const.$)?

6 Experiment-Related Exercises

Data evaluation (the bullet points in section 5):

1. Separate coherent and incoherent scattering from elastic scan (diffrun) and plot it.
2. Evaluate the data containing $I(Q,t)$ vs t with the models as described in the previous section and discuss the results.

General questions:

1. Why are no iron yoke magnets used in the construction of a NSE spectrometer?
2. What is the maximum field inside the main precession coils of the J-NSE?
3. What determines the resolution of the spin echo spectrometer?
4. How does the signal look like if the scattering is spin-incoherent? (Hint: in this case 2/3 of all neutron spins get flipped in the scattering process.)

5. What is the measured effect of the spin echo spectrometer?
6. What is measured finally?

References

[1] F. Mezei, editor. *Neutron Spin Echo, Proceedings Grenoble 1979*, volume 128 of *Lecture Notes in Physics*. Springer, 1980.

[2] D. Richter M. Monkenbusch, R. Schätzler. *Nucl. Instr. Meth. in Phys. Res. A*, 399:301–323, 1997.

[3] D. Richter, M. Monkenbusch, A. Arbe, and J. Colmenero. *Adv. Polym. Sci.*, 174:1–221, 2005.

Contact

J-NSE

Phone: 089/289-14903
Web: http://www.jcns.info/jcns_nse

Olaf Holderer

Jülich Centre for Neutron Science, Outstation at the FRM II
Forschungszentrum Jülich GmbH

Phone: 089/289-10707
e-Mail: o.holderer@fz-juelich.de
Web: http://www.jcns.info

Michaela Zamponi

Phone: 089/289-10793
e-Mail: m.zamponi@fz-juelich.de
Web: http://www.jcns.info

KWS-1 & KWS-2

Small Angle Neutron Scattering

H. Frielinghaus, M.-S. Appavou

Jülich Centre for Neutron Science
Forschungszentrum Jülich

Manual of the JCNS Laboratory Course Neutron Scattering

Contents

Fig. 1: *Representation of the protein lysozyme, which has a very compact form.*

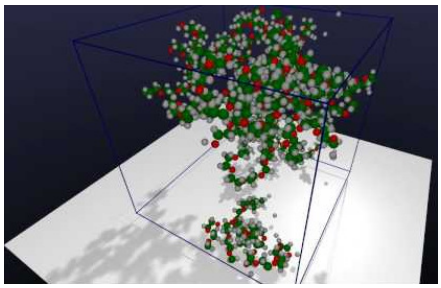

Fig. 2: *Molecular dynamics conformation of poly ethylene oxide in solution.*

1 Introduction

The objective of this lab course is to clarify the essential concepts of small-angle neutron scattering. Structures are only visible by a scattering experiment if there is an appropriate contrast. For neutrons one often uses the exchange of ^{1}H by ^{2}H, i.e. deuterium. The contrast of this lab course is achieved by using heavy water (D_2O) as solvent. The materials (solutes) are natural ones having normal protons.

The globular, compact lysozyme (Fig. 1) appears in chicken eggs and has anti-bacterial function. The molecule is charged, which leads to repulsive interactions. So there is a short range order, and the distance between the molecules can be determined.

The other molecule is the synthetic poly ethylene oxide (Fig. 2) with the chemical formula of $[\text{-}CH_3\text{-}CH_3\text{-}O\text{-}]_n$. It is one of the simplest water soluble polymers. The hydrogen bonds of the oxygen are responsible for attractive interactions between water and the polymer. The molecules form rather dilute coils in solution and the overall dimension of the coil will be determined by SANS. Furthermore, the fractal structure of the coil will be determined.

2 Preparing solutions in Water

A lysozyme solution of 0.02g per ml of water must be prepared. We will weigh 0.02g of Lysozyme and put it into a new Packard glas. With an Eppendorf pipette we will add exactly 1 ml D_2O. These pipettes are extremely accurate with respect to the volume. From the solution about 0.5 to 0.6ml are transferred to Hellma quartz cuvettes, which are 1mm thick. For the later evaluation we need a highly accurate concentration. So all weights need to be written down as exactly as possible.

For the poly ethylene oxide solution we chose the same concentration. Since the polymer exists

in small platelets the tiny amount of polymer will not be that accurately prepared. Corrections can be either done by chosing a different volume of heavy water or by just writing down the exact weights. However, stay below 0.04g/ml for the concentration!

3 The Measurement at KWS-1 and/or KWS-2

These two solutions are now being measured in the small-angle neutron scattering instrument KWS-1 (or KWS-2). The wavelength of neutrons is set to 7Å. The collimation is fixed to 8m. The samples are placed as close as possible to the detector, to measure the largest Q values possible. Both samples will be measured at detector distances 2m and 8m. The offset between the sample position and the detector of about 30cm leads to effective detector distances of about 1.7m and 7.7m.

The sample holder will be filled with the two samples. In addition, the empty beam and a plexiglass plate are measured for absolute calibration. For a good statistical measurement the following times are set: 8m detector distance for 20min, and 2m detector distance 10min. The total measuring time for the 4 positions will be about 2 hours. The measurement is typically started before lunch, and can be evaluated in the afternoon. It is quite likely that an internal employee will start separate measurements during the afternoon until the next morning in order to use the valuable measuring time overnight.

4 Evaluation of the Scattering Data: Absolute Calibration

The measured data is raw data at first and describes the intensity on the detector. The data has to be corrected for the effectiveness of the different detector channels. Then the empty beam measurement is subtracted to account for the zero effect of the instrument. Then the intensities are expressed as absolute units using Eq. 5.5 and are radially averaged, because for the isotropic scattering samples, the intensity does not depend on the polar angle. To perform all these steps we will be using a software available in our institute, called QtiKWS. However, since the understanding of the Eq. 5.5, as such, is more important than the exact technical understanding of the evaluation, the results are produced relatively quickly by the software, namely, $\mathrm{d}\Sigma/d\Omega$ as a function of the scattering vector Q for our samples. This data will be provided for the students to do the final evaluation. In the following, this evaluation is described.

5 Evaluation of Lysozyme Scattering Curves

The position of the maximum $Q_{\max}$ provides information on the typical distance of the proteins in solution. This can be calculated to $\ell = 2\pi/Q_{\max}$. Knowing the weight of the protein in water (0.02g/cm^3) there is an alternative way to calculate the average distance. The molar mass of the protein is 1.43×10^4g/mol. The number density of the protein is therefore $n/V = 0.02\text{g/cm}^3/(1.43 \times 10^4\text{g/mol}) = 1.40 \times 10^{-6}\text{mol/cm}^3 = 8.42 \times 10^{-7}\text{Å}^{-3}$. For a simple cubic packing the typical distance is given by $\ell = \sqrt[3]{V/n}$. For a hexagonal packing the

typical distance is $\ell = \sqrt[6]{27/256}\sqrt[3]{V/n}$. This distance is the minimum distance of the planes important for the scattering experiment, and the next neighbor distance of the hexagonal lattice is $\sqrt{8/3}\ \ell = \sqrt[6]{2}\sqrt[3]{V/n}$. Both calculated distances of the cubic and hexagonal structure are to be compared with the measured one.

6 Evaluation of the Polymer Scattering

In a first step we have to prepare the scattering data for background subtraction. We plot the original data of the two detector distances in a log-log plot, i.e. $\log_{10}(d\Sigma/d\Omega) \rightarrow \log_{10} Q$. After this, we will see a plateau at high Q which indicates the constant incoherent scattering. Taking the average of the last (say 10) points will give us the estimate of the background. A new column with the background subtracted will be generated for the 8m and 2m measurements. Finally, the two data sets should be combined to yield a single data set.

Now, we will aim at the overall appearance of the chain, i.e. we will determine the chain dimension. For this purpose the Guinier approximation can be applied. The general appearance of the Gunier scattering law was already given in eq. 5.35 and reads:

$$\frac{d\Sigma}{d\Omega}(\mathbf{Q}\rightarrow 0) = \frac{d\Sigma}{d\Omega}(0) \cdot \exp\left(-\frac{1}{3}Q^2 R_g^2\right) \tag{1}$$

For this purpose we plot the logarithm of the background corrected intensity against the square of the scattering vector, i.e. $\ln(d\Sigma/d\Omega) \rightarrow Q^2$. The highest Q will lead to large values that we are not interested in. So the plot has to be truncated to the rather small Q, say $Q^2 = 0..4 \times 10^{-4}\text{Å}^{-2}$. Here, we do a linear regression and take the slope S as a result only. It has the units Å^2. From this we can calculate the radius of gyration using $R_g = \sqrt{-3S}$. From previous measurements we know that it is roughly 60Å large.

For the fractal structure we plot the data in a log-log plot again (background corrected). There is the Gunier region indicated by flat scattering at low Q. At high Q the data will have very large noise, and maybe negative values might appear from the subtraction. In the middle, the scattering should be linear, indicating a power law characteristic for fractal structures. Again, we use a linear regression to determine the slope α. From the ideal polymer without interactions we learned that the exponent would read $\alpha = 2$ (see eq. 5.50). When taking the attractive interactions of the solvent into account, the exponent would be rather $\alpha = 1.70$. The reciprocal value α^{-1} is called Flory exponent and takes the ideal values of 0.5 or 0.588 for non-interacting chains and chains in a good solvent, respectively. Please make your own judgement!

7 Preparatory Exercises

(I) Lysozyme in D_2O

The first sample of the Neutron Lab Course at the SANS instrument KWS-1 (KWS-2) will be Lysozyme in heavy water (D_2O). This protein is rather globular (diameter ca. 5 nm). The Coulomb interactions of this charged molecule lead to liquid-like short-range-ordering. This will be observed in the SANS scattering experiment by a correlation peak. Simple estimations will be made now:

1. Give the connection between the number density ϕ and the unit cell parameter assuming a simple cubic lattice!
2. The chemical concentration c is usually given in g/L or mg/ml. The molar mass of the molecule is 14307g/mol. What is the connection between the chemical concentration and the number density?
3. The correlation peak appears at a scattering vector $Q_{\max}$. How would it relate to the unit cell parameter of a simple cubic lattice? What is the dependence of $Q_{\max}$ as a function of the chemical concentration c?
4. Please rationalize the relations of the hexagonal packing with respect to the cubic packing! The spacing of the planes is shorter by a value of rougly 0.69 (larger Q value compared to cubic). The nearest neighbor has a larger distance of ca. 1.12 times the cubic packing.

(II) Polymer in Solution

We will look on the overall dimension of the chain and on the fractal structure of the chain.

1. The Appendix B derived the Guinier scattering law for any shape of particles while in the main manuscript the first application was the compact sphere. How has the compactness of a polymer in a good solvent to be seen? Is there any restriction for the Gunier scattering for polymers?
2. At large Q we observe a constant background from incoherent scattering. The hydrogen atom has a incoherent cross section of 80×10^{-24}cm^2, and the deuterium atom 2×10^{-24}cm^2. The concentration of hydrogen from the polymer is roughly 50 times smaller than the concentration of deuterium from the heavy water. On the basis of these numbers estimate the ratio of background from the polymer and the solvent!
3. The fractal structure means that looking inside a coil still finds the situation of the connectivity of a chain on smaller length scales compared to the overall chain. The chain is self-similar on length scales (between the overall coil dimension and the monomer dimension). The different exponents α of 2 and 1.7 for ideal chains and polymers in a good solvent describe different compactness of the structure. Rationalize the difference between a non-interacting chain and a chain that "feels" its own presence!

Contact

KWS-1 & KWS-2

Phone: +49-89-289-14324 & +49-89-289-14326
Web: http://www.jcns.info/jcns_instruments

Henrich Frielinghaus

Jülich Centre for Neutron Science
Forschungszentrum Jülich GmbH
c/o TUM, FRM 2
Lichtenbergstrasse 1
85747 Garching

Phone: +49-89-829-10706
e-Mail: H.Frielinghaus@fz-juelich.de

Aurel Radulescu

Jülich Centre for Neutron Science
Forschungszentrum Jülich GmbH
c/o TUM, FRM 2
Lichtenbergstrasse 1
85747 Garching

Phone: +49-89-829-10712
e-Mail: A.Radulescu@fz-juelich.de

Zhenyu Di

Phone: +49-89-289-10758
e-Mail: Z.Di@fz-juelich.de

Artem Feoktystov

Phone: +49-89-289-10746
e-Mail: A.Feoktystov@fz-juelich.de

Marie-Sousai Appavou

Phone: +49-89-289-10747
e-Mail: M.S.Appavou@fz-juelich.de

Noemi Szekely

Phone: +49-89-289-10739
e-Mail: N.Szekely@fz-juelich.de

KWS-3

Very Small Angle Neutron Scattering Diffractometer with Focusing Mirror

Vitaliy Pipich

Jülich Centre for Neutron Science
Forschungszentrum Jülich

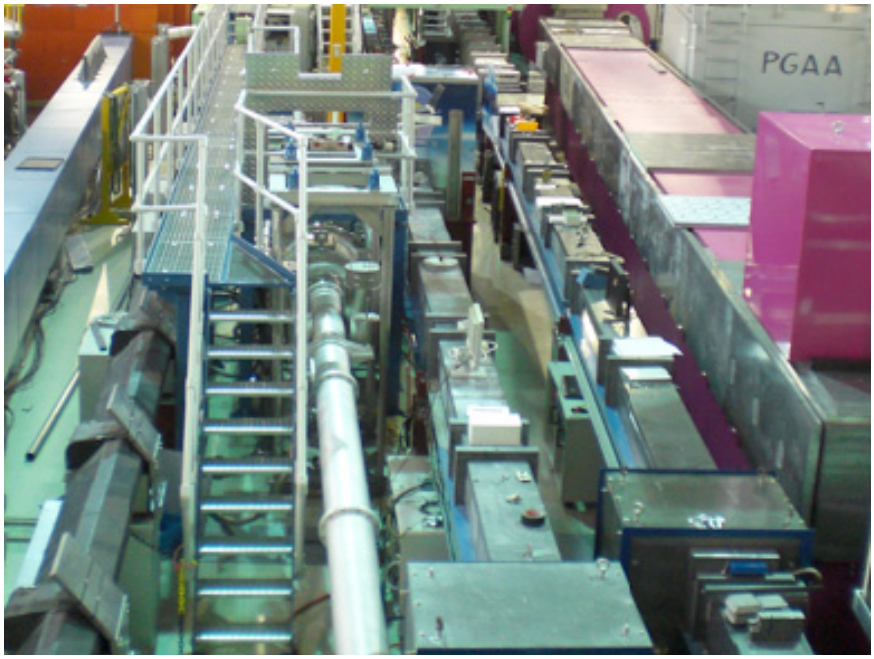

Manual of the JCNS Laboratory Course Neutron Scattering

Contents

1 Introduction

Ultra small angle (USANS) and small angle neutron scattering (SANS) experiments are performed by two different types of instruments to cover a combined Q-range from 10^{-5}Å^{-1} up to 1Å^{-1}. Double crystal diffractometers are used for USANS experiments, whereas the "standard" SANS experiment is performed using a pinhole camera. In principle, the Q-range of both instrument classes overlaps. Typical USANS instruments like S18 (ILL) or PCD (NIST) may reach maximum Q-vectors of $5 \cdot 10^{-3}$Å^{-1}. The disadvantage of these instruments is that they do not allow taking a full area image on a 2D position sensitive detector. On the other hand, the well-known pinhole instrument D11 at Institut Laue-Langevin (France) reaches a minimum Q-vector of $3 \cdot 10^{-4}$Å^{-1} by use of largest possible wavelength 22Å and sample-to-detector distances (>40 m). But the required instrumental settings push both types of instruments to their limits, mainly due to signal-to-noise level and the reduced flux at sample position. The use of neutron lenses as additional elements of a pinhole SANS instrument has been tested to overcome this intensity problem [1].

An alternative design is realized by the KWS-3 instrument [2]. The principle of this instrument is a one-to-one image of an entrance aperture onto a 2D position-sensitive detector by neutron reflection from a double-focusing elliptical mirror. It permits to perform SANS studies with a scattering wave vector resolution between 10^{-4} and 10^{-3}Å^{-1} with considerable intensity advantages over conventional pinhole-SANS instruments and double crystal diffractometers. Therefore it perfectly bridges the "Q-gap" between USANS and SANS: Very Small Angle Scattering (VSANS). The increasing need for these intermediate Q-vectors arises from the growing interest in biological and colloidal samples, which partially deal with length scales in the µm range. An investigation of the multilevel structures in partially crystalline polymer solutions performed using a combination of those three above depicted types of SANS instruments can be found in [3].

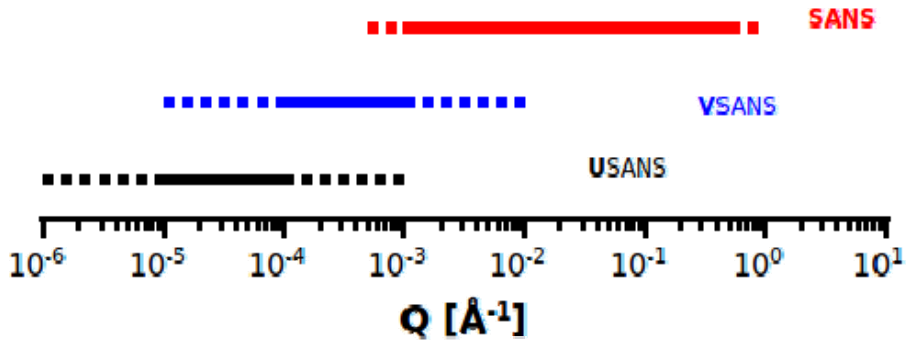

Figure 1: Focused VSANS fills space between USANS (double crystal diffractometer) and classical SANS instruments.

The main innovation and challenge of KWS-3 was to build a large mirror having a shape as close as possible to an ellipsoid and with a surface roughness less than 5 Å. The mirror is a

1.2 m long, 0.12 m wide and 0.05m thick toroidal double focusing mirror of 11 m focal length. At such a short mirror length with respect to the focal length, the toroidal shape is a good enough approximation to an elliptical shape. The reflection plane has been chosen to be horizontal, reducing the deterioration of the image due to gravity. A photo of the mirror is given in Figure 1.

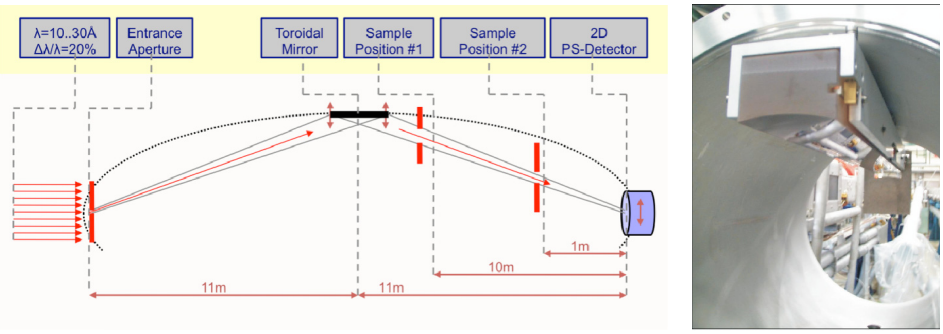

Figure 2:(left) layout of KWS-3;(right) toroidal mirror installed in vacuum its chamber.

KWS-3 is optimized for very small angle scattering range from 10^{-4} to $3\cdot10^{-3}$Å^{-1}. For last cold source filling and instrument configuration the flux at the sample position (and detector) is near **11500** counts per full sample area by use 12.5Å wavelength with 20% wavelength spread, 2x2 mm^2 entrance aperture and 20x100 mm^2 beam size sample-to-detector distance at 9.5 meters.

2 VSANS applications

All applications of the classical SANS could be investigated by VSANS by taking into account Q-resolution of VSANS. The conventional fields of application of very small angle scattering studies are:

- particles in solution [protein aggregates, polymers, micelles, ceramics];
- porous materials [cement, paste, rocks, coal etc.];
- inhomogeneous metallic alloys;
- bulk samples with artificial regular structure [phase gratings];

and other inhomogeneities on a size range from 50 nm to 5 μm, often in addition to SANS spectra, but also diffraction, reflection and refraction studies on surfaces.

3 Preparatory Exercises

1. The contrast variation (CV) is a very important feature of the neutron scattering. What is the scattering length density (SLD) ρ? How to calculate the SLD? What is the definition of the scattering contrast Δρ? How to carry out the contrast variation experiment in case of an aqueous solution of particles?

2. The standard Q-range of KWS-3 is from 10^{-4} to $3\cdot10^{-3}$ Å^{-1}. What the size of particles could be investigated in this Q-range? What are the form factor P(Q) and structure factor S(Q)? In which case the scattering intensity $d\Sigma/d\Omega(Q)$ could be represented as a product of the structure factor and form factor $d\Sigma/d\Omega(Q)= d\Sigma/d\Omega(0)\cdot P(Q)\cdot S(Q)$? What is the physical "content" of the forward scattering $d\Sigma/d\Omega(0)$ [I(0)]?
3. The standard wavelength at KWS-3 is 12.5Å. What are disadvantages of this wavelength? What should we correctly select before sample preparation?
4. What is the difference between pine-hole SANS and focused SANS? Why the beam size at KWS-3 is 20cm^2?

4 Experiment Procedure

Within the frame of this practicum we will explore aquaeous solution of monodisperse polystyrene (PS) microspheres with diameter 8000Å and the initial concentration 1% of particles in H_2O. In future, this sample will be used at KWS-3 as "a standard sample" to check the performance of instrument, absolute calibration, instrument resolution.

In Table 1 there is collected information about PS microspheres obtained from the producer; additionally all necessary information about H_2O and D_2O is listed there.

Table 1. Parameters of used components

	Polystyrene Spheres	H_2O	D_2O
Scattering Length Density [Å^{-2}]	$1.41\cdot10^{-6}$	$-0.56\cdot10^{-6}$	$6.50\cdot10^{-6}$
Density, 20°C [g/cm^3]	1.05	1.0	1.05
Radius [Å]	4000±45		

The contrast variation is proposed to proceed simply by step-by-step adding of D_2O to the initial H_2O solution of spheres. To estimate how much of D_2O we should add, the simulation of the forward scattering should be done as function of D_2O concentration:

$$\frac{d\Sigma}{d\Omega}(0) = \Phi_{Spheres} V_{Spheres} \left(\rho_{Spheres} - \rho_{Water}\right)^2,$$

where $V_{Spheres}$ is volume of PS spheres, $\rho_{Spheres}$ SLD of PS spheres, ρ_{Water} SLD of D_2O/H_2O mixture, $\Phi_{Spheres}$ volume fraction of PS spheres in D_2O/H_2O mixture. We could rewrite the above-mentioned equation in terms of Φ_0 and Φ_{D2O}, the volume fraction of PS spheres in the initial H_2O solution and volume fraction of D_2O in D_2O/H_2O mixture respectively:

$$\frac{d\Sigma}{d\Omega}(0) = \frac{\Phi_0(1-\Phi_{D2O})}{1-\Phi_0\Phi_{D2O}} V_{Spheres} \left[\rho_{Spheres} - \rho_{H2O} - \Phi_{D2O}(\rho_{D2O} - \rho_{H2O})\right]^2.$$

In Figure 3 the forward scattering $d\Sigma/d\Omega(0)$ as a function of Φ_{D2O} and Φ is plotted. At the starting point of the experiment (Φ_{D2O}=0) we have PS spheres in pure H2O and maximal volume fraction of spheres $\Phi_{Spheres} = \Phi_0 = 1\%$. Minimum of the plotted curve corresponds to the matching point of PS spheres in water. In Table 2 seven points around matching concentration are labeled with "CV" mark. In case of CV, from the scattering curves of above-mentioned samples we need to extract only "integral" parameter forward scattering to

extract information about minimum of the forward scattering, and plot it as function of D_2O content.

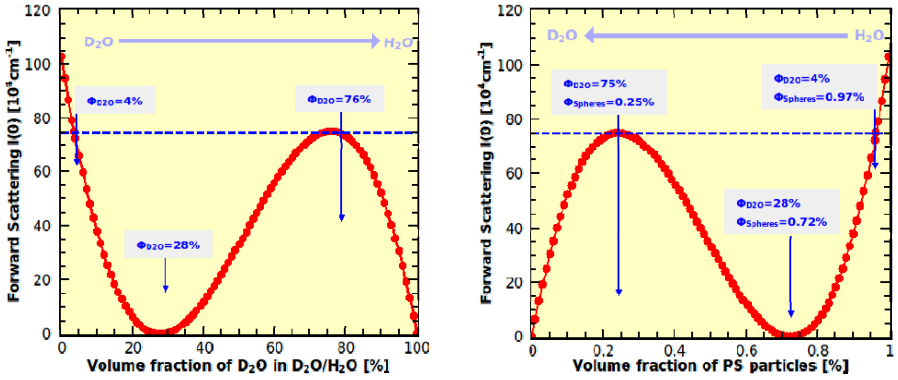

Figure 3. Forward scattering as a function of Φ_{D2O} and Φ.

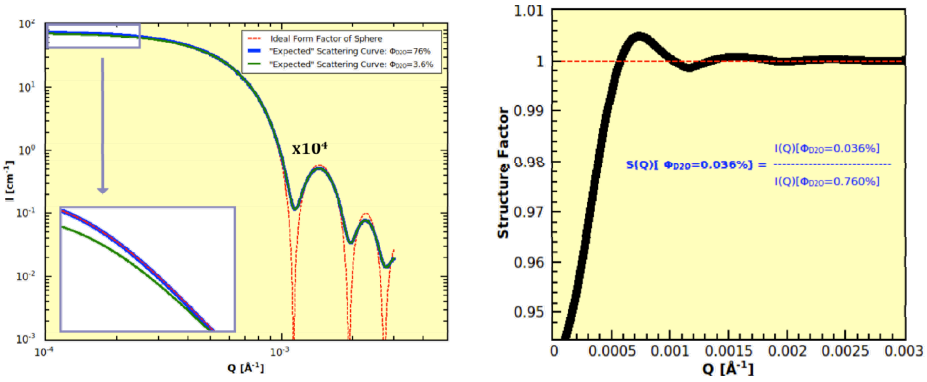

Figure 4: Expected results. (Left) the scattering signal in case of Φ_{D2O}=0.04 and 0.76. In the amplified inset is the small angle part of the calculated scattering curves. In case of Φ_{D2O}=0.04 there is clear suppression of the forward scattering due to the hard sphere interactions. Calculated scattering curve in case of the sample with Φ_{D2O}= 0.76 shows no interaction term. Red curve is pure form factor of PS spheres without taking into account instrumental resolution function. (Right) Ration between Φ_{D2O}=0.04 and Φ_{D2O}=0.76 is plotted here. So the forward scattering and form factor of both sample are the same, and in case of Φ_{D2O}=0.76 sample S(Q) =1, therefore this ratio is the structure factor of Φ_{D2O}=0.04 sample.

Next step is the investigation PS spheres in case of sample with D_2O content 76% [PS content 0.25%]. This point is located at the local maximum (see Figure 3). At this level of the dilution the structure factor is definitely undetectable. Please read carefully caption of Figure 4 to understand the logic of planned experiment.

Table 2. Samples for practicum; CV: samples for the contrast variation; FF, SF: sample for form and structure factor determination.

Φ_{D2O}	0 ^{CV}	3.6$^{FF, SF}$	10 ^{CV}	20^{CV}	30^{CV}	40^{CV}	50^{CV}	60^{CV}	76 ^{FF}
$\Phi_{Spheres}$	1.00	0.96	0.9	0.8	0.7	0.6	0.5	0.4	0.24
I(0)[10^4cm^{-1}]	103	75.2	38	6.5	0.47	12.01	33.2	55.9	75.2

5 The experiment and data reduction

All samples listed in Table 2 we will measure with (Sample) and without (Sample-DB) beamstop. The first one should be measured much longer than the second one. Additionally the empty cell [with (EC) and without (EC-DB) beamstop] and the black current (BC) run will be measured and used for data reduction of all datasets.

What to measure?

I_{Sample}, $I_{Sample\text{-}DB}$, I_{EC}, $I_{EC\text{-}DB}$, I_{BC} [counts per current pixel, normalized by monitor]

Sample transmission:

$$T = I_{Sample-DB} / I_{EC-DB}$$

Empty cell and black current subtraction:

$$I = (I_{Sample} - I_{BC}) - T \cdot (I_{EC} - I_{BC})$$

Absolute calibration:

$$\frac{d\Sigma}{d\Omega}(Q) = \frac{I(Q)}{d \cdot T \cdot \varepsilon_D \cdot \langle I_{EC-DB} \rangle \Delta\Omega(Q)}$$

where d sample thickness, T sample transmission, ε_D detector efficiency, $\Delta\Omega$ solid angle per current pixel, $<I_{EC\text{-}DB}>$ counts on sample.

6 Experiment-Related Exercises

Within our "one-day-experiment" at KWS-3 it would be nice to get as much as possible information about above mentioned sample, like:

a) the form factor P(Q) of PS spheres from sample with Φ_{D2O}=0.76; "real" radius R and polydispersity of the PS microspheres;
b) the structure factor S(Q) in case of Φ_{D2O}=0.04 and decide about the interactions between spheres: could we neglect the structure factor S(Q) during data analysis?

c) the scattering length density of PS spheres by H_2O/D_2O contrast variation. At matching point, the SLD of microspheres and water are equal. Polystyrene in microspheres is amorphous or crystalline?

References

[1] Eskilden, M. R. et al., Nature 391, 563 (2000);
Frielinghaus, H. et al., J. Appl. Cryst. 42, 681 (2009);
[2] Alefeld, B. et al., Physica B 283, 330 (2000);
Kentzinger, E. et al., Physica B 350, e779 (2004);
Goerigk, G. et al., J. Appl. Cryst. 44, 337 (2011);
[3] Radulescu A. et al., Macromolecules 39, 6142 (2006)

Contact

KWS-3

Phone: 089/289-14325
Web: http://www.jcns.info/jcns_kws3
http://iffwww.iff.kfa-juelich.de/~pipich/dokuwiki/doku.php/kws3

Vitaliy Pipich

Jülich Centre for Neutron Science JCNS
Forschungszentrum Jülich GmbH
Outstation at FRM II
Phone: 089/289-10710
e-Mail: v.pipich@fz-juelich.de
Web: http:// iffwww.iff.kfa-juelich.de/~pipich

Zendong Fu

Jülich Centre for Neutron Science JCNS
Forschungszentrum Jülich GmbH
Outstation at FRM II
Phone: 089/289-10716
e-Mail: z.fu@fz-juelich.de

TREFF

Reflectometer

S. Mattauch and U. Rücker

Jülich Centre for Neutron Science
Forschungszentrum Jülich

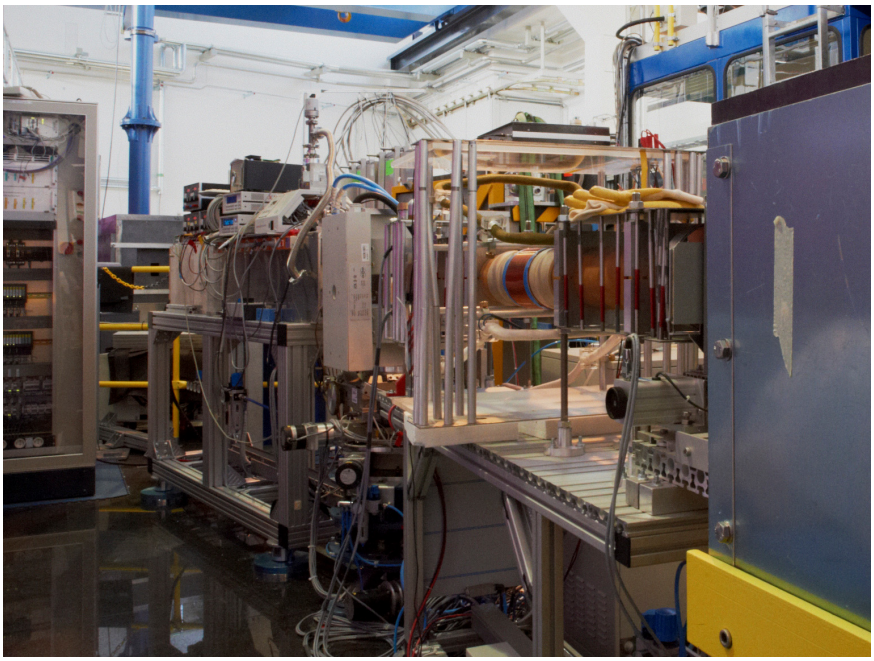

Manual of the JCNS Laboratory Course Neutron Scattering

Contents

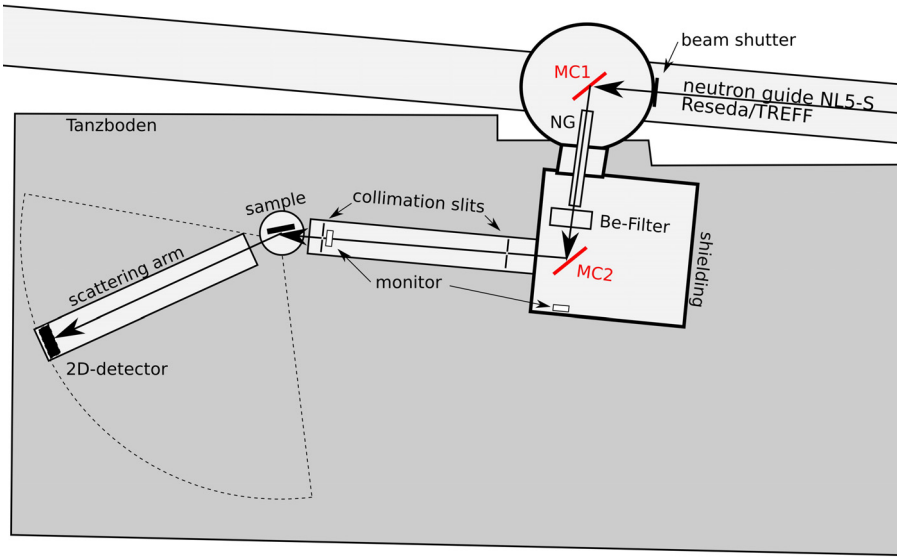

Fig. 1: *Sketch of the reflectometer TREFF@NOSPEC in top view.*

1 Introduction

The neutron reflectometry TREFF@NOSPEC at the neutron guide NL5-S is part of the neutron guide laboratory at the research reactor FRM II in Garching. TREFF is a joint facility of JCNS and the neutron optics group of FRM II. It is used for the investigation of magnetic layered structures as well as neutron optical components for the installation and improvement of neutron scattering instruments.

Figure 1 depicts the neutron reflectometer TREFF in the neutron guide hall of the FRM II research reactor. Essentially, it consists out of a double monochromator, the collimation path, the sample table with several stages of translation and rotation and, finally, the scattering arm with a position sensitive detector. The distance between the collimation slits is 1820mm and 450mm between the second slit and the centre of rotation of the sample table. For this experiment the wavelength is set to λ=4.73 Å.

2 Preparatory Exercises

The following questions will be asked during the practical course at TREFF:

1. In the sketch (Figure 1 of the instrument you will find a Be-filter and a NG (neutron guide) between the MC1 and MC2. What are they used for?

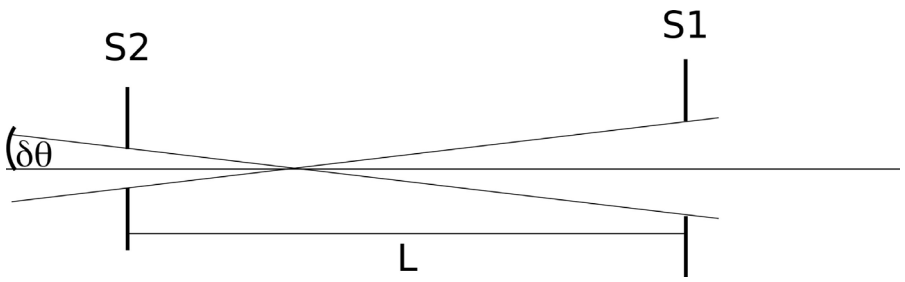

Fig. 2: *This drawing should help you to solve question 5.*

2. In the introduction the used wavelength was given with λ=4.73 Å. Which other wavelength are possible and how do you achieve these?
3. Depict a reflectivity curve of a substrate only
4. Depict a reflectivity curve of a substrate plus a layer
5. Calculate the divergence of a beam passing two slits S1 and S2 in a distance of L (see Figure 2)
6. Calculate the angle of collimation of the neutron beam to sufficiently resolve reflectivity oscillations of a 80nm thick monolayer on a substrate. What slit sizes follow for this reflectometer

3 Experiment Procedure

The aim of this experiment is the investigation of a nickel monolayer deposited on a glass substrate with unknown composition. Using neutron reflectometry the thickness of the nickel layer should be determined.

1. Perform a reflectivity experiment on the sample's back side and analyse the critical angle. To get sufficient collimation of the neutron beam, 0.6mm slit size for S1 and S2 should be taken.
2. Take the reflectivity curve of the Ni-monolayer system with the suitable collimation angles, so speaking the slit size for S1 and S2 calculated in the section before
3. Do like 3) but with a slit size of 3mm for S1 and S2.

3.1 The experiment itself

We (in the end it will be you) will mount the sample on the sample table and pre-align it with an appropriate tool (what could it be) parallel to the neutron beam. After some alignment scans

with the neutron beam we will measure the reflectivity curve step by step of the sample (see chapter Experiment Procedure).

3.2 Data reduction

The instrument saves the number of counts as a function of scattering angle.

3.3 Data evaluation

For systems such as multilayers the scattered intensity is determined by the difference in the potential of each layer (contrast). The potential is given by the **scattering length density** $\rho_{sld} = \sum_j b_j \rho_j$ with the scattering lengths b_j and the particle number densities ρ_j. The index j runs over all kind of atoms of the layer. The scattering length density is comparable to the optical density in light optics.
The **refraction index** of each layer is given by

$$n \gg 1 - \frac{\lambda^2}{2\pi}\rho_{sld} = 1 - \delta$$

.
With the **angle of total external reflection** $\Theta_c \sim \sqrt{2\delta}$, which is usually small, it follows

$$k_{c,z} = k\sin(q_c) \gg kq_c = \frac{2\pi}{\lambda}\sqrt{2\frac{\lambda^2}{2\pi}\rho_{sld}} = \sqrt{4\pi\rho_{sld}}$$

for the **critical wave vector**. For a monolayer system the **reflected amplitude** of each interface $r_{f,1}$ and $r_{f,2}$ can be calculated by the Fresnel formulae (Equation 16 in chapter 12 of the lectures book).
Neglecting roughness at the sample surface and at the interface between layer and substrate, for the amplitude at the surface one gets

$$r_{f,1} = \frac{k_{z,vac} - k_{z,lay}}{k_{z,vac} + k_{z,lay}} \quad \text{and at the interface} \quad r_{f,2} = \frac{k_{z,lay} - k_{z,sub}}{k_{z,lay} + k_{z,sub}}$$

with

$$k_{z,vac} = k\sin(q) \quad , \quad k_{z,lay} = \sqrt{k_{z,vac}^2 - 4\pi\rho_{sld,lay}} \quad \text{and} \quad k_{z,sub} = \sqrt{k_{z,vac}^2 - 4\pi\rho_{sld,sub}}$$

.
The superposition of both amplitudes yields the reflected amplitude of a monolayer sample

$$R = [r_{f,1} + r_{f,2}\exp(2ik_{z,lay}d)]\,\frac{\exp(-2ik_{z,vac}d)}{[1 + r_{f,1}r_{f,2}\exp(2ik_{z,lay}d)]}$$

with the film thickness d. The **reflected intensity** is given by re mean square of R. For $k_{z,vac} > 3k_{c,z}$ the intensity can be calculated in **Born approximation** by

$$|R|^2 \gg \frac{\pi^2}{k_{z,vac}^4}\left[\rho_{sld,lay}^2 + (\rho_{sld,lay} - \rho_{sld,sub})^2 + 2\rho_{sld,lay}(\rho_{sld,lay} - \rho_{sld,sub})\cos(2k_{z,vac}d)\right]$$

4 Experiment-Related Exercises

1. calculate from the reflectivity curve of the glass substrate the scattering length density $\rho_{sld,sub}$
2. Describe the differences and explain them between the measurement of the Ni monolayer with the 3mm slit and the slit size you have calculated.
3. Calculate the scattering length density $\rho_{sld,sub}$ of the Ni monolayer using:

molar volume	V_{Ni}=6.59 cm^3 mol^{-1}
Avogadro number	N_L=6.02 10^{23} mol^{-1}
coherent scattering length	b_{Ni}=10.3 fm

4. Determination of the thickness d of the Ni monolayer using the reflectivity formula in Born approximation. At first, estimate d based on the distance of the fringes of the reflectivity (see Data evaluation chapter).

References

Your lecture book of the year

Contact

TREFF

Phone: 089/289-10768
Web:

Stefan Mattauch

JCNS
Forschungszentrum Jülich GmbH

Phone: 089/289-10709
e-Mail: s.mattauch@fz-juelich.de

Denis Korolkov

Phone: 089/289-10722
e-Mail: d.korolkov@fz-juelich.de

Andreas Ofner

Neutronenoptik Gruppe
Forschungsneutronenquelle Heinz Maier-Leibnitz (FRM II)

Phone: 089/289-14677
e-Mail: andreas.ofner@tum.de

TOFTOF

Time-of-flight spectrometer

G.G.Simeoni

Forschungsneutronenquelle Heinz-Meier-Leibnitz (FRM II)
Technische Universität München

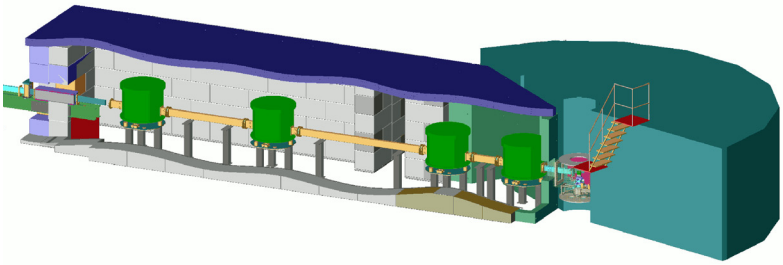

Manual of the JCNS Laboratory Course Neutron Scattering

Contents

1 Introduction

These notes have been written bearing in mind two complementary scopes.
On one side they are intended to introduce you to the experiment at TOFTOF, on the other side they are intended to guide you throughout a critical elaboration of the scientific concepts during and after the experiment at TOFTOF. This means that you are expected to read in advance only the first part of this text.
By the way, your background knowledge should be sufficient for reading the whole text in advance. The second part is therefore left to your time availability and to your curiousity.

With this experiment we will understand what is typical for a liquid dynamical behaviour, how this can be experimentally investigated and then theoretically interpreted.
Specifically, the present introduction together with the measurements at TOFTOF are intended to answer the following questions:

- Which are the macroscopic physical observables (*what can be measured?*)
- How does the experimental technique work (*how can they be measured?*)
- Which is the relationship between microscopic and macroscopic properties (*how the experimental data can be described by a theoretical model?*)
- Which is the interplay between dynamics and thermodynamics when moving on the phase diagram (*which is the influence of the thermodynamic parameters pressure and temperature on what we measure?*)

1.1 Liquid systems and Neutron scattering

Liquid systems belong to the common experience of everyday life [1]. Their thermo-physical properties have been deeply investigated over the last century, due to their relevance for a broad range of applications:

- biology, biophysics, biochemistry, life sciences
- liquid metals and alloys
- geo- and planetary physics (supercritical fluids, interior of planets, seismic propagation, volcanoes, rock formation)
- energy (batteries, fuel elements, plasma physics)
- industry (pharmaceutics, solvents, refrigeration media, components of glues, resins, etc)

Nonetheless, an exhaustive microscopic description is far from having been achieved up to now and often relies on phenomenological models. As a consequence, a satisfactory description of the liquid dynamics is still missing.

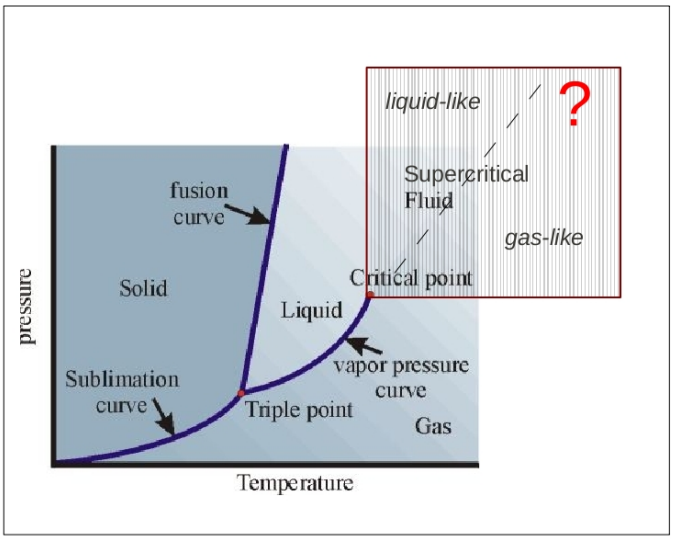

Fig. 1: *P-T phase diagram showing the four condensed states of simple substances, with emphasis on the sub- and supercritical fluid regions.*

The development of the physics of liquids is intimately connected with the development of neutrons scattering and statistical mechanics [2–6]. The success of this fruitful scientific synergy is mostly due to the charge-neutrality of these subatomic particles. Indeed neutrons interact directly with the nuclei, differently from X-rays which are scattered by the surrounding electrons. Thus the atomic positions can be unequivocally identified by those of the nuclei, without invoking the second Born-Oppenheimer approximation typical for X-ray scattering (the so-called *adiabatic approximation*). The atoms are described by (un)deformable (say *hard* or *soft*) spheres, just like statistical mechanics does. In the cold-thermal region ($\lambda > 1$ A), their energy (< 0.1 eV) is not sufficient to promote electronic excitations (few eV), whereas is comparable with the elementary atomic ones (like acoustic and optical phonons). This way the measured intensity, i.e. the *double differential cross section*, can be correlated to the *dynamic structure factor S (q,ω)* and other quantities relevant for the statistical mechanisms.

1.2 Liquid systems: open questions

Despite its formal simplicity, the thermodynamic description of certain phases of the matter is not trivial at all and still contains some fundamental open questions.
Fig. 1 represents a typical P-T phase diagram. We identify the *sublimation curve* (coexistence of solid and gas), the *melting curve* (coexistence of liquid and solid) and the *boiling curve* (coexistence of liquid and gas). The latter is also referred to as *vapour-pressure curve* or *liquid-vapour coexistence line*. Both melting and boiling curve branch off from the triple point, where the three phases are simultaneously in equilibrium. While no experimental evidence of an upper limit to the extension of the fusion curve has been recorded sofar (even though theoretically predictable), it is well-known that the liquid-vapour coexistence curve ends at the critical point.

This has been often described with two distinct phases at the same density mixing and spreading into each other. It means that liquids and gases can continuously convert one into each other without volume change: this is a *second order phase transition*. Any distinction between liquid and gas falls down and the equation of state (both for the ideal case as well as in the Van der Waals formulation) looses its validity [7–12].

On one side, it is nowadays clear that the investigation of the condensed matter cannot be limited to the description provided by the so-called *equilibrium-thermodynamics*. Indeed many scientific research fields (chemistry, optics, biology, cosmology, informatics etc.) often deal with irreversible processes and entropy production. Physical systems (more or less) far away from the thermodynamic equilibrium, if put under external perturbation, can reach new static-dynamical configurations. This happens when the system experiences *local fluctuations* of some macroscopic quantity, able to affect the thermal and mechanical stability of the system. For liquids, this is the case of the density (Fig. 2). Apparently (=over a large scale) the system is under equilibrium, but in reality (=over a short scale) it experiences a lot of local fluctuations. One distinguishes between a *linear regime* (like diffusion and thermoelectricity) and a *non-linear regime* (like the information theory, the biological evolution and other irreversible processes). When far away from the equilibrium, small changes of an external condition (like the pressure) can produce sudden, non-linear response by the system, which leads to instability and biforcation. This represents the essence of what the Nobel-price Ilya Prigogine called *dissipative structures* [13, 14].
On the other side, whereas the supercritical fluid phase is considered thermodynamically homogeneous, the same does not apply to the dynamics. Recently a *dynamical crossover*, i.e. a qualitative change in the dynamical properties, has been detected by means of inelastic X-ray scattering. For the first time, the evidence of a *liquid-like*-to-*gas-like* transition has been provided [15, 16]. The supercritical fluid phase turned out to be parted into two distinct dynamical regions, reminiscent of the subcritical fluid partition. These findings triggered a lot of scientific discussion about the nature of the supercritical fluid and the boiling curve, with the publication of numerous theoretical works, the revival of past concepts and the introduction of new ones. The need of dynamical investigations and *dynamical lines* has been more and more claimed over the last two years [17, 18]. Specifically, at the moment the discussion is focused on the origin (and the name) of the dynamical line separating the two supercritical regions. Other crucial point is wheater it does emanate out from the critical point, as natural continuation of the boiling curve, or just lies nearby: the theoretical interpretation could differ significantly, with important consequences also for the thermodynamic description. All this stressed once again the lack of a satisfactory theoretical model for the liquid collective excitations, and of a systematic investigation of the pressure-behaviour even in the subcritical region [19]. It should be now clear why a deeper understanding of the classical liquid dynamics is required first.

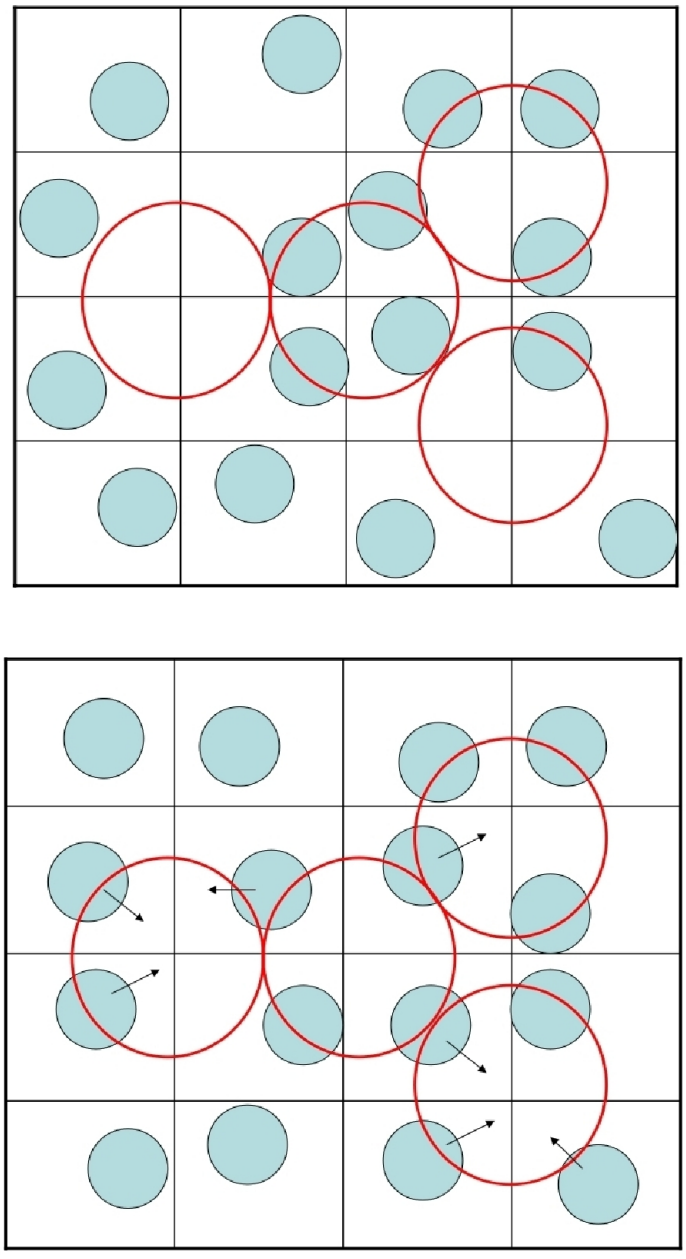

Fig. 2: *DENSITY FLUCTUATIONS*
2D schematic approximation of a typical liquid microscopic structure with macroscopic average density $\rho = N/S$ (N number of particles, L the edge of the surface, $S = L^2$ area of the system). The ratio S/N defines a grid of smaller squares with area $l^2 = S/N$ and edge $l = L/\sqrt{N}$. Each small square is occupied in average by just one atom, in agreement with the value of the macroscopic density: $N/S = \frac{1}{S/N} = 1/l^2$. When looking the system over the rescaled distance 'l', however, we get sensitive to the local fluctuation of the atomic position with respect to centre of the small square. Red circles suggest a different 'grid': their radius 'l' is compatible with the binning of the squared grid, but the local density is different: empty regions coexist with crowded regions (up) and this changes as a function of time (down)

2 Neutron Spectroscopy

The main conceptual difficulty in performing a scattering experiment is probably its formalism, developped in the conjungated space. Differently from the investigated systems, where one spontaneously thinks in terms of space and time, the natural variables for the Neutron Spectroscopy are Q and ω. Beside the formal elegance of the Fourier transforms connecting the two spaces, one could ask why and if this is really necessary.
The main reason is that most of the neutron spectrometers are literally built along the *scattering triangle* formed by the incident and scattered neutron. Moreover, a scattering experiment must satisfy the conservation of momentum and energy, which can be expressed by simple linear equations only in the (Q,ω) space.

2.1 The neutron source FRM II

In general there are two techniques in order to "produce" neutrons – spallation and nuclear fission. During spallation, huge nuclei (e. g. lead) are bombarded with protons, subsequently split and, among others, emit neutrons. The FRM II is a nuclear reactor used as a neutron source. Here ^{235}U captures a thermal neutron and thereby becomes unstable. The nucleus fissures and, among others, emits three fast neutrons.

These fast neutrons must be slowed down (moderated) to thermal energies, that is room temperature, in order to initiate a new fission. The moderated neutrons are further needed for the neutron scattering experiments. The moderation occurs in D_2O of about 300 K which encloses the core.

In order to further slow down the neutrons, and thereby match their energies to the ones of atomic motions, a tank containing liquid D_2 at 25 K is located close to the fuel element. From this *cold source* several neutron guides lead the neutrons to the instuments. Inside these guides, the neutrons are transported by total reflection at the outer walls. The time of flight spectrometer TOFTOF is located at the end of neutron guide 2a in the neutron guide hall.

2.2 The time-of-flight spectrometer TOFTOF

The *cold neutrons* move with a velocity of several hundred m/s. Hence one can determine the kinetic energy of the neutrons comfortably by a time of flight (TOF) measurement along a certain distance. If one sets the initial energy of the neutrons before the scattering event to a well-known value and measures the final energy (or velocity) after the scattering process, the energy transfer can be determined. Since the position of the detectors is fixed, the scattering angle is also known.

During time of flight spectroscopy the energy transfer is measured by a time of flight measurement of the neutrons. The advantage of the time of flight technique is that a huge range of momentum and energy transfer can be captured simultaneously.

TOFTOF is a multi chopper time of flight spectrometer with direct geometry [20]. This means that all neutrons have (more or less) the same energy before interacting with the sample. After being scattered by the sample, the energy transfer can be determined. Both, the tuning of the

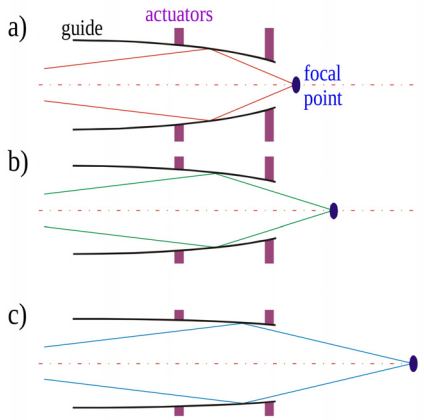

Fig. 3: *Adaptive Optics: depending on the curvature of the neutron guide, it's possible to shift the position of the focus*

energy of the incident neutrons (their wavelength) and the determination of the energy of the scattered neutrons is done by time of flight.

The neutrons are directed to the spectrometer through a neutron guide, which has a supermirror coating. The last part of the neutron guide, the so-called *exchange guide*, allows to switch between two options:

- a linearly-tapered neutron guide, slightly focusing the beam over a sample area of about 2.5 x 4 cm^2 (width x height)
- a non-linearly tapered, focusing neutron guide, able to squeeze the beam over a sample area smaller then 1 cm^2. An increased neutron flux over a reduced sample area is fundamental for the investigation of small samples, like those under extreme-environmnent conditions. Recently installed at the instrument, it couples the leading-edge supermirror coating with the Adaptive Optics technology (Fig.). It represents the first device in the world of such category suitable for Neutron Spectroscopy, and came already successefully routinely into operation with several complex set-ups (high pressure cells, electrostatic- and electromagnetic levitators, high temperature furnaces) [21].

The primary spectrometer consists of seven rotating chopper discs which are placed in evacuated vessels (colored green on the cover page). The discs are made of carbon fibre composites and are coated with neutron-absorbing boron. On opposing sides, slits have been manufactured into the discs through which neutrons can pass. The first and last pair of choppers rotate in opposite direction each.

The incoming white neutron beam is pulsed by the first pair of choppers (pulsing choppers). The short neutron pulse consists of fast and slow neutrons. Thus the pulse spreads along the way to the last chopper pair. These last two choppers (monochromating choppers) select a narrow range of wavelengths out of the pulse. The third and fourth chopper filter out higher orders (higher order removal choppers).

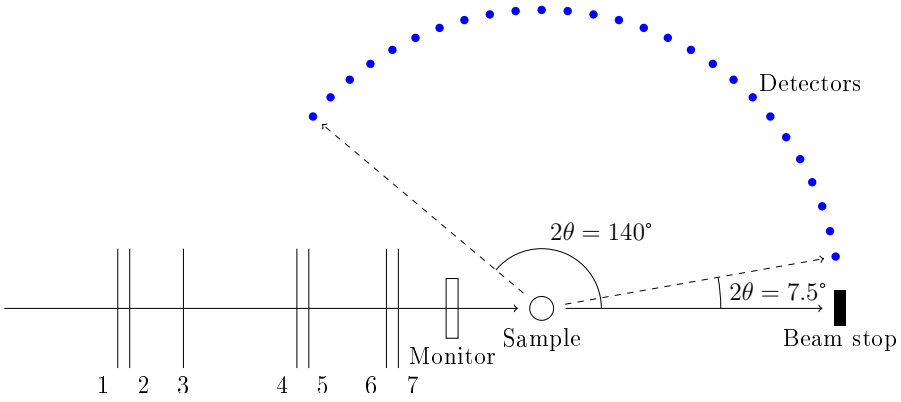

Fig. 4: *Schematic drawing of TOFTOF. Following the neutron guide, first are choppers 1 & 2 which work together with 6 & 7 as velocity selector. Choppers 3 & 4 remove higher orders, 5 is the frame overlap chopper. The time needed for the neutrons to get from the sample to the detectors encodes their energy.*

The fifth chopper is the frame overlap chopper. After the scattering process some neutrons fly towards the detectors. It is essential that all scattered neutrons of one pulse are detected before the neutrons from the next pulse arrive. The overlap of slow neutrons from a pulse with fast neutrons of the following pulse inside the secondary spectrometer is called frame overlap. The frame-overlap-chopper blocks out several pulses, in order to avoid such an overlap.

A good energy resolution can be achieved with a high rotational speed of the chopper discs (up to 22000 revolutions/minute). The energy resolution of the spectrometer can be changed continuously in the range from roughly 5 μeV to 5 meV (Fig. 5). By defining the energy uncertainty one can modify the time of observation in the range from roughly 1 ps to 1 ns.

The intensity of the incident neutron beam is recorded with a monitor, which is located between the primary spectrometer and the sample. A ionization chamber is used as a monitor, filled with fissile matter (^{235}U). The incoming neutrons trigger a fission and the high-energy nuclear fission products generate a clear voltage pulse, due to their high ionization density.

After passing the monitor, the neutrons hit the sample. Most of the neutrons are transmitted and reach the beamstop, but about 10 % of the neutrons are scattered in all possible directions. Some neutrons move towards the detectors and enter the flight chamber, which occupies the space between the sample and detectors. The chamber is filled with argon in order to avoid unwanted scattering with air molecules.

Altogether 1000 ^{3}He-detectors (40 cm long and 3 cm in diameter) are placed tangential to the Debye-Scherrer-circles and also tangential to an imaginary spherical surface with a radius of 4 m around the position of the sample. Thus the flightpath from the sample to the detectors is 4 m long. The scattering angle 2θ covers a region from 7.5° to 140°. The detection of the scattered neutrons inside the ^{3}He-detectors occurs via a (n,p)-reaction. Hereby the neutrons are registered and tagged with a time stamp. The amount of detected neutrons is saved in time of flight bins for each detector in raw data files.

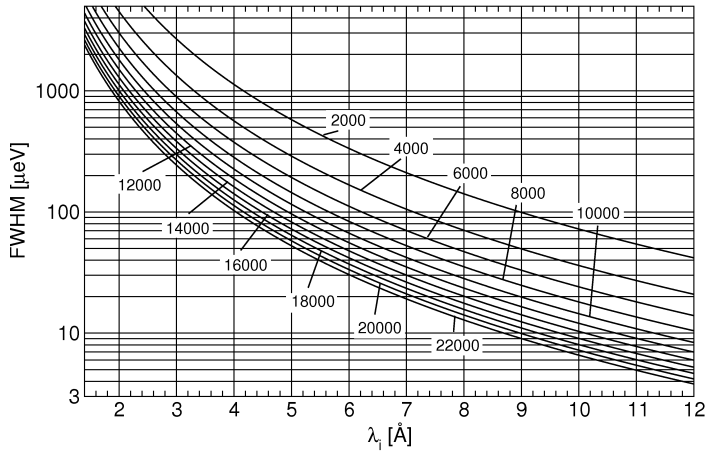

Fig. 5: *Calculated energy resolution of the TOFTOF spectrometer shown for several chopper rotation speeds as function of the initial neutron wavelength. The chopper rotation speeds are given in rounds per minute (rpm) [20].*

2.3 Principle of a scattering experiment

For the mathematical formulation of the *double differential scattering cross section* we rely on the theoretical lectures given by R. Zorn.
Here we summarize only a few key concepts directly related with the geometry of a time-of-flight spectrometer.
The quantities directly measured during the experiment are the scattering angle 2θ and the time of flight of the scattered neutrons. From them, two important quantities are derived (Fig. 6).

- The scattering vector $\mathbf{Q}$ is defined as the difference between the wave vector $\mathbf{k}_f$ of the scattered wave (f as "final") and the wave vektor $\mathbf{k}_i$ of the incident wave (i as "initial"). The momentum gained or lost during the scattering process can be calculated by

$$\Delta\mathbf{p} = \hbar\mathbf{Q} = \hbar(\mathbf{k}_f - \mathbf{k}_i) \; . \tag{1}$$

  However, the momentum transfer is commonly not noted. Instead, the scattering vector is commonly stated in units of inverse Ångstrom.

- The energy transfer ΔE is defined as the energy of the neutron after E_f and before E_i the scattering process:

$$\Delta E = \hbar\omega = \hbar(\omega_f - \omega_i) = \frac{\hbar^2(|\mathbf{k}_f|^2 - |\mathbf{k}_i|^2)}{2m_n} \; . \tag{2}$$

  The energy transfer is measured in meV. Often, ω is written incorrectly instead of $\hbar\omega$.

The absolute value of the wave vectors $\mathbf{k}$ is defined as $|\mathbf{k}| = 2\pi/\lambda$, with an refractive index $n \approx 1$ (which is a very good approximation for neutrons). However, the scattering vector

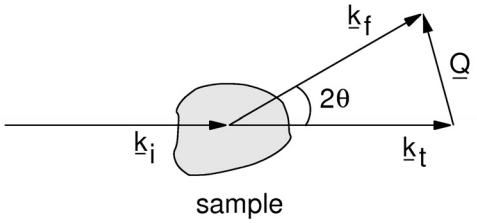

Fig. 6: *Schematic representation of a scattering experiment.* $\mathbf{k}_{i,f,t}$ *are the wave vectors of the initial (incoming), final (scattered) and transmitted neutrons, respectively.* $\mathbf{Q}$ *is the scattering vector.*

cannot be measured directly, only the wave vector of the incident and scattered neutrons. Using the law of cosine one obtains a general equation for converting k_i and k_f to Q:

$$|\mathbf{Q}|^2 = |\mathbf{k}_i|^2 + |\mathbf{k}_f|^2 - 2|\mathbf{k}_i||\mathbf{k}_f| \cos(2\theta) \; . \tag{3}$$

In the case of elastic scattering, the energy transfer is zero. Hence $|\mathbf{k}_i| = |\mathbf{k}_f|$ simplifies the equation to

$$Q = \frac{4\pi}{\lambda} \sin\left(\frac{2\theta}{2}\right) \tag{4}$$

where $Q = |\mathbf{Q}|$.

2.4 The dynamic structure factor: elastic, quasi-elastic and inelastic contributions

As underlined in the previous section, the *double differerential cross section* represents the probability that an incident neutron with energy E_i and wavevector $\mathbf{k}_i$, after the interaction with the sample, possesses energy E_f and wavevector $\mathbf{k}_f$.
Differently from a triple-axis spectrometer, at a time-of-flight spectrometer like TOFTOF it is possible to cover a broad energy and Q-range during a single measurement. The boundaries are set by the energy of the incoming neutrons and the extension of the detector bank, and define the so-called *dynamical range*.
Depending on the property of the neutron or on the property of the sample which one wishes to underline, different distinctions for the neutron scattering are possible:

- coherent vs. incoherent
- elastic, quasi-elastic, inelastic
- single-particle vs. collective
- static vs. dynamic

These distinctions are quite useful during the theoretical description, but strictly speaking one cannot force the system to exhibit only one (or a few) of them. Whether they happen depends only on the physics of the sample and often, during one experiment, they happen all simultaneously. However, in many cases it is possible either to tune the settings of the instrument or to play with the isotopic substitution for enhancing just some of them.
When dealing with spectroscopic techniques, both with light and neutrons, the first natural distinction is given by the energy-position with respect to the elastic line:

- *elastic*, when inside the instrumental energy resolution
- *quasi-elastic*, when exceeding the instrumental energy resolution but still centered around the elastic line ($E = 0$)
- *inelastic*, when not centered at $E = 0$. This is the direct consequence of being a *many-body excitation*. They can be represented by *quantized quasi-particles*, and therefore lead to the presence of two peaks, whose energy shift is symmetric with respect to the elastic line. (We note that, due to the kinematic limitations, the accessible dynamical range is asymmetric with respect to the elastic line. As a consequence, quite often only one of the two inelastic peaks can be experimentally observed)

This definition does not independent on the choice of the sample.
However, their coherent or incoherent nature, as well as their physical meaning, do.
In the case of liquids, the dynamical structure factor contains always a superpositon of:

- *coherent elastic scattering*, related to the *static structure factor* and therefore to the *pair distribution function* (one can imagine a TOF machine like a quite expensive powder diffractometer with excellent time-of-flight resolution and relaxed Q-resolution, able to remove great part of the background contributions with respect to standard diffractometers)
- *incoherent quasi-elastic scattering*, related to the diffusion mechanisms, cluster and nanodomain formation or confinement in complex structures
- *coherent inelastic scattering*, related to acoustic and optical waves

3 Experiment

3.1 The system

As you will be learning during the experiment, liquid partake of both solid and gaseous nature, and present therefore both single-particle and collective features:

- **Diffusion**, a typical single-particle phenomenon, which in dense simple fluids (=liquids) is generally accounted by the *jump model* and described by the *Arrhenius' law*.
- **Visco-elastic acoustic propagation**, which represents the behaviour of the fundamental collective excitations.

We note that diffusion and acoustic propagation are intimately connected by the *fluctuation-dissipation theorem*.
Water is far from being what is generally considered a *simple liquid*, since it exhibts so many anomalies as probably no other liquid substance does. Most of them are at the origin of the life on the Earth.
However, as long as only the diffusive dynamics is concerned, it represents a good candidate for testing the validity of the *Arrhenius' law* and the *jump-diffusion model*.
The *diffusion* represents a quite general phenomenon in which single particles, not constrained on an equilibrium position, move freely across a medium, disturbed only by the numerous collisions with the other particles. In this experiment we consider only the *thermal diffusion*, where entire atoms or molecules move. However, diffusive processes are possible also for other species like electrons, ions, holes.
Depending on the way the collisions affect the temporal propagation of the single particle, one distinguishes between *normal, sub-* and *superdiffusion*. The *Brownian motion* is an example of *normal diffusion*. It is intuitive to understand that the same temporal evolution on the macroscopic scale can be originated by different temporal evolutions on the microscopic scale. Indeed, atoms could move constantly at the same drift velocity or could slow down for a while and then suddenly accelerate. The first case corresponds to the *linear diffusion*, described by the *Fick's law*, whereas the second case is accounted by the *jump-diffusion model*. Why such different behaviours can appear on the microscopic scale depends on the specific atomic local structure (for more details, see the *Supporting materials*).
Independently from the model, the thermal diffusion is promoted by the thermal energy and the diffusion coefficient will increase accordingly to the temperature. The mathematical formulation of this physical evidence leads to the well-known *Arrhenius' law*:

$$D(T) = D_0 exp\big(-\frac{E_a}{k_B T}\big) \tag{5}$$

A huge advantage of investigating liquid water is due to the fact that, by isotopic substitution (D_2O in spite of H_2O), an excellent incoherent-to-coherent contrast can be achieved. This allows the measurement of the incoherent quasi-elastic scattering and of the coherent elastic scattering $S(Q)$ [22]. Consequently, We are going to investigate the influence of both pressure and temperature on the diffusion coefficient, as well as on the position of the first diffraction peak of $S(Q)$.

3.2 The experimental set up

There are different ways of generating pressure on a sample. In the case of liquids, pressures in the range of a few kbar are sufficient for determining considerable alterations of the atomic structures. Technically speaking this is a great advantage, because *gas-* or *hydraulic pressure cells* can be used.
The pressure cell itself is made by a particular Al-alloy whose tensile properties, combined with the particular technical design, allow to support strains up to a 7 kbar. After filling the liquid sample inside the cell, a thin capillary connects it to an hydraulic piston, which contains the pressure trasmitting medium. In the case of water the experiment is particularly easy, because the pressure transmitting medium is also the sample: by compressing the water in the capillary,

one generates pressure on the water in the pressure cell. One can control with great precision the pressure *in-situ*, since it corresponds to the pressure read on the hydraulic piston.

3.3 Data analysis

The instrument saves the number of counts as a function of scattering angle and time-of-flight, $N(2\theta, \text{tof})$. Therefore a data reduction is required for applying corrections and transform the raw data, thus converting them into a scattering function $S(Q, \omega)$. Data reduction (and later on also data evaluation) is done with the program FRIDA [23], and includes the following steps:

1. sum of separated runs performed under the same thermodynamic conditions
2. removal of signal originated by electronic disturbance on the detectors
3. normalization to the neutron flux
4. normalization to the detector efficiency
5. proper handling of the frame-overlap chopper
6. conversion to the (Q, ω) space (without forgetting the Jacobian of the transformation time-to-energy...)
7. correction for the Debye-Waller factor and the the term k_i/k_f
8. correction for the Bose-Einstein thermal population factor

For simplicity, we disregards the multiple scattering correction within this experiment.

After the data reduction performed with FRIDA different sets of data, collected on different samples and under different thermodynamic conditions, will be compared. In the H_2O sample the QENS broadening will be fitted with the standard diffusion model as well as with the jump diffusion model, to get the pressure- and/or temperature-dependence of the diffusion coefficient and check the validity of the *Arrhenius' law*. In the D_2O sample, on the contrary, we will focus on the position of the first diffraction peak and correlate the change in the atomic distances with the change in the thermal diffusivity.

3.4 The jump-diffusion model

The *jump-diffusion model* is based on the image of the *cage*.

"*The incoherent inelastic scattering cross section of slow neutrons from liquids is calculated using a simple model in which the liquid is assumed to have a appreciable short range order in a quasi-crystalline form. Diffusive motion takes place in large discrete jumps, bewtween which the atoms oscillate like in a solid. The model predicts a definite, easily calculable cross section which is not dominated by diffusion effects as when continuous diffusion is assumed, but shows a characteristic variation with angle which could be looked for experimentally. The related pair*

correlation functions are dominated at small r and t by vibrational effects" [24] The model is basically that proposed by Frenkel for liquids close to the melting point in which he assumes that the liquid has locally a lattice-like structure.
The motion of the single atom is then characterized by two time scales [24–27]:

- τ_0, which represents the time spent by the atom confined in the cage
- τ_1, which is the time needed by the atom for moving freely out from one cage and inside a new one

($\tau_1 << \tau_0$)

If now one compares the assumptions of the *standard diffusion* (Brownian motion) with the those of the *jump diffusion model*, one always obtains a Lorentzian shape for the quasi-elastic broadening, but two different functional shape for the Q-dependence of the diffusion coefficient. In the case of the *standard diffusion* which obeys the *Fick's law*, one obtains:

$$S_{\text{diffusion}}(Q,\omega) = \frac{1}{\pi}\frac{|\Gamma_d(Q)|}{\omega^2 + \Gamma_d(Q)^2}\ , \tag{6}$$

whose full-width at half maximum $|\Gamma_d(Q)|$ corresponds to

$$|\Gamma_d(Q)| = 2\hbar D \cdot Q^2 \tag{7}$$

D is the *diffusion coefficient* and is normally given in (m^2/s).

In the case of the *jump diffusion* model, i.e. if we assume the atoms to be often trapped into the cage of the neighbouring atoms, $|\Gamma_d(Q)|$ can be described also as:

$$|\Gamma_d(Q)| = 2\hbar f(Q) \tag{8}$$

where

$$f(Q) = \frac{1}{\tau_0}\big(1 - \frac{1}{(1 + (Ql_0)^2)^2}\ \big) \tag{9}$$

In the limit of small Q, i.e. big distances, we are no more sensitive to the local presence of the cage. In that limit, the *jump diffusion model* reproduces the standard diffusive behaviour, being:

$$D = \frac{2{l_0}^2}{6\tau_0} \tag{10}$$

τ_0 corresponds to the time which the atom spends trapped into one cage.

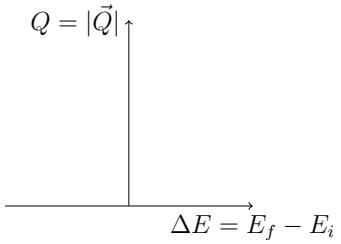

4 Questions

Here some questions for familiarise with the practical details of a TOF experiment.
Please read them in advance and start thinking about. During the the time you'll spend at TOFTOF there will be also the opportunity to discuss and answer them together.

1. do you expect QENS contribution from the D_2O sample?
2. Why is the sample container made of aluminum?
3. To calculate the energy of neutrons in meV with a well-known wavelength given in Å, one can use a formula
$$E \approx \frac{a}{\lambda^2} \,. \tag{11}$$
Determine a numerical value for a. How big is the initial energy E_i of the neutrons in the current experiment?
4. What is the maximal energy transfer from the neutron to the sample?
5. What is the maximal energy transfer from the sample to the neutron?
6. Draw at least six scattering triangles (as shown in Fig. 6) for these points in the dynamical range:
   - Elastic scattering with a scattering angle of 7.5°; with a scattering angle of 140° (the first & last detector at TOFTOF)
   - Same scattering angles with neutron energy gain
   - Same scattering angles with neutron energy loss
7. Locate those points in this dynamic range plot:
   and determine which area in this plot is accessible in the current scattering experiment
8. would it be possible to measure the acoustic phonons in water at TOFTOF? (the typical sound speed for longitudinal phonons is about 1500 m/s).
9. assuming a jump-diffusion model, how does the pair correlation function look like?
10. under a physical point of view, which is the microscopic difference between the origin of the Debye-Waller factor and the diffusion?

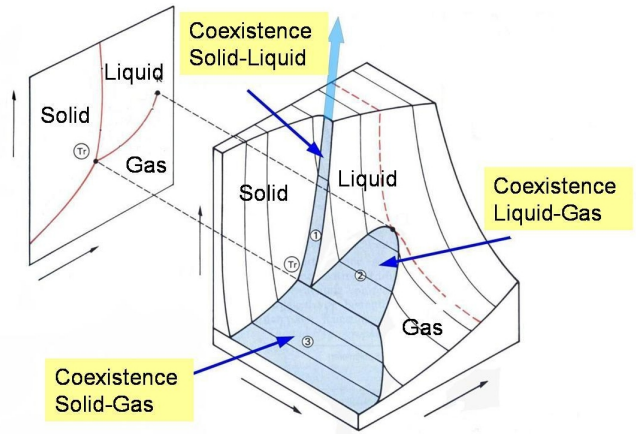

Fig. 7: *3D equation of state with its projection onto the P-T plane*

5 Supporting material: Theory of liquid systems

5.1 Equation of state and phase diagrams

One of the major merits of the thermodynamics is its capability of describing the collective behaviour of a many-body system by means of just a few macroscopic variables.
An equation of state is a functional relationship between these thermodynamic variables (pressure, temperature and density), which defines the locus of all (P,T, ρ) points corresponding to a state of equilibrium. A phase diagram is nothing that the projection of this surface onto one of the three planes generating its tridimensional (P,T, ρ) space (Fig. 7). Specifically, the P-T phase diagram turns out to be the most useful diagram for visualizing the thermodynamic boundaries of all phases of the matter. The solid lines define the P-T range of stability of each phase, on the lines themselves two distinct phases coexist and upon crossing one solid line a phase transition takes place. These are the so-called *first oder phase transitions* and are always accompanied by a discontinuity of an extensive quantity (such as volume or entropy).
Considering that the most relevant thermodynamic quantities (specific heats, compressibility, thermal conductivity and other thermodynamic response functions) are defined as derivatives of extensive quantities, the discontinuity of the latter at the phase transition determines a discontinuity in the thermodynamic quantities (their left and right derivatives differ). Here some examples:

$$C_V = (\frac{\partial Q}{\partial T})_T = T(\frac{\partial S}{\partial T})_V \tag{12}$$

$$C_P = (\frac{\partial Q}{\partial T})_P = T(\frac{\partial S}{\partial T})_P \tag{13}$$

$$K_T = -\frac{1}{V}(\frac{\partial V}{\partial P})_T = \frac{1}{\rho}(\frac{\partial \rho}{\partial P})_T \tag{14}$$

$$K_S = -\frac{1}{V}(\frac{\partial V}{\partial P})_S = \frac{1}{\rho}(\frac{\partial \rho}{\partial P})_S \tag{15}$$

being ρ the mass density and S the entropy of the system.

Thus thermodynamic response functions are generally monitored when looking for whatever phase transition. Experimentally it is impossible to quantify the absolute internal energy of the sample, it is often difficult (and not necessary) to observe its structure, but it is quite easy to measure quantities like the specific heats as a function of changes of pressure or temperature.

5.2 Dynamics: What is a liquid?

The most appropriate answer is probably: *An intermediate phase between solid and gas*.
With respect to their atomic structure, liquids share with gases features like the atomic mobility and the absence of long-range order, but are characterized by high packing fraction and density values comparable with those of solids.
"The central problem in an attempt to understand the nature of the liquid from first principles is that of accounting for its bulk macroscopic properties in terms of the structure, motion, and mutual interactions of the molecules of which it may be presumed to be composed. Even leaving out of account still more difficult questions concerned with liquid's characterisitic fluidity, and asking only about those of its properties that characterize it in a state of equilibrium (its density, specific heat, compressibility, and so forth), we are yet far from convincing and comprehensive account of the connection between the macroscopic and microscopic levels." [28]

With respect to the dynamics, the liquid motions result by the superposition of *solid-like*, lattice vibrations around equilibrium positions and *gas-like*, ballistic-collisional diffusive motions. These two contributions couple so strongly to each other that its impossible to develop a theory treating one of the two as simple perturbation.
At this point it's worth to mention the *Mode-Coupling Theory* (MCT) for viscous liquids, developed by W. Goetze and coworkers in Mn̈chen (TUM -Department of Physics) [29–31].

5.3 Cage effect

The result of the combination of *solid-like* and *gas-like* character is generally depicted by the so-called *cage effect*.
Let's observe one single atom (Fig. 8):

1. **for very short times**, corresponding to distances shorter that the interatomic ones, it behaves like a free-particle and experiences pure ballistic motion

2. **for intermediate times**, it collides with the neighbours but, due to the high packing fraction, cannot escape their *cage*. It remains therefore confined in a certain area, resembling a lattice vibration

3. **for long times**, the continuous collisions and the corresponding energy transfer with the surrounding succeed in relaxing the cage for a while, and the atom can escape the confinement (this is often referred to as *jump-diffusion model*)

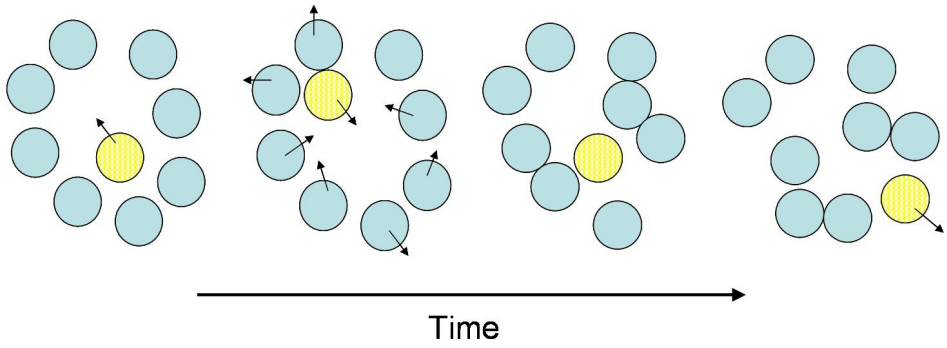

Fig. 8: *Schematic description of the cage effect and its temporal evolution: trapping by the neighbouring atoms and escape*

The image of the *cage* fits quite well with the traditional distinction in solids, liquids and gases based on energetic considerations. The dynamics of a physical system is namely determined by its free energy, which accounts for the competition between potential energy $|U_{pot}|$ and kinetic energy E_{kin} (and other thermodynamic potentials, if applicable):

- solids: $|U_{pot}| >> E_{kin}$
- liquids: $|U_{pot}| \approx E_{kin}$
- gases: $|U_{pot}| << E_{kin}$

Following a statistical-mechanics approach, the potential energy represents the confinement by the cage and the kinetic energy the probability of escaping the cage after several collisions. This is clearly a thermally activated process: the higher the temperature, the higher the kinetic energy and the atomic velocity, the higher the frequency of the collisions and the energy transfer to the surroundings in the unit of time. Macroscopically, this is described by the *Arrhenius' law* for the diffusion coefficient and the viscosity.
The immage of the *cage* is only the simplest microscopic description of a disordered medium, but it turned out to be often sufficiently successeful in describing the effects of the short-range order on the macroscopic phenomena.

5.4 Relaxation mechanisms

Just like people, physical systems don't like to be disturbed. When perturbed, they will react to the best of their possibilities in order to minimize the disturbance. Sometimes this will restore the initial equilibrium, sometimes will lead to a new one. Depending on the specific atomic structure, this implies either the propagation of the disturbance, or its local dissipation or a combination of both (damped propagation). As a matter of fact, the system will:

- either transfer the disturbance to another region of the system (something similar to a *domino effect*)

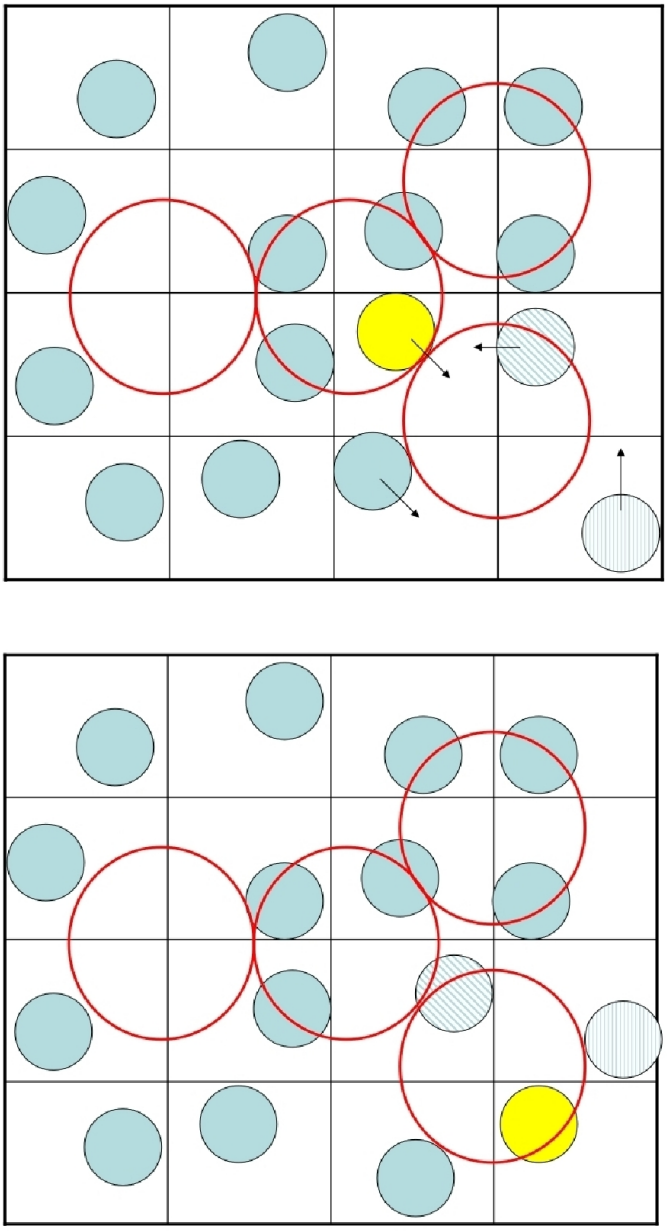

Fig. 9: *COOPERATIVE REARRANGEMENTS*
Due to the real dimensions of the atoms, to their kinetic energy and short-range Coulombian repulsion, it's impossible the double occupancy of a small square l^2 by two atoms simultaneously. An atom can enter another area only forcing a group of atoms to collectively rearrange themselves. Assuming to be able to label each atom, they will finish in different areas, but the single occupancy will be satisfied.

- or promote a local structural rearrangement (like changing place in the bus when it starts getting to crowded close to the entrance)
- or generate heat dissipation (when one has no other alternative...)

The second option, however, is possible only in dense disordered systems (liquids and supercritical fluids), where the interplay between the high density and the atomic mobility introduces additional *decay channels*. Let's consider a longitudinal collective wave (say a *phonon*). This will involve a coordinated motion of a great amount of atoms, and is therefore possible only assuming that the wave possesses enough energy for inducing it. In disordered systems, however, the same amount of energy can be spent for promoting a local rearrangement of the atoms: when the wave arrives, they change their spatial configuration in spite of propagating the input to their neighbours. When this happens, the perturbation is considerably damped or even stopped over a short-range scale. This is something analogous to the invenction of the wheel, which can lower the friction by converting a linear motion into a rotational one. These mechanisms are called *relaxations* and are characterized by *relaxation times*. Generally speaking, a density fluctuation will always force the atoms to move somewhere else. This translates into a velocity disturbance, which can relax through collision or heat dissipation, with the latter producing a temperature disturbance. Any disturbance determines a relaxation of the system towards a more equilibrated situation (which could differ from the original one). How these relaxations happen depends on the shear and bulk viscosity (velocity disturbance), and on the thermal conductivity (temperature disturbance).
This provides a sintetic description of the *Linear Hydrodynamics*:

- τ_{th}, the time required for thermal diffusion to take place
- τ_α, related to collective rearrangement of the local structure

In the case of complex liquids, exhibiting additional microscopic degrees of freedom, also a third relaxation is to be considered:

- τ_β, due to microscopic intramolecular rearrangement and normally called *instantaneous*, since the characteristic timescale is much shorter than that generally investigated.

For the purposes of the current experiment at TOFTOF, let's focus on τ_α, the so-called *structural relaxation*. Every time that an atom exits the *cage*, the local density fluctuates from its equilibrium value, and the local structure becomes unstable under the pressure of the high packing fraction. The atoms are therefore forced to reorganize themselves towards another, more homogeneous, spatial configuration (Fig. 9). This can be represented by a local density gradient and its corresponding particle flux (mass transport, *Fick's law*). Moreover, the *cage* is not isolated but embedded in a system of other "cages & escaping particles", all interacting with each other at a certain degree (depending on the density value). This is a collective (many-body) process, which involves the simultaneous, cooperative rearrangement of the particles : it cannot be easily decomposed in the sum of several independent pair contributions. It represents quite well the essence of a typical *complex system* and it's probably at the origin of the difficulty of its collective description.
The time required by the cage for relaxing and releasing the energy accumulated during the collisions corresponds to τ_α, and the phenomenon has been often modeled as the charge and discharge of a condensator (Fig. 10)

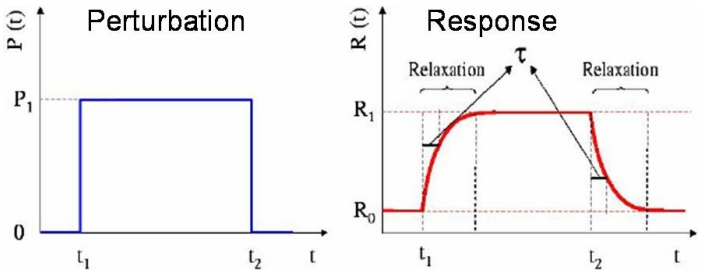

Fig. 10: *Response to an external perturbation: Charge and discharge of a condensator as model for the relaxation mechanisms*

5.5 Q-dependence: the dynamical regimes

Dense disordered systems, like liquids and glasses, are characterised by the absence of long-range order. Still, some short-range correlations persist, and their physics strongly depend on the length scale taken into consideration.
When averaging the dynamic properties over the whole system (i.e. in the *continuum limit*), the typical textbook hydrodynamic behaviour is observed. When looking at the interatomic scale, however, one appreciates the local deviations from the average behaviour: indeed, one could either observe the collisions between two atoms or the motion of one atom between two collisions (Fig. 2). The typical length scale, over which the system is observed, is inversally proportional to the momentum Q transferred by the probe (photons or neutrons) to the sample. The values of Q are considered *small* or *big* with respect to the position of the first diffraction peak of the *static structure factor S(Q)*. Let's call it Q_1. As shown by Fig (Fig. 11) we can distinguish three different regimes [32]:

- **Collective regime** for $Q < Q_1$ (as shown in next paragraph, this includes different acoustic regimes, accessible by tuning the frequency of the probe)
- **Kinetic single-particle regime** for $Q > Q_1$, where phenomena due to the motions of single particles are observed
- **Free particle regime** for $Q >> Q_1$, where Q corresponds to a length scale shorter than the typical interatomic scale and single particles can be regarded as isolated

5.6 Frequency-dependence: the visco-elasticity

An acoustic wave is a pressure wave which propagates across a medium by generating a spatial-time periodic deviation of the local density with respect to its equilibrium value: rarefaction and compression zones alternates. In the case of liquids, this interacts with their continuous intrinsic atomic rearrangements (vibrations, diffusion, cage effect, relaxation mechanisms).
The frequency of the acoustic wave introduces a characteristic experimental observation time. As a consequence, entering the *high-frequency dynamical regime* the response of the system deviates from the pure hydrodynamics, and starts getting sensitive to the complexity of the atomic structure. This rules both for single-particle and collective properties and defines the

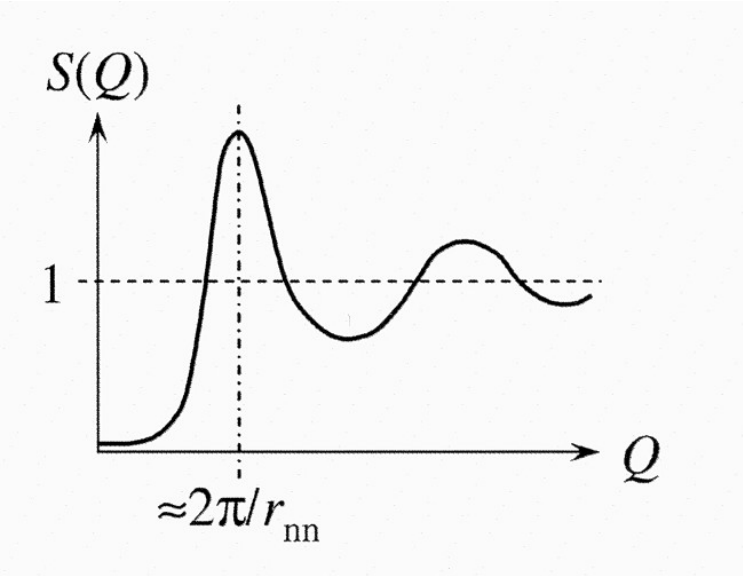

Fig. 11: *Static structure factor*

realm of the *Generalized Hydrodynamics*, where thermodynamic constants are replaced by Q-dependent thermodynamic functions. This is the case also for the diffusion coefficient, where the typical hydrodinamic values are approached only in the limit of $Q = 0$. Let's call ω the frequency of the investigated excitations: then $\tau = 1/\omega$ will be the corresponding experimental observation time. By comparing τ with τ_α two scenarios are possible:

- *liquid-like*, viscous behaviour: $\tau > \tau_\alpha$, and the local structure has enough time for reorganizing itself, thus damping the wave propagation
- *solid-like*, elastic behaviour: $\tau < \tau_\alpha$, and the wave propagates undisturbed, seeing the local atoms as *froozen*

The sound speed is defined as the slope of the dispersion curve, which roughly correponds to the ratio between the frequency ω of the acoustic excitations and its momemtum tranfer Q at small Q values. Due to the presence of relaxation mechanisms, activated at low propagation frequencies but froozen at high propagation frequencies, the high-frequency regime is then caracterized by an enhancement of the apparent sound speed with respect to the low-frequency regime. Roughly speaking: if one calculates the slope of the acoustic phonons measured by Brillouin light spectroscopy and does the same with data taken by x-ray or neutron spectroscopy, the values are different and much higher in the second case.

This phenomenon is called *positive sound dispersion* or *fast sound*, and is commonly considered the dynamical fingerprint of a *liquid-like behaviour* [33].

5.7 The pair distribution function

Differently from solids, where the atoms are well localized around the lattice equilibrium positions, in liquids only a probabilistic approach can be developed. As long as the typical supercritical density values are not reached, the *pairwise interaction* among particles is a good approximation. The *pair distribution function* g(r) describes the probability of finding two particles at a distance r. It is nothing but a way of measuring and testing the spatial distribution of the particles in a given plane (no tridimensional information is provided). It is an oscillating function of **r**, whose amplitude decreases as **r** increases. Being a density of probability, the maxima correspond to the most probable interparticle distances, while negative values denote the impossibility to found two particles a particular distance **r**. A liquid an isotropic system, thus **r** can be replaced by *r*.
The shape of the g(r) reflects that one of the interatomic potential energy. Let us now consider for simplicity, without loosing generality, a Lennard-Jones interatomic potential. The maxima of g(r) correspond to the minimum of the potential V(r) (i.e. the equilibrium position), while the minima of the g(r) arise from the small-r repulsive part of V(r). Since the amplitude of g(r) is more and more damped whit increasing r, the oscillations do not extend indefinitely but tend to the asymptotic unitary value. The number of distinguishable maxima provides the number of (not) direct neighbours with which a particle holds somewhat spatial correlation along a given direction. At this point we remember that the so-called *static structure factor* S(Q) is related to the pair distribution function by a Fourier transform:

$$S(\mathbf{Q}) = 1 + n \int d\mathbf{r}[g(\mathbf{r}) - 1]exp(i\mathbf{Q} \cdot \mathbf{r}) \tag{16}$$

Since Q is the conjugated variable of **r**, S(Q) embodies the counterpart of the pair distribution function in the Q-space. Powder diffractometers are the typical instruments dedicated to the investigation of the $S(Q)$. However, without carrying out the entire mathematical calculations, we can observe that *coherent elastic scattering* responsible for the diffraction pattern is measured also within an experiment at time-of-flight spectrometer [34]
The *double-differential cross section* can be separated as:

$$\left(\frac{\partial^2\sigma}{\partial\Omega\partial E'}\right) = \left(\frac{\partial^2\sigma}{\partial\Omega\partial E'}\right)_{coh} + \left(\frac{\partial^2\sigma}{\partial\Omega\partial E'}\right)_{incoh} \tag{17}$$

$$\left(\frac{\partial^2\sigma}{\partial\Omega\partial E'}\right)_{coh.} = \left(\frac{\partial^2\sigma}{\partial\Omega\partial E'}\right)_{coh.el.} + \left(\frac{\partial^2\sigma}{\partial\Omega\partial E'}\right)_{coh.inel.} \tag{18}$$

For the elastic case, using the formal definition of the coherent cross section:

$$\left(\frac{\partial^2\sigma}{\partial\Omega\partial E'}\right)_{coh.el.} = N\langle b\rangle^2\, S(Q,\omega)_{coh.el.} \tag{19}$$

and integrating over the whole energy range (in the experiment this roughly corresponds to the energy resolution):

$$\left(\frac{\partial\sigma}{\partial\Omega}\right)_{textcoh.} = N\langle b\rangle^2 \mathrm{S(Q)} \tag{20}$$

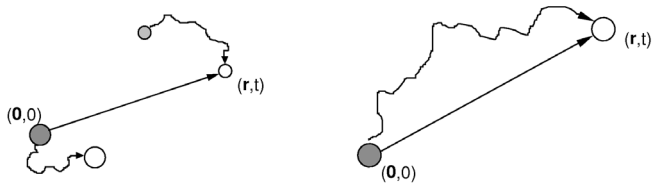

Fig. 12: *Left: distinct pair correlation, right: self pair correlation. In the case distinct, the second particle may be a different one than the first one but it doesn't have to.*

5.8 The pair correlation functions

We observe that the asymptotic unitary value of g(r) is typical of a structureless system. This is reasonable, considering that it corresponds to the macroscopic level, where the matter can be considered as a continuum. Owing to that, it is also often introduced the *pair correlation function* G(r), which weights the degree of correlation of the fluid:

$$G(r) = g(r) - 1 \tag{21}$$

.

In the case of a gas, G(r) is identically null.

Aiming at describing the dynamics of the system, the time-dependent pair correlation functions are fundamental. When introducing the temporal evolution, it's possible to follow either one single particle or the correlations between different particles. For this reason, the time-dependent *pair correlation function* $G(r,t)$ can be dividided into a *distinct* and a *self* contribution.

The *distinct pair correlation function* $G_D(\mathbf{r},t)$ gives the probability to find a particle j at time t at the place $\mathbf{r}$ if this or another particle i was at time $t = 0$ at the origin $\mathbf{r} = \mathbf{0}$, as shown in Fig. 12. The pair correlation function is

$$G_{\mathrm{D}}(\mathbf{r},t) = \frac{1}{N}\sum_{i=1}^{N}\sum_{j=1}^{N}\int \langle \delta\{\tilde{\mathbf{r}} - \mathbf{R}_i(0)\} \cdot \delta\{\tilde{\mathbf{r}} + \mathbf{r} - \mathbf{R}_j(t)\}\rangle \,\mathrm{d}\tilde{\mathbf{r}}\,, \tag{22}$$

with the number of particles N, an integration variable $\tilde{\mathbf{r}}$ and the place $\mathbf{R}_j(t)$ of particle j at time t. The angle brackets $\langle\rangle$ denote an ensemble average.

The *self pair correlation function* or *auto-correlation function* $G_{\mathrm{S}}(\mathbf{r},t)$ gives the probability to find one particle at time t at place $\mathbf{r}$ if this very particle was at time $t = 0$ at the place $\mathbf{r} = \mathbf{0}$, see again Fig. 12. It is defined as

$$G_{\mathrm{S}}(\mathbf{r},t) = \frac{1}{N}\sum_{i=1}^{N}\int \langle \delta\{\tilde{\mathbf{r}} - \mathbf{R}_i(0)\} \cdot \delta\{\tilde{\mathbf{r}} + \mathbf{r} - \mathbf{R}_i(t)\}\rangle \,\mathrm{d}\tilde{\mathbf{r}}\,. \tag{23}$$

In the following, we will assume that the samples are powder samples (i. e. not single crystals, so for example liquids) and will therefore use the absolute value of $\mathbf{r}$, r, instead of the vector.

It is possible to calculate the *distinct* and *self* pair correlation functions from the scattered intensities. Roughly, the calculation is as follows.

Looking at the momentum and energy change of the neutrons during the scattering process, one obtains the *double differential scattering cross section* which can be seen as the sum of a coherent and an incoherent part:

$$\frac{\partial^2\sigma}{\partial\Omega\partial E'} = \frac{k_f}{k_i}\frac{N}{4\pi}\left(\sigma_{\text{coh}}S_{\text{coh}}(Q,\omega) + \sigma_{\text{inc}}S_{\text{inc}}(Q,\omega)\right) . \tag{24}$$

It denotes the probability that a neutron is scattered into the solid angle $\mathrm{d}\Omega$ with an energy change $\mathrm{d}E'$, with N the number of scattering nuclei.

The Fourier transform in time and space of the coherent scattering function $S_{\text{coh}}(Q,\omega)$ is nothing but the *distinct* pair correlation function $G_{\text{D}}(r,t)$ and the Fourier transform in time and space of $S_{\text{inc}}(Q,\omega)$ is the *self* correlation function $G_{\text{S}}(r,t)$.

If a scatterer performs several motions simultaneously (but independently from each other), the resulting scattering function is a convolution in energy space of the single scattering functions, for example

$$S_{\text{total}}(Q,\omega) = S_{\text{diffusion}}(Q,\omega) \otimes S_{\text{internal motion}}(Q,\omega) . \tag{25}$$

If two scatterers perform two motions independently from each other and both cause scattering, the recorded total scattering function is simply the sum of the two scattering functions, for example

$$S_{\text{total}}(Q,\omega) = S_{\text{solute}}(Q,\omega) + S_{\text{solvent}}(Q,\omega) , \tag{26}$$

Due to the limited number of supporting points it is not possible to anti-transform the experimental data for getting the pair correlation functions. Therefore, one proceeds the other way round: after inventing a plausible correlation function, one performs a Fourier transform of this theoretical function to a scattering function and checks if this can describe the data.

The hereby obtained theoretical scattering function $S_{\text{theor}}(Q,\omega)$ is fitted to the measured scattering function $S_{\text{meas}}(Q,\omega)$ after convolving the theoretical scattering function with the measured instrumental resolution. The instrumental resolution is often determined using a vanadium sample which is a static, incoherent scatterer.

5.9 Diffusive mechanisms

All them belong to those *transport phenomena* accounted by the *linear thermodynamics*. As far as the direct correlations are concerned, the motion is described by the *Green-Kubo equations*:

- Fourier's law (thermal conductivity)
- Fick's law (thermal diffusivity)
- Ohm's law (electrical conductivity)

The crossed effects (like the thermo-conductivity), on the other side, are described by the *Onsager's equations*.

Under a microscopic point of view, the thermal diffusion is ruled by the *Langevin equation*, which describes the motion of a particle in a viscous medium:

$$m\frac{d\mathbf{v}}{dt} = -\alpha\mathbf{v} + \eta(t) \tag{27}$$

The friction coefficient α embodies the collective action of the surrounding medium on the moving particle, whereas $\eta(t)$ accounts for thermal fluctuation and is generally called *noise*. The *noise* is a function which contains information about the microscopic structure of the system, its spatial correlations and local temperature (the so-called *thermal bath*).
Let us consider first the case of the Brownian motion: this is purely markovian (random walk), and the *noise* presents no spatial-temporal correlation.

We define with $\mathbf{r}(t) = (x(t), y(t), z(t))$ the instantaneous position of a molecule, and considere an isotropic medium where $\mathbf{r}$ can be replaced by r. Then, in absence of an external force:

$$< \delta r >= r(t) - < r >= 0 \tag{28}$$

The same doesn't apply to the *mean squared displacement* $< \delta r^2 >$, whose time-behaviour reflects the microscopic structure of the system.

The most general definition of the *diffusion coefficient* is:

$$D = \frac{1}{2}\lim_{t\to 0}\frac{d}{dt} < dx^2 > \tag{29}$$

whose extension to the three-dimensional space leads to:

$$D = \frac{1}{6}\lim_{t\to 0}\frac{d}{dt} < dr^2 > \tag{30}$$

(in an isotropic medium $< dx^2 >=< dy^2 >=< dz^2 >= \frac{1}{3} < dr^2 >$)

In the case of *normal diffusion* (say *Brownian motion*), the experimental observation time determines two distinct regimes [35]:

- short-time ballistic regime, where the transient component dominates: $< \delta r^2 >= \frac{KT}{m}t^2$
- long-time viscous regime: $< \delta r^2 >= \frac{6KT}{\alpha}t$

In the case of *normal diffusion* D is a constant and the long-time behaviour can be rewritten as:

$$< \delta r^2 >= 6Dt \tag{31}$$

In the case of other mechanisms affecting the single-particle propagation, a different functional relationship between the diffusion coefficient and the observation time could appear. According to this, three different options are possible: *normal*, *sub-* and *super-diffusion*.

Up to now we focused on the equation of motion of the single particle. An alternative description is based on the equation of motion of the spatial correlations (i.e. the temporal evolution) of the particle itself.
This leads to the *Fokker-Planck equation*

$$\frac{\partial P(x,t)}{\partial t} = D\frac{\partial^2 P(x,t)}{\partial^2 x} - F\frac{\partial P(x,t)}{\partial x} \tag{32}$$

which represents something analogous to the *Langevin equation* for a quite general distribution of probability P(x,t). It can be demostrated that the *self pair correlation function* $G_{\mathrm{S}}(r,t)$ is solution of this equation. This provides an excellent connection between experimental observables (like the diffusion coefficient) and theoretical calculations (like the correlation functions). F describes whatever external force acting on the diffusing particle, in analogy with the temporal correlations of the noise $\eta(t)$. In absence of external force, i.e. when the noise $\eta(t)$ is totally uncorrelated (Markovian process), the *Fokker-Planck equation* reduces to the *Fick's law*:

$$\frac{\partial P(x,t)}{\partial t} = D\frac{\partial^2 P(x,t)}{\partial^2 x} \tag{33}$$

References

[1] M.W. Zemanski, "Heat and Thermodynamics" (1968) New York:McGraw-Hill.

[2] U.Balucani and M. Zoppi, "Dynamics of the Liquid State" (1994) New York: Oxford University Press.

[3] J.-P. Boon and S. Yip, "Molecular Hydrodynamics" (1980) New York:McGraw-Hill.

[4] J.-P. Hansen and I.R. McDonald, "Theory os Simple Liquids" (1986) London:Academic.

[5] S.W. Lovesey, "Theory of Neutron Scattering from Condensed Matter" (1987) Oxford: Clarendon Press

[6] W.Montfrooji and I. de Schepper, "Excitation in simple liquids, liquid metals and superfluids" (2009) Oxford University Press.

[7] J.D. Van der Waals, *Zeitschrift Physikalische Chemie* **13**, 657 (1894).

[8] B. Widom, *Journal of Chemical Physics* **43**, 3892 (1965).

[9] B. Widom, *Journal of Chemical Physics* **43**, 3898 (1965).

[10] S. Fisk and B. Widom, *Journal of Chemical Physics* **50**, 3219 (1969).

[11] H.E. Widom, "Phase Transitions and Critical Phenomena", (1972) London: Academic Press.

[12] H.E. Stanley, "Introduction to Phase Transitions and Critical Phenomena", (1971) Oxford University Press.

[13] D.K. Kondepudi and I.Prigogine, "Modern Thermodynamics" (2005) Wiley.

[14] I. Prigogine and D.K. Kondepudi, "Thermodynamique. Des moteurs thermiques aux structures dissipatives" (1999) Odile Jacob, Paris.

[15] G.G. Simeoni, T. Bryk, F.A. Gorelli, M. Krisch, G. Ruocco, M. Santoro and T. Scopigno, *Nature Physics* **6**, 503 (2010).

[16] P.F. McMillan and H.E. Stanley, *Nature Physics* **6**, 479 (2010).

[17] V.V.Brazhkin and K.Trachenko, *Physics Today* **65**, 68 (2012).

[18] V.V.Brazhkin, Yu.D. Fomin, A.G. Lyapin, V.N.Ryzhov,and K.Trachenko, *Phys. Rev. E* **85**, 031203 (2012).

[19] N.W. Ashcroft, "International School Enrico Fermi on High Pressure Phenomena" (2002) Societa' Italiana di Fisica.

[20] T. Unruh, Jürgen Neuhaus, and Winfried Petry, *Nucl. Instrum. Methods Phys. Res. A* **580**, 1414 (2007).

[21] G.G. Simeoni et al., "Focusing Adaptive Optics: Neutron Spectroscopy under Extreme-Conditions environments", in preparation

[22] J.Teixeira, M.-C. Bellissent-Funel,S.H. Chen, A.J. Dianoux *Phyisical Review A* **31**, 3 (1985).

[23] J. Wuttke and F. Kargl, "FRIDA data analysis version 1.2" (2006) `http://sourceforge.net/projects/frida`.

[24] C.T. Chudley and R.J. Elliott, *Proc. Phys. Soc.* **77**, 353 (1961).

[25] B.N. Brockhouse, *Nuovo Cimento Suppl.* **9**, 45 (1958).

[26] B.N. Brockhouse, *Phyisical Review Letters* **2**, 287 (1959).

[27] B.N. Brockhouse and N.K. Pope, *Phyisical Review Letters* **3**, 259 (1959).

[28] B. Widom, *Science* **157**, 3787 (1967).

[29] W. Goetze, in "Les Houches Summer School of Theoretical Physics" Session LI (1989).

[30] W. Goetze, "Liquids, Freezing and the Glass Transition", edited by J.P. Hansen, D. Levesque and J. Zinn-Justin (1991) pp.289-503

[31] D.R.Reichman and P.Charbonneau, "Mode-coupling theory" *Journal Statistical Mechanics* (2005) P05013.

[32] A. Cunsolo, PhD- Thesis, Universita' La Sapienza, Roma, Italy

[33] T. Scopigno, G. Ruocco and F. Sette, *Rev. Mod. Phys.* **77**, 881 (2005).

[34] A. Furrer, J. Mesot and T. Straessle, "Neutron Scattering in Condensed Matter Physics" (2009) World Scientific.

[35] J.-P. Bouchaud and A. George, *Physics Reports* **195**, 127-293 (1990).

Contact

TOFTOF

Phone: 089/289-14881
Web: http://www.frm2.tum.de/wissenschaftliche-nutzung/spektrometrie/toftof/index.html

Dr. Giovanna G. Simeoni

Forschungsneutronenquelle Heinz Maier-Leibnitz (FRM II)
und Physik Department E13
Technische Universität München

Phone: 089/289-14975
e-Mail: giovanna.simeoni@frm2.tum.de

Band / Volume 51
Exploring the electronic properties of novel spintronic materials by photoelectron spectroscopy
A. Herdt (2012), ii, 126 pp
ISBN: 978-3-89336-831-0

Band / Volume 52
Quantum Information Processing
Lecture Notes of the 44th IFF Spring School 2013
February 25 – March 8, 2013 Jülich, Germany
D. DiVincenzo (Ed.) ca. 1000 pp
ISBN: 978-3-89336-833-4

Band / Volume 53
Real-Space Finite-Difference PAW Method for Large-Scale Applications on Massively Parallel Computers
P.F. Baumeister (2012), vi, 212 pp
ISBN: 978-3-89336-836-5

Band / Volume 54
Einfluss unkonventioneller Medien auf die Selektivität ThDP-abhängiger Enzyme
T. Gerhards (2013), XIV, 199 pp
ISBN: 978-3-89336-846-4

Band / Volume 55
Aufbau einer Vierspitzen-Rastertunnelmikroskop/Rasterelektronenmikroskop-Kombination und Leitfähigkeitsmessungen an Silizid Nanodrähten
E. Zubkov (2013), 150 pp
ISBN: 978-3-89336-848-8

Band / Volume 56
Interplay between magnetic and dielectric phenomena at transition metal oxide interfaces
D. Schumacher (2013), IV, 128 pp
ISBN: 978-3-89336-855-6

Band / Volume 57
Single $NdPc_2$ Molecules on Surfaces: Adsorption, Interaction, and Molecular Magnetism
S. Fahrendorf (2013), viii, 100 pp
ISBN: 978-3-89336-856-3

Band / Volume 58
Heyd-Scuseria-Ernzerhof Screened-Exchange Hybrid Functional for Complex Materials: All-Electron Implementation and Application
M. Schlipf (2013), XV, 170 pp
ISBN: 978-3-89336-857-0

Band / Volume 59
Orbital-dependent exchange-correlation functionals in density-functional theory realized by the FLAPW method
M. Betzinger (2013), vi, 173 pp
ISBN: 978-3-89336-858-7

Band / Volume 60
Structural influences on electrical transport in nanostructures
R. D. Frielinghaus (2013), viii, 190 pp
ISBN: 978-3-89336-867-9

Band / Volume 61
Study of intermolecular interactions in hetero-organic thin films
B. Stadtmüller (2013), viii, 198 pp
ISBN: 978-3-89336-871-6

Band / Volume 62
Structure, magnetism and excitations in some Mn-based magnetocaloric effect compounds
M. Gottschlich (2013), 175 pp
ISBN: 978-3-89336-874-7

Band / Volume 63
Neutron Scattering
Lectures of the JCNS Laboratory Course held at Forschungszentrum Jülich and at the Heinz Maier-Leibnitz Zentrum Garching
edited by Th. Brückel, G. Heger, D. Richter, G. Roth and R. Zorn (2013),
ca 350 pages
ISBN: 978-3-89336-880-8

Band / Volume 64
Neutron Scattering
Experiment Manuals of the JCNS Laboratory Course held at Forschungszentrum Jülich and at the Heinz Maier-Leibnitz Zentrum Garching
edited by Th. Brückel, G. Heger, D. Richter, G. Roth and R. Zorn (2013),
ca. 150 pages
ISBN: 978-3-89336-881-5

Weitere ***Schriften des Verlags im Forschungszentrum Jülich*** unter
http://wwwzb1.fz-juelich.de/verlagextern1/index.asp

Schlüsseltechnologien / Key Technologies
Band / Volume 64
ISBN 978-3-89336-881-5

JÜLICH
FORSCHUNGSZENTRUM